The University Of Sheffield.

SELECTIVE LASER MELTING OF SAM1651, AN IRON-BASED BULK METALLIC GLASS

Navid Manai

A thesis submitted in partial fulfilment of the requirements for the degree of Doctor of Philosophy

The University of Sheffield

Department of Materials Science and Engineering

July 2017

به پدر و مادر عزیزتر از جانم

Acknowledgments

First of all, I would like to sincerely thank my supervisor, Professor Iain Todd for his constant support, valuable advice and guidance, endless help and encouragement throughout my doctorate. I am sure at times, you wondered what on earth I was doing, but without your invaluable patience and constant encouragement, I would not have got here.

I really appreciate the financial support for this project provided by the Department of Materials Science and Engineering, without which this work would not have been possible.

I would like to thank the members of staff in the Department of Materials Science and Engineering at the University of Sheffield. To Ben Palmer, Michael Bell, Beverley Lane, Ian Watts, Frank Fletcher, Paul Hawksworth and Dr Nik Reeves for their kind generous help during endless hours of sample preparation and characterisation. To Karen Burton and Ann Newbould for their considerate support in dealing with the administration-related matters.

Big love to the fellow students in our group, Lampros, Laura, John, Amit, Chris, Everth, Jon and Sam who made my time in the department enjoyable. To James Hunt, who always met my technical and purchasing requests with a big smile and actually made them happen and to Haider Ali whose invaluable advice and help improved the quality of this work significantly.

Samira, your kindness, patience and love kept me going throughout the sleepless nights of these years; I cannot thank you enough but I'll try my best, khanoom. Finally, I want to express my deepest gratitude to my parents, Bijan and Bita, who have been my rock in every second of my life and have made it possible for me to pursue my dreams. You are and will always be my role models in life.

Abstract

Fe-based bulk metallic glasses, have been shown to demonstrate exceptional strength, hardness, soft magnetic properties, high electrical resistivity, high corrosion resistance and large glass forming ability. They also have low production costs, since the main constituent element is Iron which in comparison to other bulk glass forming alloys are much cheaper to manufacture. Hence, various magnetic and structural applications have been suggested for parts made out of these alloys.

Selective laser melting process as an additive manufacturing route was utilised to circumvent the issue of size and shape limitation in fabrication of parts out of bulk metallic glasses. Specimens of the SAM1651 Fe-based BMG alloy were fabricated to investigate the effects of different SLM processing parameters on the microstructure of these parts. They were examined through optical microscopy and X-ray diffraction and the influence of point distance, hatch spacing, layer thickness, laser power, exposure time and substrate temperature was individually investigated to demonstrate how they result in different amounts of porosity, lack of fusion defects, cracking and crystallization in the fabricated samples.

Through utilising the results of a finite element analysis, it was shown that a combination of the occurring thermal gradient and cooling rate in individual melt pools produced as a result of using different laser power and exposure time values can determine and predict the existence and relative amount of crystallization in these specimens. It was also demonstrated that through increasing the temperature of the substrate, the amount of cracking occurring in the microstructure of the specimens can be reduced, which is due to decreasing the influence of the thermal gradient mechanism through decreasing the amount of thermal gradient present in the heat affected zone of individual melt pools.

Furthermore, normalized energy density input was shown to be an appropriate indicator to predict the level of defect formation and crystallization relatively and therefore a processing map was constructed which consequently presented a processing window for fabrication of specimens by selective laser melting out of SAM1651 BMG alloy. Using the processing parameters in this processing window, samples with complex shapes were manufactured to demonstrate the feasibility of their fabrication with amorphous microstructure and minimal defect formation.

Since the making of specimens out of SAM1651 alloy, with no cracking and porosity, was unsuccessful, future approaches were suggested in order to manufacture fully amorphous dense parts with no cracking using the SLM process and glass forming alloys. Also, further modelling was proposed to investigate the effect of hatch spacing, layer thickness and point distance values on the residual thermal stresses occurring in the selective laser melting process.

Table of Contents

1. Introduction

Bulk metallic glasses are a relatively new class of glassy alloys which can be produced with a large (more than 1 mm) section thickness or diameter and unlike the previously discovered amorphous alloys, they require significantly smaller cooling rates to produce (by an order of 10^6) (Schneider, 2001). The supercooled liquid region (the temperature range between the glass transition temperature and the crystallization temperature) is one of their attractive characteristics, in which their formability increases by orders of magnitude (Y. Ge *et al.*, 2010). They possess higher strength, the values of which exceed the strength of corresponding crystalline alloys approximately twofold (for example, Ti-based BMGs have an ultimate strength of about 2.2 GPa, while for crystalline titanium alloys, it is only 1.1– 1.3 GPa) (Inoue, 1995; Johnson, 1999). The conditional yield stress ($\sigma_{0.2}$) for Cu-based, Ti-based, and Zr-based BMGs reaches ~2 GPa; for Ni-based BMGs ~3 GPa, for Fe-based BMGs ~4 GPa, for Fe and Co-based BMGs ~5 GPa, and for BMGs based on the Co–Ta–B alloys ~6 GPa. Metallic glasses possess not only large strength, but also high hardness, wear resistance, and elastic deformation (ε) up to 2%. Another important advantage of BMGs is their high corrosion resistance, including passivation in certain solutions (Pang *et al.*, 2004). The main cause of this phenomenon is the presence of a single-phase structure and absence of specific crystal lattice defects such as dislocations and grain boundaries. In addition, Iron-based and cobalt-based alloys are excellent magnetically soft materials with an exclusively low coercive force (e.g. 0.25 A/m for $Co_{43}Fe_{20}Ta_{5.5}B_{31.5}$ (Akihisa Inoue *et al.*, 2003)), sufficiently high saturation magnetization (e.g. 1.51 T for $Fe_{76}Si_9B_{10}P_5$ (Makino *et al.*, 2008)), and permeability.

Bulk metallic glasses (BMGs) have been the subject of extensive research worldwide, in the past three decades, since they were produced, in the 1990s. They have received huge attention from both metallurgical and glass researchers, because of their phenomenal properties. Whilst they display highly impressive elastic characteristics, their room temperature plasticity has been their main downturn, as it seems to be almost non-existent. The absence of conventional mechanisms of plastic deformation, for example, dislocation or twin-type ones, which are inherent to crystalline alloys, determines the low plasticity of amorphous alloys (Pozdnyakov and Glezer, 2002). This means forming these glass-forming alloys, into desired shapes, through conventional processing procedures, has been constantly under study. However, metallic glasses are still not as brittle as oxide ones, and in general they occupy an intermediate place by the value of fracture toughness between ceramics and crystalline alloys. Moreover, it should be noted that recently produced BMG alloys $Zr_{61}Ti_2Cu_{25}Al_{12}$ (He *et al.*, 2011) and $Pd_{79}Ag_{3.5}P_6Si_{9.5}Ge$ (Demetriou *et al.*, 2011) possess a record-high fracture toughness of about 100 MPa$\sqrt{m}$.

Bulk metallic glasses have important application regions in connection with high mechanical properties (Ashby and Greer, 2006; N Nishiyama, Amiya and Inoue, 2007). These materials are already used to fabricate sport goods, watches, shields of electromagnetic waves, optical devices, moving parts of micromachines, pressure sensors, the Coriolis flow meters (Nobuyuki Nishiyama, Amiya and Inoue, 2007), medicine tools, bioimplants (especially in the case of nanostructured metallic glasses (Chen *et al.*, 2013)) and biodecomposable implants (Zberg, Uggowitzer and Löffler, 2009; Yu *et al.*, 2013). In addition, they can be used as wear-resistant and corrosion-resistant coatings (Petrzhik *et al.*, 2005). BMG alloys exhibit high solubility of hydrogen (for example, palladium-based alloys) and, being saturated with it, show considerable resistance to embrittlement. They turned out promising for application in

separators for fuel elements owing to the good penetration ability of hydrogen through membranes by Zr–Hf–Ni (Hara *et al.*, 2003) and Ni–Nb–Zr (Yamaura *et al.*, 2003) alloys. Powders of Mg-based and Fe-based metallic glasses manifest excellent efficiency in the decomposition reaction of azo dyes compared with iron-based powders, their crystalline analogs, and crystalline magnesium (J. Wang *et al.*, 2012; J.-Q. Wang *et al.*, 2012). Thin amorphous oxides on the BMG surface can be used to fabricate electronic devices (Trifonov *et al.*, 2015), while Fe–Cr–Zr BMG thin films have optical transmittance up to 0.9 with the conservation of electrical conductivity and ferromagnetism (Louzguine-Luzgin *et al.*, 2014).

Fe-based bulk metallic glasses, specifically, have been shown to demonstrate exceptional strength, hardness, soft magnetic properties, high electrical resistivity, high corrosion resistance and large glass forming ability. They also require low production cost, since the main constituent element is Iron which in comparison to other bulk glass forming alloys like zirconium, titanium, palladium and magnesium based alloys is much cheaper to manufacture. Various applications have been reported for Fe-based BMGs due to these properties, such as Liqualloy cores which are used in noise suppression sheets, AC-DC convertors, DC-DC convertors, shot peening balls (A Inoue *et al.*, 2003), coatings on disk cutters for tunnel-boring machines (Farmer *et al.*, 2009), coatings for maritime applications (Farmer *et al.*, 2005) and coating for the inside of the transportation vessels containing spent nuclear waste (Choi *et al.*, 2007).

One of the main constraints in fabricating parts out of bulk metallic glasses, through conventional methods, has been the size and shape of the specimens since they were first discovered. This is due to the requirement for keeping the cooling rate during solidification above the critical cooling rate of the glass forming alloy in every part of the specimen being fabricated which means the size of the samples has been limited to rods with diameters of

smaller than 20mm or plates with limited thickness. Recently, production methods like thermoplastic forming which involve manufacturing of the BMG parts in their supercooled liquid region has been shown to be successful in partially overcoming this size and shape issue, however for larger sizes and more complex shapes, they still do not seem to be the solution.

This is why, additive manufacturing and specifically selective laser melting (SLM) of specimens with bulk metallic glass alloys has been the subject of investigation lately. Since this net shape production method is carried out in a point-by-point manner in which every point experiences cooling rates of up to 10^8K/s, theoretically fabrication of fully amorphous parts with any size and shape should be feasible. In practice, however, because of the thermal history that the specimens experience during the SLM process, it has been reported that some samples include crystallized components and/or structural defects in their microstructure.

Some have cracks which has been attributed to the thermal gradient mechanism occurring in the heat affected zone (HAZ) of the melt pools created during the SLM process. Because of the high temperatures experienced in the upper layers of the HAZ, they would tend to thermally expand, however the lower temperature material in the lower layers of the HAZ and the surrounding material restricts this expansion and this causes compressive stresses in these upper layers which can be larger than the yield strength of the material and hence cause plastic deformation. After this compressively deformed material cools down, the compressive state of its stress changes into residual tensile stress and these residual stresses can be the cause of crack formation, delamination and disconnection from the base plate in the SLM fabricated parts. To resolve this, pre-heating the substrate or rescanning of each layer with the laser beam has been studied for a range of glass forming alloys.

Others have crystallised phases which have been associated with the glass forming alloys experiencing temperatures above their crystallization temperature. Also, the material in the heat affected zone experiences temperatures between T_m and T_g, which means if enough heat accumulation occurs in this area, crystallization is possible through structural relaxation. So, by increasing the number of pulses used in fabrication of specimens, which translates into more accumulation of heat in the HAZ, more of the crystallized component can be observed in the heat affected zone. Optimisation of the processing parameters of the selective laser melting process contributing to the energy input density of the laser beam has been shown to be effective in keeping the specimens amorphous.

In this study, SAM1651, a Fe-based glass forming alloy, with the composition of $Fe_{48}Cr_{15}Mo_{14}C_{15}B_6Y_2$ (atomic percent), was used to investigate the influence of different SLM processing parameters, namely, laser power, exposure time, point distance, hatch spacing, layer thickness and substrate temperature on the crystallization behaviour and formation of different defects like porosity, cracking and lack of fusion defects. In order to do this, 5x5x2.5mm cubes were manufactured through the selective laser melting process with different processing parameters and their microstructure were examined using optical microscopy and X-ray diffraction. Afterwards through optimisation of these processing parameters and balancing the formation of these defects, several complex specimens were fabricated to demonstrate the feasibility of manufacturing fully amorphous parts with minimal defects.

2. Literature Review

2.1. Amorphous Alloys

The microstructure of solid materials can be either crystalline (morphous) or amorphous. Crystalline solids have a long-range structural order with a recognizable lattice, which consists of a unit cell periodically repeating in three dimensions and a space group. Glasses on the other hand are disordered or exhibit order over a length scale that can be from short-range to medium-range, hence comparatively are called amorphous. They have an atomic configuration that, from a topological point of view, is relatively disordered, however they show characteristics of an isotropic solid (Miller and Liaw, 2008).

For thousands of years, it was accepted as a universal law, that when a metallic liquid is cooled down from above its melting temperature to room temperature at an ordinary cooling rate of about 1 Ks^{-1}, it will solidify into a crystalline structure. However, in 1960, Duwez et al discovered the first exception, when they vitrified $Au_{75}Si_{25}$ alloy from its molten state. It was found that when the metallic liquid is solidified at a very fast cooling rate (about 10^6 Ks^{-1}), the resulting product could have a disordered atomic structure, which is very much like the one present in the liquid state (Klement, Willens and Duwez, 1960).

The need to utilize a high cooling rate, however, meant that the final specimen had to have at least one dimension small enough to allow every part of the specimen to be vitrified upon solidification. So, at the time, it was assumed that ribbons, foils, films and powders would be the only metallic products that could be made with an amorphous structure. Furthermore,

due to precipitation of a crystalline phase and consequently catastrophic embrittlement inside the specimens, experiments to increase their size were proved to be failures, which strengthened the above-mentioned theory (Chen, 2000).

2.2. Bulk Metallic Glasses

These amorphous alloys did not exhibit any glass transition temperature or supercooled liquid region (the thermal range between glass transition temperature and crystallization temperature) prior to crystallization, upon heating (Inoue and Takeuchi, 2011). Yet, in the 1980s, a series of studies was started to look into the effects of structural relaxation on the properties of amorphous alloys. Among other characteristics, a quantitative evaluation of the change in configuration enthalpy (the internal energy of the metallic glass which can be different if it is in a relaxed or unrelaxed atomic configuration) was studied in the annealed state; and for that, the supercooled liquid region was selected as a relaxed reference point, since it is in an internal equilibrium.

As a result, amorphous alloys which would show a clear glass transition temperature and a wide supercooled liquid region were needed to be developed to give more reliable, reversible and quantitative data on structural relaxation. So, in a period between 1988 and 1992 a series of metallic glasses with these properties were found (Akihisa *et al.*, 1988; Inoue, Zhang and Masumoto, 1990; Inoue *et al.*, 1991). Having a larger supercooled liquid region (SCLR) meant that these alloys would be more stable and resistant toward crystallization in their SCLR, which on its own, meant that they could be produced and shaped in bulk form by conventional casting methods and under slower cooling regimes.

2.2.1. Glass Forming Ability

Soon it was realized that if a metallic glass part with a bigger geometry was to be made, or as it is called, a bulk metallic glass specimen, the alloy would need to have a high glass forming ability (GFA). Basically, the GFA of an amorphous alloy is the outcome of a competition between two elements; stability of the liquid phase and stability of the resulting crystalized phase. Thus, if the liquid phase is stabilized somehow, and the precipitation of the crystalized phase is hindered, then the glass formation ability will be improved.

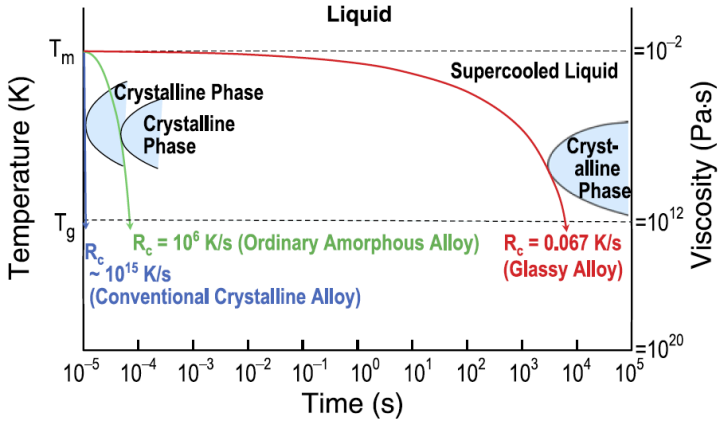

Figure 2.1- Schematic illustration comparing cooling rates needed to fabricate crystalline, amorphous and bulk glassy specimens (Inoue and Takeuchi, 2011).

Essentially, the larger the glass forming ability of an alloy is, the lower the critical cooling rate of the solidification process needs to be. Critical cooling rate values for some bulk metallic glasses have been shown in the table below. It also means the critical thickness of the resulting specimen would be larger. The problem is that, it is not easy to measure the critical cooling rate accurately. So, a range of different indicators have been proposed over the years to facilitate predicting the glass forming ability of a metallic glass.

Alloy Composition	R_c (K s^{-1})
$Au_{77.8}Ge_{13.8}Si_{8.4}$	3×10^6
$Ca_{60}Mg_{25}Ni_{15}$	24
$Ca_{65}Mg_{15}Zn_{20}$	<20
$Cu_{50}Zr_{50}$	250
$Cu_{48}Zr_{48}Al_4$	<40
$Cu_{42}Zr_{42}Ag_8Al_8$	4.4
$Fe_{43}Cr_{16}Mo_{16}C_{10}B_5P_{10}$	100
$Fe_{40}Ni_{40}P_{14}B_6$ (Metglas 2826)	4.4×10^7
$Hf_{70}Pd_{20}Ni_{10}$	124
$La_{55}Al_{25}Cu_{20}$	58
$La_{55}Al_{25}Ni_{20}$	69
$Mg_{65}Cu_{25}Gd_{10}$	1
$Mg_{65}Cu_{25}Y_{10}$	100
$Mg_{65}Cu_{15}Ag_5Pd_5Gd_{10}$	0.7
$Mg_{65}Cu_{7.5}Ni_{7.5}Ag_5Zn_5Gd_5Y_5$	20
$Nd_{60}Co_{30}Al_{10}$	4
$Ni_{62}Nb_{38}$	57
$Ni_{65}Pd_{15}P_{20}$	10^5
$Pd_{78}Cu_6Si_{16}$	550
$Pd_{40}Ni_{40}P_{20}$	128
$Pd_{42.5}Cu_{30}Ni_{7.5}P_{20}$	0.067
$Pd_{40}Cu_{25}Ni_{15}P_{20}$	0.150
$Pd_{40}Cu_{30}Ni_{10}P_{20}$ (without fluxing)	1.58
$Pd_{40}Cu_{30}Ni_{10}P_{20}$ (with flux treatment)	0.1
$Pd_{30}Pt_{17.5}Cu_{32.5}P_{20}$	0.067
$Pd_{82}Si_{18}$	1.8×10^3
$Pd_{82}Si_{18}$	800
$Pd_{81}Si_{19}$ (with flux treatment)	6
$Zr_{65}Al_{7.5}Ni_{10}Cu_{17.5}$	1.5
$Zr_{41.2}Ti_{13.8}Cu_{12.5}Ni_{10.0}Be_{22.5}$	1.4
$Zr_{46.25}Ti_{8.25}Cu_{7.5}Ni_{10.0}Be_{27.5}$	28
$Zr_{57}Cu_{15.4}Ni_{12.6}Al_{10}Nb_5$	10

Table 2.1- Critical cooling rates (Rc) for formation of glassy phases in different alloy systems (Suryanarayana and Inoue, 2011)

Here, four of these indicators will be briefly explained.

a) Characteristic temperatures: The characteristic temperatures used in determining the GFA of an alloy include the glass transition temperature T_g, the crystallization temperature, T_x, and the melting temperature of the alloy, T_m. Many combinations of these temperatures have been used to predict the glass forming behaviour of different alloys, but among all, the supercooled liquid region ΔT_{xg} (Equ.1) (Turnbull, 1969) and

the reduced glass transition temperature T_{rg} (Equ.2) (Davies and Lewis, 1975) have been mostly utilized. More recently, the γ parameter (Equ.3) (Lu and Liu, 2003) has been introduced which has an even better correlation with GFA.

$\Delta T_{xg}=T_x-T_g$ *Equation - 2.1*

$T_{rg}=T_g/T_m$ *Equation - 2.2*

$\gamma \propto T_x/T_g+T_m$ Equation - 2.3

Also, considering the fact that T_m can be a measure of stability of the liquid and that T_x is a measure of thermal stability of the glass, Mondal and Murty (Mondal and Murty, 2005) proposed a simple parameter, T_x/T_m. This parameter holds for various metallic glasses, and also shows a good correlation with the R_c. The parameter, as claimed, is very useful particularly in cases where a distinct T_g is not observed.

Based on theoretical calculations using the fragility concept and the nucleation theory, Fan et al (Fan, Choo and Liaw, 2007) proposed a dimensionless criterion, ϕ, with T_{rg} and ΔT_x, where α is 0.143:

$$\phi = T_{rg}\left(\frac{\Delta T_x}{T_g}\right)^{\alpha} \qquad \textit{Equation – 2.4}$$

Two other indicators based on Turbull's classical nucleation and growth theory were proposed:

$$\delta = \frac{T_x}{T_m - T_g} \qquad \textit{Equation – 2.5}$$

$$\beta = \frac{T_x . T_g}{(T_m - T_x)^2} \qquad \textit{Equation – 2.6}$$

By calculating the characteristic temperatures of tens of metallic glass compositions and correlating with the critical thickness, both parameters were claimed to have a better fitting than other parameters thus developed.

b) Structural factors: The main framework, within which researchers who are trying to make new metallic glasses work, is the famous set of rules proposed by Inoue (Inoue, 2000). The major contributing factors are:

   1) Having a multicomponent alloy system, consisting of three or more elements. This is termed as the confusion principle (Greer, 1993), and the logic behind it is that adding more and more elements hinders growth of the crystalline phase since it would make atomic rearrangement on a longer scale necessary, for crystallization to happen.
   2) Having a considerable atomic size mismatch among the constituents, which leads to higher packing density and smaller free volume. As a result, atomic diffusivity decreases, making atomic rearrangement and hence crystallization more difficult.
   3) Having a high negative heat of mixing between the elements. This increases the interfacial energy at the solid–liquid interface, which results in decelerating local atomic rearrangements and crystal nucleation rate, thereby extending the supercooled liquid stability.

c) Thermodynamic indicators: Calculations based on the Miedema's model (an empirical theory for calculating enthalpy of mixing in various binary systems both for the liquid and solid state (Miedema, Boom and De Boer, 1975; Boom, Boer and Miedema, 1976). In the case of metallic glasses, it involves the calculations of the formation enthalpy of amorphous phase, solid solutions, and intermetallic compounds) predict that the difference in formation enthalpy of crystalline and amorphous phases enhances the crystallization process. Also, the larger the formation enthalpy of the amorphous phase is, the higher the GFA of alloys will be. So, one of the indicators that has been

proposed to evaluate the glass forming ability is γ^* which works by combining these two elements (Xia *et al.*, 2006a):

$$\gamma^* \propto \Delta H^{amor}/(\Delta H^{inter}-\Delta H^{amor}) \qquad \textit{Equation – 2.7}$$

where ΔH^{amor} is the formation enthalpy of the amorphous phase and ΔH^{inter} is the formation enthalpy of the crystalline phase. The higher the absolute value of ΔH^{amor} is, the better the GFA is; and the smaller the enthalpy difference between the intermetallic phase and the amorphous phase is, the better the GFA is (Xia *et al.*, 2006). Another thermodynamic parameter that has been used to predict the GFA of a potential metallic glass is Gibbs-energy (the free energy change between amorphous and solid solution) (Rao, Bhatt and Murty, 2007), since it is reported to have a strong correlation with reduced glass transition temperature.

d) The eutectic factor: The formation of metallic glass is the result of the suppression of the crystallization process during cooling. Therefore, the best glass formation composition may also be termed as the composition with the minimum driving force for crystallization. By using phase diagrams, if the driving forces or competitive growth behaviours for the crystallization of all the intermetallic or eutectic phases can be depicted, the optimum glass-forming composition may be derived. Drawing liquidus temperature profiles has often been used to find eutectic points, since studying compositions near a eutectic point is an effective way of discovering new bulk metallic glass forming alloys (Turnbull, 1969). A parameter, suggested recently (Cheney and Vecchio, 2007), is α, which measures the depth of a eutectic point and is obtained by calculating a weighted liquidus temperature:

$$\alpha = \frac{\sum_{i=1}^{n} x_i T_i}{T_l} \qquad \text{Equation – 2.8}$$

where n is the number of the constituent elements, x_i is the atomic fraction of the element i and T_i is the melting temperature of the element i. It has been reported that the larger the α parameter of a metallic glass composition is, the higher its GFA will be and that glass forming compositions have α parameters which are larger than 1.

Nevertheless, it has been increasingly recognized that inspecting one of these parameters does not give a good understanding of all the glass forming compositions and in order to find an alloy with a high GFA, a combination of these factors has to be taken into account. For example, γ^* parameter is capable of representing the GFA of most alloys, but it is less accurate in assessing the GFA of the compositions whose decisive competing crystalline phase upon cooling is different from that upon heating (Lu *et al.*, 2008). The indicators based on structural parameters do not involve kinetic factors, and thus, cannot be used alone to predict GFA (Lu, Bei and Liu, 2007). The indicators based on Miedema's model may be lack of precision in calculation due to limited data and/or error in the empirical data (de Oliveira *et al.*, 2008). Therefore, the combination of multiple indicators may be a more effective way to evaluate GFA of BMGs.

2.2.2. Synthesis

Bulk metallic glasses are generally synthesized using either solidification or solid-state processing. A number of different methods have been used over the years, to make BMGs by utilizing the solidification principles. Processes like water quenching, in which the alloy is encapsulated in a vacuum-sealed quartz tube, melted and then quenched in a water bath, providing a high cooling rate of up to 100 K s^{-1}. It is one the oldest ways of making bulk metallic glass specimens (Chen, 1974).

More modern methods of making BMG parts involve using arc melting and then performing suction (Inoue and Zhang, 1995) or injection casting in copper moulds. As a result of solidification under high pressure or sucking force, one advantage of these modern techniques lies in the elimination of cavities and holes and the other is the relatively high cooling rate that can be achieved (Inoue and Zhang, 1995). Different variations like unidirectional zone melting (Inoue *et al.*, 1994) and centrifugal casting (Nowosielski and Babilas, 2007) have also been practiced.

Achieving complete amorphisation by using mechanical milling has been reported in a number of different compositions (Seidel, Eckert and Schultz, 1995; Eckert, 1999; Lee *et al.*, 2007). There is no melting involved in the solid-state processing. In the initial stages, elemental layers are produced, but with time passing, their thickness decreases and eventually amorphisation occurs. Some of the parameters that are involved in determining the final state of the products are milling speed, ball to powder ratio, milling energy and the atmosphere in which the milling takes place.

2.2.3. Crystallization

Since metallic glasses are metastable materials they will crystallize if they receive enough heating energy. Three different regimes of devitrification has been categorized (Herold and Koster, 1978); polymorphous, primary and eutectic crystallization. In the polymorphous regime, the glass precipitates into a crystal, which has the same composition as the starting glassy matrix. However, if the precipitation has a different composition than the glass, then it has been crystallized under the primary regime. And finally, if the resulting crystal has two

separate crystalline phases as a result of a eutectic reaction, which has occurred during the devitrification, then the eutectic regime has taken place.

An unexpected phenomenon, which was discovered after achieving metallic glasses in bulk form, was that nanocrystals could be produced when BMG parts are partially crystallized. It has been discussed that a fine scale separation, taking place inside the melt or even the glass, before the devitrification begins, can control the crystallization to be nano-sized (Busch *et al.*, 1995). So, for example if a large number of nuclei is generated upon quenching, it could lead to a high nucleation rate and a low growth rate and hence yield nanometric crystals inside the glassy matrix after partial crystallization. Also, in some alloy compositions, adding certain elements, which would interact with others (e.g. Au, Ag, Ti, Nb, Pt or Pd to Zr-based BMGs), can increase the chance of achieving nanocrystals by nucleating clusters inside the glass (Inoue, 2000).

2.3. Deformation Behaviour

Bulk metallic glasses exhibit excellent mechanical and physical properties, which promise specific applications in the future. They generally have high strength, hardness, wear resistance, corrosion resistance, surface quality, fatigue-endurance and good fluidity on casting. Some of the mechanical properties of different metallic glass alloys are shown in the table below.

Element				Content, at %				σ_y	σ_f	E	HV
1	2	3	4	1	2	3	4				
Ce	Al	Cu	Co	68	10	20	2		1180	31.34	
Ce	Al	Cu	Fe	68	10	20	2		1232	32.7	
Ce	Al	Cu	Nb	68	10	20	2		1165	30.95	
Ce	Al	Cu	Ni	68	10	20	2		1198	31.93	
Co	Fe	Ta	B	38	25	5.5	31.5		5185	268	
Cu	Hf	Ti	Ta	56.4	23.5	14.1	6	2125	2100	104	
Cu	Zr	Ag	Al	45	45	7	3		1836	110	540
Cu	Zr	Ag	Al	45	45	5	5		1890	112	556
Cu	Zr	Ag	Al	45	45	3	7		1912	112	561
Cu	Zr	Hf	Ag	45	25	20	10		2000	122	579
Cu	Zr	Ti	Be	55.5	27.75	9.25	7.5		2450	146	710
Cu	Zr	Ti	Y	58.8	29.4	9.8	2	1780	2050	115	
Fe	Si	B	Nb	72	9.6	14.4	4		4200	200	
La	Al	Cu	Ag	62.5	12.5	20	5		640	36	201
La	Al	Cu	Ag	55	15	20	10		758	42	208
Mg	Cu	Ni	Gd	65	5	20	10		874	54	
Mg	Y	Zn	Cu	65	10	5	20		860	74	
Ni	Nb	Ti	Zr	60	15	10	15		2770	156	
Ni	Si	B	Nb	72	7.68	16.32	4		2510	77	870
Ni	Si	B	Ta	72	7.68	16.32	4		2730	75	920
Ni	Ta	Ti	Zr	60	15	15	10		3180	67	
Pd	Cu	Ni	P	40	30	10	20		1640		515
Pd	Cu	Si	P	79	6	10	5	1475	1575	82	
Pd	Pt	Cu	P	35	15	30	20	1410			470
Pt	Cu	Ni	P	57.5	14.7	5.3	22.5	1400	1470		
Ti	Ni	Cu	Sn	50	20	25	5		2050	102	650
Ti	Ni	Cu	Sn	50	20	23	7		2200	105	670
Ti	Ni	Cu	Sn	50	22	25	3		2050	98	640
Zr	Al	Co	Cu	55	20	20	5	2000	1960	92	
Zr	Al	Ni	Pd	65	7.5	10	17.5	1340	1510		
Zr	Cu	Ni	Al	52	32	4	12		1780	88	501
Zr	Cu	Ni	Al	52	30	6	12		1820	93	506
Zr	Cu	Ni	Al	50	26	12	12		1878	88	498
Zr	Cu	Ni	Al	50	34	4	12		1905	91	517

Table 2.2- Composition and mechanical properties of bulk metallic glasses (Louzguine-Luzgin, Louzguina-Luzgina and Churyumov, 2012)

However, there is a common flaw among almost all of the bulk glassy alloys and that is failing catastrophically in load-bearing tensile conditions. They show almost zero plastic strain. This is why a great deal of research has been carried out to study the deformation behaviour of

bulk metallic glasses under different conditions and a brief summary of which will be presented here.

2.3.1. Deformation Modes

Depending on the conditions under which a bulk metallic glass specimen is processed, it would go through one of two very different modes of deformation. If the deformation process is carried out in its supercooled liquid range and with a low strain rate, the homogenous regime will be predominant in which each volume element of the specimen contributes to the strain and this will result in a uniform deformation (Schuh, Hufnagel and Ramamurty, 2007).

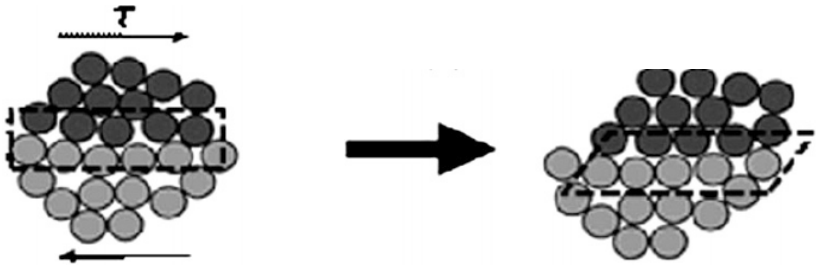

Figure 2.2- A cluster of atoms, called a shear transformation zone, accommodating shear strain through intense deformation (Schuh, Hufnagel and Ramamurty, 2007).

In contrast, if the BMG part is processed below its glass transition temperature and/or with a high strain rate, the inhomogeneous mode of deformation will prevail. In the latter case, upon applying pressure, the fundamental unit of plasticity, the shear transformation zone (STZ), which is a cluster of closely packed atoms, will be rearranged and intensely distorted to accommodate the shear strain. So, if the shear stress is large enough, propagation and agglomeration of these zones will trigger the formation of large planar bands of STZs, termed as shear bands. These bands are responsible for the plastic deformation of metallic glasses at

room temperature and since the shear strain is localized in these thin and discrete shear bands, brittleness and lack of ductility would be inevitable causing sudden and catastrophic fractures. Consequently, unlike the homogeneous deformation, the BMG sample does not experience any plasticity when it is deformed in an inhomogeneous manner (Schuh, Hufnagel and Ramamurty, 2007).

A series of compression/tensile tests have been carried out to study the effect of temperature, applied pressure and strain rate on the mechanical behaviour of bulk metallic glasses. By investigating stress-strain curves of BMG samples (e.g. in Fig. 2.3-(b)) at different temperatures and strain-rates, their yield (for homogeneous deformation) and maximum stress (for inhomogeneous deformation) were obtained (Kawamura *et al.*, 1996). They were used to construct two sets of maps demonstrating their temperature and strain rate dependency.

As shown in Fig. 2.3(b) at a constant temperature, the yield stress of the samples (defined by open symbols and governed by the homogenous regime) increases upon increasing strain rate up to a critical strain rate, where the deformation mode changes from homogeneous to inhomogeneous. Above this critical strain rate, the maximum stress (defined by solid symbols) decreases upon increasing strain rate (Kawamura *et al.*, 1996). Identifying this critical strain rate for each temperature is one of the important objectives of performing these tests, since it is highly desired to be in the homogeneous regime of deformation, when processing bulk metallic glasses, as they show a ductile and almost superplastic behaviour in this deformation mode.

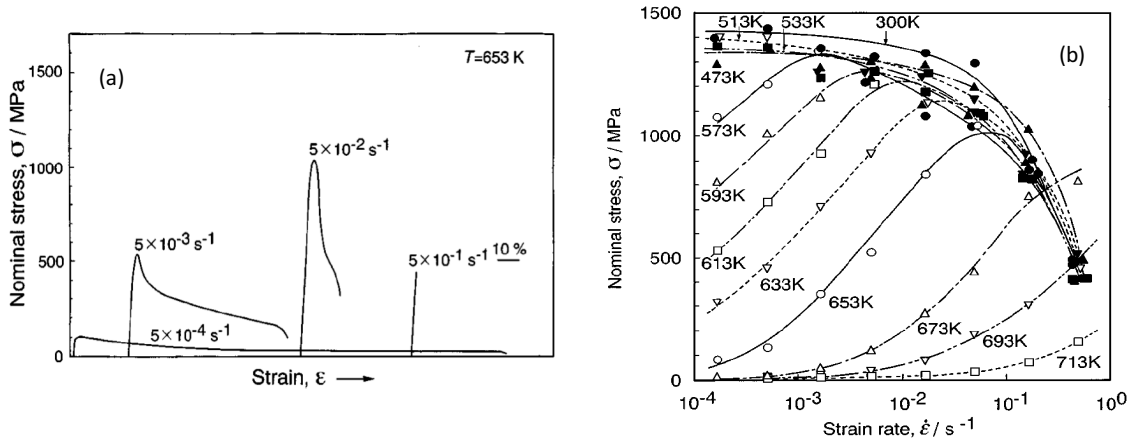

Figure 2.3- Stress-strain curves of the $Zr_{65}Al_{10}Ni_{10}Cu_{15}$ alloy at 653K and under different strain rates, produced by tensile testing, indicating the change in deformation mode at the strain rate of 5×10^{-1} s^{-1} (a). Strain rate dependence of stress in a range of temperature, revealing the critical strain rate at which the deformation mode changes at each temperature (b). Open and solid symbols represent homogeneous and inhomogeneous deformation, respectively (Kawamura *et al.*, 1996).

The same logic has been applied to plot the curves shown in Fig. 2.4-(b). For each strain rate, the critical temperature after which the deformation mode would change to homogenous regime was obtained from this map. It is clearly demonstrated that in the inhomogeneous regime, the maximum stress is almost independent of temperature and when the deformation mode changes to homogenous, the yield stress abruptly decreases with increasing temperature (Kawamura *et al.*, 1996). Comparatively, the yield stress of a BMG in its supercooled liquid region can be orders of magnitude less than its room temperature stress. This can be very beneficial when processing BMG parts in their SCLR, since they would require much less working pressure.

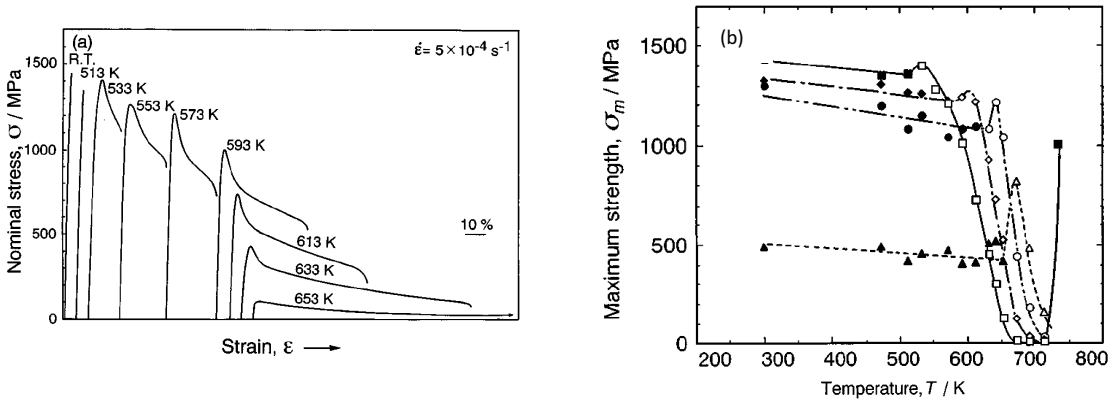

Figure 2.4- Stress-strain curves of the $Zr_{65}Al_{10}Ni_{10}Cu_{15}$ alloy at different temperatures and at a strain rate of 5×10^{-4} s^{-1}, produced by tensile testing, indicating the change in deformation mode at the temperature of 513K (a). Temperature dependence of stress in a range of different strain rates, revealing the critical temperature at which the deformation mode changes under each strain rate (b). Open and solid symbols represent homogeneous and inhomogeneous deformation, respectively (Kawamura *et al.*, 1996).

It has been suggested by Argon (Argon, 1982), that the equation below can express the interaction between different parameters affecting the homogenous deformation of glassy alloys, where $\dot{\varepsilon}$ is the strain rate, $\dot{\varepsilon}_0$ and α are constants, *H* is the activation energy for flow, *R* is the universal gas constant, *T* is temperature and σ is the stress:

$$\dot{\varepsilon} = \dot{\varepsilon}_0 \exp\left(-\frac{H}{RT}\right) \sinh\left(\frac{\alpha\sigma}{RT}\right) \qquad \text{Equation – 2.9}$$

Moreover, when studying the homogeneous deformation, one of the most important mechanical characteristics of the supercooled liquid is having a high strain rate sensitivity exponent.

$$m = \Delta log\sigma / \Delta log\dot{\varepsilon} \qquad \text{Equation – 2.10}$$

where *m* is the strain rate sensitivity exponent. A high *m* value means the alloy will have a high elongation to failure and a high necking resistance. In order to have superplastic behaviour, *m* should be more than 0.3, however bulk metallic glasses usually exhibit *m* values greater than 0.8 in their supercooled liquid region (Kawamura *et al.*, 1998).

2.3.2. Viscosity and Flow

The influence of strain rate on viscosity of bulk metallic glasses has been investigated and it is conceived that in the lower strain rates, their viscosity is almost independent of the strain rate, which indicates a Newtonian flow (equilibrium state). However, as strain rate increases, viscosity of BMG specimens becomes strongly strain rate dependent, decreasing rapidly as the strain rate increases, exhibiting a non-Newtonian flow (non-equilibrium state). This implies that they change their flow behaviour as strain rate increases from a low strain rate regime to a high strain rate regime (Y. N. Ge *et al.*, 2010). On the other hand, temperature is equally important in determining the flow properties of bulk metallic glasses. When a glassy alloy is below its glass transition temperature and in a solid glassy state, as the strain rate of the experiment increases, its viscosity decreases showing a non-Newtonian flow. But, when the temperature increases and the metallic glass specimen goes into its supercooled liquid region, the viscosity becomes independent of the strain rate (at low strain rates of course) exhibiting a Newtonian flow (Kawamura *et al.*, 2001). This is how viscosity maps (e.g. Fig. 2.5) are produced showing the conditions in which each bulk glassy alloy would be in the Newtonian flow which is desirable for processing BMGs or in the non-Newtonian flow range.

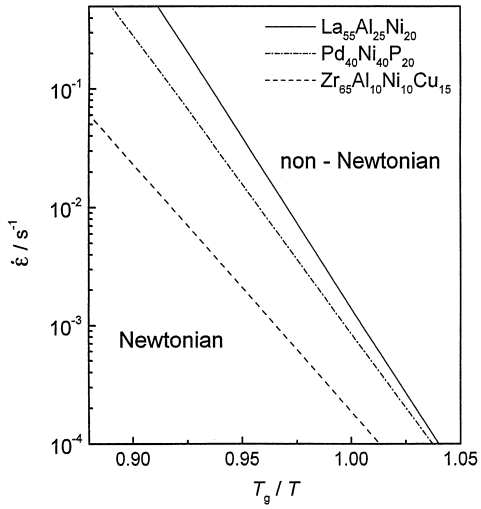

Figure 2.5- A viscosity map indicating the regions in which these three BMG alloys would flow Newtonian or non-Newtonian depending on the strain rate and temperature (normalized by glass transition temperature) of the process (Kawamura *et al.*, 2001).

Furthermore, several studies have been carried out trying to explain and formulate the viscosity behaviour of bulk metallic glasses in their equilibrium state. Some use the famous Vogel-Fulcher-Tamman (VFT) equation. It is well known that the Angell version of the equation (Angell, 1995), presented below, can accurately reproduce viscosity of a material in an equilibrium state, which is how BMG parts behave in their supercooled liquid region (Kawamura *et al.*, 2001). The formulation is described by the equation below:

$$\eta = \eta_0^* exp\left(\frac{mT_0}{T_0 - T}\right) \qquad \text{Equation – 2.11}$$

where η_0^* is a fitting parameter, m is the fragility parameter and T_0 is the VFT temperature. The problem with this relation is that it gives a good description in the vicinity of the glass transition temperature but not the whole supercooled liquid state (Kawamura *et al.*, 2001). This is exactly what the free volume theory can provide with the following relation (Cohen and Grest, 1979), where *E, F* and *G* are fitting parameters (these parameters are given for two bulk metallic glasses as examples in Table 2.3):

$$log\eta = \frac{E+2F}{T-T_0+\{(T-T_0)^2+GT\}^{1/2}} \qquad \text{Equation – 2.12}$$

Alloy composition	E	F	G	T_0 (K)	M
$La_{55}Al_{25}Ni_{20}$	-2.854	49.094	9.823	777.0	35
$Pd_{40}Ni_{40}P_{20}$	-2.334	202.88	22.898	774.7	54

Table 2.3- Parameters used in Equation (9) for $La_{55}Al_{25}Ni_{20}$, $Zr_{65}Al_{10}Ni_{10}Cu_{15}$ and $Pd_{40}Ni_{40}P_{20}$ (Kawamura *et al.*, 2001)

Finally, in order to classify the sensitivity of different fluids against thermal changes, the fragility concept has been introduced as the slope of viscosity vs temperature at the glass transition temperature and is expressed by (Novikov, Ding and Sokolov, 2005):

$$m = \frac{dlog\eta}{d(T_g/T)}|_{T=T_g} \qquad \text{Equation – 2.13}$$

A low *m* value (like 32 for B_2O_3 melt) shows that the liquid is strong and a high *m* (like 73 for salol) indicates that the liquid is fragile and very susceptible to changes in temperature (Böhmer *et al.*, 1993). It has been demonstrated (Table 2.3) that the bulk metallic glasses in their supercooled liquid region exhibit different values of *m*, but can be classified into relatively strong liquids. Finally, it should be reminded that the strain rate sensitivity and the fragility parameters are both identified in the literature with the letter *m*, and since they are two different concepts, confusing them should be avoided.

2.4. Processing

Although bulk metallic glasses lack room temperature plasticity, a window of processing exists for them, as they exhibit superplastic behaviour in their supercooled liquid region. So, researchers have taken this opportunity to shape and form glass forming metallic alloys by

using methods like hot rolling (Martinez, Kumar and Schroers, 2008), microfabrication (Kumar, Tang and Schroers, 2009) and foaming (Schroers, Veazey and Johnson, 2003) to make BMG parts in different shapes and sizes. Here, a number of these processing techniques will be summarized.

2.4.1. Hot Rolling

The room temperature plastic behaviour of bulk metallic glasses is dramatically different when they have at least one dimension smaller than 1mm (Guo *et al.*, 2007). This is why, a large portion of the processing methods, used for forming BMGs, are the ones that would result in such dimensions. One of these techniques is hot rolling, which takes advantage of the SCLR properties of BMGs and produce sheets of metallic glass with small thicknesses that exhibit high plasticity (Martinez, Kumar and Schroers, 2008).

A common problem in processing methods like compression moulding is the high friction, which hinders material flow inside the die. Since this problem develops because of the considerable physical contact between the die and the metallic glass, using lubricants has been tried to reduce it; however, not only is the improvement marginal, but it also ruins the final surface finish (Martinez, Kumar and Schroers, 2008). In the case of hot rolling though, the contact area between the rolls and the metallic glass part is limited to a very thin line, substantially decreasing the flow resistance.

One of the main concerns in hot rolling, like in any other thermoplastic forming process, is keeping the deformation mode in the homogenous and especially Newtonian regime. This goal is achieved by referring to deformation maps, in which the appropriate temperature and strain rate is depicted. For maintaining homogenous deformation, it is also advised to keep

the BMG's temperature in the upper half of the supercooled liquid region while processing. So, in order to shield the hot glassy part from the coldness of the rolls, they should be placed inside pack rolling material and sheets of steel, while rolling is taking place. Plus, by placing silicon moulds between the packing material and the metallic glass, submicron imprinting on the surface of BMG specimens has been carried out utilizing hot rolling (Martinez, Kumar and Schroers, 2008).

2.4.2. Microfabrication

Microfabrication is the process of making micro and nanostructures. In the case of metallic glasses, nanoimprinting (which is embossing nano-features from a mould onto a thermoplastic material) seems to be more beneficial, since it takes advantage of the superplastic behaviour of the glassy alloys in their supercooled liquid region. In this process (also called nano-moulding), the BMG forming alloy is heated up into its SCLR and placed on a hard mould, which is usually silicon (Schroers, Pham and Desai, 2007), quartz (Guo, 2007), or alumina (Kumar, Tang and Schroers, 2009), since they can retain their strength over a wide range of temperatures. Then pressure is applied onto the BMG specimen to shape the nano-features onto its surface. Afterwards, the ceramic mould is dissolved (alumina in KOH (Kumar, Tang and Schroers, 2009) and silica in POH (Schroers, Pham and Desai, 2007)) leaving features on the surface of the BMG specimen. If the features are needed to be freestanding, a process called hot scrapping can be carried out in which a scrapper is used to hot separate the parts from the reservoir (Schroers, Pham and Desai, 2007).

The Hagen-Poiseuille equation can be used to model the nano-moulding process:

$$P = \frac{32\eta}{t}\left(\frac{l}{d}\right)^2 - \frac{4\gamma cos\theta}{d} \qquad \text{Equation – 2.14}$$

where *P* is the required pressure for the flow to take place, η is BMG's viscosity, *t* is the filling time, *l* is the die length, *d* is the die diameter, γ is the metallic glass-vacuum surface energy, and θ is the contact angle between the mould channel and the liquid (Kumar, Tang and Schroers, 2009). As the channel diameter decreases the capillary effect which is described by the second part of the equation becomes more influential and at diameters smaller than 1μm, the moulding regime will be dominated by capillary forces instead of the viscosity, which is represented by the first part of the equation.

As depicted in Equation – 2.14, the capillary force is strongly dependent on the wetting characteristics of the BMG forming alloy in contact with the channel wall. For complete anti-wetting conditions (θ =180°) the applied pressure has to overcome very high capillary pressures and for complete wetting conditions (θ = 0°) the moulding process would be out of control since the fluid would fill the mould spontaneously (Kumar, Tang and Schroers, 2009). So, an ideal glass-forming alloy for nanoimprinting would have partial wetting conditions with the mould, a large crystallization time and low viscosity in its SCLR to reduce the required pressure for the moulding process to take place.

Nano-moulding bulk metallic glasses can be used to fabricate parts for various applications such as lithography masks, medical implants and MEMS. MEMS are micro-electromechanical systems that are used in diverse areas like gyroscopes, digital projectors, DNA chips, etc. BMG forming alloys can be prime candidates for making MEMS. For example, the high yield strength of these alloys can be of use in sensors and actuators in high shock environments, their high wear resistance can be used in RF dielectric switches and their excellent resilience would be useful for making springs. Initially the fatigue behaviour of bulk metallic glasses was

assumed to be subpar compared to crystallized alloys. In the amorphous ribbons and monolithic BMG at early stages, the fatigue ratio (σ_w/σ_B), which is defined as the ratio of the fatigue limit (σ_w) to the tensile or compressive strength (σ_B), was very low, for example, 0.05 (Izumi *et al.*, 1984; Gilbert, Lippmann and Ritchie, 1998) compared to the ratio in the practical crystalline alloys, that is, about 0.5 in a steel and 0.2 in an Al alloy under pulsating tension (Tanaka, 1982). Recently, however, even in the monolithic BMGs, the case was shown that the σ_w/σ_B indicated about 0.3–0.5. It is pointed out that there is a possibility the small σ_w/σ_B at early stages occurred due to initial defects included in the BMG (Y. Wang *et al.*, 2004; Qing and Bing, 2005). Furthermore, it is conceivable that the σ_w in the BMG originally shows a very high value in comparison with that in the crystalline alloys as the fatigue crack initiation in the BMG as well as the tensile or compressive fracture needs the wide range of simultaneous slip because of the no dislocation in the BMG. So, applications like springs are well suited for these materials.

2.4.3. Foaming

Because of their ultra-high strength to weight ratio, NASA is currently looking into developing a hardened uniform bulk metallic glass foam and they hope that it would help them build a lighter and stronger spacecraft to save fuel and endure collisions in outer space (Johnson and Veazey, 2008). One way of foaming bulk metallic glasses (Schroers, Veazey and Johnson, 2003) is carried out by first fabricating a foam precursor, and then activating the expansion of the bubbles inside that precursor. The precursor can be produced by enclosing hydrated powder with the metallic glass inside a quartz tube and heating it inside a furnace at a temperature above the melting point of the alloy. During this time, the water inside the

powder vaporizes and gets entrapped inside the molten alloy in the form of uniformly distributed bubbles. Then the quartz tube is quenched in water and the precursor is ready for the next step of foaming. This precursor is then heated to an elevated temperature under 1 bar of argon pressure; after reaching temperature equilibrium, the pressure is dramatically reduced activating bubble expansion process inside the precursor.

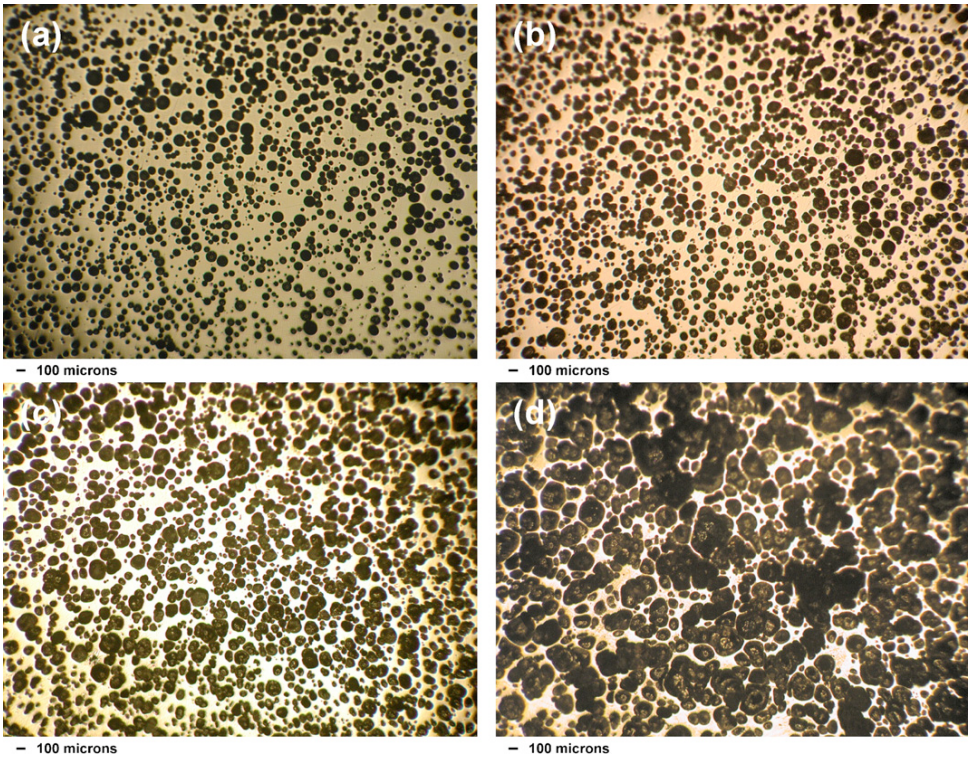

Figure 2.6- Evolution of bubbles inside the foam at 25% porosity (a), 38% porosity (b), 49% porosity (c) and 70% porosity (Demetriou *et al.*, 2007).

This step of foaming metallic glasses is essentially increasing the entrained porosity. The expansion mechanism is proposed to be bubble growth until the porosity reaches a threshold (about 50-70%) at which the bubbles would be critically packed. After this point, the bubbles start to coalesce and impinge (as shown in Fig. 2.6) which would change the expansion mechanism to growth of clusters of bubbles (Demetriou *et al.*, 2007).

2.4.4. Composite Fabrication

As mentioned before, plastic deformation of bulk metallic glasses at room temperature occurs through evolution of shear bands in which the plastic strain is localized and it results in embrittlement and sudden failure of BMG specimens under pressure. Consequently, this form of embrittlement has been considered to be an intrinsic defect of bulk glassy alloys. However, it has been suggested (Liu *et al.*, 2007) that the formation of multiple shear bands can increase the plasticity of BMG specimens, as each shear band would contribute to accommodating the plastic strain and none would carry enough to cause rupture.

One method employed to accomplish this goal is by fabricating BMG matrix composites in which the second phase would act as a barrier to the propagation of the shear bands which if not controlled, would cause the metallic glass to fail (Ma, 2003). This would result in formation of multiple shear bands, dramatically increasing the plasticity of glass forming alloys at room temperature.

Several methods have been used for fabrication of bulk metallic glass composites, three of which would be compared here. The first technique is carried out by adding solid second phase particles to a batch of a glass forming alloy and melting/casting them together (Zhang, Ishihara and Inoue, 2002). The volume fraction of the second phase infiltrated inside the BMG matrix can be very high in this method, but the choice of the material used for the second phase is very limited, since only high melting temperature materials like carbides can be used.

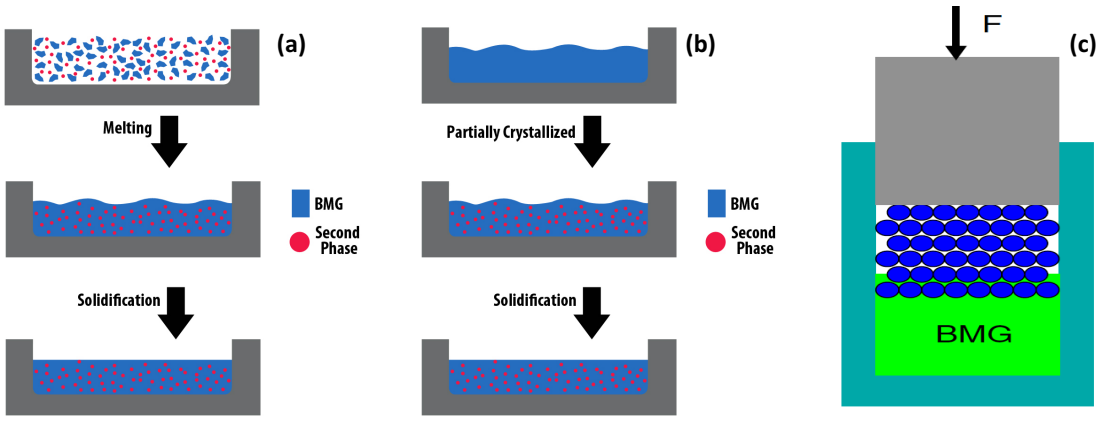

Figure 2.7- Different methods of fabricating bulk metallic glass matrix composites; melting with second phase (a), partial crystallization (b) and thermoplastic forming (c)

The second technique is partially crystallizing the bulk metallic glass either during or after solidification (Ma, 2003). The BMG alloys that can undergo this partial devitrification process are limited and the volume fraction of the second phase produced inside the matrix is very low. However, since the matrix-second phase bonding is chemical, they exhibit stronger bonds upon applying pressure.

The third way of fabricating BMG composites is by utilizing a thermoplastic forming method in which the matrix and the second phase particles are both heated up to the supercooled liquid region of the bulk metallic glass and an external pressure is applied to infiltrate second phase particles into the matrix, taking advantage of the softening of the BMG (Schroers, Nguyen and Croopnick, 2007). The choice of second phase particles for this method is very high, since the process is carried out at relatively low temperatures. High fraction volume of the second phase can be achieved in this technique.

2.5. Fe-Based Bulk Metallic Glasses

Since 1995, when the first Fe-based bulk metallic glass, $Fe_{72}Al_5Ga_2P_{11}C_6B_4$, was synthesized using copper mould casting (Inoue and Gook, 1995), they have been an attractive group of materials to work with because of their high strength (≈4 GPa) and hardness (i.e. 11 to 13 GPa), soft magnetic properties, high electrical resistivity, high corrosion resistance, large glass forming ability and low production cost (Inoue, Shinohara and Gook, 1995; Guo *et al.*, 2008, 2013; Guo, Wu and Liu, 2009)(Lu *et al.*, 2004)(Shen *et al.*, 2005)(Inoue and Shen, 2004).

In Table 2.4 and Table 2.5 the mechanical properties of some Fe-based bulk metallic glasses and some conventional engineering metallic alloys are shown for comparison. However, they present a big challenge which is their very low plasticity causing catastrophic failure in the form of brittle fracture at room temperature (Gu, Poon and Shiflet, 2007).

Alloy composition	σ_y/GPa	σ_f/GPa	$\varepsilon_{pl.}$/%	*G*/GPa	*K*/GPa	*E*/GPa
$Fe_{65}Mo_{14}C_{15}B_6$	3·4	3·8	0·6	73	195	195
$(Fe_{0·9}Co_{0·1})_{64·5}Mo_{14}C_{15}B_6Er_{0·5}$	3·7	4·1	0·55	73	175	192
$Fe_{59}Cr_6Mo_{14}C_{15}B_6$	3·8	4·4	0·8	77·4	188	204
$Fe_{49}Cr_{15}Mo_{14}C_{13}B_8Er_1$	3·9	4·04	0·1	82·5	201	220
$Fe_{49}Cr_{15}Mo_{14}C_{15}B_6Er_1$	3·75	4·14	0·25	81·9	200	220
$Fe_{49}Cr_{15}Mo_{14}C_{18}B_3Er_1$	3·6	4·09	0·4	80·2	200	210
$Fe_{49}Cr_{15}Mo_{14}C_{19}B_2Er_1$	…	…	…	78·8	199	209
$(Fe_{0·9}Co_{0·1})_{58·5}Cr_6Mo_{14}C_{15}B_6Er_{0·5}$	3·7	4·1	0·35	76·2	190	200
$Fe_{71}Mo_5P_{12}C_{10}B_2$	2·45	3·15	3·6	62	…	…
$Fe_{66}Mo_{10}P_{12}C_{10}B_2$	2·55	3·25	1·7	66·1	176	176
$Fe_{65}Cr_2Mo_9P_{10}C_8B_6$	2·9	3·55	1·0	66·8	174	177
$Fe_{63}Cr_3Mo_{10}P_{12}C_{10}B_2$	2·6	3·4	3·2	65·3	178	178
$Fe_{61}Mn_{10}Cr_4Mo_6C_{15}B_6Er_1$	4·16	…	…	75	146	193
$Fe_{53}Cr_{15}Mo_{14}C_{15}B_6Er_1$	4·2	…	…	75	180	195
$(Fe_{0·75}B_{0·2}Si_{0·05})_{96}Nb_4$	3·16	3·4	0·225	…	…	180
$[(Fe_{0·5}Co_{0·5})_{0·75}B_{0·2}Si_{0·05}]_{96}Nb_4$	4·07	4·21	0·225	…	…	210
$[(Fe_{0·8}Ni_{0·2})_{0·75}B_{0·2}Si_{0·05}]_{96}Nb_4$	…	4·30	0·215	…	…	215
$[(Fe_{0·5}Ni_{0·5})_{0·75}B_{0·2}Si_{0·05}]_{96}Nb_4$	…	4·05	0·215	…	…	197
$[(Fe_{0·6}Co_{0·3}Ni_{0·1})_{0·75}B_{0·2}Si_{0·05}]_{96}Nb_4$	…	4·2		…	…	210

Table 2.4- Mechanical properties of Fe-based bulk metallic glasses. σ_y: yield strength; σ_f: fracture strength; $\varepsilon_{pl.}$: plastic strain; G: shear modulus; K: bulk modulus; E: Young's modulus; (Suryanarayana and Inoue, 2013)

Material	Form and Condition	Yield Strength (MPa)	Tensile Strength (MPa)	Elongation in 2 in., %	Shear Modulus (GPa)	Young's Modulus (GPa)
Inconel 625	Rod Hot Rolled Annealed	482	965	50	81	207
Stainless Steel 316L	Sheet Annealed	220	517	50	77	193
Aluminium Alloy 6061	Sheet Annealed	55	124	25	26	69
Brass 70/30	Strip Annealed	76	303	66	41	110
Ti-6Al-4V	Sheet Annealed	896	965	13	42	114
Maraging Steel 18-300	Aged at 900°C	1930	1999	8	73	190
Magnesium Alloy AZ31B	Sheet Annealed	151	255	21	16	44

Table 2.5- Mechanical properties of some conventional crystallized alloys (The International Nickel Company, 1982).

2.5.1. Ductility of Fe-Based Bulk Metallic Glass

In order to investigate the ductility of Fe-based bulk metallic glasses, they have been put into three different categories according to their composition: FeC(B), FeP(C) and FeB-based bulk

metallic glasses(Guo *et al.*, 2014). In terms of the glass forming ability of the Fe-based bulk metallic glasses, the diagram in Fig. 2.8 presents the maximum diameter of the rod possible for each composition accompanied by the year it was discovered. It has been suggested the glass forming ability of different bulk metallic glasses correlates to some of their elastic properties (Wang, 2012) which indicates these three different categories of Fe-based BMGs might present distinct mechanical behaviour, similar within their own category and different from the other two.

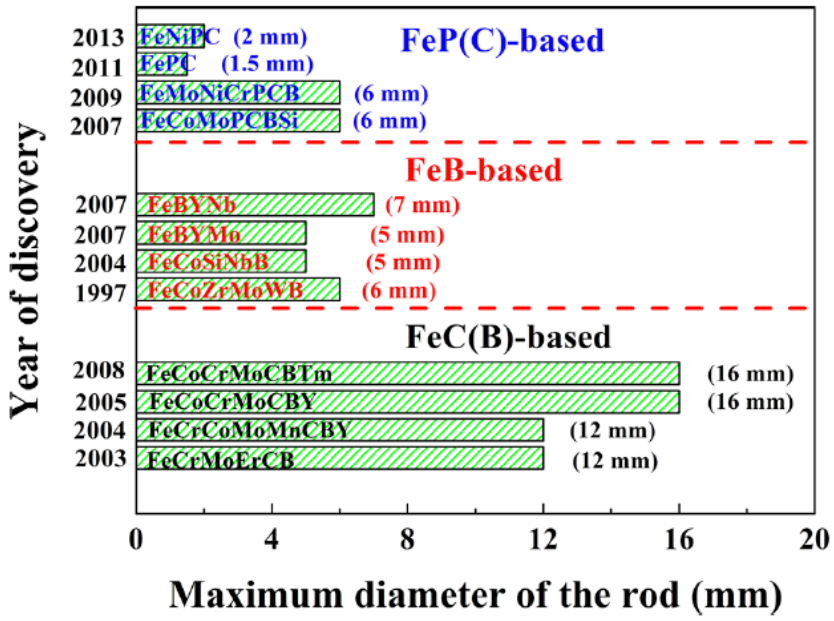

Figure 2.8- Glass forming ability of different Fe-based BMGs and their year of discovery (Guo et al., 2014)

The FeP(C)-based BMGs are shown to have a higher ductility and lower strength compared to the other two categories(Guo *et al.*, 2014). This has been attributed to the stable multiple shearing happening during the deformation inside the FeP(C)-based BMGs as opposed to formation of a single prominent shear band which would undertake the plastic deformation in other Fe-based BMGs causing a catastrophic failure.

To explain this, Guo et al utilized the concept of activation energy of shear flow as the barrier

to initiating shear banding. The quantitative expression of this energy barrier proposed by Johnson (Johnson and Samwer, 2005) is dominated by the shear modulus for a frozen-in atomic configuration at the glass transition temperature. Furthermore, Guo showed that most often FeP(C)-based BMGs have a lower shear modulus and a higher Poisson's ratio compared to the other two categories (shown in Fig. 2.9).

This lower shear modulus would mean a lower shear flow activation energy barrier to shear banding and consequently a larger plastic deformation as a result. Also, the higher Poisson's ratio translates into a lower ratio of shear modulus to bulk modulus. A smaller shear modulus helps the propagation of shear bands and a larger bulk modulus, energetically hinders the transition of a shear band into a crack.

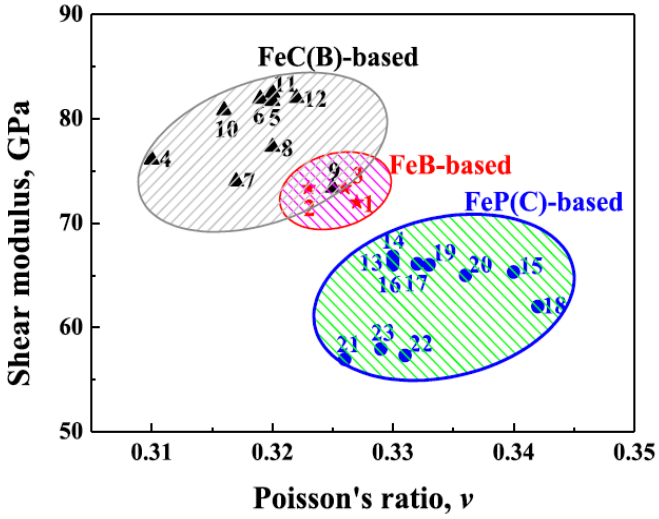

Figure 2.9- Shear modulus vs Poisson's ratio for different categories of Fe-based bulk metallic Glasses (Guo et al., 2014)

The concept of using the ratio of shear modulus over bulk modulus (μ/B) to predict the ductile or brittle behaviour of crystalline solids was studied long ago (Rice and Thomson, 1974), and recently the same approach has been adopted in regards to Fe-based bulk metallic glasses (Lewandowski *et al.*, 2008). It has been shown that the toughness of Fe-based BMGs correlates with changes in μ/B ratio as well as with Poisson's ratio. As presented in Fig. 2.10,

as the μ/B increases and Poisson's ratio decreases, fracture behaviour of the alloy in question changes from tough to brittle. The critical value for μ/B at which this change happens seems to be about 0.41-0.43, above which the alloy would be brittle (Lewandowski, Wang and Greer, 2005).

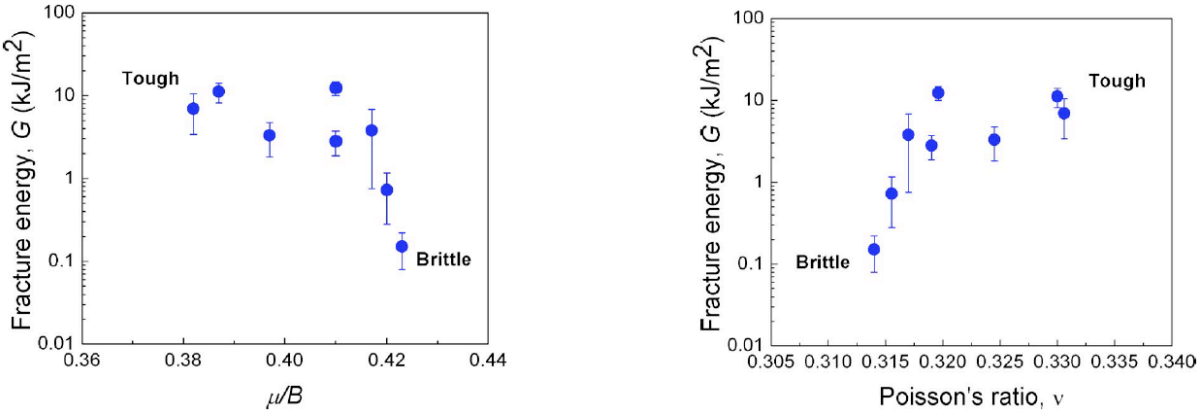

Figure 2.10- The correlation of fracture energy with μ/B and Poisson's ratio for a variety of Fe-based BMGs.

2.5.2. Role of individual Elements in the Composition of Fe-Based Bulk Metallic Glasses

Fe-based bulk metallic glasses synthesized to date are the metal-metalloid type in which 80% is the metallic component and the remaining 20%, the metalloid component (Suryanarayana and Inoue, 2013) (It is worth mentioning that all the compositional percentages are atomic percentage, at%, unless specifically stated otherwise). The metallic component has usually been from the Iron group, meaning Fe, Ni and Co and sometimes other metals such as Ta, Mo, Ga, Cr, Nb, Al and Mn were used as well. In terms of the metalloid component, Si, P, B and C are the elements that are added to the composition. Rare earth elements like Y are sometimes also added in a small amount. The role of some of these constituent elements of Fe-based bulk metallic glasses is discussed below.

2.5.2.1. Yttrium and Other Similar Rare Earth Elements

The addition of Yttrium or similar REs such as Dy, Yb and Gd has been shown to improve the glass forming ability of Fe-based bulk metallic glasses (Lu, Liu and Porter, 2003; Ponnambalam, Poon and Shiflet, 2004). The effect of Y and similarly Ln has been explained through one of Inoue's conditions for production of bulk metallic glasses, namely the large atomic size mismatch between the elements included in the composition of the alloy intended for production of a bulk metallic glass.

It has been suggested that the presence of a large atom solute would increase the atomic-level stress so much for the crystalline phase not to be able to remain stable and hence result in the vitrification of the melt upon solidification (Lu, Liu and Porter, 2003). This is how Yttrium and similar elements help the glass forming ability through destabilization of the crystalline state, since the atomic size of Y, for instance, is 1.4 times that of Fe.

Also because of their low solubility in the Fe carbides which is the primary crystalline phase produced upon devitrification, the Y atoms would need to diffuse in a long range manner during solidification which would hinder nucleation and growth of this crystalline phase and improve the stability of amorphous structure (Lu *et al.*, 2004). Influence of Y addition to Fe-based BMGs has also been explained through increasing viscosity of the alloy which in turn would slow down nucleation and growth of crystalline compounds (Farmer *et al.*, 2007). However, this increase in the viscosity of the alloy also means that gas atomization of the resulting material would not be as easy and that it would result in irregular powder particles, similar to the image shown in the Fig. 2.11, instead of spherical ones.

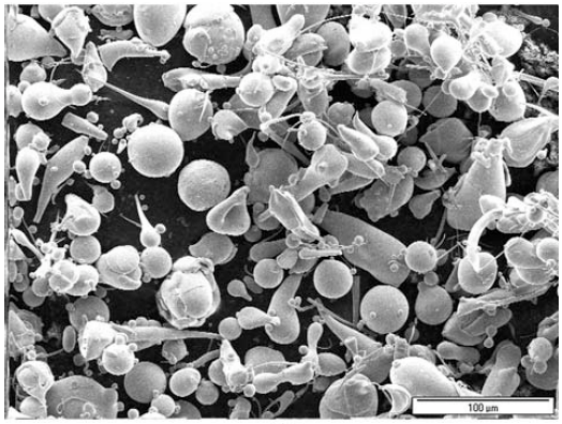

Figure 2.11- Particle morphology of SAM1651 powder (Ajdelsztajn et al., 2009)

2.5.2.2. Thulium

In the case of Fe-Co-Cr-Mo-C-B for example, the addition of 2-3% Tm to the composition has been shown to significantly improve the glass forming ability of the alloy. Considering the fact that this addition does not change the melting point of the alloy, it has been suggested that this enhancement of the GFA can be attributed to the positive effect the addition of Tm atoms would have in formation of large range atomic configuration because both Mo and Tm atoms would act as glue atoms. Thulium also has one of the largest atomic size ratios to the other constituting elements of the alloy, which would cause an Yttrium-like effect in the microstructure (Suryanarayana and Inoue, 2013).

2.5.2.3. Nickel

It has been reported that a small addition of Ni can improve the soft magnetic properties of the Fe-based bulk metallic glasses significantly through the improvement of the magnetic exchange interaction. Ni addition has also been shown to improve the electrical behaviour, namely in the Fe-Co-Zr-Mo-W-B system, however it was concluded that this improvement is

most likely associated with the change in the magnetic properties of the alloy (W. H. Wang *et al.*, 2004).

2.5.2.4. Cobalt

Addition of Cobalt to Fe-based BMGs has been shown to improve the glass forming ability of the resulting alloy substantially. The reason for this behaviour was attributed to the influence of Co on lowering the liquidus temperature when partially replacing Fe, stabilizing the supercooled liquid and destabilizing the competing crystalline phases (Shen *et al.*, 2005). Furthermore, the partial replacement of Fe atoms with Co would necessitate the long range atomic configuration rearrangement if the $Fe_{23}(B,C)_6$ and $Co_{23}(B,C)_6$ are going to precipitate from the surrounding amorphous microstructure simultaneously which would improve the glass forming ability of the resulting bulk metallic glass (Amiya and Inoue, 2008). It has also been reported that the addition of cobalt and partially substituting Fe can improve hardness as well as fracture strength, due to stronger atomic bonding between the constituent elements (Inoue, Shen and Chang, 2004).

2.5.2.5. Boron and Carbon

Addition of both Boron (Ajdelsztajn *et al.*, 2009)(Farmer *et al.*, 2007) and Carbon at less than 5% has been shown to help enable the glass formation in Fe-based BMGs (Hu *et al.*, 2003).

2.5.2.6. Other Elements

Chromium, Molybdenum and Tungsten have been reported to provide corrosion resistance

in Fe-based BMGs (Ajdelsztajn *et al.*, 2009)(Farmer *et al.*, 2007). Molybdenum for example has been shown to do this by increasing the stability of the resulting passive film (Tan *et al.*, 1996). Mo has also been shown to increase the GFA of Fe-based alloys (A. Inoue, T. Masumoto, S. Arakawa, 1978). Moreover, Zr addition increases the glass transition temperature and adding Mn would decrease the liquidus and Curie temperature (Zheng *et al.*, 2009).

2.5.3. Applications of Fe-Based Bulk Metallic Glasses

One of the main characteristics of the Fe-based BMGs is their good soft magnetic properties. For example, Liqualloy which is in the Fe-TM-P-C-B-Si alloy family has been utilized to produce Liqualloy cores which are used in noise suppression sheets, AC-DC convertors and DC-DC convertors. The Liqualloy spherical powders have been transformed into a flake shape through bead milling treatment and combined with resin, Liqualloy sheets were produced which demonstrate high ability to convert electromagnetic noise into heat and hence can be used for electromagnetic noise cancelation purposes, for instance in digital still cameras. They also present good radio frequency identification which has been used in higher functional mobile phones and can obtain long transmission distances.

Other alloy systems, namely Fe-Nb-B-Si and Fe-Nb-Cr-P-B-Si, have been utilised to produce soft magnetic powder cores through cold consolidation of glassy powder and resin (Lewandowski, Wang and Greer, 2005). They show the smallest core losses compared to other magnetic powder cores. Similar soft magnetic bulk metallic glasses have been used in solenoid valves, position sensors, magnetic sensors and antennas for radio controlled watches (Suryanarayana and Inoue, 2013).

As to possible structural applications for Fe-based bulk metallic glasses, the relative low cost of alloy production combined with their superior glass forming ability which translates into cost-effective amorphous powder production for different particle sizes through water atomization, has given rise to the manufacturing of shot peening balls with much longer endurance periods compared to conventional materials. These shot peening balls that were manufactured from $Fe_{44}Co_5Ni_{24}Mo_2B_{17}Si_8$ exhibit very high yield strength and elastic elongation limit and can cause larger and deeper compressive residual stresses on the surface of the target as depicted in the Fig. 2.12 (A Inoue *et al.*, 2003). Because of the high hardness and enhanced abrasion resistance of these materials, it has also been suggested for them to be used in applications like coatings on disk cutters for tunnel-boring machines (Farmer *et al.*, 2009).

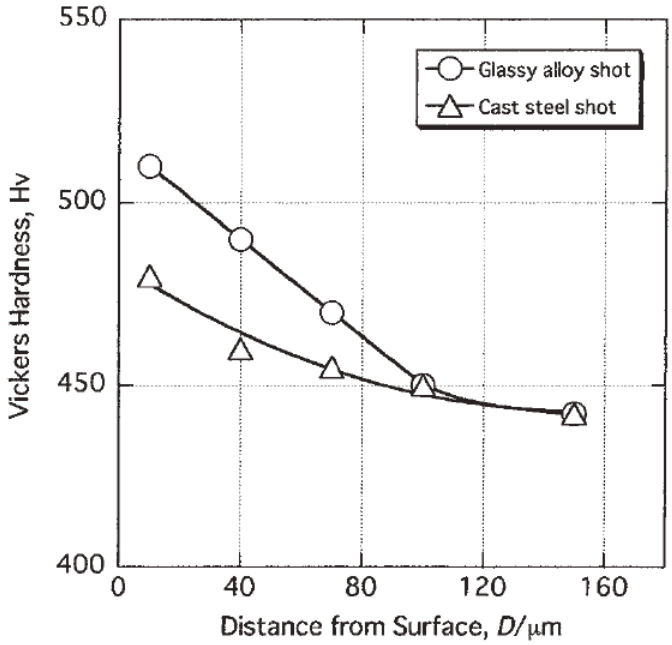

Figure 2.12- Vickers hardness versus distance from the shot surface of the carbon steel sheet after shot peening using Fe-based metallic glass and cast steel shots (A Inoue *et al.*, 2003)**.**

Furthermore, in order to take advantage of the good corrosion and wear resistance of the Fe-based bulk metallic glasses, a high velocity oxygen fuel spray coating technique has been utilised to coat different metallic substrates using $Fe_{50}Cr_{15}Mo_{15}C_{14}B_6$ metallic glass powder. Compared to that of SUS 304 steel and Cr-coated plate, the spray coated glassy alloy layer exhibits significantly higher Vickers hardness and much better corrosion resistance. The metallic glass coated layer tested by a ring-on-disc wear test also demonstrates a smoother surface compared to cast iron and tool steel. To put these favourable properties to use, the inner surface of a soldering vessel was coated with this glassy alloy and after months of usage, no recognisable sign of erosive solder melt attack had been detected (Suryanarayana and Inoue, 2013).

Thermally spray coated (Kishitake, Era and Otsubo, 1996) and bulk (S. Pang *et al.*, 2002) Fe-Cr-Mo-C-B and Fe-Cr-Mo-C-B-P (S. J. Pang *et al.*, 2002) have been reported as materials with very good corrosion resistance, alongside several other Fe-based metallic glasses examined for their passive film breakdown potential, performance during salt fog testing and corrosion rate (Farmer *et al.*, 2004, 2005, 2006). High corrosion resistance of Fe-based bulk metallic glasses, namely SAM1651, has also been the basis of trials in developing coatings for maritime applications (Farmer *et al.*, 2005).

Furthermore, plans have been under evaluation in order to use spray coating of these alloys on large area substrates including steel reinforcing bar, and the expectation is that this could dramatically decrease the corrosion in the infrastructure and hence reduce the associated cost of repair and replacement (Farmer *et al.*, 2009).

It has also been suggested that these materials could be used for coating the inside of the transportation vessels containing spent nuclear waste or to insulate welds and heat affected

zones from environments that could cause stress corrosion cracking (Farmer *et al.*, 1991). They can be a good option for replacing expensive nickel-based alloys, as they would be much more cost effective. In the case of SAM2X5 ($Fe_{49.7}Cr_{17.7}Mn_{1.9}Mo_{7.4}W_{1.6}B_{15.2}C_{3.8}Si_{2.4}$), the alloy shows remarkable neutron absorption properties, up to 4 times greater than borated stainless steel which is why long-term storage of spent nuclear fuel may be a suitable application for it (Choi *et al.*, 2007). Also, Gadolinium as one of the interesting elemental additions to Fe-based bulk metallic glasses, which is useful in enhancing the glass forming ability, can be further studied in terms of the major role it can play in thermal neutron absorption (Shih and Brugger, 1992) and pave the way for the nuclear waste application of this class of BMGs.

2.6. SAM1651, an Fe-Based Glass Forming Alloy

The Fe-based bulk metallic glass forming alloy which is the material being studied in this research has a composition of $Fe_{48}Cr_{15}Mo_{14}C_{15}B_6Y_2$ (atomic percent). As shown in the sections below, it has been shown to have remarkable corrosion and mechanical properties. Therefore, it is being considered for several applications such as an inner coating for a transporting vessel for nuclear waste.

2.6.1. Thermal, Mechanical and Physical Properties of SAM1651

The onset of glass transition temperature of bulk SAM1651 has been reported as 566°C (Shen *et al.*, 2005), 573°C (Seghairi *et al.*, 2012), 575°C (Ponnambalam, Poon and Shiflet, 2004) and 584°C (Farmer *et al.*, 2007). The onset of crystallization temperature for Bulk SAM1651 has been reported as 613°C (Shen *et al.*, 2005), 623°C (Miller, 2010), 615°C (Seghairi *et al.*, 2012)

and 653°C (Farmer *et al.*, 2007). The onset of glass transition temperature for thin ribbon SAM1651 has been presented as 579°C (Seghairi *et al.*, 2012) and the onset of crystallization temperature as 653°C (Miller, 2010) and 597°C (Seghairi *et al.*, 2012). The melting temperature to liquidus temperature has been reported as: 1105-1180°C (Ponnambalam, Poon and Shiflet, 2004), 1115-1191°C (Shen *et al.*, 2005), 1116-1187°C (Seghairi *et al.*, 2012) and finally Farmer et al presents the melting point as 1121°C. The critical cooling rate has been reported as 80K/s (Farmer *et al.*, 2007) and 140K/s (Miller, 2010).

The Vickers Hardness of SAM1651 was presented as 11.4 GPa (Shen *et al.*, 2005) and 13.1 GPa (Seghairi *et al.*, 2012) and the fracture strength of the alloy as 3200 MPa (Shen *et al.*, 2005). The elastic modulus of this Fe-based BMG has been shown to be about 174 GPa and it's Poisson's ratio as 0.349 (Seghairi *et al.*, 2012). Table 2.6 below presents some of the other properties of SAM1651.

Density, kgm^{-3}	7310
Melting temperature, K	1394
Latent heat of fusion, Jkg^{-1}	$3.25 \cdot 10^5$
Specific heat capacity, $Jkg^{-1}\ K^{-1}$	460
Thermal conductivity, $Wm^{-1}\ K^{-1}$	22.5

Table 2.6- SAM1651 properties (Ajdelsztajn et al., 2009)

2.6.2. Corrosion Resistance of SAM1651

The high corrosion resistance of SAM1651 has provoked numerous studies to investigate corrosion characteristics of this material in different environments of which some findings will be reported here. The polarization behaviour of SAM1651 compared to Hastelloy C-22 (which is the favoured alloy to be used for the nuclear waste containers) has been shown to be superior in 90°C seawater, 105°C 5M $CaCl_2$ and 90°C 3.5 molal NaCl. Better resistance to

localized corrosion has also been shown in 105°C 5M $CaCl_2$ compared to Hastelloy C-22, as it demonstrates higher breakdown potential (Lian, Day and Farmer, 2006). However, in regards to the high temperature application of SAM1651, the operating temperature has to be kept below the glass transition temperature, as the formation of crystalline compounds translates to the loss of corrosion resistance properties of the alloy (Farmer *et al.*, 2007).

Crevice corrosion of SAM1651 in comparison to Hastelloy C-22 in 100°C 4M NaCl has also been studied. The crevice corrosion needed a more positive oxidizing potential to initiate on SAM1651 than on Hastelloy C-22 and once started, the corrosion current was sustained at a lower value. Furthermore, it repassivated more readily with a chromium-rich oxide passive film on its surface (Shan, Ha and Payer, 2009).

Galvanic corrosion of SAM1615 in combination with SS 316L, 1018 C-steel and Hastelloy C-22 was examined in 0.6M NaCl solution. For an equal area of SAM1651 to 1018 C-steel, at room temperature, SAM1651 was the cathode and the rate of corrosion for 1018 C-steel was slightly increased, but when an anode to cathode ratio of 1:100 was used, the corrosion rate of 1018 C-steel was increased 50 times. When coupled with SS 316L, in the same conditions, SAM1651 was the anode, however the galvanic effect and hence the corrosion rate was negligible. Finally, when coupled with Hastelloy C-22, both at room temperature in 0.6M NaCl and at 80°C in 3M NaCl, Hastelloy C-22 was the anode with a slight galvanic effect (Ha and Payer, 2009).

2.6.3. Devitrification Behaviour of the SAM1651 Alloy

The amorphous structure is a metastable phase which can transform into a more stable structure, namely a crystalline phase, when heated at a high enough temperature and for a

long enough period. This is called devitrification. The primary precipitate compound in all Fe-based metallic glasses has been reported to be a complex fcc $M_{23}(B,C)_6$ metastable phase which transforms to different equilibrium crystalline phases upon further annealing. It is because of the similar local atomic configuration of this phase to that of its supercooled amorphous surroundings that this is the typical phase to form first upon annealing (Suryanarayana and Inoue, 2013).

In the case of the SAM1651 alloy, the main crystalline phase resulting from the devitrification process has been shown in a study to be $Fe_{23}(C,B)_6$ and in the case of excess oxygen when this process is happening, Y_2O_3 (Seghairi *et al.*, 2012)(Katakam, Santhanakrishnan and Dahotre, 2012). In another study, as received samples were examined by TEM and it was determined the amorphous structure included Mo and Y rich islands, shown in Fig. 2.13. After heat treatment the microstructure was comprised of an amorphous matrix with crystalline $(Cr,Fe)_{23}C_6$ and fewer M_7C_3 particles and the Mo and Y rich islands. None of the Mo/Y rich islands were observed to include the crystalline particles which was attributed to the higher glass forming ability in these areas due to higher concentrations of Yttrium in them (Miller, 2010).

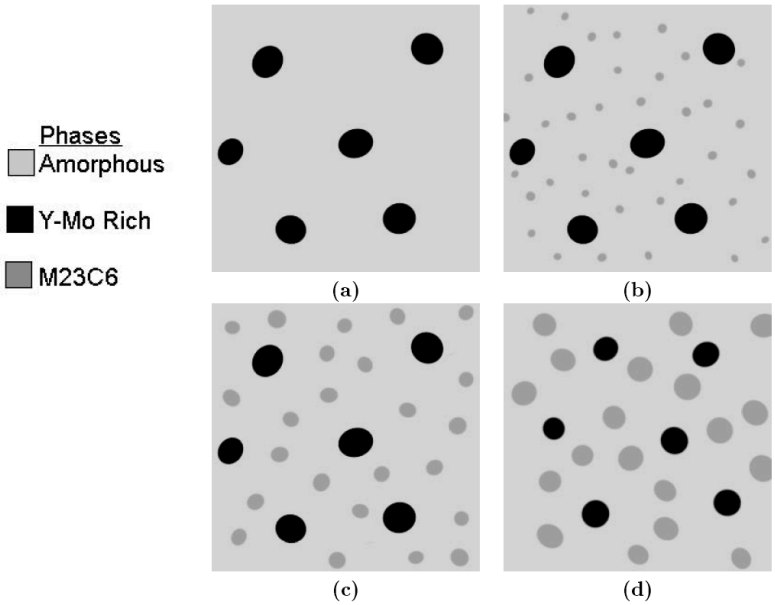

Figure 2.13- Schematic of the microstructure of the samples (a) as received, after heat treatment at (b) 600 °C, (c) 700 °C and (d) 800 °C for 3 hours (Miller, 2010).

The effect of heat treating SAM1651 on its devitrification was also reported (Manh, 2010). Upon heating the specimens at 800°C for an hour and at 700°C for 3, 24 and 72 hours, $(Cr,Fe)_{23}C_6$ and $(Cr,Fe)_7C_3$ crystalline phases were observed in XRD patterns (Fig. 2.14).

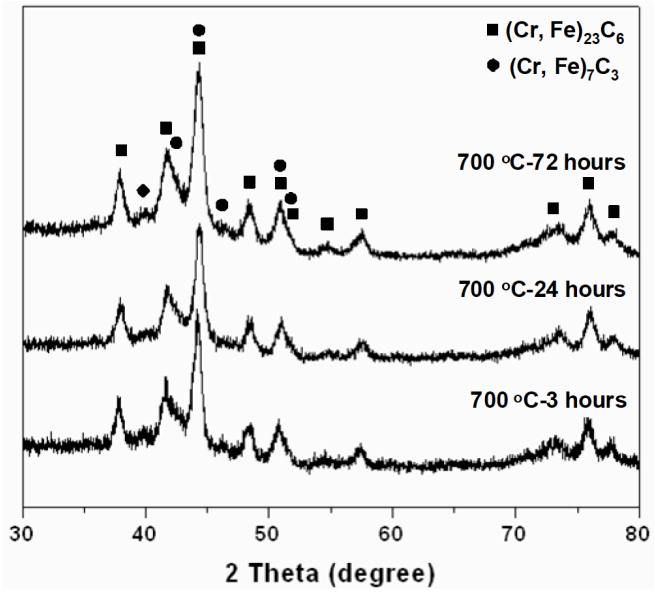

Figure 2.14- XRD pattern of SAM1651 heat treated at 700°C for 3, 24 and 72 hours (Manh, 2010)

Although no TTT diagrams could be located for the SAM1651 alloy, Hildal reported that for cooling rates lower than the critical cooling rate of SAM1651 during casting, the resulting microstructure was $M_{23}C_6$ nanoparticles within an amorphous matrix and decreasing the cooling rate much further, resulted in the crystalline phase becoming dendritic (Hildal, Sekido and Perepezko, 2006).

The effect of exposure time on devitrification during the heat treatment of the SAM1651 samples has also been investigated (Nouri, Liu and Lewandowski, 2009). It was reported that when the samples were held for longer times at temperatures near the glass transition temperature and above (from 562°C to 620°C), the hardness of the specimens increased as shown in Fig. 2.15. While the hardness of the samples that were held at temperatures below 500°C did not change with exposure time. And, for the samples heated at 500°C, measured hardness increased as well.

Nouri et al explained this correlation through the effect of devitrification of the samples during the heat treatment and how this change in the microstructure of the specimens changed the viscosity of the samples at each temperature and exposure time. Through TEM imaging, they showed how, at temperatures above 500°C, increasing the exposure time, destabilizes the microstructure of the SAM1651 alloy resulting in nanocrystallization. This phenomenon directly causes increasing of the viscosity of the alloy which in turn results in the increasing of the hardness of the material.

For temperatures below 500°C, no changes in the hardness of the material was observed, because there is no crystallization happening in this temperature range according to TEM imaging. However, at 500°C, increasing of the hardness can be observed as the exposure time value increases. This was explained through thermal relaxation of the amorphous

microstructure which resulted in increasing of the viscosity and hence hardness.

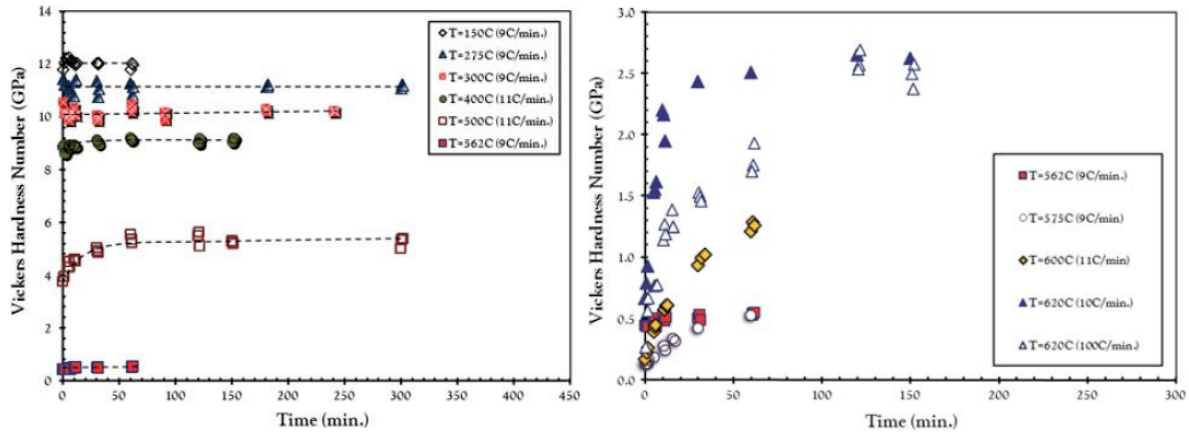

Figure 2.15- Effect of exposure time on the hardness of different samples held at 150°C to 620°C with the heating rate used, shown in the legend (Nouri, Liu and Lewandowski, 2009).

They also presented the effect of the initial heating rate, before each specimen reached the final temperature, and concluded that at shorter exposure times, larger heating rates cause the hardness of the material to be lower. This is because faster heating rates limit and slow down the amount of microstructure evolution causing the viscosity and hence hardness of the specimen not to increase as much as it would, compared to slower initial heating rates. This difference in the hardness of the specimens disappeared after enough exposure time (about 100 minutes) was passed.

2.7. Selective Laser Melting Process

Selective laser melting is an additive manufacturing process that uses a laser beam to melt metallic powder, among other materials, in selected areas dictated by computer aided design (CAD) to fabricate specimens in a layer by layer manner. This data has to be processed through software like Autofab to provide slice data with STereoLithography format to the SLM machine which would produce information of where the laser needs to scan in each layer and

also generate support for overhanging areas of the specimens. The SLM process (as shown in Fig. 2.16) commences when the first layer of powder is distributed on top of a substrate and the laser beam scans and melts selected parts of the powder bed according to the processing parameters dictated through the computer-generated file.

These processing parameters, i.e. laser power, scanning speed, layer thickness and hatch spacing are chosen to produce melt tracks that are fused together with the ones next to them in each layer and with the previous layer. Afterwards, the substrate is lowered and the next layer of powder is laid on top of the previous layer and the process repeats until the whole specimen is completely fabricated. The process is carried out inside a building chamber and under an inert atmosphere like Argon to prevent oxidation of the heated metal. After the whole part is manufactured the excess powder is removed and the specimen is detached from the substrate (Yadroitsev, 2009).

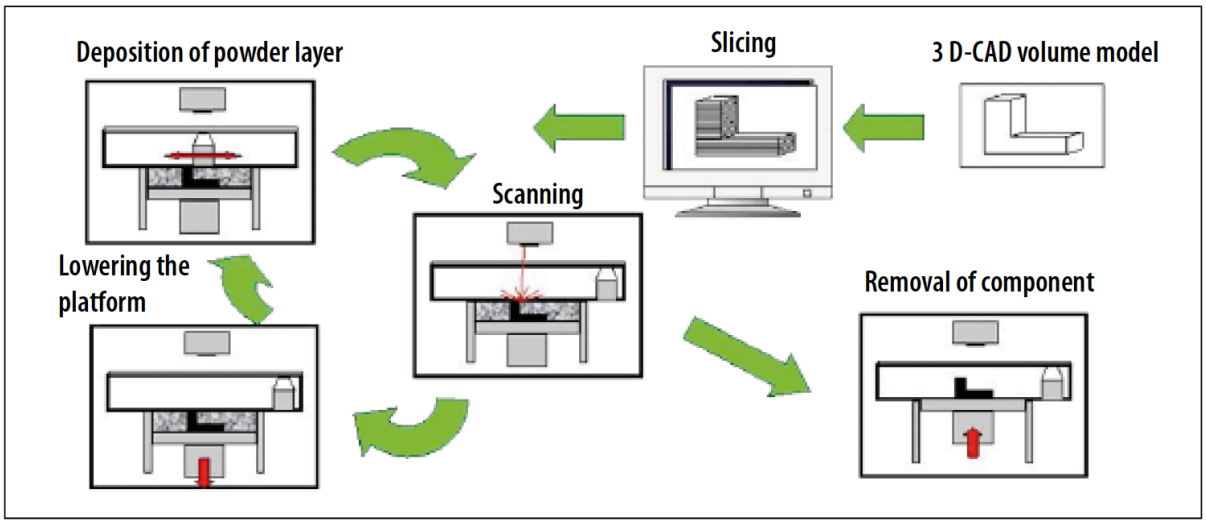

Figure 2.16- Principle of the SLM process (Bremen, Meiners and Diatlov, 2012).

The laser beam used in the SLM process was first adopted from the selective laser sintering process, namely a CO_2 laser with a wavelength of 10.6µm, and then a Nd:YAG fibre laser with

a wavelength of 1.06µm and an Yb:YAG fibre laser were utilised instead, since metallic powders have a higher absorptance to radiation of these wavelengths in the infrared region (Tolochko *et al.*, 2000). Absorptance in SLM, defined by the ratio of the laser energy absorbed by the material to the laser energy incident upon the material, determines the efficiency of the process and can even decide whether a specific powder can be processed using a specific laser.

It is worth mentioning that the absorptance of the metallic powder can be drastically different and higher from that of its bulk form, which is because of the high levels of reflections of the laser beam between different powder particles (Manakari, Parande and Gupta, 2016). The effect of the energy distribution of the laser beam has also been studied, showing that, in the case of AA6061 aluminium alloy for example, compared to a Gaussian beam profile, a uniform beam profile can achieve a larger melt pool width and hence increase the efficiency of the process by providing the opportunity to increase the hatch spacing used and reduce the processing time consequently (Loh *et al.*, 2014).

Together with absorptivity, layer thickness, hatch spacing, laser power and scanning speed (shown in Fig. 2.17) determine the volumetric energy density input that is responsible for raising the temperature of and melting the powder particles. Layer thickness for example is usually selected to be 20-100µm, balancing between resolution achievable and the flowability of the powder. If the energy input is too low, balling may occur due to lack of wettability of molten pool with the previous layer deposited (Li *et al.*, 2012) and if it is too high vaporisation might be the result (Krakhmalev and Yadroitsev, 2014). Therefore, optimisation of these processing parameters is essential in achieving a high densification in the selective laser melting process.

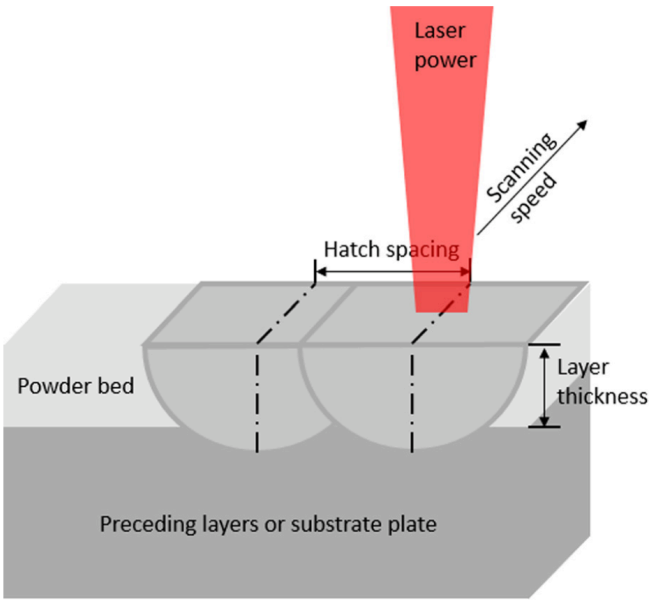

Figure 2.17- Sketch of the SLM processing parameters (Yap et al., 2015)

Furthermore, thermal properties of the material used in the SLM process, like thermal conductivity, specific heat capacity and latent heat, also determines the thermal response that the material would have, in powder and bulk form, to the energy input of the laser. The size of the powder particles is another key factor and studies have shown that smaller sizes would require smaller energy densities to produce high density specimens and better surface finish (Spierings, Herres and Levy, 2011). However too small, and the particles might agglomerate together due to Van der Waals forces and cause poor powder flowability which is essential for good powder deposition in the SLM process.

2.8. Defects in Selective Laser Melting

Several different types of defects can develop inside the microstructure of specimens manufactured using the SLM process. Porosity, cracking, lack of fusion defects, inclusions and segregations are some of the defects that can be found in these specimens, usually

formed as a result of the intrinsic material characteristics and/or usage of unoptimised processing parameters which are categorized in Fig. 2.18. Here, the main three defects associated with the SLM process will be discussed along with how they are formed and how they can be prevented.

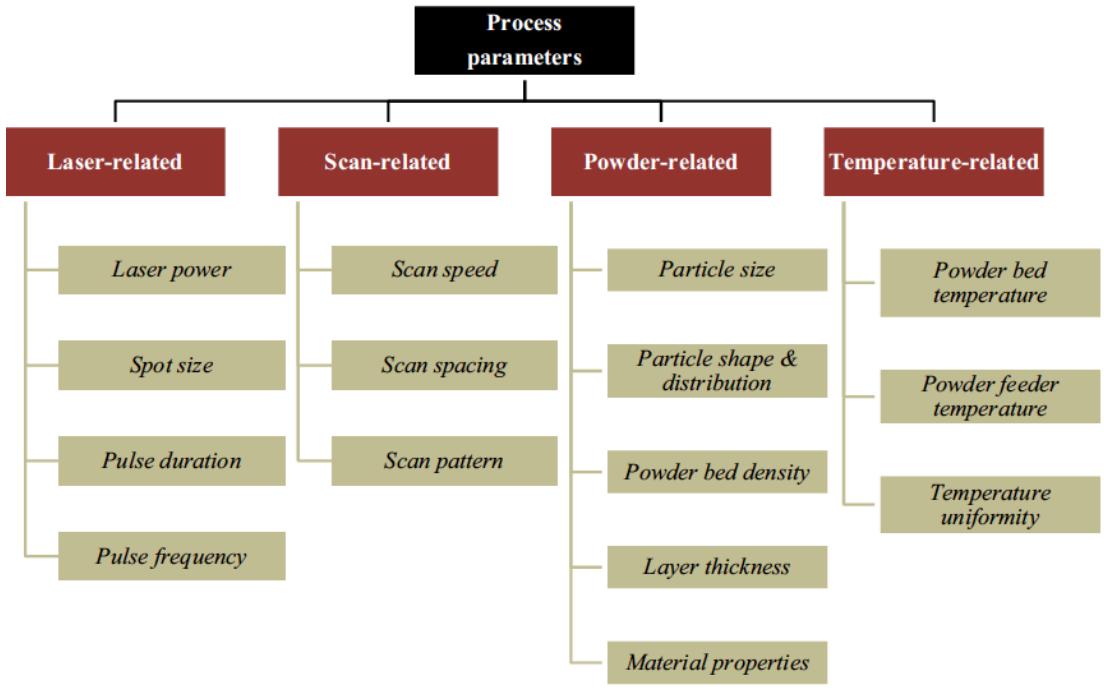

Figure 2.18- Controlling parameters in the selective laser melting process (Aboulkhair et al., 2014).

2.8.1. Pores

Pores are defined as small (typically less than 100µm in diameter) and spherical holes, randomly distributed in the SLM manufactured sample (as shown in Fig. 2.19) and several reasons have been mentioned for their presence in the microstructure of the specimens. For instance, if the powder particles used for the SLM process have internal pores, caused in their production stage during gas atomization, the entrapped gas in these pores would remain in the microstructure of the specimen because of the melting and solidification rate of the SLM process (Aboulkhair *et al.*, 2014). Similarly, if the packing density of the powder used is low,

because of the high temperature of the molten pool and hence high gas solubility in the liquid metal, the gas between the powder particles may dissolve in the molten pool and remain there as a result of the high solidification rate and cause porosity.

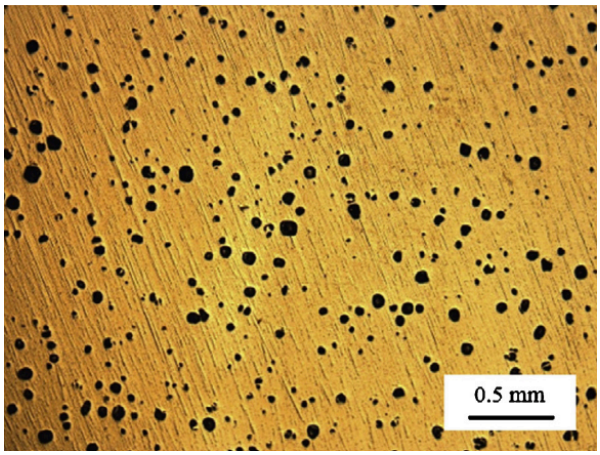

Figure 2.19- Optical images of pores in microstructure of an SLM fabricated Ti–6Al–4V specimen(Gong, Rafi, *et al.*, 2014)

It has also been suggested that some pores may be formed as a result of the incomplete remelting of the local surfaces from the previous layer which would cause high roughness and small ridges on the surface of the previous layer to which the molten metal would not be able to reach and hence porosity would form (Qiu, Adkins and Attallah, 2013). Furthermore, vaporisation has been reported to be one of the underlying causes of porosity. When the laser energy input is high enough, the low melting temperature constituent elements of the alloy may be vaporised and because of the high solidification rate of the process, the gas bubbles would not have enough time to rise to the surface of the molten pool and escape and their entrapment would result in the formation of porosity (Gong, Rafi, *et al.*, 2014).

Moreover, size and morphology of the powder particles used in the SLM process has been shown to influence the porosity and density of the resulting specimens. It was reported that smaller sized and spherical powders (as opposed to a more irregularly-shaped powder

morphology) would fabricate specimens with higher densities and lower porosity values, due to better packing and flowing characteristics of the aforementioned powders (Li *et al.*, 2010; Zhang *et al.*, 2011).

2.8.2. Lack of Fusion Defects

Lack of fusion defects are irregularly-shaped holes (usually larger than pores) which are formed in the microstructure of specimens fabricated through SLM (as shown in Fig. 2.20) due to insufficient energy input into the molten pool. This can result in the molten track having a smaller width which would mean that consecutive tracks may not overlap sufficiently and hence some powder particles would remain unmelted. Or, the depth of the molten pool would be small which would mean that successive deposited layers would not overlap properly which would result in some powder particles remaining unmelted and hence lack of fusion defects would form as a result (Vilaro, Colin and Bartout, 2011; Gong, Rafi, *et al.*, 2014; Liu *et al.*, 2014). Therefore, other than increasing laser power and/or decreasing scanning speed which would increase the volume of each melt pool, decreasing the hatch spacing and layer thickness can help in preventing these defects (Yadroitsev, Bertrand and Smurov, 2007)(Aboulkhair *et al.*, 2014).

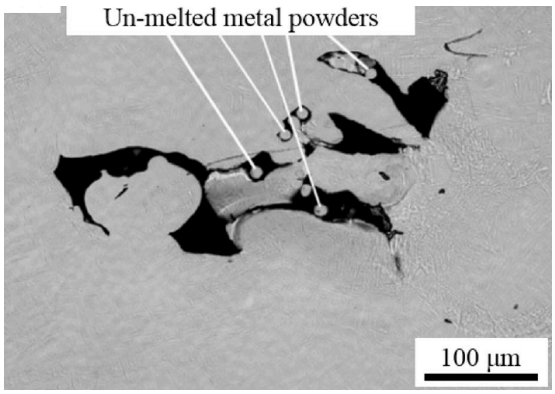

Figure 2.20- Optical image of a lack fusion defect in an SLM-fabricated specimen out of Ti-6Al-4V (Liu et al., 2014)

If these defects are formed on the surface of the deposited layer, the roughness of the surface in their area may cause poor flow of the molten metal in the next layer and hence larger interlayer defects may form as a result (Zhou *et al.*, 2015). For the more readily oxidised alloys like AlSi10Mg, formation of an oxidised layer may contribute to a decrease in the wettability of the surface of the previously deposited layer causing the flow of the molten metal to be partially blocked and hence interlayer lack of fusion defects may form as a result (Read *et al.*, 2015).

Scanning strategy can also play a role in the formation of defects in SLM fabricated specimens. Unidirectional and zigzag strategies have been associated with higher energy density input in the beginning and the end of each track due to unstable laser power and reduced scanning speed which could cause defect formation in these areas (Thijs *et al.*, 2013). Lack of fusion defects have been reported to be more prevalent between scan tracks and layers deposited using these two scanning strategies (Maskery *et al.*, 2016). Cross hatching and island strategy scanning has been utilised to produce a more uniform energy input (Jhabvala *et al.*, 2010) and hence inhibit defect accumulation in the same location. They have also been shown to result in reduced residual stresses and hence less cracking in the SLM manufactured specimens (Matsumoto *et al.*, 2002).

2.8.3. Cracking

The specimens manufactured with the selective laser melting process experience very high cooling rates of up to 10^8K/s (Gu *et al.*, 2012) which introduces large temperature gradients that in turn result in large residual stresses in the fabricated samples. This situation, especially for stainless steels and nickel-based super alloys which have low thermal conductivity and

high thermal expansions can result in crack initiation and propagation in the parts made through the SLM process (Zhao *et al.*, 2009; Li *et al.*, 2010; Carter, Attallah and Reed, 2012; Carter, Essa and Attallah, 2015).

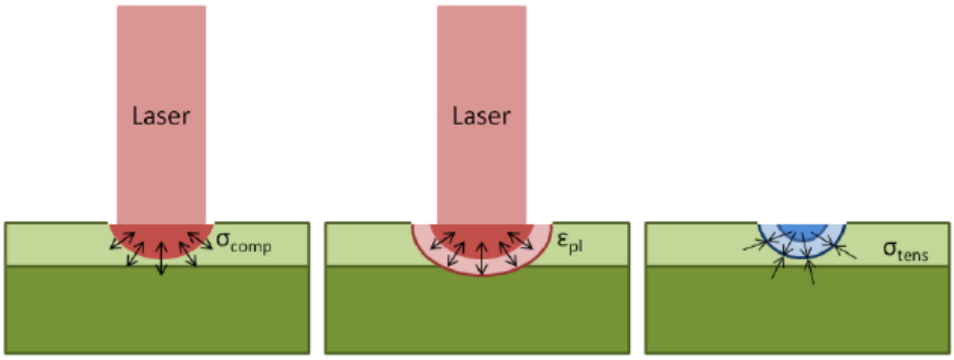

Figure 2.21- Schematic of the thermal gradient mechanism in the SLM process (Kempen et al., 2013)

The thermal gradient mechanism (shown in Fig. 2.21) has been identified as one of the main phenomenon in the selective laser melting process that causes residual thermal stresses in fabricated specimens (Kruth *et al.*, 2004; Mercelis and Kruth, 2006; Shi *et al.*, 2007; Kempen *et al.*, 2013). While the laser beam is applied to the powder bed and the molten pool is being created, due to the rapid heating of the upper layers, underneath the melt pool (i.e. in the HAZ), and due to the rather slow heat conduction, a large thermal gradient is created.

Because of the high temperatures experienced in the upper layers of the HAZ, they would tend to thermally expand, however the lower temperature material in the lower layers of the HAZ and the surrounding material restricts this expansion and this causes compressive stresses in these upper layers which can be larger than the yield strength of the material and hence cause plastic deformation. After this compressively deformed material cools down, the compressive state of its stress changes into residual tensile stress and these residual stresses can be the cause of crack formation, delamination and disconnection from the base plate in

the SLM fabricated parts (as shown in Fig. 2.22). It has been demonstrated that the most effective way to reduce these thermal stresses is through pre-heating of the substrate which decreases the aforementioned thermal gradients (Shiomi *et al.*, 2004; Mercelis and Kruth, 2006; Kempen *et al.*, 2013).

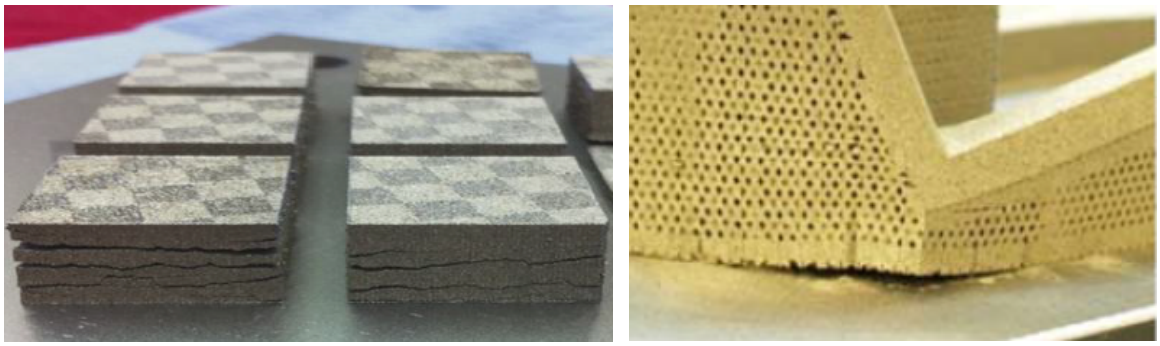

Figure 2.22- Delamination (left) (Kempen et al., 2013) and separation from the baseplate (right) (Zaeh and Branner, 2010) resulting from residual stresses in the SLM-fabricated specimens.

Formation of micro-cracks in the microstructure of some SLM fabricated parts (e.g. CM247LC nickel-based super alloy and commercially pure titanium) has been associated with the high energy input caused by the usage of high laser power and/or low scanning speed. This high energy input results in a more severe contraction of the melt pool during solidification which in turn facilitates the formation of solidification micro-cracks in the microstructure of the specimens. Utilizing a smaller energy input has been shown to eliminate these defects (Gu *et al.*, 2012; Carter *et al.*, 2016).

Clearly, the interconnected nature of defect formation in the selective laser melting process means that changing the processing parameters in order to prevent the formation of one type of defect might result in facilitating the formation of another type of defect. For example, as shown in Fig. 2.23, if the energy density used in the SLM processing of CMSX486 Ni-based super alloy was to increase to decrease the lack of fusion defects fraction (calculated by presenting the sum of the area of lack of fusion defects as a percent of the total micrograph

area), an increase in the cracking density (calculated by dividing the sum of crack lengths, measured in all of the micrographs taken from a specimen, by the total area of the micrographs) would occur as a result (Carter, Essa and Attallah, 2015).

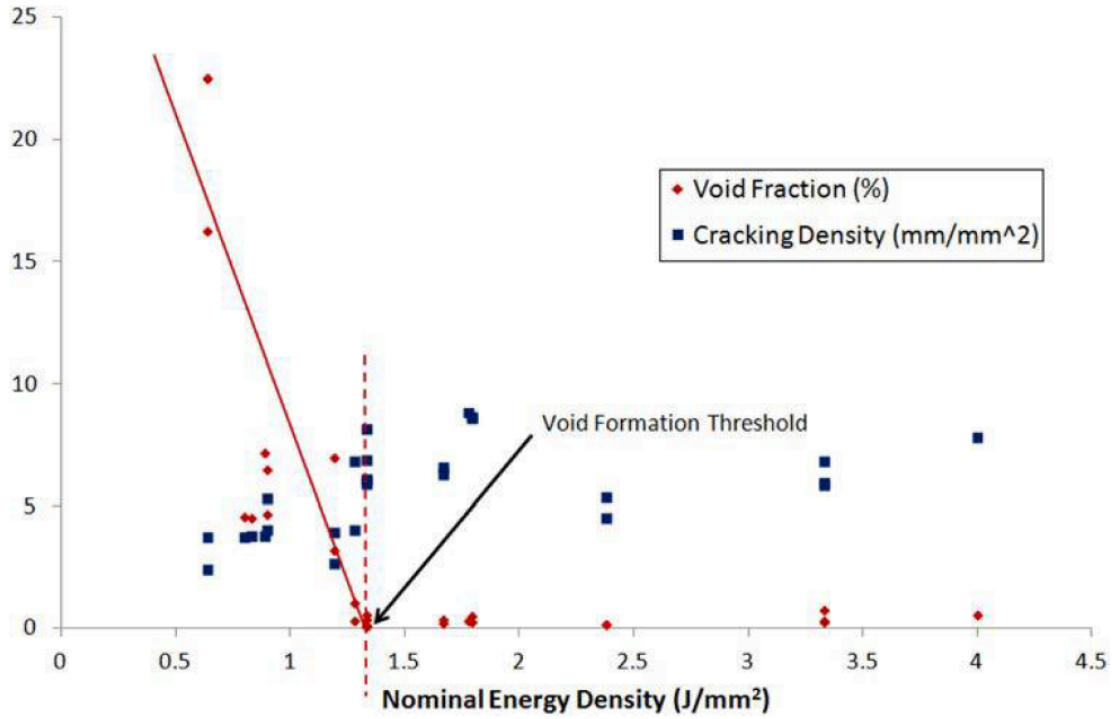

Figure 2.23- Plot of lack of fusion (void) defects fraction and cracking density against energy density (Carter, Essa and Attallah, 2015).

2.9. Normalised Energy Density Input

Laser melting includes the use of several processing parameters and when combined with the characteristic thermo-physical properties of different materials used as feedstock in fabrication of samples through this process, a complicated picture arises. The interaction between all of these factors makes the prediction of the properties of the resulting specimens difficult. This is why in order to be able to investigate the influence of these factors on the microstructure and properties of the laser melting products, processing maps have been developed that demonstrate how these parameters interact.

In an attempt (Ion, Shercliff and Ashby, 1992) to provide a useful tool to prepare these processing maps, dimensionless parameters for representing laser power and scanning speed were identified, through application of an analytical heat flow model, as:

$$q^* = Aq/[r_B\lambda(T_m - T_0)] \qquad \text{Equation – 2.15}$$

$$v^* = vr_B/\alpha \qquad \text{Equation – 2.16}$$

where q* is the dimensionless laser power, A is the surface absorptivity coefficient, r_B is the beam radius and λ, α and T_m are the thermal conductivity, thermal diffusivity and melting temperature of the material being processed respectively. T_0 is the initial temperature at which the material is being processed which can be assumed to be the substrate temperature as well. v^* and v are the dimensionless and nominal laser beam speed respectively. Ion et al. (Ion, Shercliff and Ashby, 1992) considers the use of q* and v* to help predict the maximum temperature and heating rate of the material being processed, in a heating cycle.

In order to adapt this approach with selective laser melting (and electron beam melting), an extended version of the above-mentioned strategy was developed which include the dimensionless parameters representing layer thickness and hatch spacing (Thomas, Baxter and Todd, 2016):

$$l^* = {}^{2l}/_{r_B} \qquad \text{Equation – 2.17}$$

$$h^* = {}^{h}/_{r_B} \qquad \text{Equation – 2.18}$$

where l* and h* are the dimensionless layer thickness and hatch spacing respectively, l is the layer thickness and h is the hatch spacing value used in the SLM process. In this approach, the thermo-physical properties of the powder were assumed to be unchanged during melting. They were also assumed to be identical to those of the bulk material for simplification

reasons. Hence, a dimensionless parameter representing the volumetric energy density input of the laser beam was identified:

$$E_0^* = \frac{q^*}{v^* l^* h^*} = \left[{Aq}/{(2vlh)}\right]\left[{1}/{\rho C_p (T_m - T_0)}\right] \qquad \text{Equation – 2.19}$$

where E_0* is the normalised energy density input, ρ is the density and C_p is the specific heat capacity of the material being processed. Using large values of E_0* was shown to lead to excessive heat input into the material and insufficient amounts were considered to be the cause of lack of fusion defects in the microstructure of the final specimen.

2.10. Finite Element Analysis of the Selective Laser Melting Process

Experimental measurement approaches to investigate the residual stresses occurring in the specimens manufactured by the selective laser melting process can provide a basic level of insight which can cost less if it is done qualitatively. However, to get a more detailed understanding of the stress situation, more expensive and time consuming quantitative techniques need to be utilised. To get the advantages of both these measurement routes, simulation has been used which can provide a greater comprehension of the influence of different processing parameters on the formation of residual stress, and save time and money through decreasing the number of samples that have to be fabricated in carrying out the research.

Various studies have been performed in order to develop Finite Element Method (FEM) simulations for analysing the effect of different parameters on the thermal gradients which have been identified as the main source of formation of residual stresses in the SLM process (Matsumoto *et al.*, 2002; Roberts *et al.*, 2009; Gusarov and Smurov, 2010). There are two

approaches taken in these studies, both modelling the laser exposure as a moving heat source. One is the use of a global model which deals with the whole part being simulated as opposed to trying to model every melt track involved in the process and this can be beneficial since computational time and power is usually constrained (Zaeh and Branner, 2010). The other approach has been to use a three dimensional thermomechanical model to simulate the transition between powder to solid which would provide not only the residual stresses remained in the specimen, after it has been fully fabricated, but also the short term stresses and temperatures during the laser exposure and deposition of the material (Dai and Shaw, 2004).

In one research, the melting and solidification of powder particles were modelled through FEM simulation of a single spot on the powder bed (Shiomi *et al.*, 1999). The validation for this modelling was performed by comparing the weight of the solidified material obtained through both calculation and experiments and the study concluded that the influence of laser power is more significant compared to the laser irradiation time when it comes to the maximum temperatures occurring in the melt pool. Furthermore, in an initial attempt that considered the alteration of characteristics when the material transforms from powder to liquid and then to solid, prediction of the resulting thermal stresses through modelling the temperature distribution in a single layer fabricated by selective laser melting of metallic powder was done (Matsumoto *et al.*, 2002). Although, the simulation did not take into account the influence of the base plate on the thermal profile of the specimen, nor the change in the characteristics of the alloy during the rise in the temperature.

This oversight was partially amended by developing a model for simulating the thermal profile of several layers in the selective laser melting process while considering a more refined

version of the thermal conductivity of the powder (Roberts *et al.*, 2009). Further enhancement could be applied by the inclusion of the properties of the material in the mushy zone in the model (Zehner and Schulunder, 1970). Also, utilisation of thermally dependent characteristics of the material has been demonstrated to assist in development of a simulation of the SLM process that resulted in the optimisation of the processing parameters which in turn helped fabricate specimens with the intended amount of pores in its microstructure (Song *et al.*, 2012). This clearly presents the high value of having the accurate thermal profile through getting the right modelling tool to be able to adopt the right parameters for obtaining the desired microstructure.

In another study, a three-dimensional model of a layer was constructed by considering the laser irradiation as a volumetric heat source and taking the temperature dependant properties of the powder and the solid into account (Foroozmehr *et al.*, 2016). The FEM simulation was further enhanced by calibrating the optical penetration of the laser beam (defined as the depth of the powder bed at which the energy intensity of the beam decreases to 1/e of its value at the surface (Fischer *et al.*, 2002)) with the experimental results. The simulated melt pool sizes which were modelled considering the transition of the material from powder to liquid to solid were in agreement with the results from the experiments. A similar approach was taken in FEM modelling of the SLM processing of Ti6Al4V powder to examine the influence of scanning strategy on the resulting residual stresses (Parry, Ashcroft and Wildman, 2016). The extreme temperatures reported in this study, which were ignored in the estimation of the thermal stress, might be the result of the fluid flow which hugely affects the heat transfer in the melt pool (Mills *et al.*, 1998).

Surface tension has been shown to dictate the regime of the heat transfer in the melt pool, as well as the shape of the melt pool through influencing physics of the melting behaviour occurring in the selective laser melting process (Khairallah and Anderson, 2014). This was demonstrated through a multi-physics modelling of the SLM process which also confirmed that considering the stochastic nature of the powder can greatly enhance the validity of the result of the simulation. Although developing computational fluid dynamics modelling is more expensive than FEM simulations and involve a deep understanding of the fluid dynamics, they have been shown to be able to better model the melt pool size and temperature profile occurring in the specimens fabricated by SLM (Yuan and Gu, 2015).

Therefore, some have tried to accommodate the effect of the Marangoni convection inside the melt pool, by incorporating the concept of enhanced thermal conductivity in their less computationally expensive FEM simulation approaches. In this regard, it has been shown that using an anisotropic enhanced thermal conductivity instead of an isotropic one can provide a better simulating tool for modelling the effect of melt pool convection on the morphology of the melt pool and the thermal distribution occurring in the selective laser melting process (Safdar *et al.*, 2013). Validation of this model through comparison with the melt pool size of the experimental results indicated that utilization of enhanced thermal conductivity could effectively model the Marangoni convection in the melt pool, reducing the need for developing a more complex CFD model.

Finally, utilising a surface heat source and combining the use of enhanced thermal conductivity with consideration of change in thermal properties of the material at different temperatures has been shown to be able to predict the thermal gradients and cooling rate values occurring in the fabrication of specimens of an AA-2024 aluminium alloy by selective

laser melting (Lopez-Botello *et al.*, 2017). Validation of the simulation was carried out by comparing the predicted and experimental microstructure of the samples which were presented to be similar. This is why an FEM simulation incorporating the enhanced thermal conductivity was chosen to model the thermal gradients, cooling rates and melt pool sizes obtained through SLM manufacturing of the specimens out of SAM1651 glass forming alloy.

2.11. Laser Assisted Deposition of Bulk Metallic Glasses

Laser assisted additive manufacturing can provide a suitable processing route for bulk metallic glasses, as the very high cooling rates occurring during the process are usually higher than the critical cooling rate of most BMGs. However, high thermal gradients involved in the process combined with the intrinsic brittleness of most bulk metallic glasses could cause severe defects like cracks, curling or even delamination in the parts produced through these processes. Here, efforts in trying to manufacture parts out of different BMG alloys are discussed.

2.11.1. Al-Based Bulk Metallic Glasses

For the $Al_{86}Ni_6Y_{4.5}Co_2La_{1.5}$ glass forming alloy, the effect of laser power on the microstructure, defect formation and mechanical properties of resulting parts during the selective laser melting process was investigated (Li, Kang, Huang, Zhang, *et al.*, 2014). In order to so, single tracks of the Al-based amorphous powder were melted using 80W, 120W, 160W and 200W laser power while keeping the scanning speed as 1000mm/s. Through variations of the laser power utilized in this experiment, various energy density distributions and heat transfer processes were reported to occur in the tracks melted. It was shown that at higher laser

power values, the energy density distribution was more dominant in determining the morphology of the scanned tracks, resulting in a Gaussian-like cross section. On the other hand, at lower laser power values, heat transfer processes were determined to be the dominant force in formation of the shape of the cross section, resulting in a sub-circular pattern.

Different energy density distribution and heat transfer processes caused by the usage of different laser power values, was also reported to cause diverse thermal histories in various parts of the melt tracks. This resulted in different microstructure, hardness, elastic modulus and plastic behaviour in those parts due to the different cooling rates experienced. For instance, it was mentioned that contrary to the expectation that higher laser power would result in a high cooling rate and hence amorphisation of the microstructure, the large thermal fluctuations increased the possibility of heterogeneous chemical composition and hence volume of the crystallization observed in the microstructure of the melt tracks.

As to the crack formation behaviour occurring inside the melt tracks, it was reported that at high laser power values, cracks could be observed in the microstructure of the tracks (shown in Fig. 2.24) which were attributed to the large thermal stresses caused during the SLM process. At smaller laser power values, cracks were also observed which were associated with reduced strength of the metallic glass which in turn was caused by the formation of lack of fusion defects inside the structure of the melt tracks. So, optimization of the processing parameters was suggested to be the solution to producing crack-free specimens.

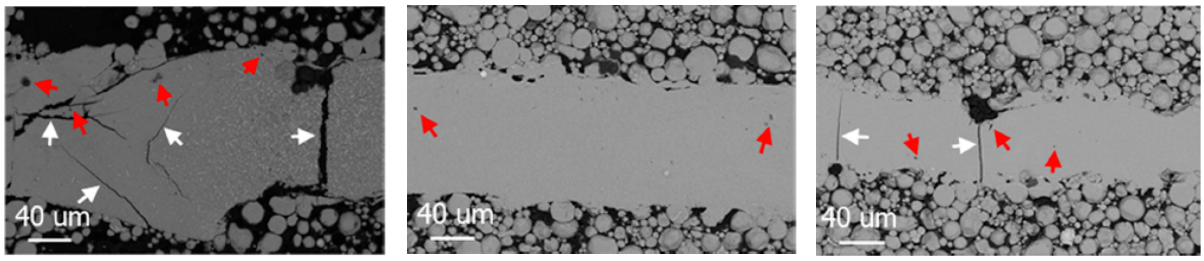

Figure 2.24- SEM backscattered images of the X-Y cross section of melt tracks made with 200W (left), 120W (middle) and 80W (right). Red arrows indicate the pores and white arrows show the cracks formed during the SLM process (Li, Kang, Huang, Zhang, et al., 2014).

The influence of the temperature of the substrate on the bonding between the part and the substrate has been investigated for an Al-based glass forming alloy, namely $Al_{86}Ni_6Y_{4.5}Co_2La_{1.5}$ (Li *et al.*, 2015). In order to do this, a 100µm layer of the pre-alloy powder was melted on a pure aluminium substrate, with the laser scanning speed of 750mm/s and laser power of 120W. The experiment was carried out with the substrate at two different temperatures, once at RT and then at 250°C (which is lower than the alloy's glass transition temperature).

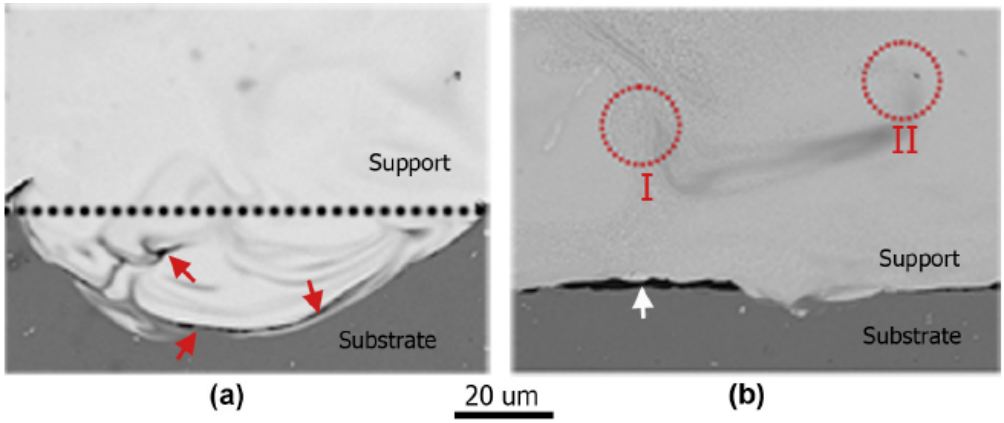

Figure 2.25- SEM images of the interface between the BMG layer and the substrate at 250°C (a) and RT (b). Red arrows indicate the Al oxide formed during the SLM, the white arrow shows the gap between the substrate and the BMG layer and areas I and II demonstrate the crystallized parts in the BMG layer (Li et al., 2015).

As shown in Fig. 2.25, in the case of the substrate at 250°C, the interface between the substrate and the BMG layer seems to be melted in a semi-circular manner with good bonding between the two. When the substrate was at room temperature, however, the substrate

does not seem to be melted at all and there is a gap between the substrate and the BMG layer. Also, there is crystallization in the microstructure of the BMG layer when the substrate was at room temperature, which is not the case for the high temperature substrate experiment. This behaviour was explained with the help of a multi-physics-based computational model estimating the temperature distribution and cooling rate occurring at the interface between substrate and the BMG alloy.

It was shown that the area in which the temperature was higher than the melting point of the substrate (660°C) is larger when the substrate was kept at 250°C compared to when it was at RT, which is why some of the substrate was melted in the former and not the latter. It was also indicated that although the model predicted that the cooling rate of the melted areas should be higher than the critical cooling rate of the BMG alloy for both experiments, the gap between the BMG layer and the unmelted substrate (when the substrate was kept at room temperature) meant that the heat transfer from the melted BMG layer to the substrate was greatly reduced, causing the cooling rate occurring in the BMG laser to be lower than its critical cooling rate, in some areas, which in turn caused crystallization to happen. They concluded that, for this alloy, the higher substrate temperature would be beneficial for improving bonding between the BMG layer and the substrate and also to prevent crystallization in the microstructure of the BMG alloy.

In another study on a similar Al-based glass forming alloy, $Al_{85}Ni_5Y_6Co_2Fe_2$, the role of re-scanning each layer was investigated, as a strategy to minimize the thermal gradient occurring during the SLM process and hence preventing the formation and propagation of cracks inside the microstructure of the resulting specimen (Li, Kang, Huang and Sercombe, 2014). In order to show the effectiveness of this strategy, a cube was manufactured (shown in Fig. 2.26), to

the lower half of which just the initial laser scanning was applied and to the top half, a laser re-scan was applied after each layer was deposited and melted through the initial scan. The initial scan had a laser power and scanning speed of 200W and 625mm/s respectively and the rescanning was carried out with the same scanning speed, but a smaller laser power of 80W.

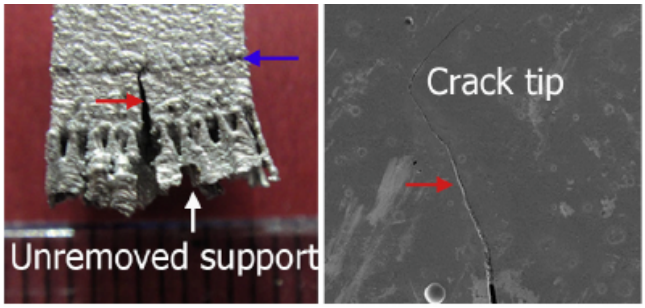

Figure 2.26- The cube made from Al-based glass forming alloy (left). The blue line indicates where the rescanning strategy began. The SEM image of the tip of the crack (right) (Li, Kang, Huang and Sercombe, 2014).

As evident in the image, the lower half of the cube has a relatively large macro-crack, however the top half seems to be crack free. As to how this strategy would achieve this task, it was explained that re-scanning at each layer would carry out in-situ stress relieving within each layer. The initial higher power scan melts the powder layer, but introduces large thermal gradients inside the specimen, and then the second, lower power scan increases the temperature of the material in the affected layer to above the glass transition temperature of the glass forming alloy, allowing the thermal stresses to be rapidly reduced through viscous flow of the material, since the alloy experiences superplasticity in the supercooled liquid region. It was also reported that the hardness of the specimen manufactured through the rescanning strategy is higher than that of the part made with just the initial laser scanning procedure. The reason for this enhancement, could be the reduction of free volume through the stress relief provided through the rescanning, which has been known to increase the hardness of BMG alloys (Gu *et al.*, 2013).

2.11.2. Zr-based Bulk Metallic Glasses

In an effort to examine the influence of the laser energy input and the type of substrate on the formation and nature of a crystallized component in the heat affected zone, single-layered specimens were manufactured out of a Zr-based metallic glass, namely $Zr_{58.5}Cu_{15.6}Ni_{12.8}Al_{10.3}Nb_{2.8}$, through the LENS^{TM} process (Sun and Flores, 2010). Fully amorphous and fully crystallized plates with the same composition of the powder mentioned above were used as substrates for this experiment. A laser power of 150W and two scanning speeds of 14.8 and 21.2mm/s were utilised to create two different laser energy input values.

When the powder was deposited using the higher energy density on the amorphous substrate, formation of a layer of spherulites, with the same composition as the amorphous matrix around them, were observed in the HAZ around the melt tracks that were solidified into an amorphous microstructure. On the other hand, when the smaller energy density input was used, almost no spherulites could be found around the amorphous tracks and the whole deposited layer was fully amorphous. This can be explained through the effect of the laser energy input on the temperature of the solid material around the melt track which is called the HAZ. If the energy input is high enough, the temperature of the material in the HAZ increases above the crystallization temperature of the glass forming alloy and hence crystallization occurs in the HAZ.

In the second stage of the experiment the amorphous Zr-based powder was deposited on the crystallized substrate (which was obtained through annealing an amorphous plate at its crystallization temperature) using the lower energy density value. Zr_2Cu nanocrystals, similar to what could be found in the microstructure of the underlying crystallized substrate, were the only crystallized phases observed in the HAZ, with no sign of any spherulites. It was

suggested that when the laser had scanned the powder, it had melted a part of the crystallized substrate underneath as well as the powder and the nanocrystals in the HAZ are the high melting point remnants of the crystalline phases which were present in the substrate and that were not melted during the laser melting of the substrate.

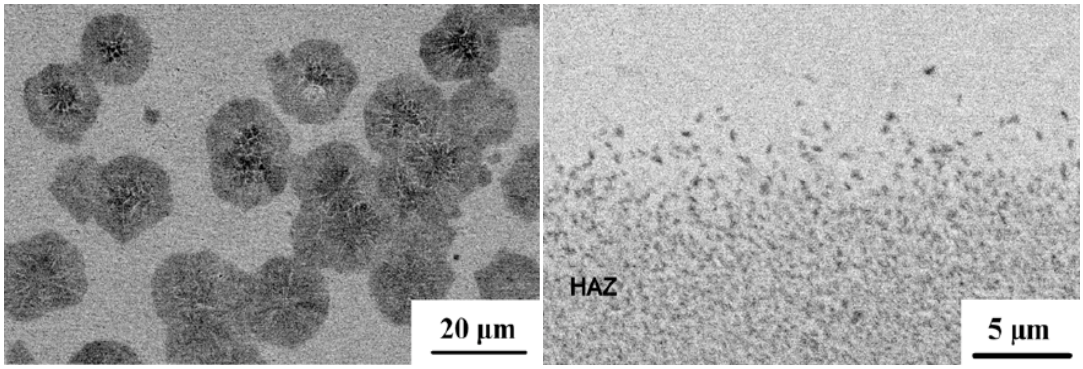

Figure 2.27- Microstructure of the spherulites in the HAZ of the melt tracks made through using high laser energy density to deposit on an amorphous substrate (left) and the nanocrystals in the HAZ of melt tracks made using low laser energy density to deposit on a crystallized substrate (right). (Sun and Flores, 2010)

As to the difference of the microstructure of the spherulites and the Zr_2Cu nanocrystals (shown in Fig. 2.27), it was said that the spherulites, about 20µm in diameter, formed in the HAZ, during the fast laser melting condition, were the result of the hindered nucleation and rapid growth at a temperature close to the melting point of the glass forming alloy. However, the nanocrystals were formed during the annealing of the amorphous plate (to turn it into a fully crystallized substrate) and hence were the result of isothermal annealing condition which allows for diffusion-controlled phase separation and hence formation of Zr_2Cu and other nanocrystalline phases.

In another study, the effect of heat accumulation on the HAZ was investigated through fabrication of specimens out of $Zr_{55}Al_{10}Ni_5Cu_{30}$ using a 300W pulsed laser (Yang *et al.*, 2012). It was shown that as the number of pulses used in the melting of each melt pool increased, the possibility and amount of formation of crystallized components in the HAZ increased

accordingly. The bands of crystalized components were identified to be fcc $Al_5Ni_3Zr_2$ nanocrystals surrounding micro-sized hcp dendrites, as shown in Fig. 2.28.

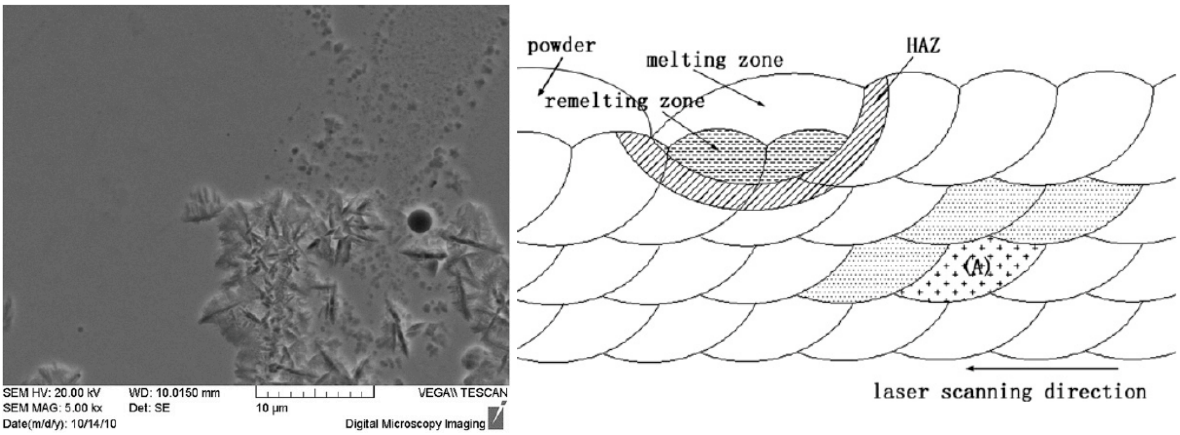

Figure 2.28- SEM image of the microstructure of nanocrystals and dendrites in the HAZ (left) and schematic diagram of the laser solid forming process showing the different zones that the material can be in during this process. (Yang et al., 2012)

Through a finite element model, it was shown that, according to its thermal history, each point in the fabricated specimen can belong to either of three categories: remelted zone, heat affected zone or thermo-stable zone. The material in the thermo-stable zone experienced a cycle of high heating rate during melting and high cooling rate during solidification and after that, it's temperature never increased to above the glass transition temperature of the glass forming alloy, hence crystallization was deemed impossible in this zone. Similarly, for the material in the remelted zone every time a temperature above the glass transition temperature was experienced, it went through melting and solidification cycles, and apart from that, its temperature never increased above T_g, which again meant no crystallization could happen in this zone.

However, the material in the heat affected zone experienced temperatures between T_m and T_g, which means if enough heat accumulation occurred in this area, crystallization was possible through structural relaxation. So, it was shown that by increasing the number of

pulses used in fabrication of the specimens, which translates into more accumulation of heat in the HAZ, more of the crystallized component could be observed in the heat affected zone only.

Finally, the effect of scanning strategy and laser energy density on the microstructure of the specimens of a Zr-based BMG, namely $Zr_{52.5}Ti_5Cu_{17.9}Ni_{14.6}Al_{10}$ manufactured through the SLM process has been investigated (Li *et al.*, 2016). The laser power used in these experiments was kept at 200W and various scanning speeds and hatch spacing values were used to obtain different laser energy densities. It was reported that when lower laser energy densities were used, the resulting microstructure was less crystallized and when it was low enough a fully amorphous microstructure was achieved. This can be observed in the XRD patterns shown in Fig. 29, considering the fact that as the scanning speed increases the energy density input decreases as a result.

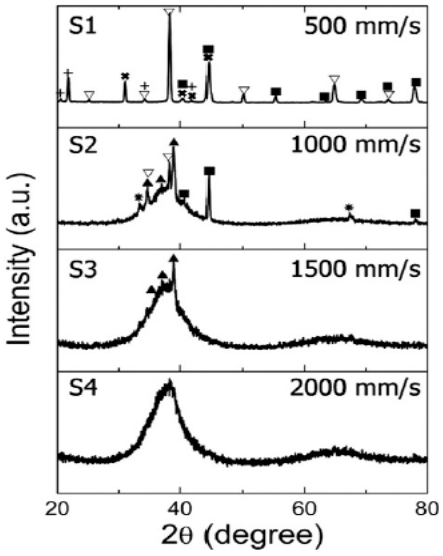

Figure 2.29– XRD patterns of Zr-based samples, showing more crystallization as scanning speed decreases (Li et al., 2016).

The reason for this was attributed to the non-uniform melt flow occurring as a result of a high energy density which would cause elemental segregation and hence change the composition

of the glass forming alloy in some areas of the melt pool. This would facilitate the precipitation of crystallized phases in the microstructure of these specimens. In contrast, a low laser energy density would keep the homogeneity of the composition of the melt and result in a fully amorphous structure.

It was also reported that, keeping the exposed laser energy density constant, introducing a remelting stage after the deposition of each layer produced specimens that had less crystallized components inside them or were fully amorphous. This was also associated with the role that the second melting scan would have on homogenising the chemical composition of the material in each layer that is similar to the intended glass forming alloy composition and hence produce samples with an amorphous microstructure.

2.11.3. Fe-based Bulk Metallic Glasses

Feasibility of the production of a defect-free Fe-based BMG, namely SHS7574, with a composition of $Fe_{35}Cr_{25}Mo_{15}W_{10}Mn_5C_3Si_2B_5$, using the SLM process, has been investigated (Ye and Shin, 2014). In order to do so, a single layer and a 6-layer deposition of the powder was carried out on a 304L stainless steel substrate. The substrate was preheated to 422°C and a laser power of 350W and scanning speed of 36mm/s was utilised. The XRD pattern of all specimens indicated that the microstructure of the samples was composed of an amorphous phase and a crystalline compound determined to be $Cr_{1.07}Fe_{18.93}$.

Through the examination of the SEM images of the single layer specimen, it was shown that the microstructure of the deposited layers consisted of an amorphous phase in each melt track surrounded by a crystallized phase in the HAZ. This was indicative of the fact that the cooling rate experienced in the melting of each single track was sufficient for formation of an

amorphous phase, however, the reheating, when depositing successive tracks, caused the temperature of the already deposited material to increase above the crystallization temperature of the Fe-based BMG and hence the formation of the crystallized phase in the HAZ.

Similarly, as shown in Fig. 2.30, the microstructure of the multi-layer deposited BMG alloy, consisted of the amorphous layer and the crystalline phase in the HAZ area around each track and each layer, although the crystalline regions were coarser compared to that of the single layer. The reason for this was attributed to heat accumulation after each layer which caused the previously precipitated crystalline regions to act as nuclei and coarsen as a result.

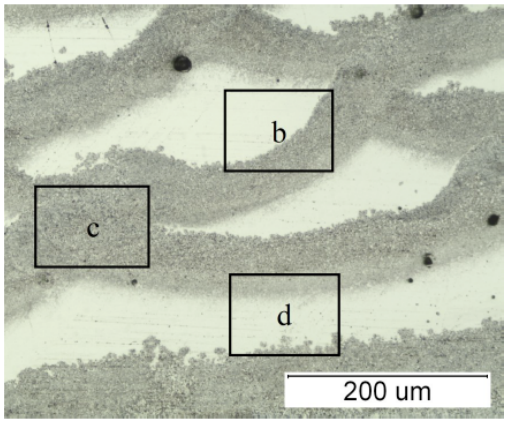

Figure 2.30- Optical microscopy of the deposited multi-layer specimen, showing a featureless amorphous phase and the crystallized phase in the HAZ between each melted track and layer (Ye and Shin, 2014).

Another finding of the study was the effect of an interval time period after each track was deposited on the crystallization behaviour of the glass forming alloy. It was reported that when the interval period of 5s, used in the original experiments mentioned above, was eliminated the resulting microstructure was dramatically different, showing almost no sign of the amorphous phase and consisting of coarse crystalline grains. This was explained through the fact that without the interval time, the deposited material gets reheated shortly after

reaching its maximum temperature which translates into an insufficient cooling rate during solidification of the melted material and hence full crystallization of the specimen.

In another study, the role of laser power and scanning speed on the density of specimens manufactured out of the $Fe_{68.3}C_{6.9}Si_{2.5}B_{6.7}P_{8.7}Cr_{2.3}$ glass forming alloy (a soft magnetic material) through selective laser melting processing was examined (Jung *et al.*, 2015). It was shown that when the lower laser power and higher scanning speed values were used, the resulting specimens were either not consolidated at all or contained large irregularly shaped pores inside them. On the other hand, when higher laser power and lower scanning speed values were utilised, density of the resulting specimens improved significantly, shown in Fig. 2.31.

The formation of these irregularly shaped pores, called keyhole pores were attributed to insufficient filling of gaps by the molten metal which in turn is because of the inadequate energy input to the powder bed. This is why, by increasing the laser power and/or decreasing the scanning speed, which increases the energy input, these defects seemed to decrease significantly. Some small spherical pores also appeared in the microstructure of the specimens which were associated with the pre-existing micro-pores formed by trapped gases inside the powder during the atomization process (Aboulkhair *et al.*, 2014). It was suggested that through increasing the energy density input and hence decreasing the viscosity of the melted glass forming alloy, these pores can also be eliminated.

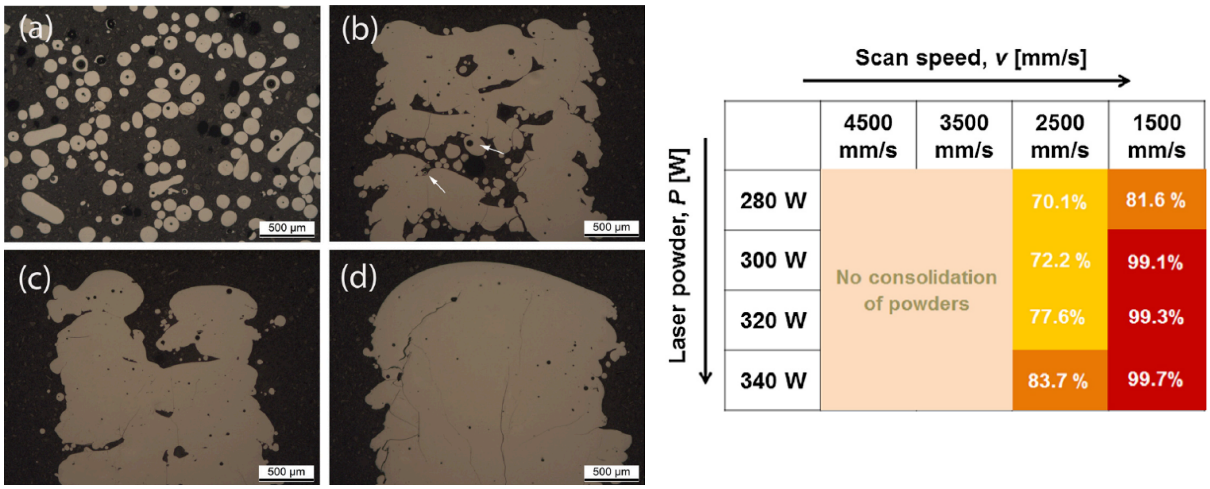

Figure 2.31- (left) Optical microscopy of (a) atomized powders and SLM samples with (b) v=2500mm/s and P=300W, (c) v=2500mm/s and P=340W, (d) v=1500mm/s and P=340W. (left) Density of the SLM specimens with various laser power and scanning speed values (Jung et al., 2015).

Cracks were the other defects that were found in the microstructure of the specimens. It was suggested that thermal contraction and solidification shrinkage during the SLM process would result in high stresses at the interface of solidifying material and the already solidified layer underneath, which in turn will cause cracking, because of the intrinsic limited ductility and fracture toughness of the glass forming alloy. Preheating the substrate was suggested to be the solution to this problem.

The saturation magnetisation of the SLM manufactured specimens and the pre-alloyed powder was shown to be almost the same. However, there were some differences in the initial part of the M-H hysteresis loop, between the two, which was attributed to the existence of pores and cracks inside the microstructure of the SLM specimens, since the shape of the M-H hysteresis loop is shown to be influenced by the geometry of the magnetic material (Moskowitz, 1993). The amorphous nature of the SLM processed specimens were verified through XRD and DSC tests.

Furthermore, another attempt to manufacture specimens out of another Fe-based glass forming alloy, namely $Fe_{74}Mo_4P_{10}C_{7.5}B_{2.5}Si_2$, through selective laser melting processing was carried out (Pauly *et al.*, 2013). Laser power of 320W and scanning speed of 3470mm/s was utilised to fabricate scaffold-shaped specimens along with reference cylinders. As shown in Fig.2.32, it was reported that the resulting samples, include small pores and cracks which were attributed to non-optimised processing parameters and the limited malleability of the glass forming alloy.

Figure 2.32- Image of the scaffold-shaped specimen still embedded in the powder, alongside the CAD-generated structure (left)and the specimen on top of the substrate and out of the powder (Pauly et al., 2013).

The XRD pattern of the specimens and the pre-alloyed powder were shown to be almost identical, however both contained small sharp reflections superimposed on a broad halo, indicating the existence of slight crystallization inside an amorphous matrix. The fact that the XRD patterns for both the powder and the SLM made specimens were similar suggested that the SLM process has not had a detrimental effect on the microstructure of the specimens, in terms of causing further crystallization.

Supplementary investigation into the composition of the pre-alloyed powder determined the existence of a small amount of Ti, Cu and Ni contaminations which had slightly changed the composition of the pre-alloyed powder, enough so that the cooling rate of the gas

atomization had not been enough to ensure full amorphisation of the powder particles. The crystalline phases present in the powder and the SLM made specimens were reported to be α-Fe, γ-Fe and $Fe_{23}B_6$ and the presence of the amorphous phase was verified through DSC testing.

Finally, in a study on the effect of specimen height on the microstructure and hardness of the specimens, cubes and thin-walled shells were fabricated out of $Fe_{58}Cr_{15}Mn_2B_{16}C_4Mo_2Si_1W_1Zr_1$ glass forming alloy on a 304 stainless steel substrate, through the LENS^{TM} (laser engineered net shaping) process (Zheng *et al.*, 2009). The alloy chosen for this experiment, although a glass forming alloy, does not have a high GFA, as evident by the crystallization present in some of the pre-alloyed gas-atomized powder particles (the larger ones).

Through XRD, SEM and TEM investigations of the specimens, it was shown that for the first layer, the microstructure seemed to be mostly amorphous with nanocrystalline α-Fe, γ-Fe, Fe_2B and $Cr_{23}C_6$ specially in the HAZ, and as the number of layers deposited increased, the crystalline phases became coarser around each melt pool and the amorphous component decreased in volume fraction, as shown in Fig. 2.33. This was attributed to the fact that, after each layer is deposited and melted, some of the energy input of the process gets accumulated in the specimen, which causes the temperature of the material to increase and hence the subsequent layers would solidify with a reduced cooling rate.

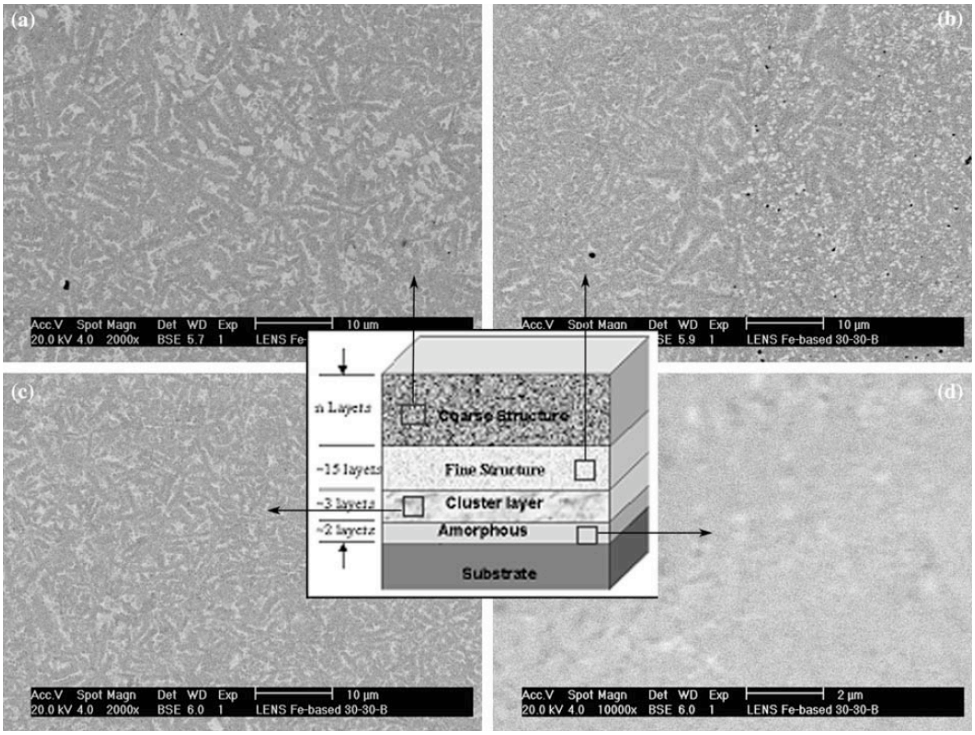

Figure 2.33- Backscattered SEM images of a LENS^{TM} deposited Fe-based cube showing increasing crystallization and coarsening of the microstructure at higher layers.

This would mean that the microstructure of the upper layers would more likely be crystallized and coarsen as the specimen gets taller. Another phenomenon that was suggested to be happening was that if the specimen was large enough so that its temperature would be higher than the crystallization temperature of the glass forming alloy, even the previously deposited layers which may have had an amorphous component in their microstructure, would completely crystallize.

Furthermore, the microstructures of the corresponding locations in the thin-walled shell specimens compared to the cubes were more crystallized and coarser. This was associated with the lower cooling rate and higher temperatures experienced in the shell layers, since the surrounding material was mostly powder with a lower thermal conductivity compared to the bulk nature of the material surrounding most of the cube layers with a faster heat dissipation

through convection. The smaller time interval between deposition of sequential layers in the shells also contributed to the accumulation of heat and hence lower cooling rates.

As for the hardness of the specimens, it was reported that as the laser exposure (here defined as laser power / scanning speed) increased, the hardness of the resulting samples decreased as a result. This was explained through the reduced cooling rate and hence higher crystallization occurring as a result of higher laser exposure. Existence of cracks in the microstructure of the specimens were very briefly mentioned and was attributed to the lack of ductility of the glass forming alloy and the intrinsic residual stress development of the LENS^{TM} process.

3. Experimental Methods and Materials

3.1. Material Composition

The powder used in this study was readily bought from LPW Technology with the nominal composition of SAM1651 which is $Fe_{48}Cr_{15}Mo_{14}C_{15}B_6Y_2$ atomic percent. LPW Technology provided the chemical analysis of the argon atomised powder, which is shown in Table 3.1. Upon receipt, a sample of the powder was sent to AMG Analytical Services for UKAS accredited composition investigation. The amount of carbon was measured through LECO combustion analysis and for oxygen investigation a LECO inert gas fusion method was utilized. As for the other elements, inductively coupled plasma FeCr analysis was used to determine the weight percentages of iron, molybdenum, chromium, boron and yttrium. Table 3.1 depicts these three sets of compositions.

	Weight Percentage						
Composition	B	C	Cr	Mo	Y	O	Fe
Nominal	1.24	3.45	14.92	25.70	3.4	-	Bal
LPW Tested	1.24	3.57	15.0	25.74	3.35	-	Bal
AMG Analyt	1.22	3.59	15.23	25.79	3.68	0.018	Bal

Table 3.1- Composition of the powder used in this study as requested (Nominal), as LPW Technologies tested and as AMG Analytical tested.

3.2. Particle Size Analysis

The powder particle size measurement was done using a Malvern Mastersizer 3000 laser diffraction particle size analyser. A 0.5-gram sample of the powder was dispersed in distilled water which has all the required characteristics as a dispersant. It provides good wetting of the sample (enabling dispersion), does not dissolve the sample, does not contain bubbles, has a suitable viscosity, is transparent to the laser beam, has a different refractive index to the sample and is chemically compatible with the materials used in the instrument.

Wet dispersion is preferred as it provides a significant reduction in particle to particle adhesion forces through the process of surface wetting, which enables agglomerated particles to be dispersed with relatively little energy input.

In a laser diffraction measurement, a laser beam passes through a dispersed particulate sample and the angular variation in intensity of the scattered light is measured (as shown in Fig. 3.1). Large particles scatter light at small angles relative to the laser beam and small particles scatter light at large angles. The angular scattering intensity data is then analysed to calculate the size of the particles that created the scattering pattern using the Mie theory of light scattering. The particle size is reported as a volume equivalent sphere diameter.

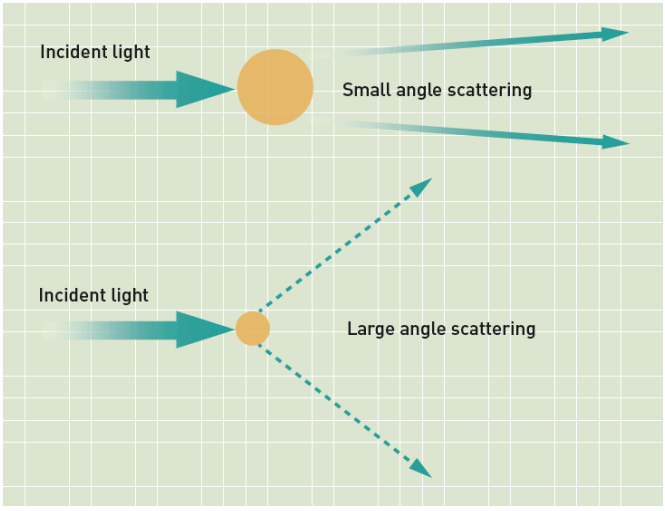

Figure 3.1- Shows the main principle in particle size analysis through laser diffraction which is: large particles scatter light at small angles relative to the laser beam and small particles scatter light at large angles.

The particle size range was measured using a stir speed of 2500rpm and in-situ continuous ultrasound option for better dispersion. The obscuration value in the test was measured to be 9.2% which is within the recommended range of 5 to 10% according to ISO13320 (2009).

3.3. X-Ray Diffraction Analysis of the SAM1651 Powder

Microstructural analysis of the powder purchased from LPW Technologies was carried out with XRD testing to see whether the powder was fully amorphous or partially crystallized. The XRD investigation was done using a Bruker D2 Phaser which utilizes Cu K-alpha wavelength. The analysis was done from 2θ equal to 30° to 80°, with a step size of 0.01 and time per step of 0.3 seconds. Although the D2 Phaser is a more reliable machine compared to the older XRD systems in terms of detection of different phases in shorter times, the brief detection period chosen for each test in this study could be a potential source of error. Although, the sheer number of XRD tests in this study made it difficult, but this issue could be resolved by utilising slower scanning speeds.

3.4. SEM Imaging of the Internal Pores within the SAM1651 Powder

In order to investigate the internal pores inside the powder particles, a sample of the powder was placed at the bottom of a plastic mounting cup and cold mounted using a Buehler EpokwicK fast cure epoxy kit 20-8128 (as shown in Fig. 3.2). A Struers Tegramin-20 grinding and polishing unit was used to first grind the resulting mounted specimen, using P800 to P2500 SiC grinding paper and then polished with 6μm and 1μm Buehler MetaDi Supreme crystalline diamond suspension.

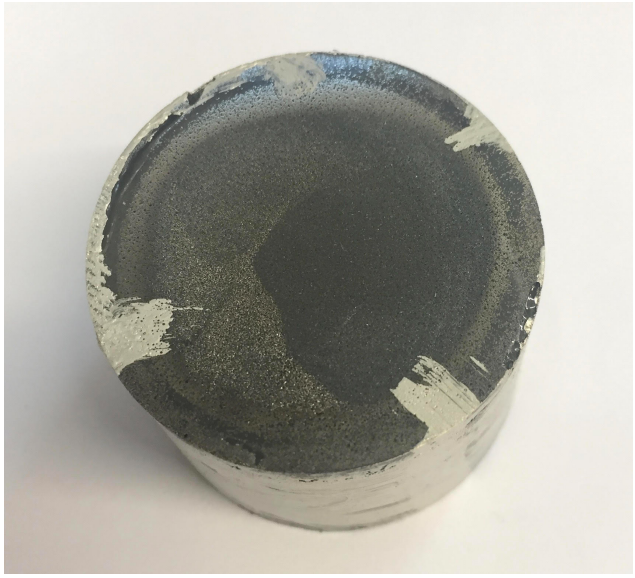

Figure 3.2- Cold mounted, grinded and polished powder used to investigate internal pores inside powder particles.

The specimen was then investigated using the FEI Inspect F50 scanning electron microscope to obtain images of the internal pores inside the SAM1651 powder particles.

3.5. Thermal Analysis of the SAM1651 Powder

For measuring the glass transition temperature, crystallization temperature and the melting point of SAM1651, 50mg samples of the powder were put in an alumina pan and then placed

inside the heating/cooling chamber of a TA Instruments Q600 SDT which uses differential scanning calorimetry for thermal analysis. To do so, it measures the heat flow from the sample while it is being heated/cooled and if the heat flow changes dramatically, it usually is a result of an endothermic (such as melting and glass transition) or exothermic (like crystallization) reaction happening in the specimen.

Two temperature ranges were examined. In one, the sample was heated in an argon atmosphere from 673K to 1023K (to determine T_g and T_x) and in another, the powder was heated from 1273K to 1473K (to determine T_s and T_l), both at a speed of 1 degree per minute. The results from this experiment were investigated using the TA Instruments Universal Analysis 2000 software and the critical temperatures required were acquired.

3.6. Sample Manufacturing Using the SLM125

3.6.1. Renishaw SLM125

All the specimens investigated in this study were manufactured using the Renishaw SLM125 machine which uses a modulated 200W infrared Ytterbium fibre laser with a central emission wavelength of 1070nm and a spot size of 35µm. As the modulated laser beam melts the powder bed in a point to point manner (as shown in Fig. 3.3), the nominal speed of the beam is controlled by three parameters: point distance, exposure time and idle speed (as depicted in Fig. 3.4).

Point distance is the distance between the two adjacent points melted by the laser and the exposure time is the duration of the laser interaction with the powder bed at each melting point. Furthermore, the idle speed is the speed at which the laser travels between two adjacent melting points while it is off. The other main processing parameters are layer

thickness (which is the thickness of each layer of powder distributed on the powder bed or in the case of the first layer on the substrate), hatch spacing (which is the distance between two adjacent melting line tracks) and laser power. Fig.9 depicts these processing parameters inside the powder bed.

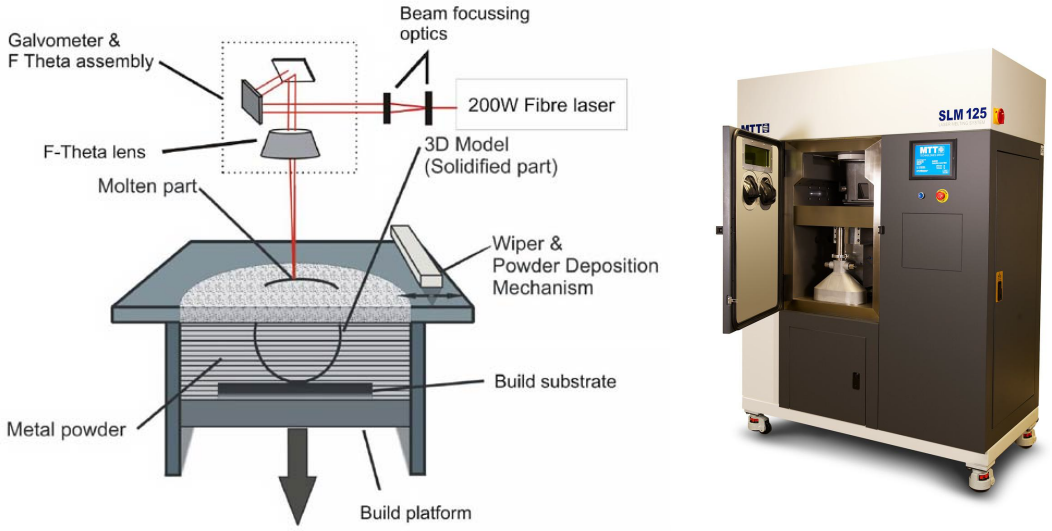

Figure 3.3- Selective laser melting mechanism (right); Renishaw SLM125 machine used to manufacture the specimens used in this study (left)

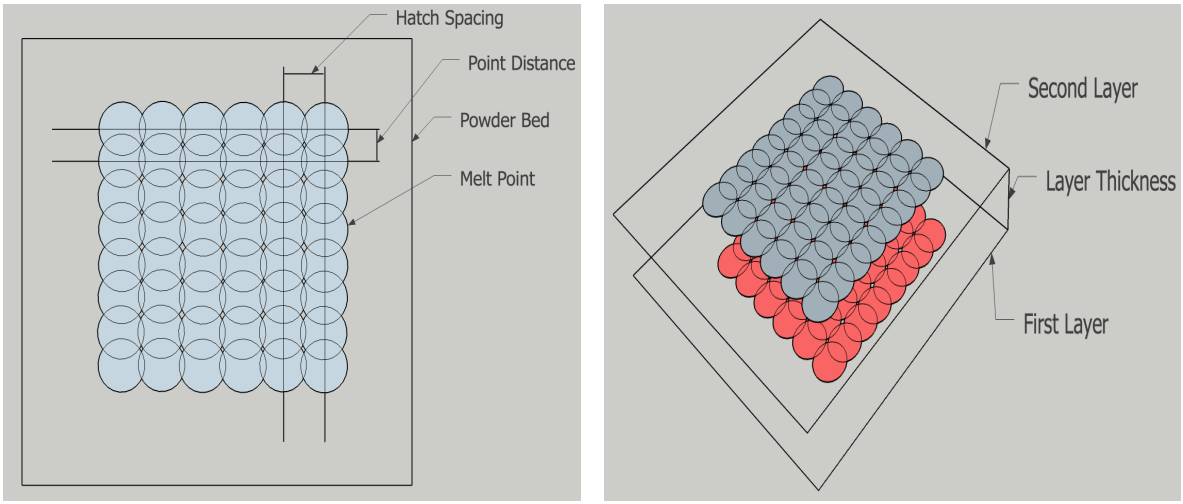

Figure 3.4- Depiction of the different processing parameters used in selective laser melting: Hatch Spacing, Point Distance (right) and Layer Thickness (left)

3.6.2. Heated Bed Setting for the SLM125

Most of the specimens however were built at higher temperatures than RT. To do so, a heated bed system was developed that enabled the SLM manufacturing to be conducted at higher than room temperature. This system is comprised of two components:

1- Cartridge Heater: As shown in Fig. 3.5, the cartridge heater is a SS-316L cylindrical piston with 6 holes vertically drilled inside of it. Five of these holes are filled with Elmatic Max K resistance heating cartridges and the sixth one is used for a thermocouple to pass through and get in contact with the substrate that sits on top of the cartridge heater.

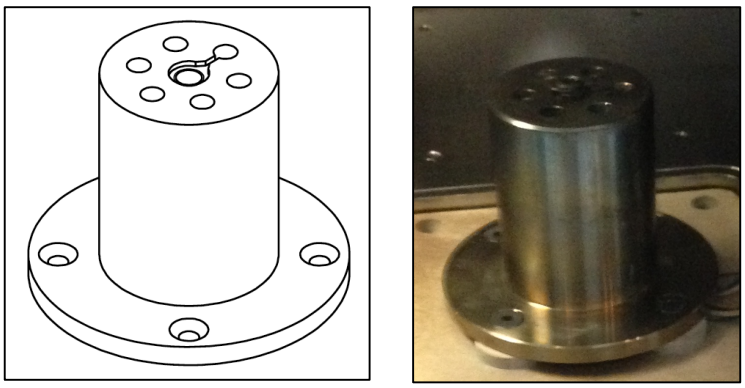

Figure 3.5- Cartridge Heater as designed (left) and inside the SLM125 chamber (right) before the elevator heater was assembled on top of it.

2- Elevator Heater: The elevator heater (as shown in Fig. 3.6) is a knuckle metal ceramic heater obtained from Elmatic Heating Elements and consists of a helically wound resistance spiral, stretched and strung through refractory ceramic bricks. The build-up of the ceramic brick provides a flexible heating mat which is placed into a rolled outer metal casing and a ceramic fibre insulation.

Figure 3.6- Elevator or knuckle heater as a part of the heated bed designed to provide higher bed temperatures

When the heating system is being assembled, the cartridge heater cylinder is placed inside the knuckle heater and every point of contact with the SLM125 build chamber is covered with TD Thermal ceramic fibre insulation (as shown in Fig. 3.7). Then the assembly is screwed on top of the build platform of the SLM125 and the temperature of both heaters is separately controlled via Elmatic temperature controllers. This heating system is capable of providing up to a temperature of 723K.

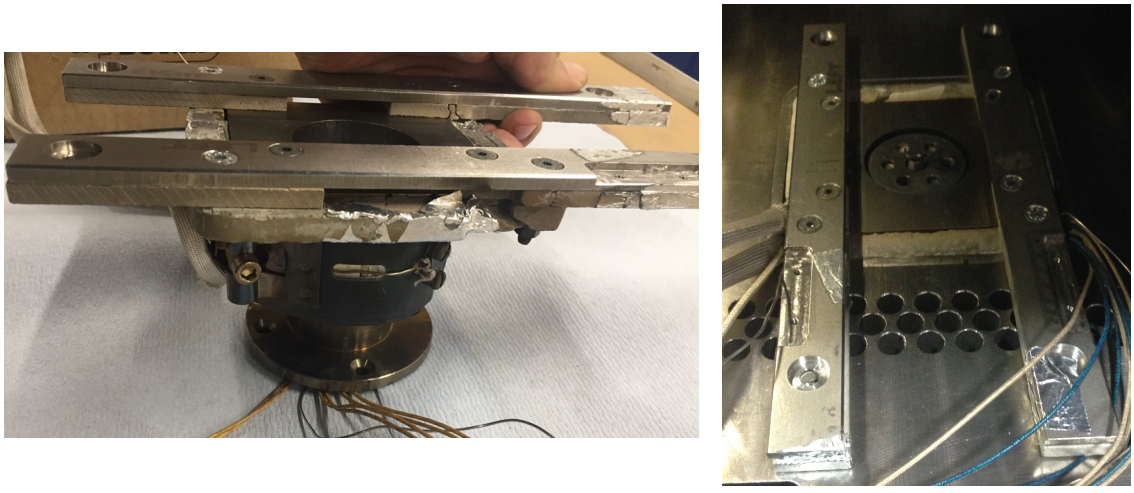

Figure 3.7- Depiction of elevator heater being placed around the cartridge heater outside the SLM125 machine (left) and the heated bed assembled inside the machine's chamber.

3.6.3. Build Data File Preparation for SLM125

The SLM125 machine as an additive manufacturing system requires a build-ready slice data file to be able to recognize the shape of the specimen that needs to be built. In this study, Marcam Engineering's AutoFab software was used for this purpose. This software usually acts as an intermediate step between the design file (CAD data) and the layered manufacturing machine and translates the former for the latter in the form of a build-ready slice MTT file. However, since the specimens needed in this study were mainly arrays of simple cubes, the design file was also created inside the Autofab software.

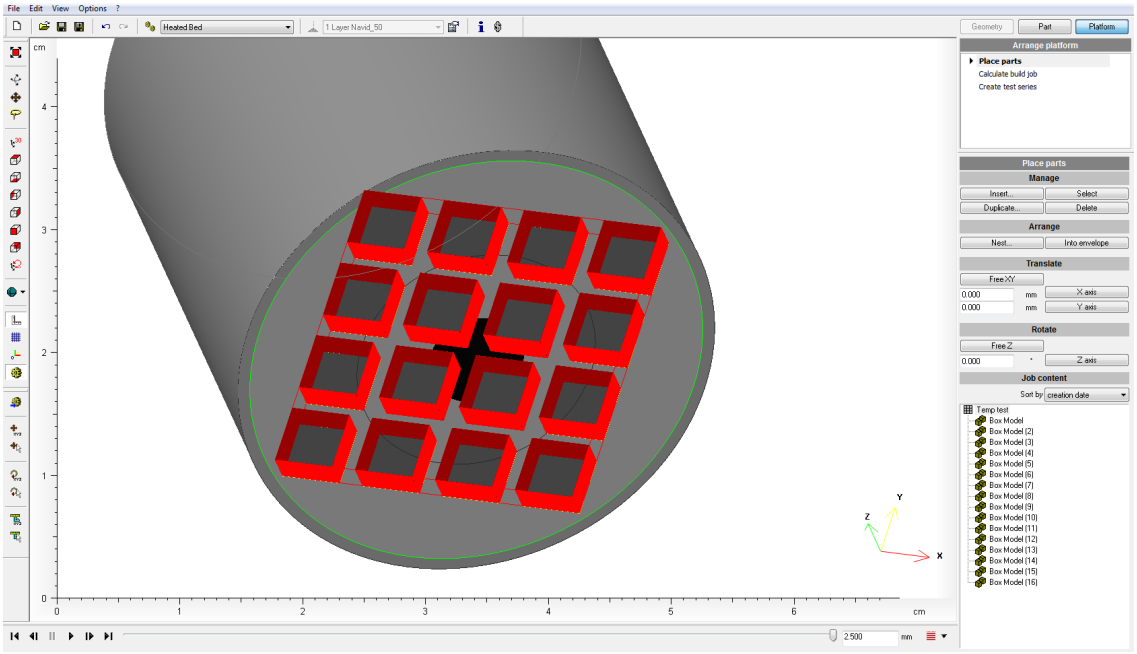

Figure 3.8- Preview of the AutoFab software at the slicing stage, while creating an array of cubes

Using this software, for each cube, the following parameters can be controlled and translated to the SLM125 machine:

a) Position of the cube

b) Processing parameters:

- Laser Power

- Exposure Time
- Hatch Spacing
- Layer Thickness
- Point Distance

c) The hatching style; In this study, a Meander scan strategy was used with 67° rotation for each layer (Fig. 3.9), since it has been shown to minimise part residual stress and the initial experiments confirmed this for the SAM1651 as well.

d) Whether additional melting at each layer would be done.

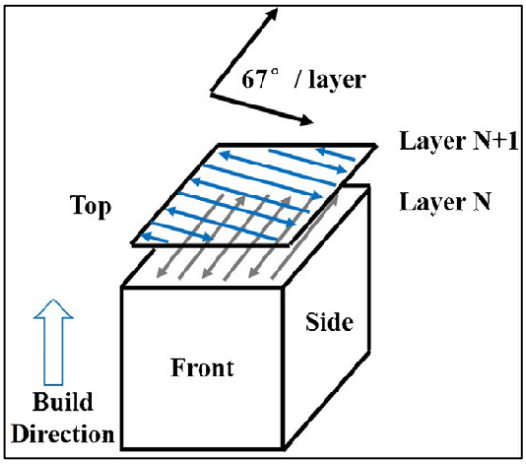

Figure 3.9- Meander scan strategy with 67° rotation of the melting contours for each new layer

3.7. Parameters Used for Specimen Manufacturing

The samples, manufactured out of the SAM1651 powder, using SLM125, were built directly on top of a Ø40x5mm 316L stainless steel disk as their substrate. The surface of the substrate was grinded and polished up to 1µm and cleaned with isopropanol to remove any residual contamination. However, it should be noted that the passivating layer on the surface of the SS 316L substrates were present before each experiment started. An array of 16 cubes, with dimensions of 5x5x2.5mm, were fabricated on each substrate (as shown in Fig. 3.10) to examine the effect of laser power, exposure time, hatch spacing, point distance, layer

thickness and substrate temperature on the defect formation and microstructure of the resulting specimens.

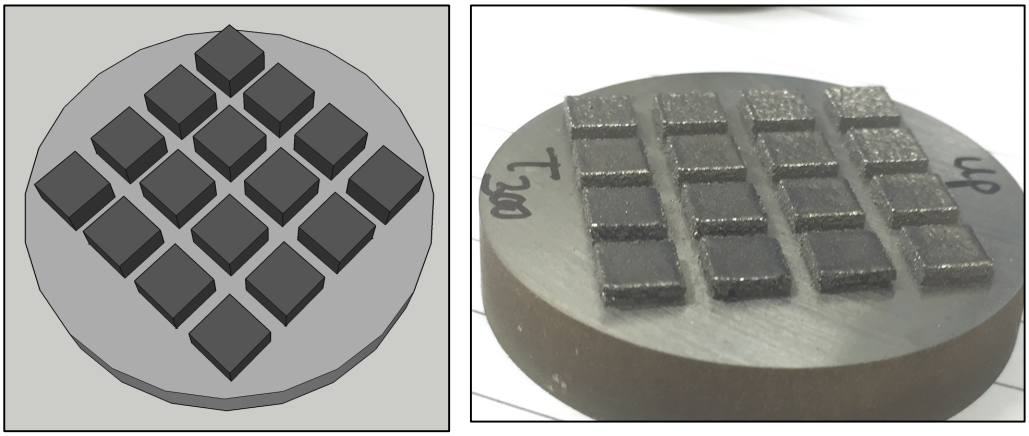

Figure 3.10- Array of 16 cubes built on a SS316L substrate to investigate the influence of temperature, laser power and exposure time

3.7.1. Specimens Fabricated to Investigate the Effect of Substrate Temperature

To determine the influence of substrate temperature on the formation of cracks, 64 cubes were built at 4 different temperatures of ambient temperature, 423K, 573K and 723K. The laser power and exposure time values used at each temperature were selected in a way that would represent a wide range of processing parameters and are shown in Table 3.2.

Temperatures Used for Each Set of Parameters: 298, 423, 573 and 723K		**Laser Power (W)**			
		120W	140W	160W	180W
Exposure Time (µm)	120µm	x	x	x	x
	140µm	x	x	x	x
	160µm	x	x	x	x
	180µm	x	x	x	x

Table 3.2- Laser power and exposure time values used in optimal substrate temperature determination experiments

After investigation of the above-mentioned sample through optical microscopy, the maximum temperature, 723K, was chosen for the rest of the cubes to be built at, since it resulted in the least amount of cracking compared to the other substrate temperatures tested.

3.7.2. The Effect of Layer Thickness

Sample fabrication for investigating the effect of layer thickness on defect formation was carried out by manufacturing samples on preheated substrates (at 450°C). The hatch spacing was kept at 100µm and the point distance was kept constant at 50µm. The layer thickness, laser power and exposure time values utilised are shown in Table 3.3. It should be noted that in order to setup the machine for each build, the layer thickness for the first layer had to be arranged manually using a piece of paper between the wiper and the substrate. Although, the thickness of the paper was aimed to be similar to the selected layer thickness for each build, this might be the source of a potential error. The layer thickness for the consequent layers was applied automatically by the machine. Also, for the 20µm and 30µm layer thickness, since the size of some powder particles (15µm-45µm) were larger than the layer thickness chosen for the build, it is assumed that the process of powder distribution eliminated the bigger particles and only left the smaller particles to be melted into cubic specimens. Essentially as the wiper moves on top of the specimen, it would leave the smaller particles on the surface of the specimen and carry the larger ones over to the overflow silo.

Exposure Time (µs)		110			120			130			140		
Laser Power (W)		120	130	140	120	130	140	120	130	140	120	130	140
Layer Thickness (µm)	20	x	x	x	x	x	x	x	x	x	x	x	x
	35	x	x	x	x	x	x	x	x	x	x	x	x
	50	x	x	x	x	x	x	x	x	x	x	x	x

Table 3.3- Layer thickness, laser power and exposure time values used in optimal layer thickness determination experiments

3.7.3. The Effect of Hatch Spacing

Cubic specimens were manufactured on a preheated substrate (at 450°C) to examine the influence of hatch spacing on the behaviour of defect formation and crystallization of the microstructure. The layer thickness and the point distance were kept constant at 50µm. The hatch spacing, laser power and exposure time values used in these experiments are listed in Table 3.4.

Exposure Time (µs)		120			130			140			150			160		
Power (W)		120	130	140	120	130	140	120	130	140	120	130	140	120	130	140
Hatch Spacing (µm)	75	x	x	x	x	x	x	x	x	x	x	x	x	x	x	x
	100	x	x	x	x	x	x	x	x	x	x	x	x	x	x	x
	125	x	x	x	x	x	x	x	x	x	x	x	x	x	x	x

Table 3.4- Hatch Spacing, laser power and exposure time values used in optimal hatch spacing determination experiments

3.7.4. The Effect of Point Distance

The influence of point distance on the formation of lack of fusion defects, cracks and crystallised components was investigated through production of specimens on a preheated substrate (at 450°C). The layer thickness and hatch spacing were kept constant at 50µm and 100µm respectively. The values used for laser power, exposure time and point distance are presented in Table 3.5.

Exposure Time (µs)		120			130			140			150		
Laser Power (W)		120	130	140	120	130	140	120	130	140	120	130	140
Point Distance (µm)	25	x	x	x	x	x	x	x	x	x	x	x	x
	50	x	x	x	x	x	x	x	x	x	x	x	x
	75	x	x	x	x	x	x	x	x	x	x	x	x

Table 3.5- Point distance, laser power and exposure time values used in optimal point distance determination experiments

3.7.5. Specimens Fabricated to Investigate the Effect of Laser Power and Exposure Time

The effect of laser power and exposure time on the formation of microstructural defects was studied in the next step. To do this, 105 cubes were manufactured using the sets of parameters shown in Table 3.6. They were built on the above mentioned stainless steel substrates in batches of 16 as shown in Fig. 3.10. Other processing parameters which were kept constant throughout this experiment were as follows: layer thickness = 50µm, hatch spacing = 100µm, point distance = 50µm and substrate temperature = 723K.

Laser Power / Exposure Time	120W	130w	140W	150W	160W	170W	180W	190W	200W
70µm					X	X	X	X	X
80µm					X	X	X	X	X
90µm					X	X	X	X	X
100µm	X	X	X	X	X	X	X	X	X

Laser Power / Exposure Time	120W	130w	140W	150W	160W	170W	180W	190W	200W
110µm	X	X	X	X	X	X	X	X	X
120µm	X	X	X	X	X	X	X	X	X
130µm	X	X	X	X	X	X	X	X	X
140µm	X	X	X	X	X	X	X	X	X
150µm	X	X	X	X	X	X	X	X	X
160µm	X	X	X	X	X	X	X	X	X
170µm	X	X	X	X	X	X	X	X	X
180µm	X	X	X	X	X	X			
190µm	X	X	X	X	X	X			
200µm	X	X	X	X	X	X			

Table 3.6- Laser power and exposure time values used to investigate their effect on defect formation

3.8. Sample Characterization of the Cubes Built by SLM

The cubes built using the selective laser melting process were kept on their substrate and cold mounted to maintain their structural integrity while they were being cut. A Buehler EpokwicK fast cure epoxy kit 20-8128 was used to cold mount the whole substrate disk and cubes together (as shown in Fig. 3.11) after it was cleaned in acetone to remove any oils and powder particle remnants.

The cold mounting epoxy/hardener mix was poured on the samples that were placed in plastic cups, using the Struers CitoVac vacuum impregnation unit which helps the cold mounting process by getting rid of any air bubbles inside the mix. The samples were kept for

10 minutes under 0.2 bar of vacuum inside the CitoVac chamber to achieve this goal. Afterwards, they were left for 5 hours in open air for the epoxy/hardener mix to harden.

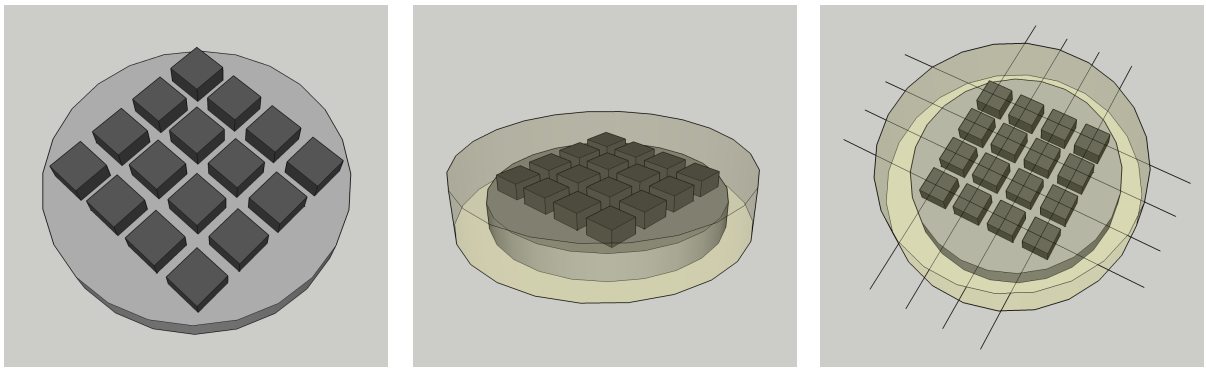

Figure 3.11- Cold mounting (middle) and cutting (right) of the cube array attached to their substrate (left)

Then the cold mounted samples were cut using a Buehler IsoMet Diamond sectioning blade 11-4245, inside the Struers Secotom-50 cutting unit. Blade rotation speed was maintained at 2500rpm and the feeding speed was kept at 0.02mm/s for every cutting process.

The cubes that were cold mounted while still attached to the substrate disk, were cut along the lines shown in Fig. 3.11. This resulted in every cube being cut into 4 quarter-cubes (Fig. 3.12-(b)) which revealed 8 internal surfaces for each cube (Fig. 3.12-(c)), 4 of which are unique as depicted below (since face 1, face 2, face 3 and face 4 are almost identical to face 5, face 6, face 7 and face 8 respectively.)

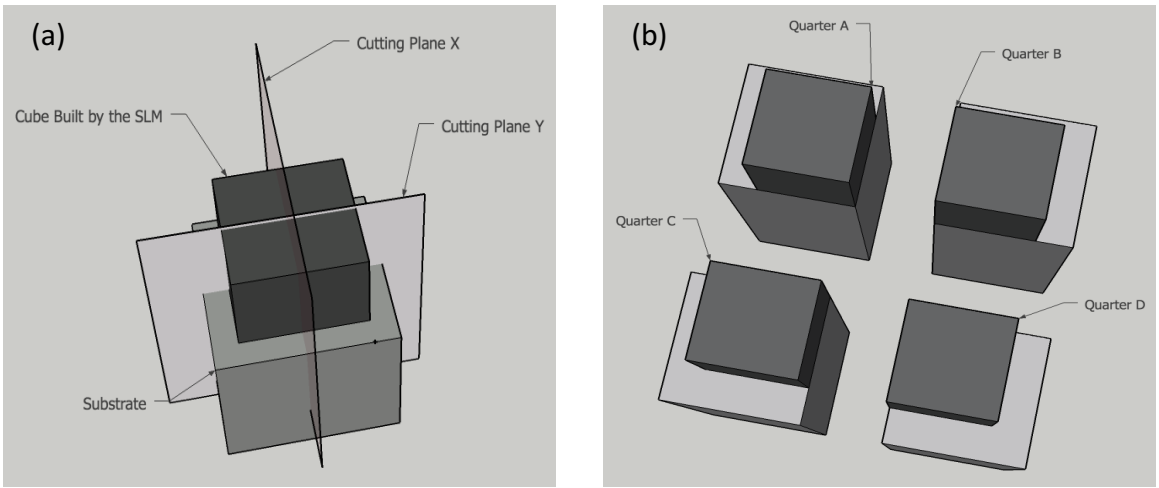

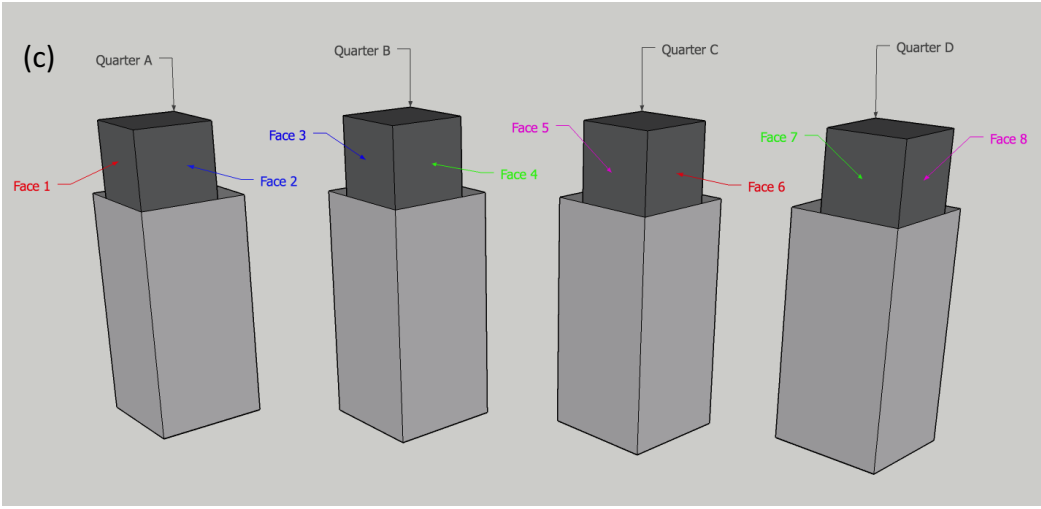

Figure 3.12- Each cube was cut along two planes (a) which would result in four quarter cubes (b) with 8 internal surfaces, four of which were unique.

Then, for each cube 4 unique internal surfaces were selected (face 1, 3, 5 and 7). They were arranged next to each other and cold mounted again following the same routine that was used to cold mount the substrate/cubes in the previous step (shown in Fig. 3.13).

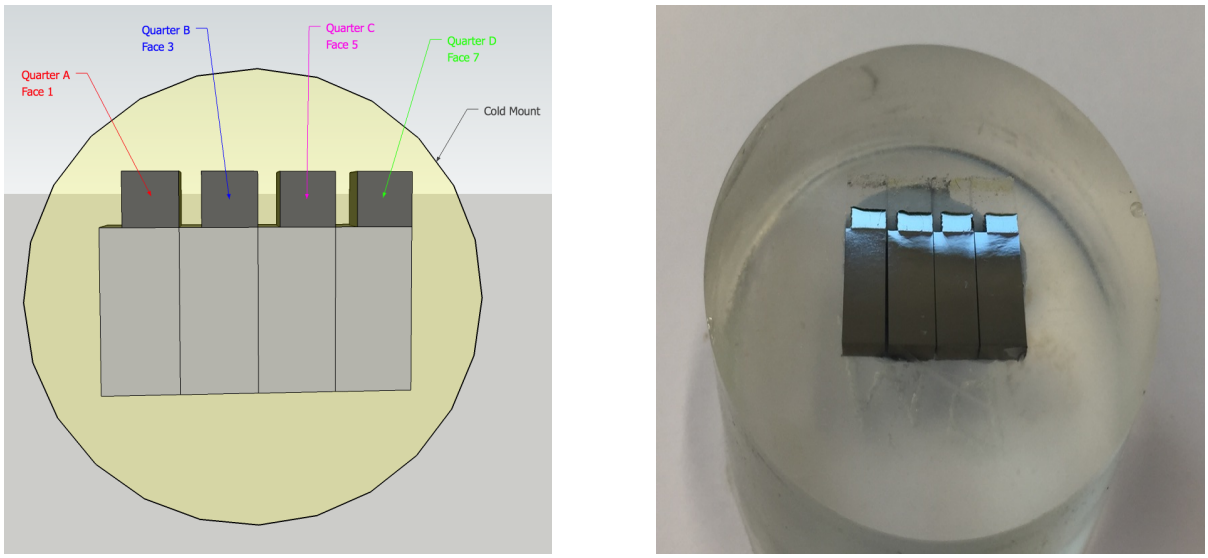

Figure 3.13- Each cube was mounted again producing 4 unique internal surfaces to be investigated

Each mounted cube was then grinded using the Struers Tegramin-20 grinding and polishing unit with P400 to P2500 SiC grinding papers and then polished with 6µm and 1µm Buehler

MetaDi Supreme crystalline diamond suspension on Buehler WhiteFelt polishing cloths. The samples were cleaned using acetone in the Eumax UD100SH-3L ultrasonic cleaner and were ready for the next step which is optical imaging.

3.9. Optical Imaging of the Internal Surfaces of the Cubes Built Using the SLM Process

The polished mounted samples were placed in a motorized Olympus BX51 optical microscope and Clemex Vision PE microscopy image analysis software was used to quantify the different defects present in the cubes built using selective laser melting processing. 50x magnification was used (5x/0.15 BD P for objective and WHN10x-H/22 for the eyepiece) to capture an image from each of the four internal surfaces available for every cube and the resulting image was analysed in the Clemex software. A routine was developed for this image analysis, provided in Fig. 3.14, with which cracks, pores and lack of fusion defects were quantified step by step.

This routine helps keep the quantification of these defects uniform for different samples since it applies the same filters on the images of different cubes. So, since the imaging conditions such as lighting, magnification, cleanliness, field stop and aperture stop were also kept constant for all the samples, the resulting defect quantification was uniformly done.

The first defect type investigated was pores. As they seem to be spherical, specifically compared to the other defects, roundness investigation was chosen as an appropriate way to identify (with red colour) and quantify them (step 008). However, because of the complexity and interconnectivity of the other two defects (cracks and lack of fusion defects) present in the microstructure of the samples investigated, each image was manually processed in the subsequent steps. For example, the lack of fusion defects which are usually larger than pores and irregular in shape were separated manually from cracks which are usually long, narrow

and interconnected (step 017). Lack of fusion defects were then identified subsequently (steps 021 and 022) as a different colour (blue). The remaining defects were identified as cracks and as mentioned before, this was checked manually for every image to make sure that the defects were identified correctly every time.

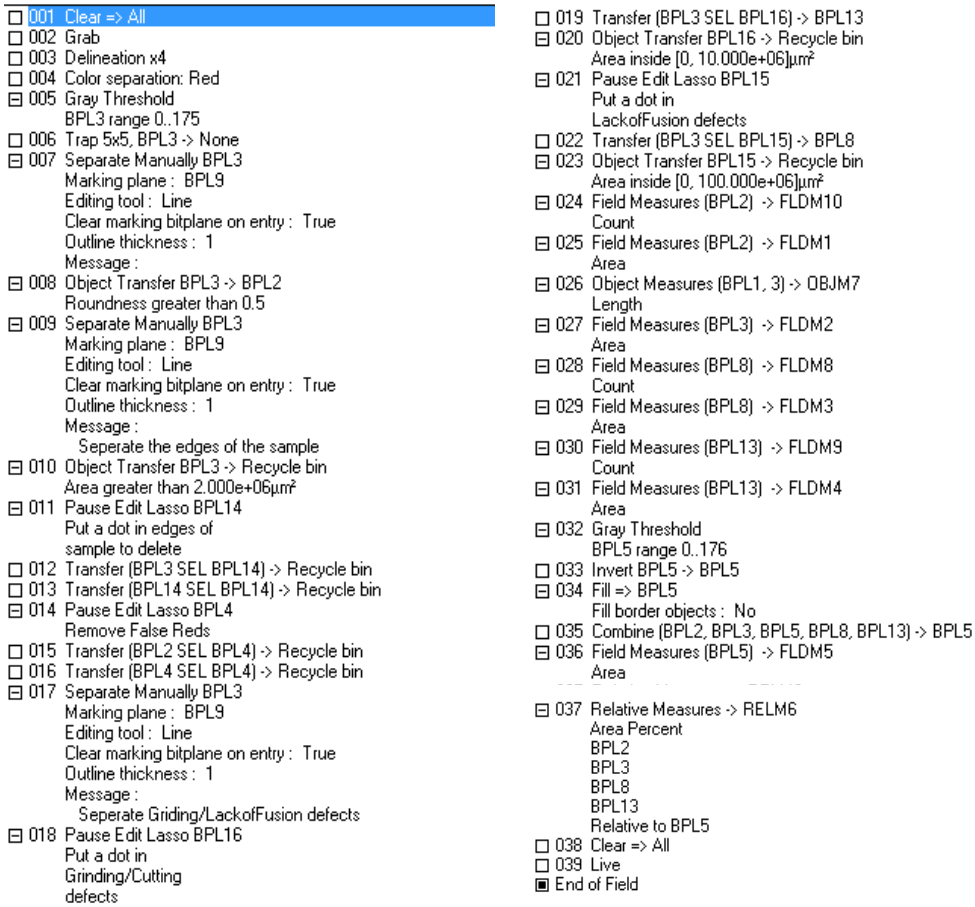

Figure 3.14- The routine used in the Clemex image analysis software helping keep the defect quantification of different specimens uniform.

As an example, for the process explained above, Fig. 3.15 illustrates how different defects were categorized by different colours:

- Red: Pores
- Blue: Lack of Fusion Defects
- Green: Cracks

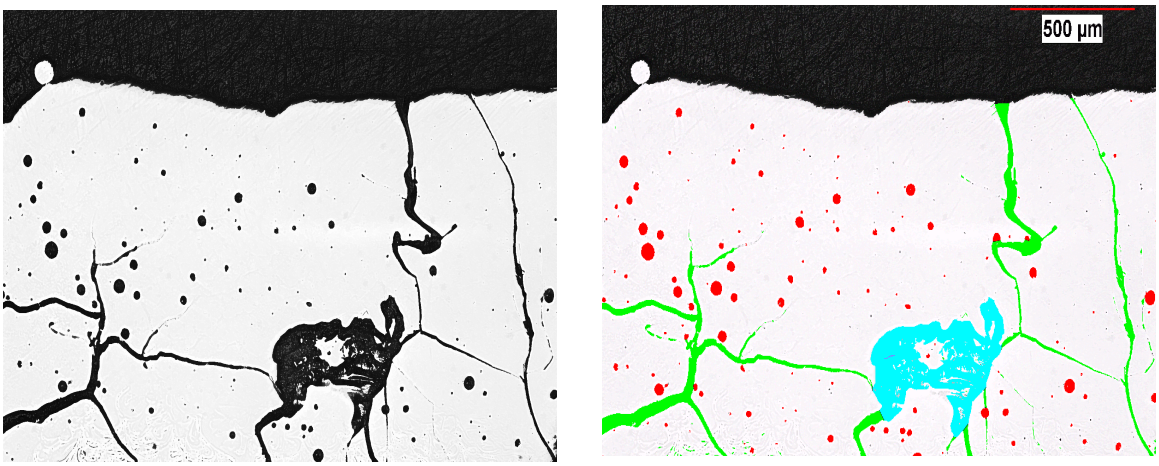

Figure 3.15- Image of an internal surface of a specimen (left), categorized by colour into 3 different defect areas

The relevant measurements for each type of defect that was obtained from one of the internal surfaces of each cube were then combined with the amount measured from the other three surfaces to get the overall quantity of these defects for a certain cube that was built using a certain set of processing parameters in the SLM.

3.10. X-Ray Diffraction of the Cubes Manufactured Using the SLM

The cubes that were manufactured for the XRD investigation were separated from their substrates leaving the bottom 0.5mm of the cube attached to the substrate. The top part was then cut in half (as shown in Fig. 3.16) with the same procedure and machine as explained above. The internal surface of the cube was subsequently cleaned using acetone and placed in the Bruker D2 Phaser XRD machine and investigated. The analysis was done from 2θ equal to 30° to 80°, with a step size of 0.01 and time per step of 0.3 seconds and the relevant XRD pattern was constructed from the data obtained, using the Bruker EVA XRD analysis software.

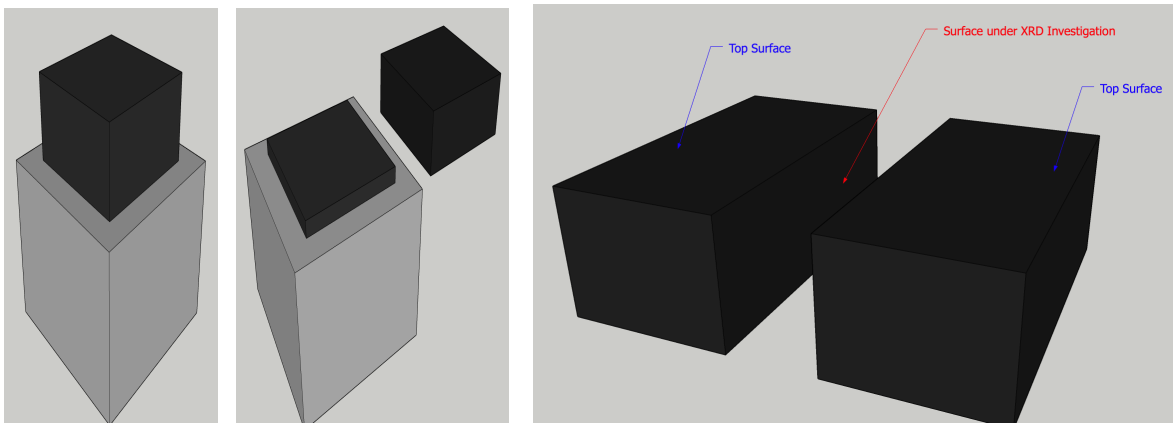

Figure 3.16- For XRD investigation, cubes were separated from their substrate and cut in half. Then the internal surface of each cube was studied via XRD analysis.

3.11. Methodology of the FEM Simulation

3.11.1. The Governing Equations

Understanding the heat transfer mechanism is significant in comprehension of the selective laser melting process, since a localised laser beam is utilised to increase the temperature to selectively melt the powder. Heat conduction equations govern the spatial and temporal distribution of the temperature:

$$\rho C_P \frac{\partial T}{\partial t} = k_{xx} \frac{\partial^2 T}{dx^2} + k_{yy} \frac{\partial^2 T}{dy^2} + k_{zz} \frac{\partial^2 T}{dz^2} + \dddot{\phi} \qquad \text{Equation} - 3.1$$

where ρ is the density, C_P is the specific heat capacity, T is the temperature, t is the time, k_{ii} is the thermal conductivity in x, y and z spatial coordinates and $\dddot{\phi}$ is the heat source term.

In this work, the heat source was simulated using a Cylindrical Laser Heat Flux model through an ABAQUS subroutine written in FORTRAN. An approximation of the heat flux density was used in the simulation (Shi *et al.*, 2007):

$$\dddot{\phi} = 0.864\alpha \frac{P}{\pi r^2} \qquad \text{Equation} - 3.2$$

where α is the laser energy absorptance, P is the laser power and r is the beam spot radius which was taken as 25µm for the Renishaw SLM125 machine (Brif, Thomas and Todd, 2015).

The 0.864 value is extracted from the numerical average computation of a Gaussian distribution, since this approach is a cylindrical heat flux equivalent representation of that. The absorptivity coefficient reported for pure Fe powder, interacting with Nd:YAG (λ = 1.06 μm) is 0.64 (Tolochko *et al.*, 2000). So, after a few trials with different values around α for pure Fe powder, 0.75 was chosen as the absorptivity coefficient of SAM1651 powder. The value reported for α in solid bulk Fe-based alloys has been given to be between 0.25 and 0.35 (Zheng *et al.*, 2009). Considering the fact that α would be smaller for SAM1651 when in solid bulk and liquid form compared to its powder form (because of the multiple reflections of the laser beam in the powder bed which would result in a higher absorptance (Yap *et al.*, 2015)) and assuming similar absorptance for liquid and bulk SAM1651, 0.3 was used as the absorptance of SAM1651 at its liquid stage (since there was no data found representing the absorptance of SAM1651 at its liquid stage).

The temporal temperature distribution was calculated through the ABAQUS FEA software version 6.13. Considering the first law of thermodynamics, it solves the general energy balance equation:

$$\vec{Q}_L = \vec{Q}_{CD} + \vec{Q}_{CV} + \vec{Q}_R \qquad \text{Equation – 3.3}$$

where $\vec{Q}_L$ is the laser heat flux, $\vec{Q}_{CD}$ is the conduction losses, $\vec{Q}_{CV}$ is the convection losses and $\vec{Q}_R$ is the radiation losses. It has been reported (Polivnikova, 2015)(Dahotre and Harimkar, 2008; Zeng *et al.*, 2015; R.P. Hoogeboom, 2016; Promoppatum *et al.*, 2017) that radiation losses are negligible and hence for simplification purposes, they were not considered in this study.

To simulate the conductive heat losses through the substrate and the powder bed, surface film conditions were defined on the five surfaces of the substrate and the four surfaces of the powder layer (Shown in Fig. 3.17). To properly approximate the conductive heat losses

through the surfaces of the substrate and powder bed, thermal conductivity of the solid and powder SAM1651 were used as convective heat transfer coefficients on the aforementioned five and four surfaces respectively. Also, a continuum material was assumed in this study instead of a discrete powder bed, for which equivalent material characteristics were assigned.

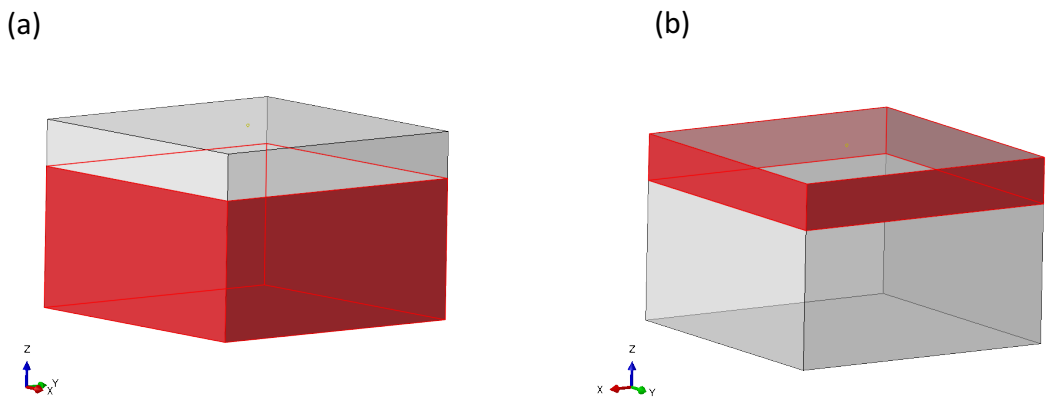

Figure 3.17- The five surfaces for conduction from the substrate (a) and the three surfaces for conduction from the powder bed (b)

3.11.2. Thermal Properties used in Developing the Model

Solidus and liquidus temperatures were measured through DSC testing of the powder. Specific heat capacity values used were assumed to be temperature dependent for simplification and along with latent heat are presented in Table 3.7:

Solid Density	Latent Heat	Specific Heat Capacity	Solidus Temperature	Liquidus Temperature
7310 $Kgcm^{-3}$	$3.25x10^{5}$ JKg^{-1}	460 $JKg^{-1}K^{-1}$	1384 K	1436 K

Table 1.7- Material properties used in the FEA model. Values for solid density, latent heat and Specific heat capacity are from the literature (Ajdelsztajn et al., 2009) and solidus and liquidus temperatures were measured through DSC testing.

The thermal conductivity which was considered for the substrate, at room temperature, was 22.5 ($Wm^{-1}K^{-1}$) (Ajdelsztajn *et al.*, 2009). It has been reported that the thermal conductivity of the metallic powders are significantly smaller than that of the bulk metallic alloys due to the gaps between powder particles which hinder the conduction of heat (Alkahari *et al.*, 2012).

For example, in the case of Ti6Al4V the thermal conductivity of the powder at room temperature is 0.145($Wm^{-1}K^{-1}$) (Parry, Ashcroft and Wildman, 2016) and 7($Wm^{-1}K^{-1}$) (Roberts, 2012) for the bulk form, which means it is smaller by a factor of 48.3. On the other hand, the morphology of the Ti6Al4V powder particles is spherical which translates into a higher packing density and hence a higher thermal conductivity compared to the case of SAM1651 powder particles in which the majority of the particles are non-spherical and even needle-shaped (as shown in the SEM images in Fig. 3.18). This effect of the powder morphology on thermal conductivity of the powder has been reported by Alkahari et al (Alkahari *et al.*, 2012). So, in absence of accurate information for the thermal conductivity for the SAM1651 powder bed, it was set as 0.25($Wm^{-1}K^{-1}$) which is smaller than that of the bulk substrate by a factor of 90. Changing this value would affect the thermal distribution for each melt spot and hence alter the melt pool size, cooling rate and thermal gradients occurring in the specimen. This value along with the values assumed for thermal conductivity of the liquid phase (discussed below) were chosen according to trial and error experiments to match the experimental results and hence contributed to developing the model that could predict the thermal behaviour of SAM1651 in selective laser melting conditions.

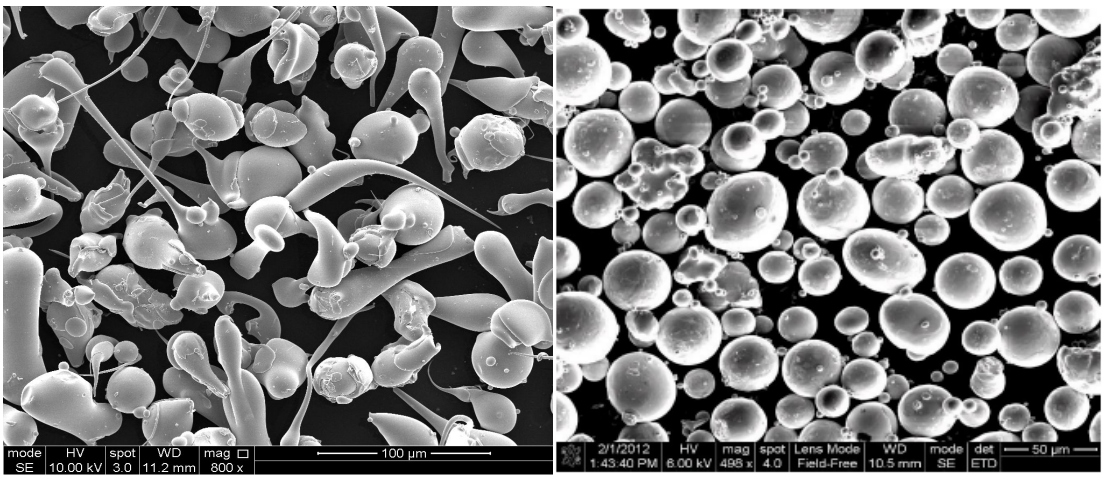

Figure 3.18- SEM images showing the morphology of SAM1651 (left) and Ti6Al4V (right) (Gong, Christiansen, *et al.*, 2014) particles.

Attempting to take in to account the fluid flow effect present in the melt pools occurring in the SLM process and artificially simulate it, an enhanced anisotropic thermal conductivity approach (Safdar *et al.*, 2013) was utilised, in which the enhanced thermal conductivity values were selected through several trials. Equation 3.4 defines the enhanced thermal conductivity, $K_{ii}{}'$, in this approach:

$$K_{ii}{}' = \gamma'_{ii} K \qquad \text{Equation – 3.4}$$

where K is the normal isotropic thermal conductivity at a given temperature, ii is the spatial coordinates and γ'_{ii} is the anisotropic enhancement factor of the concerning spatial coordinates, which is defined as:

$$\gamma'_{ii} = \begin{cases} 1 & T < T_m \\ Multiplying\ Factor & T > T_m \end{cases}$$

The anisotropic enhancement factors used in this study are shown in Table 3.8.

	γ'_{xx}	γ'_{yy}	γ'_{zz}
Powder	75.5	75.5	124.4
Substrate	20	20	124.4

Table 3.8- The multiplying factor values to obtain the anisotropic enhanced thermal conductivity values used in the FEA model

The simulated melt pool sizes were compared with the experimental melt pool sizes manufactured with the processing parameters and the enhanced thermal conductivity values that produced similar results to the experimental ones were utilised for developing the model.

As to why the multiplying factors are larger, in the xx and yy coordinates, for the powder than the substrate, it can be indicated that as the powder bed transforms into molten material, the liquid is surrounded by powder particles which allows it to move more freely and hence experience a higher heat flow inside. On the other hand, when the substrate transforms into

liquid it is limited by the solid material around it which inhibits free movement of the liquid and hence a reduced heat flow is caused by the fluid flow mechanism.

The 3D geometry and mesh is demonstrated in Figure 3.19. The model was meshed with cubic elements. The mesh size at the powder layer is 8.3x5x5µm and 10x5x5µm in the substrate. The thickness of the layer of the SAM1651 powder bed was chosen to be 50µm which was laid on a solid substrate of the same alloy with the dimensions of 150x300x300µm. At the start, when the laser irradiation begins, the heat flux is applied on a spot on the surface of the powder and it is maintained for the duration of the intended exposure time that is fed into the simulation.

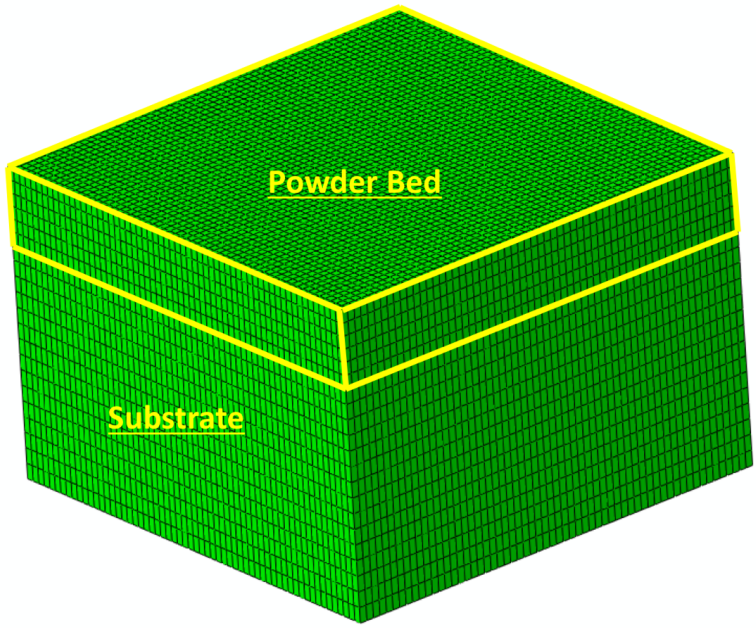

Figure 3.19- 3D finite element method geometry and mesh of the powder bed and the substrate

Since argon was used to protect against oxidation of the specimen in the SLM process, natural convection as a surface film interaction on the exposed top surface was modelled and a convective heat transfer coefficient of 0.02 mW/mm^2K was used to compensate for the convection heat losses through the top surface of the powder bed.

During the exposure of the laser, the temperature of each element was checked to figure out if it has melted or solidified and the appropriate material properties was then applied. After the laser turns off, the thermal distribution of the elements in the melt pool and its surrounding was still simulated for 2 seconds in the cooling stage, so that the cooling behaviour of the material can also be investigated.

3.11.3. Validation of the FEA Modelling

Validation of the thermal model was carried out by comparing the experimental melt pool dimensions with simulation predicted melt pool dimensions. In order to fabricate the required melt pools experimentally, first a 40mm diameter substrate disk was made through Spark Plasma Sintering the SAM1651 powder close to the alloy's melting point. This resulted in a fully dense disk, however the microstructure of the material was fully crystallised. Subsequently a single layer of the SAM1651 powder was deposited on the substrate disk, which was preheated to 450°C. Single tracks, 5mm in length, were melted on the powder bed and into the substrate using the selected laser power and exposure time values. The specimens were then cut, cold mounted, grinded and polished. Afterwards, optical microscopy was used to obtain images of the cross-section of the melt tracks and Clemex software was used to determine the dimensions of the melt pools.

Because of the high cooling rate of the SLM process, the microstructure of the whole volume of the glass forming material that goes through melting and rapid solidification would be amorphous. The contrast between the crystallized substrate and the amorphous microstructure of the melt pool was used to distinguish the interface between melt pools and the underlying substrate. The simulated melt pool dimensions were obtained through modelling individual melt pools by feeding the corresponding substrate temperature, laser

power and exposure time values into the simulation. Cross-sections of these melt pools were then analysed to get the melt pool width and depth in each case. Comparison of the cross section of experimental and simulated melt pools can be observed in Fig. 3.20 and the corresponding values for the dimensions obtained from Fig. 3.20 are presented in Fig 3.21.

Based on the fact that, according to Fig 3.20, predicted melt pool width and depth are in agreement with the values measured from the experiments, it can be stated that the FEA model prediction of the behaviour of the SAM1651 when processed with selective laser melting does correlate well with experimental results.

Another approach to validating the FEA simulation is through comparing the temperature distribution inside the experimental and simulated melt pools resulting from the selective laser melting process. However, since the data regarding the temperature distribution in the specimens fabricated out of the SAM1651 alloy was not at hand, the relationship between the simulated peak temperature in the melt pools and the corresponding laser power and exposure time values which were utilised to simulate them can be used to investigate the validity of the FEA modelling. It has been reported that increasing the laser power and exposure time would result in increasing the emerging peak temperature in the melt pool(Shiomi *et al.*, 1999). Furthermore Shiomi et al. has showed that the dominant factor in this increasing of the peak temperature is laser power rather than exposure time.

So, to investigate if the FEA simulation used in this work would be able to predict this relationship, the simulated peak temperature values occurring in the melt pool were extracted from the simulations using processing parameters presented in Table 3.9. These peak temperatures were acquired from the centre of the top surface of the melt pools (shown in Fig. 3.22) as the laser heat flux stopped and the cooling stage began.

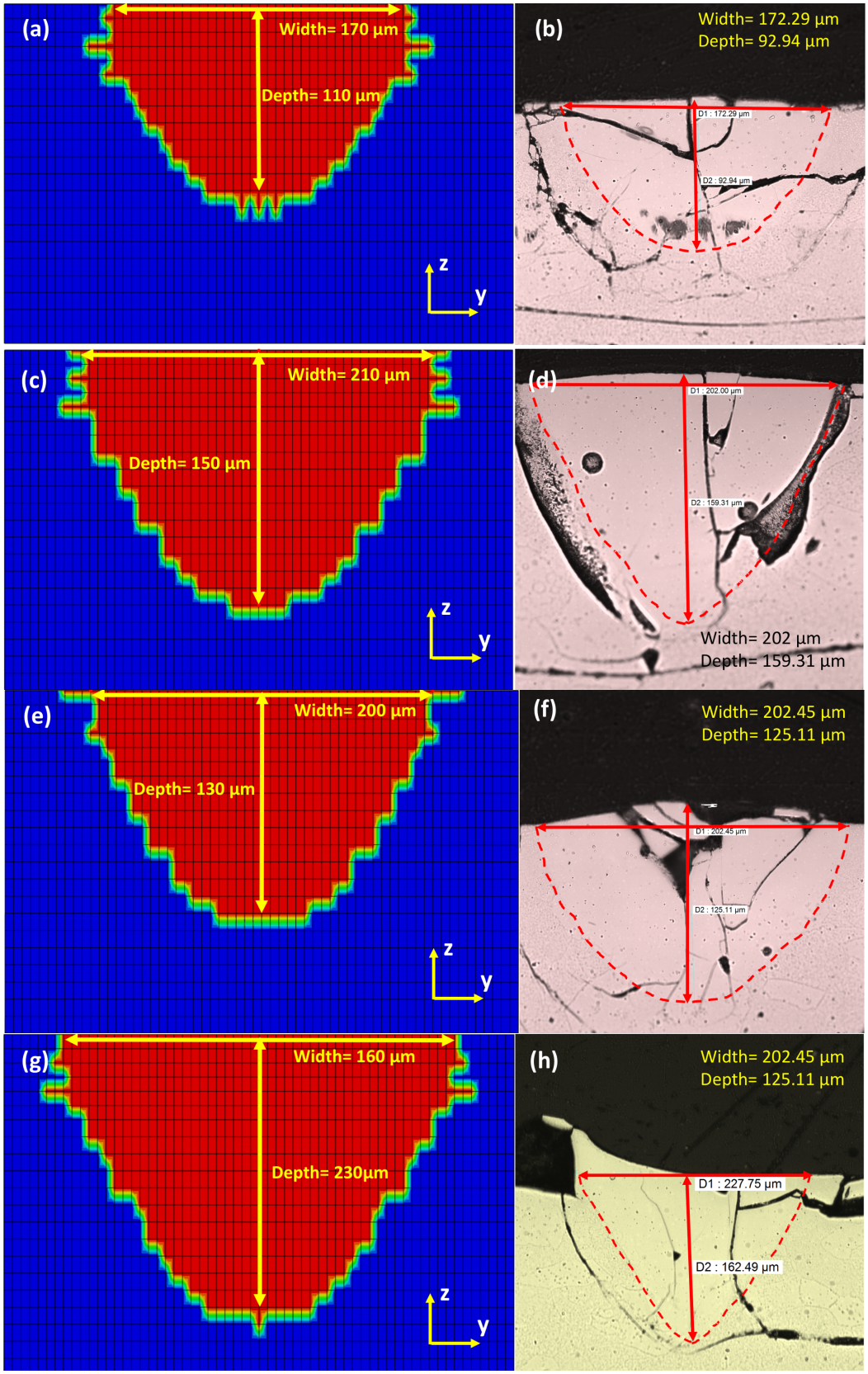

Figure 3.20- Width and depth dimensions of the cross section of the simulated and experimental melt pools fabricated using laser power and exposure time values of 140W-120µs (a and b), 160W-180µs (c and d), 180W-120µs (e and f) and 200W-180µs (g and h) respectively.

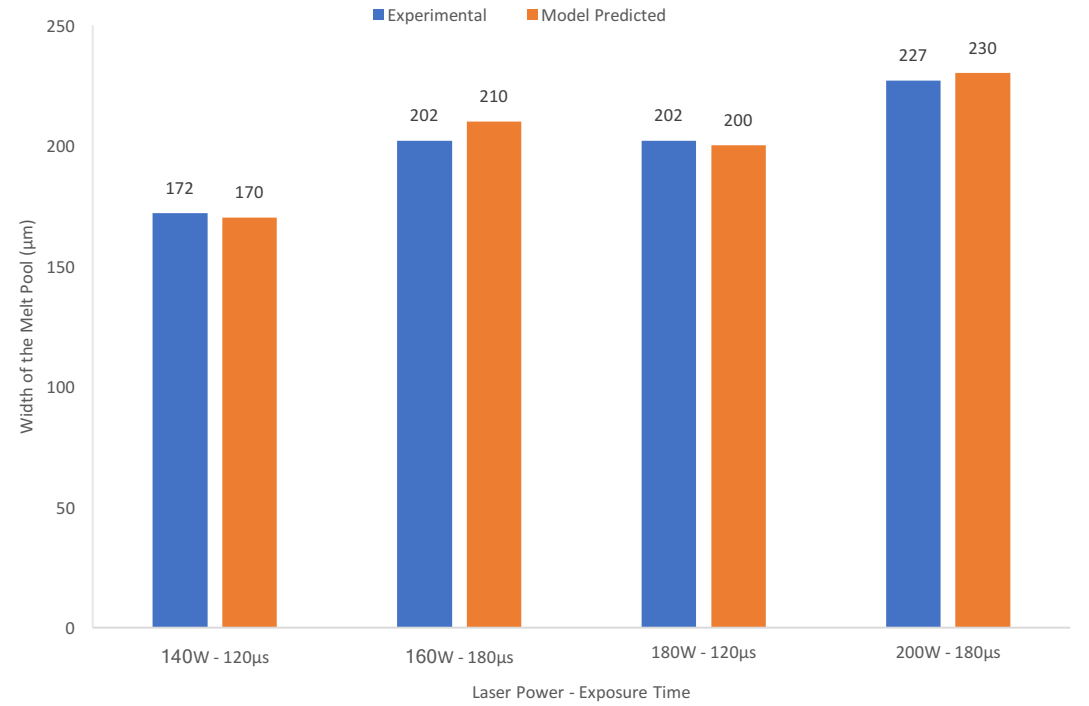

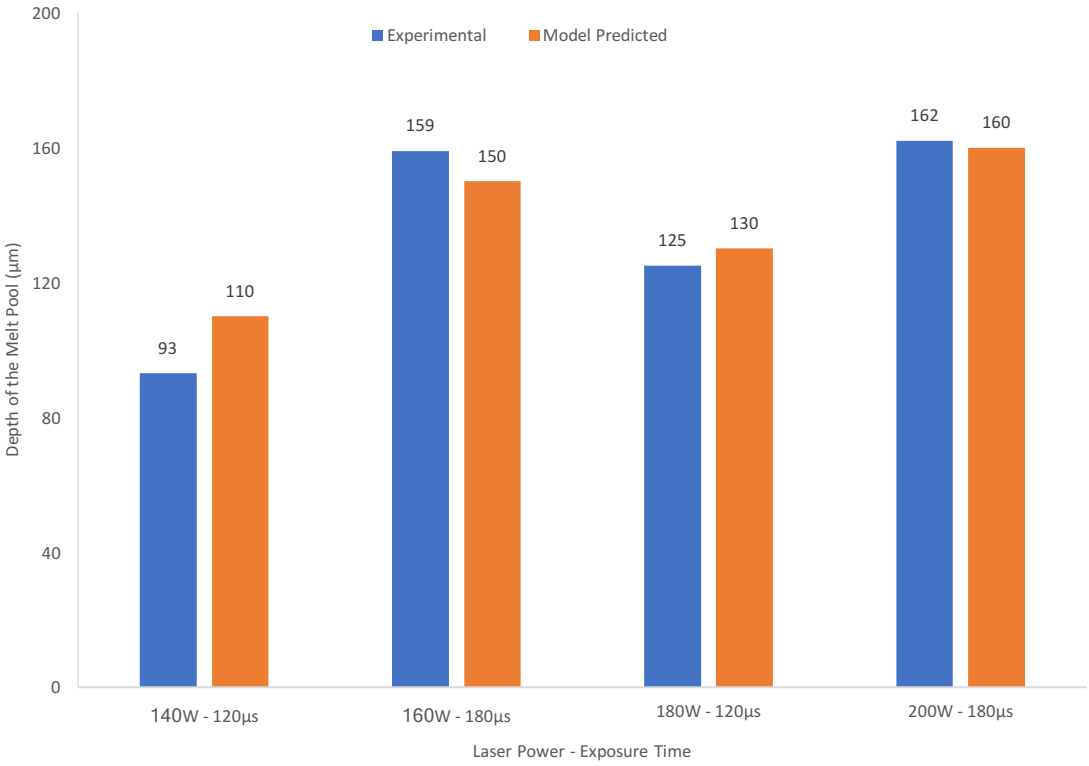

Figure 3.21- Comparison of the simulated and experimental melt pool width (top) and depth (bottom).

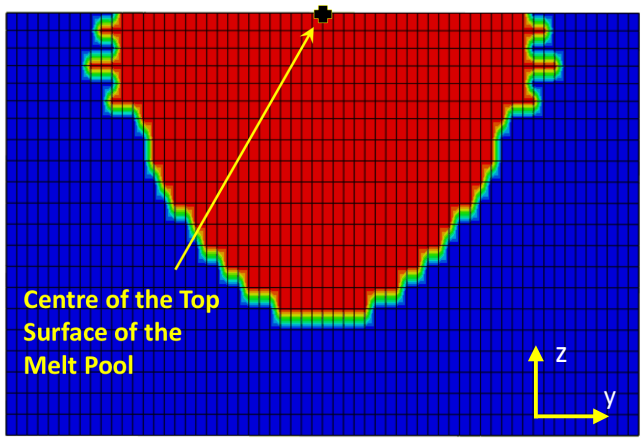

Figure 3.22- Identification of the centre of the top surface of the melt pool from which the peak temperature was extracted

The peak temperature values were then plotted against the corresponding laser power and exposure time values and are shown in Fig. 3.23. It can clearly be seen that the peak temperature in the simulated melt pool increases as the exposure time and laser power increases. Also, laser power is the dominant factor in increasing the peak temperature with exposure time demonstrating an inferior contribution toward increasing the peak temperature. The similarity between the prediction of the FEA simulation used in this work and what Shiomi et al has reported, can be taken as another approach in further validating the model.

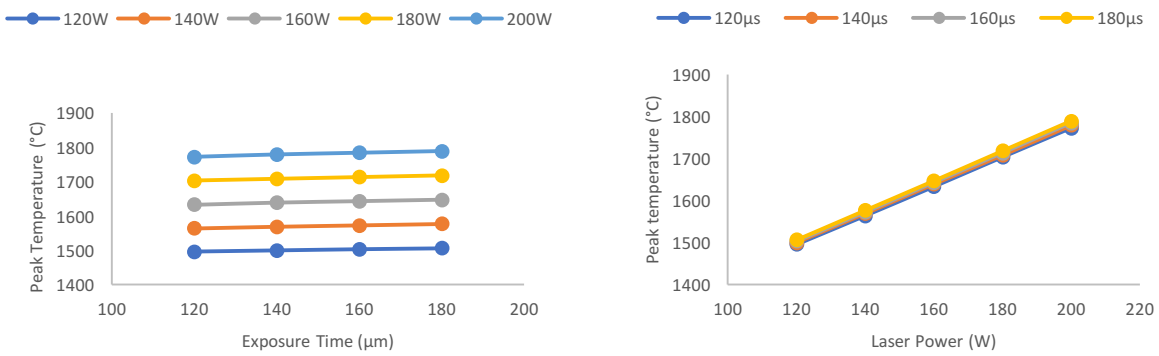

Figure 3.23- The relationship between the simulated peak temperature and the corresponding laser power (right) and exposure time (left) values used to simulate the thermal distribution in the melt pool

3.11.4. Calculating the Thermal Gradient and Cooling Rate

In order to investigate the effect of processing parameters on the cooling rate and thermal gradient which are responsible for the microstructure and the thermal stresses that occur in selective laser melting, thermal data was extracted from the FEA simulation after it was validated against experimental results.

For determining the cooling rate of the SLM process for a certain set of processing parameters, an individual melt pool was simulated, which provided the melt pool size and the thermal distribution within it. The centre of the melt pool was identified as shown in Fig. 3.24 and the thermal history of the centre was extracted starting from the laser turning off and continuing for 2 seconds in the cooling stage. Using an excel spreadsheet, the slope of the (temperature-time) cooling curve at the instance that the centre of the melt pool has cooled down to about the melting point of the material was calculated as the cooling rate.

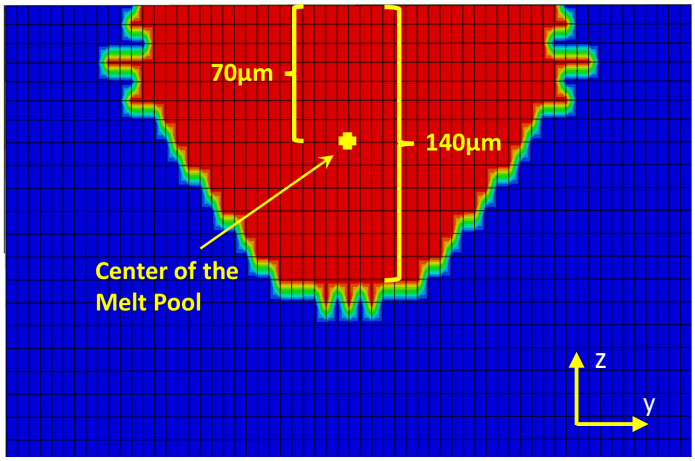

Figure 3.24- Identification of the centre of the melt pool for calculation of the cooling rate

Concerning the calculation of thermal gradient, the fact that the thermal gradient mechanism mainly operates in the solid layers underneath the melt pool was taken into consideration. Therefore, as shown in Fig. 3.25, at the instance that the laser turns off and the simulated

melt pool starts to cool down, the temperature of the solid/liquid interface at the bottom of the melt pool together with the temperature of a spot 50µm directly underneath the first spot was extracted from the FEA simulated thermal profile of the model and was used to determine the thermal gradient occurring in the process.

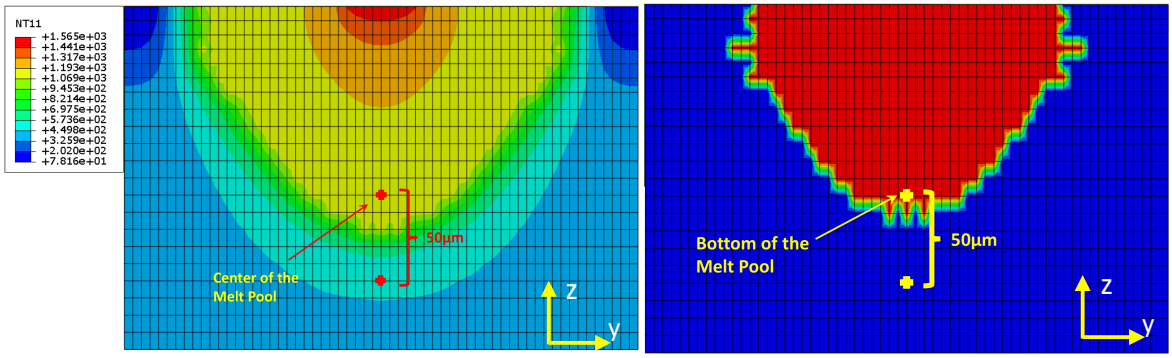

Figure 3.25- Identification of the spots in the simulated model of the melt pool substrate (right) for extracting thermal data from the simulated temperature profile (left) for calculating the thermal gradient of the SLM process.

3.11.5. Modelling Trials

The FEA simulation was used to provide the melt pool size, thermal gradient and cooling rate values as a result of using different processing parameters. The influence of laser power, exposure time and substrate temperature values were simulated in this regard and were utilised as a basis for explaining microstructure development and defect formation occurring in results obtained experimentally.

3.11.5.1. Effect of Laser Power and Exposure Time

The FEA model was used to simulate the melt pool size, thermal profile and thermal history resulting from the SLM process from which the corresponding cooling rate and thermal gradient values were calculated. The substrate temperature was kept at 450°C during these

sets of simulations. Table 3.9 shows the values that were fed into the FEA model for this purpose.

T_{Subs}=450°C		Exposure Time (µs)			
		120	140	160	180
Laser Power (W)	120	x	x	x	x
	140	x	x	x	x
	160	x	x	x	x
	180	x	x	x	x
	200	x	x	x	x

Table 3.9- Laser power and exposure time values used for simulating their effect on thermal gradient and cooling rate.

3.11.5.2. The Effect of Substrate Temperature

The substrate temperature has been reported to be closely connected to the thermal gradient values occurring in the specimens manufactured with the SLM process. On the other hand, the existence of large thermal gradients in the specimens results in thermal stresses which are detrimental to the mechanical properties of the samples and can cause cracking and delamination. So, the FEA model was edited and different substrate temperatures were used to simulate the thermal distribution values occurring in individual melt pools and their surroundings as a result. The list of the laser power and exposure time values that were used in these simulations are listed in Table 3.10.

		Laser Power (W) - Exposure Time (µs)		
		120W - 120µs	140W - 140µs	160W - 160µs
Substrate Temperature (K)	298	x	x	x
	423	x	x	x
	573	x	x	x
	723	x	x	x

Table 3.10- Laser power and exposure time and bed temperature values used for simulating their effect on thermal gradient.

3.12. Experimental Uncertainties and Errors

Similar to any other scientific work, there are errors and uncertainties involved in the measurements included in this study. Probably the largest source of experimental error in

this study stems from the fact that for each set of parameters, only one specimen was produced and characterised. Although the large number of specimens examined here can be an advantage when processing experimental data statistically, but the limitation of having only one data point for each type of defect produced as a result of utilizing each set of parameters remains a significant source of uncertainty.

The other major source of error in this research is related to the measurement of various defects through optical microscopy. Although these measurements were performed using the Clemex Vision PE microscopy image analysis software semi automatically, and manual inspection of every single image was carried out to make sure that the image analysis has been accurate, this still remains a possible source of error, either from the software or form human error. For example, as mentioned in section 3.9 and shown in Fig. 3.14, the defects that where considered as pores were the ones that had a roundness larger than 0.5 to distinguish them from small cracks and lack of fusion defects and every image was manually inspected to make sure that the software has performed this detection accurately, but it is possible that few errors might have happened and that this categorisation was not done perfectly for every image.

4. Results

4.1. SAM1651 Powder Characterisation

4.1.1. Particle Size Analysis

The purchased pre-alloyed powder was tested to obtain its particle size. As shown in Fig. 4.1, the range of the particle size of the powder was between D_{10}=17µm and D_{90}=43.8µm and the average particle size was D_{50}=26.7µm. This was in agreement with the values that LPW Technology had reported, namely 15-45µm.

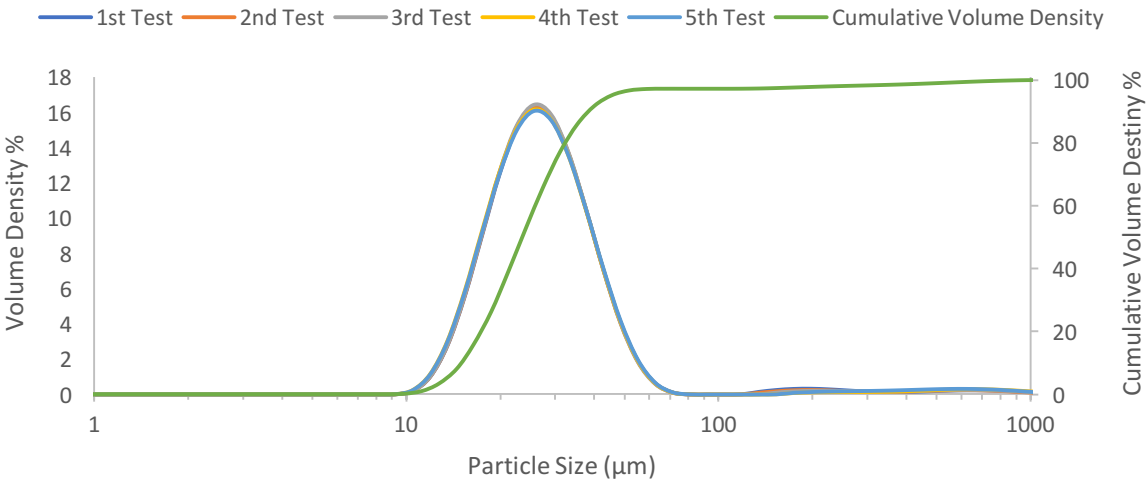

Figure 4.1- Particle size range of the SAM1651 powder

4.1.2. Morphology and Inner Structure of the SAM1651 Powder

The SAM1651 powder was imaged with the Inspect F SEM to investigate the morphology of the powder particles. The shape of most of the powder was not spherical, although some spherical particles could be observed in the images. The inner structure of the powder particles was also imaged which is shown in Fig. 4.2. Internal pores can be seen in some of

the particles. Both the elongated shape of the particles and the existence of the internal pores can be attributed to the unoptimised parameters used in the gas atomisation process during the fabrication of the SAM1651 powder.

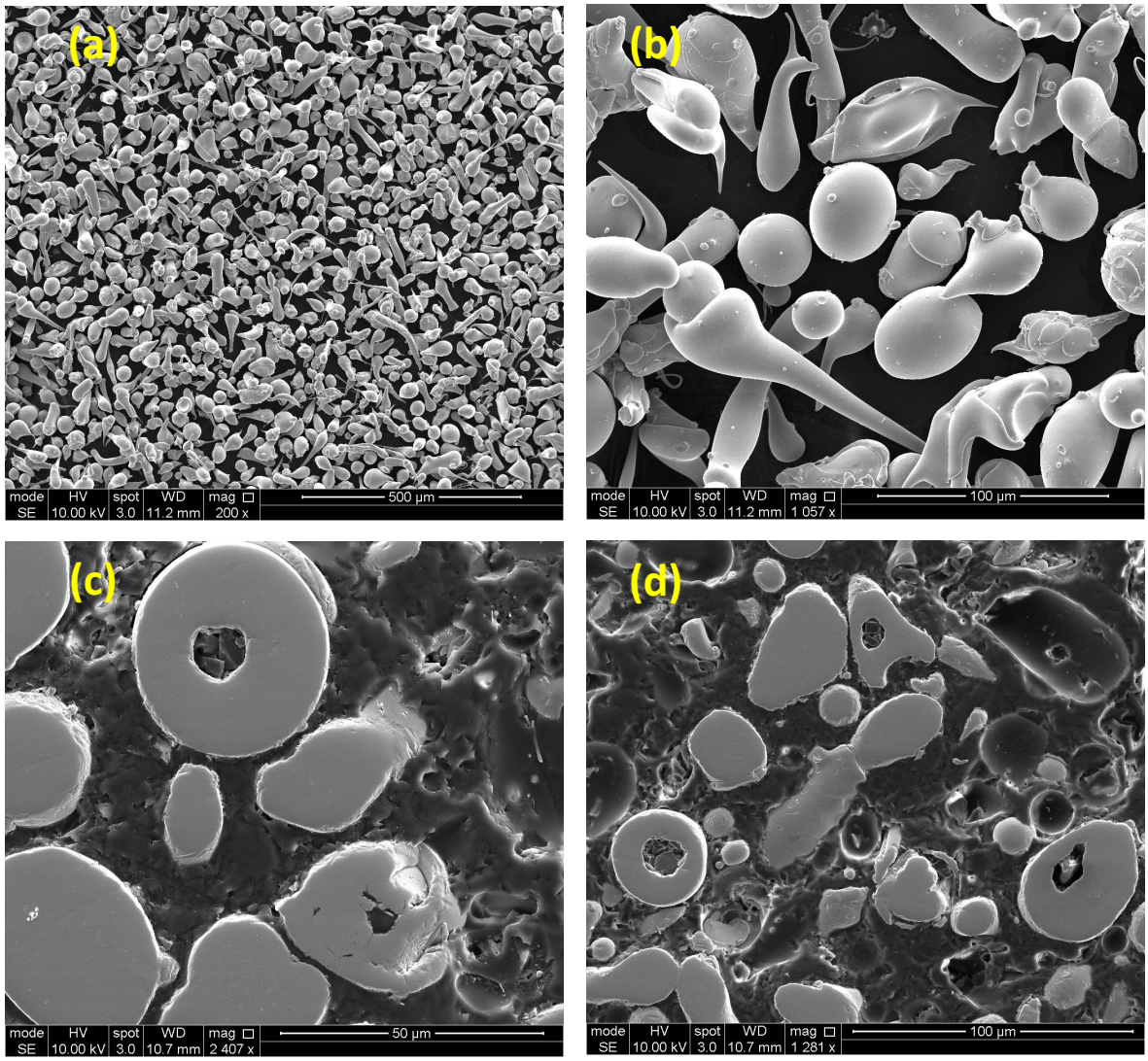

Figure 4.2- SEM images of SAM1651 powder particles (a and b) and their internal structure containing pores (c and d)

4.1.3. X-Ray Diffraction of the SAM1651 Powder

The microstructure of the SAM1651 alloy was investigated through XRD testing and the powder was shown to be fully amorphous, which was expected, as the Fe-based glass forming alloy has a relatively high glass forming ability and the production method of gas atomisation

used to fabricate the powder has a high cooling rate. As demonstrated in Fig.4.3, the XRD pattern contains a broad halo and lacks any sharp peaks which is indicative of the amorphous structure of the powder.

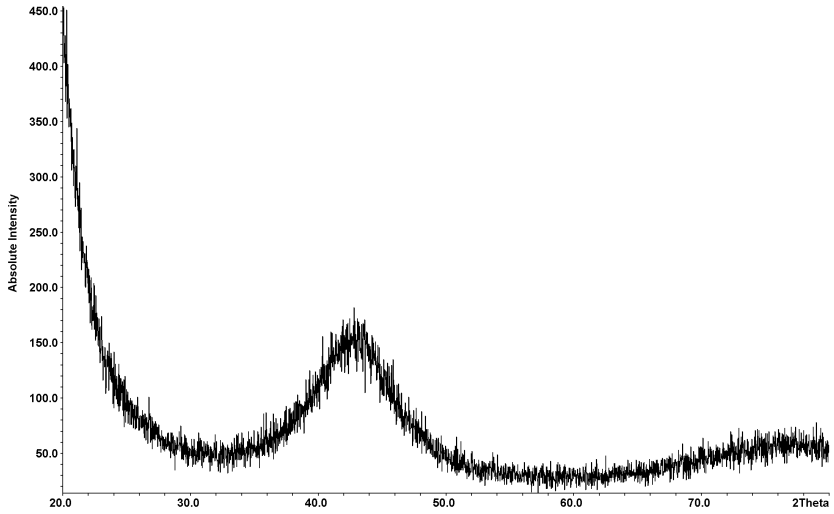

Figure 4.3- XRD pattern of the SAM1651 powder, indicating an amorphous microstructure.

4.1.4. Thermal Analysis of the SAM1651 Powder

The SAM1651 powder was investigated using the differential scanning calorimetry method to measure its glass transition temperature, onset of crystallisation, and liquidus and solidus temperatures. From the data provided by the Q600 SDT, which are presented in Fig. 4.4, these parameters were extracted and are displayed in Table 4.1.

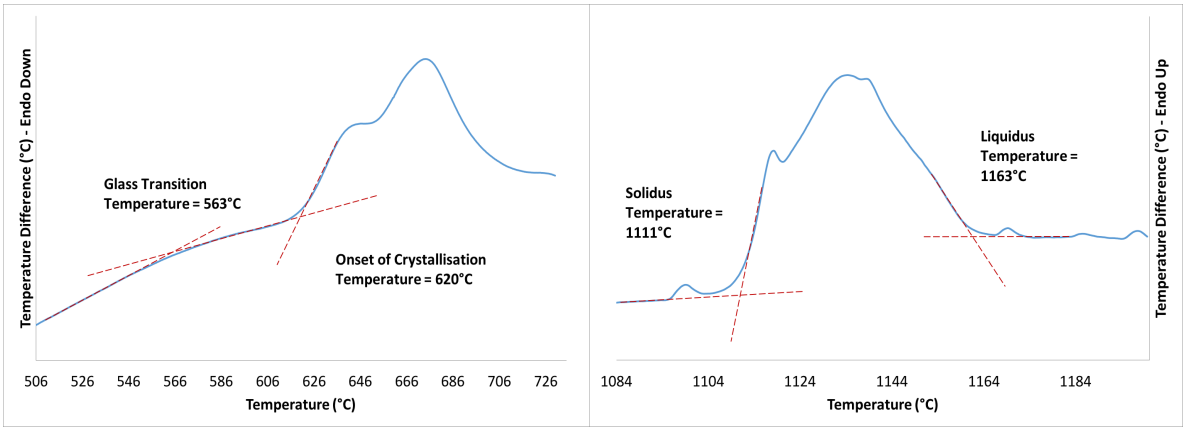

Figure 4.4- DSC diagrams of the SAM1651 characterizing glass transition, crystallization, and solidus and liquidus temperatures.

Glass Transition Temperature (°C)	Onset of Crystallisation Temperature (°C)	Solidus Temperature (°C)	Liquidus Temperature (°C)
563	620	1111	1163

Table 4.1- Characteristic temperatures of the SAM1651 alloy obtained with DSC testing at 1 °C/min.

4.2. The Influence of Laser Power and Exposure Time

4.2.1. The Effect of Laser Power and Exposure Time on Cracking and Porosity

The quantification of the optical images obtained from fabricated specimens are depicted in Fig. 4.5. The amount of cracking and porosity calculated from Equation 4.1 and 4.2 are depicted at different exposure times for each laser power.

$$Proportional\ Cracking\ (\mu m^{-1}) = \frac{(Total\ Crack\ Length)}{(Total\ Area\ of\ the\ Sample)}]\times 10^{2} \qquad \text{Equation} - 4.1$$

$$Proportional\ Porosity\ (\mu m^{-2}) = \frac{(Total\ Pore\ Count)}{(Total\ Area\ of\ the\ Sample)}]\times 10^{6} \qquad \text{Equation} - 4.2$$

It can be observed that, for a certain laser power, as the exposure time increases the amount of cracking increases to a peak and then decreases. On the other hand, the porosity of the cubes manufactured by the selective laser melting process seems to decrease to a minimum before increasing again as the exposure time of the experiments increases for a single laser power. The parameters shown in Table 4.2 were kept constant during this experiment.

Bed Temperature	Point Distance	Hatch Spacing	Layer Thickness
723 K	50 µm	100 µm	50 µm

Table 4.2- Processing parameters that were kept constant for this experiment

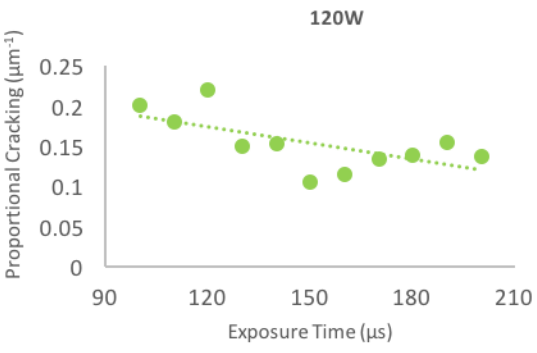

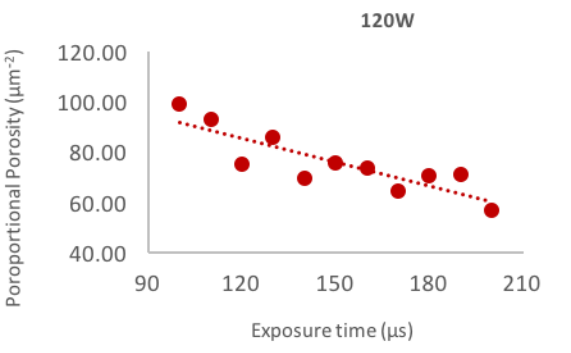

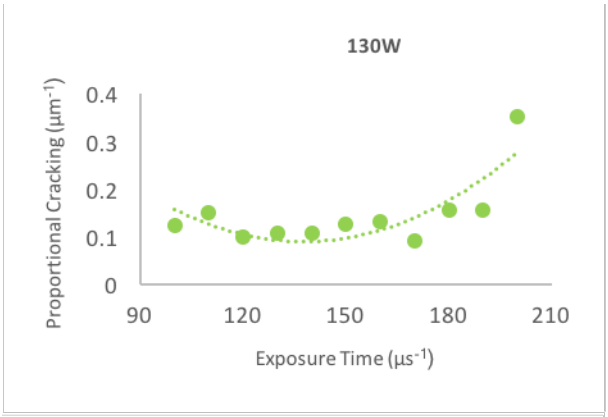
130W
Proportional Cracking (µm-1)
0.4
0.3
0.2
0.1
0
90
120
150
180
210
Exposure Time (µs-1)

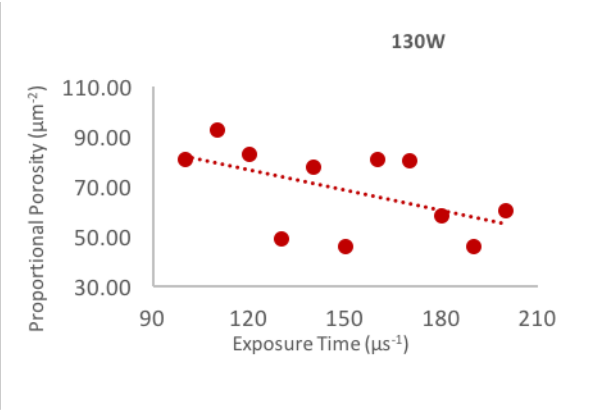
130W
Proportional Porosity (µm-2)
110.00
90.00
70.00
50.00
30.00
90
120
150
180
210
Exposure Time (µs-1)

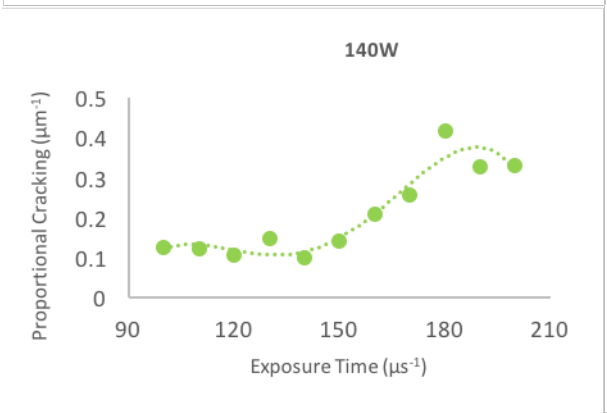
140W
Proportional Cracking (µm-1)
0.5
0.4
0.3
0.2
0.1
0
90
120
150
180
210
Exposure Time (µs-1)

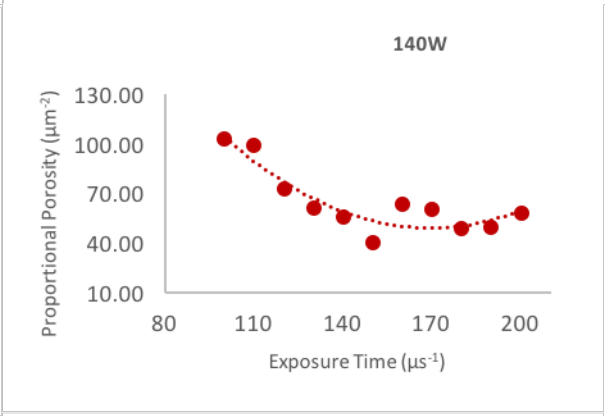
140W
Proportional Porosity (µm-2)
130.00
100.00
70.00
40.00
10.00
80
110
140
170
200
Exposure Time (µs-1)

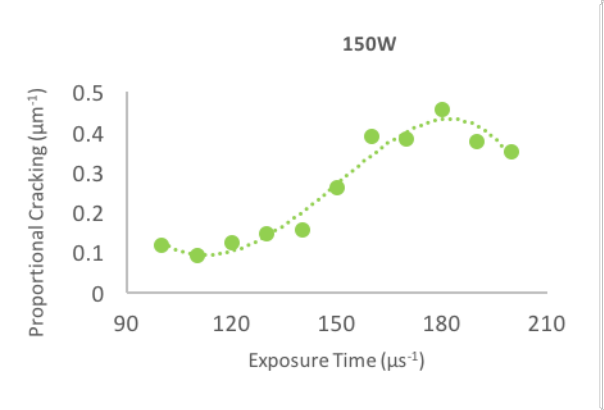
150W
Proportional Cracking (µm-1)
0.5
0.4
0.3
0.2
0.1
0
90
120
150
180
210
Exposure Time (µs-1)

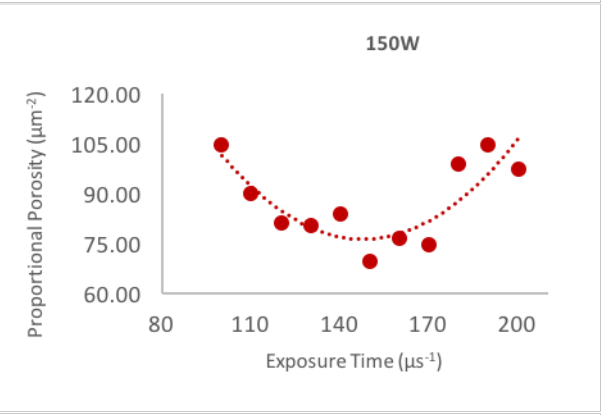
150W
Proportional Porosity (µm-2)
120.00
105.00
90.00
75.00
60.00
80
110
140
170
200
Exposure Time (µs-1)

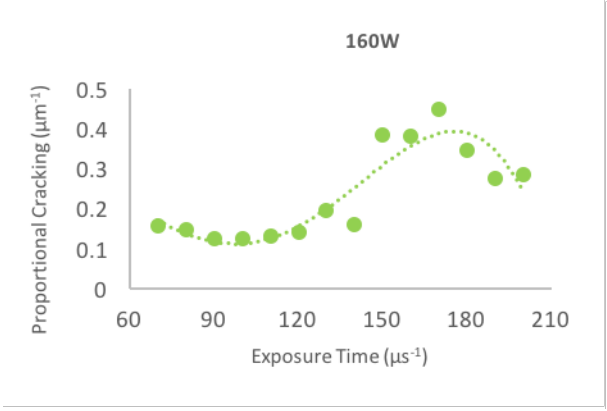
160W
Proportional Cracking (µm-1)
0.5
0.4
0.3
0.2
0.1
0
60
90
120
150
180
210
Exposure Time (µs-1)

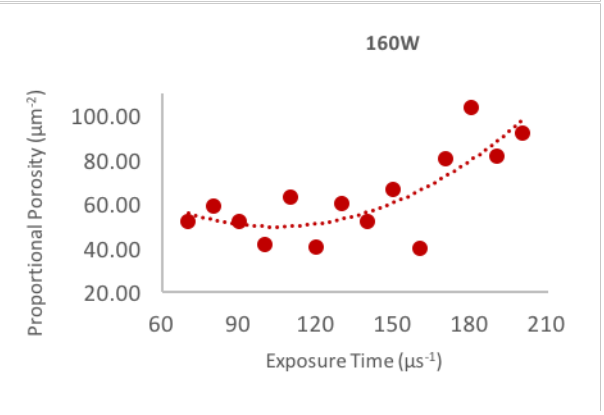
160W
Proportional Porosity (µm-2)
100.00
80.00
60.00
40.00
20.00
60
90
120
150
180
210
Exposure Time (µs-1)

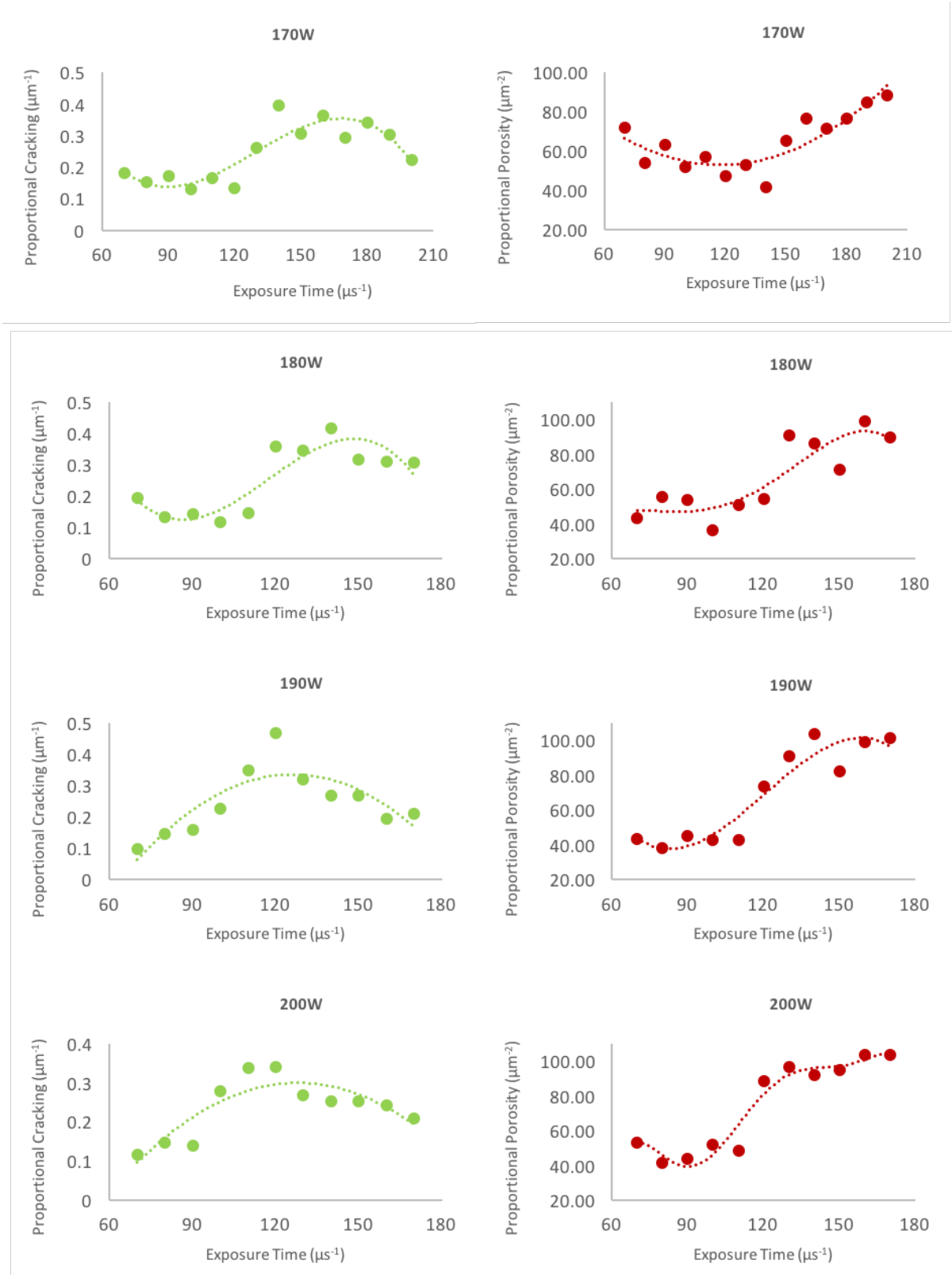

Figure 4.5- Effect of laser power and exposure time on Cracking (green) and porosity (red) of the specimens

When these two diagrams are investigated together, it can be shown that, for a certain laser power, the porosity of the samples starts to increase when the exposure time used results in the cracking to be at a maximum. This critical exposure time for each laser power seems to move toward lower values as the laser power used increases. For the samples made at 120W, this critical exposure time value is not depicted in the range shown below and judging by the trend mentioned above, it would have appeared at an exposure time larger than 200µs.

So, examining the cracking behaviour of the samples made by the SLM process seems to be a good way to investigate the effect that laser power and exposure time have on not only the cracking but also porosity of the specimens. To do so, proportional cracking values presented in the above diagram for different laser powers and exposure times are assembled in Fig. 4.6.

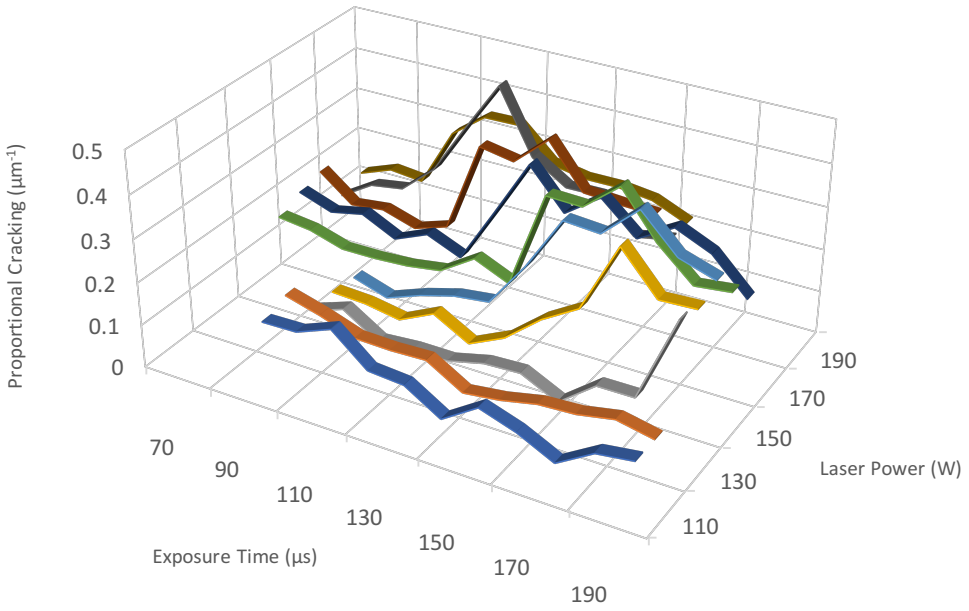

Figure 4.6- Effect of different laser power/exposure time combinations on the amount of cracking in samples

From the data presented in Fig. 4.6 the exposure time that resulted in the maximum amount of cracking was selected for each laser power. After this point, an increase in the amount of porosity can be observed which can either be attributed to vaporization or gas entrapment in

the volatile melt pool resulting from high energy density input. So, this point can be considered as the onset of in-situ pore formation and therefore to avoid this phenomenon, exposure times smaller than this amount should be used at each laser power. In Fig. 4.7 the onset of in-situ pore formation for each laser power and the area that it can be avoided is demonstrated.

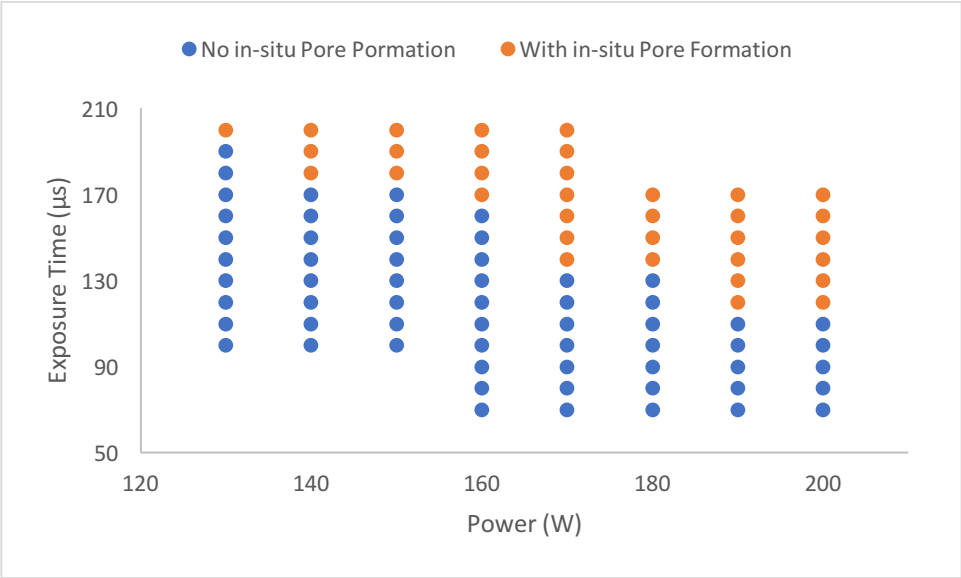

Figure 4.7- Onset of in-situ pore formation at different laser power values

Since other processing parameters were kept constant, 1D energy density (Equation 4.3) was chosen to represent the effect of laser power and exposure time on the amount of cracking and Fig. 4.8 depicts this relationship. As demonstrated in this figure, there is a region in the pattern in which the amount of cracking can get to a minimum of about 0.1-0.2(μm^{-1}) and so this would be the area of interest when choosing the processing parameters.

$$1D\ Energy\ Density = \frac{(Power)(Exposure\ Time)}{(Point\ Distance)} \qquad \text{Equation} - 4.3$$

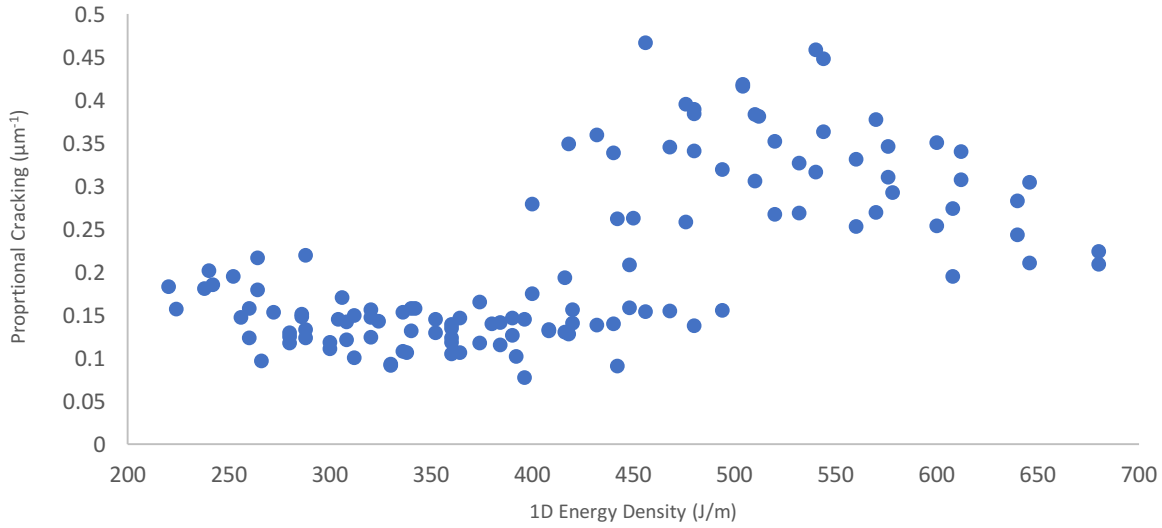

Figure 4.8- Effect of 1D energy density on the amount of cracking within different samples

From the data points in this minimum cracking region of the pattern in Fig. 4.8, the corresponding laser power and exposure time values were selected above which the amount of cracking would be larger than the lowest possible value. These parameters are shown in Fig. 4.9 which shows the maximum exposure time for each laser power at which minimum cracking would happen in samples built from SAM1651 through selective laser melting. Above this line cracking would increase as power and/or exposure time increases.

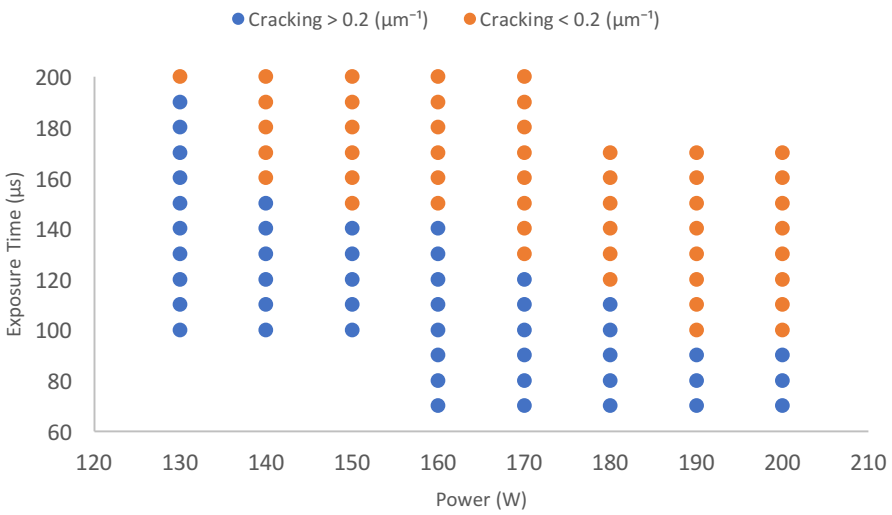

Figure 4.9- Onset of minimum cracking at different laser power values

4.2.2. Effect of Laser Power and Exposure Time on Lack of Fusion Defects

One of the defects that contributes to the low density inside the samples manufactured by the selective laser melting process is lack of fusion defects that are the result of insufficient energy input introduced into the powder at each layer. Laser power and exposure time are two of the main factors that determine the size of the melt pool created by the SLM process. If these parameters are not large enough the resulting melt pools would be small and hence some areas of the powder layer would remain unmelted.

If other processing parameters like point distance, hatch spacing and layer thickness are not relatively optimized to cover these areas, they would have the right conditions to yield lack of fusion defects. So, to investigate the role that laser power and exposure time play in the creation of these defects other parameters were kept constant and the corresponding lack of fusion defects for different exposure times at certain laser powers are represented in Fig. 4.10. The amount of lack of fusion defects here, are presented as the proportional LoF defects:

$$Proportional\ LoF = \frac{(Total\ area\ of\ the\ LoF\ Defects)}{(Total\ Area\ of\ the\ Sample)} \times 10^2 \qquad \text{Equation} - 4.4$$

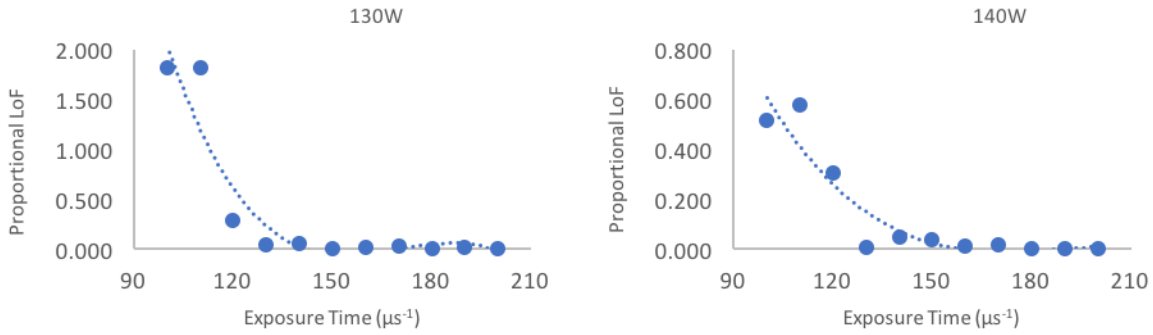

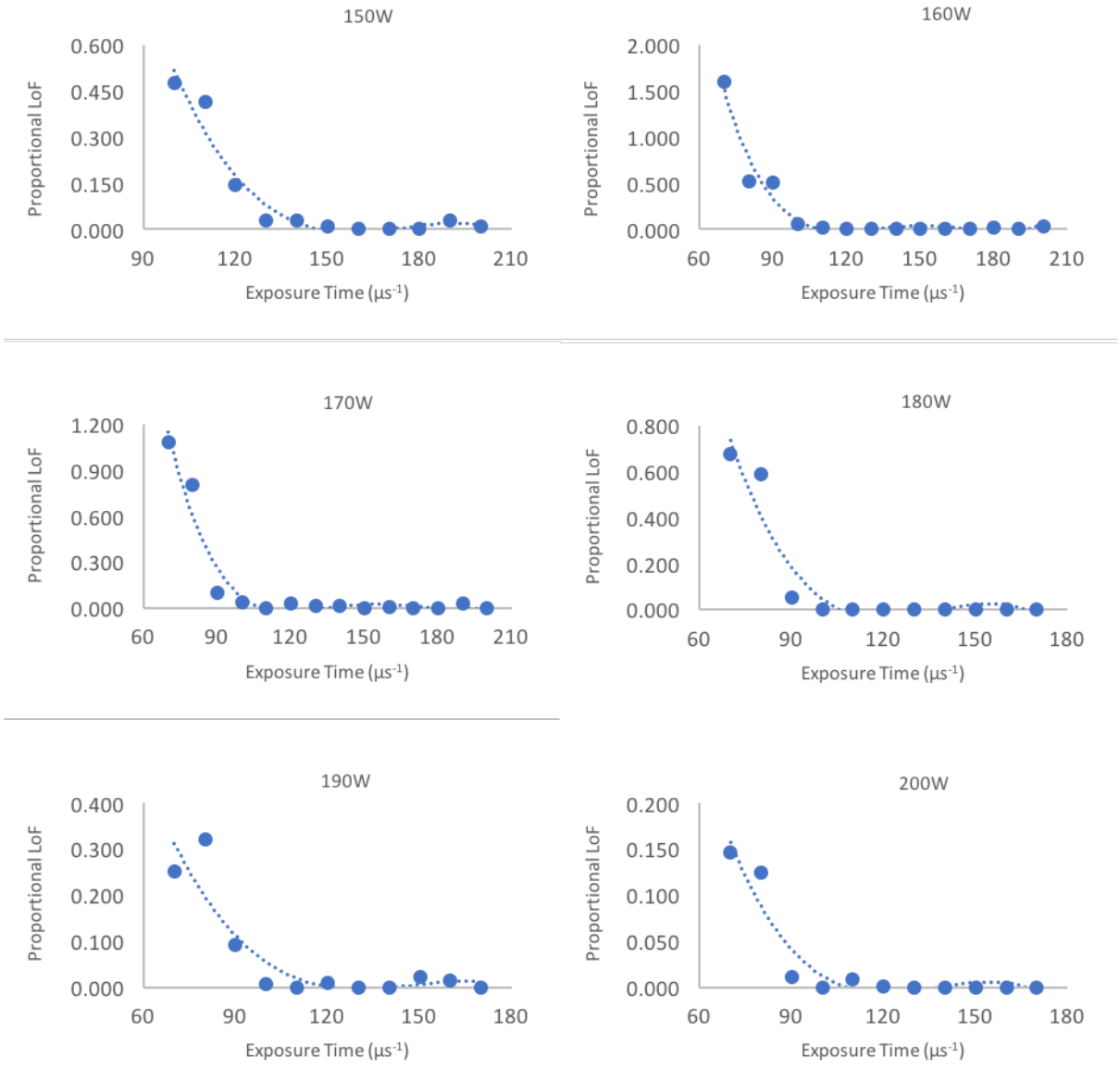

Figure 4.10- Effect of the laser power and exposure time on lack of fusion defects

It can be observed that as the laser power used in the SLM increases the exposure time needed to get rid of the lack of fusion defects decreases. To depict this phenomenon and compare the amount of lack of fusion defects for each laser power and exposure time Fig. 4.11 is constructed by assembling the data shown in Fig. 4.10.

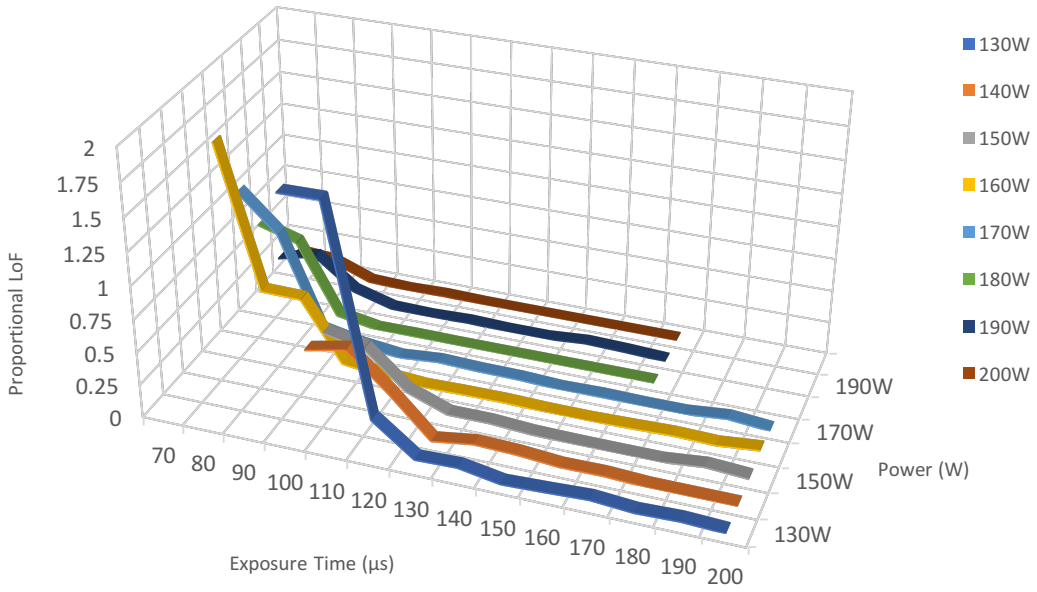

Figure 4.11- Effect of laser power and exposure time on the amount of lack of fusion defects in different samples

Fig. 4.11 shows the amount of lack of fusion defects within the samples that were discussed above. We can see that for each laser power, there is an exposure time after which the amount of lack of fusion defects would be about zero. Therefore Fig. 4.12 was constructed from the data presented in Fig. 4.11 to show the onset of formation of lack of fusion defects for each laser power along with the parameters that would cause these defects and the ones that would not.

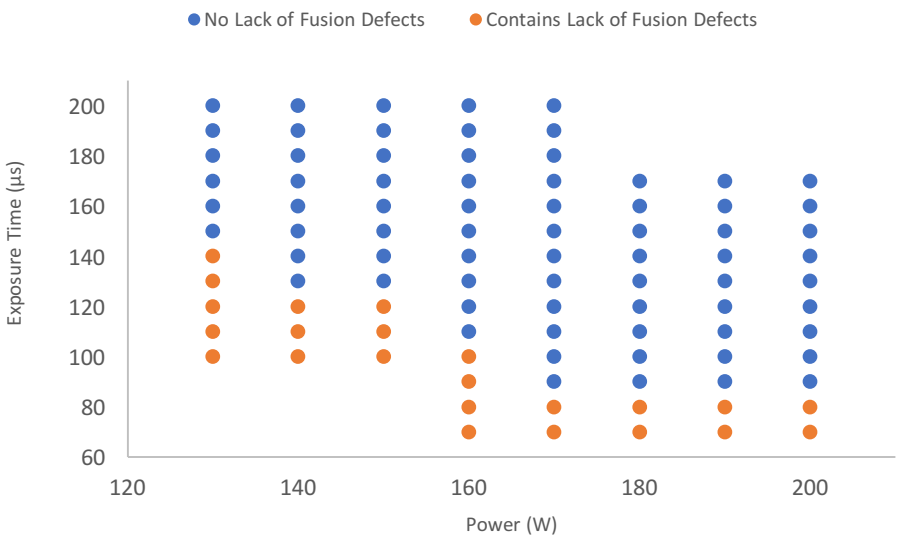

Figure 4.12- Onset of formation of lack of fusion defects at different laser power values

4.2.3. Effect of Laser Power and Exposure Time on Crystallization Behaviour

Laser power and exposure time play a significant role in determining whether the specimens that were made using the SLM process are amorphous or partially crystallized. To investigate their influence on crystallization behaviour of the SAM1561 samples, each cube was examined through XRD testing and the results are presented below in Fig. 4.13. Each graph shows the XRD patterns of the specimens manufactured using a certain laser power and different exposure times and the other processing parameters (shown in Table 4.2) were kept constant.

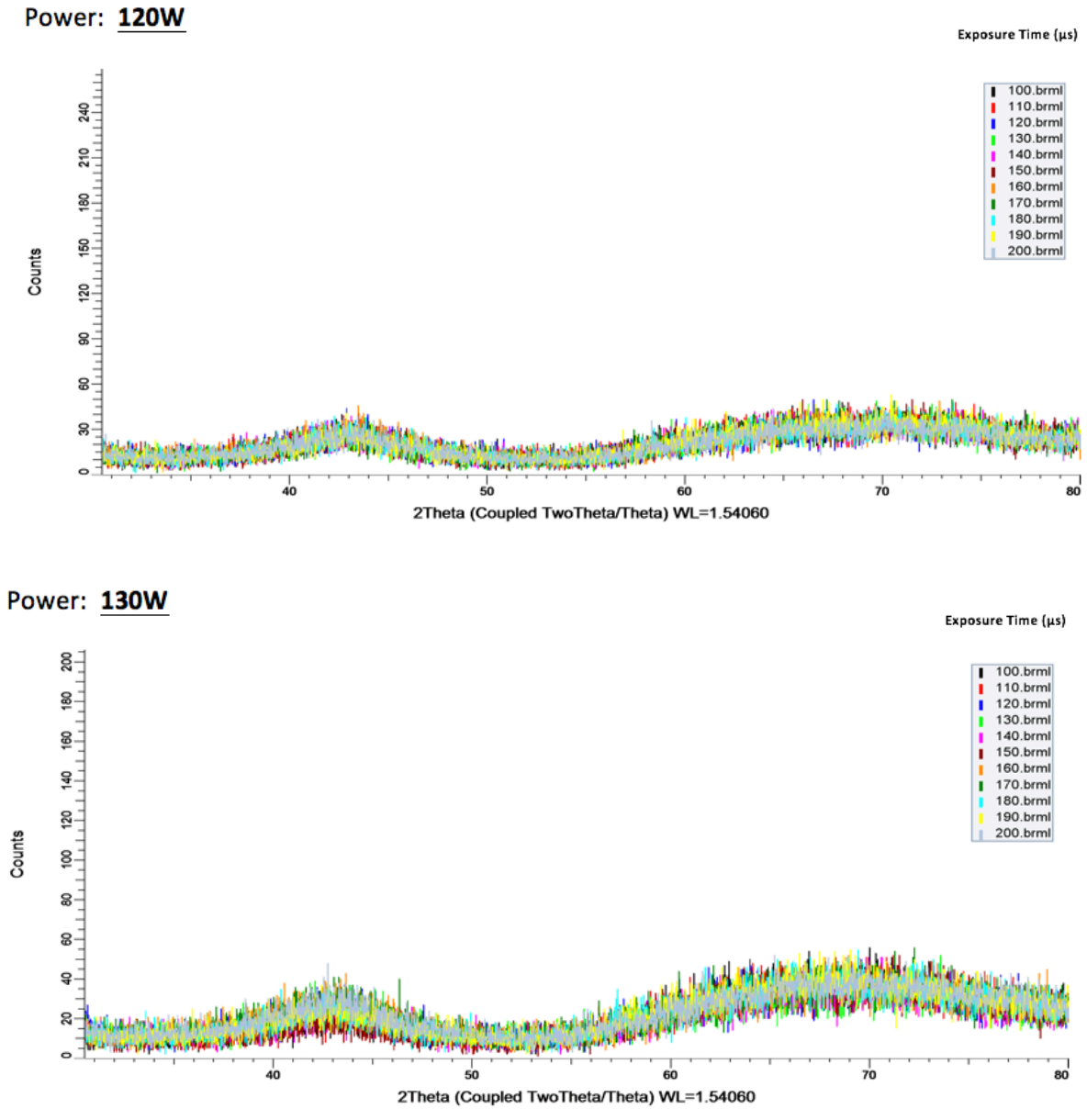

Power: **140W**

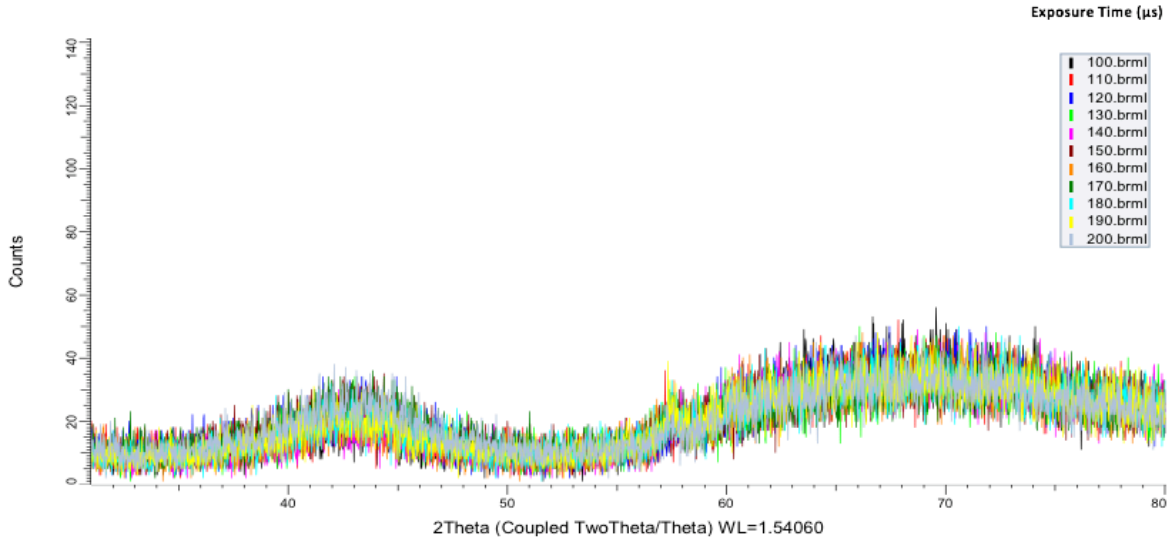

Power: **150W**

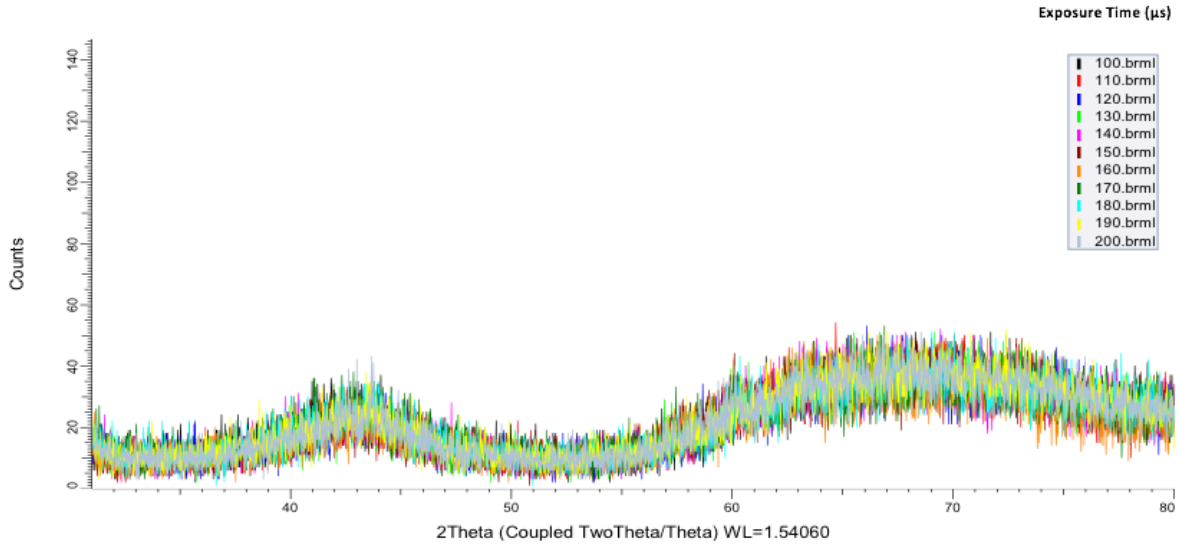

Power: **160W**

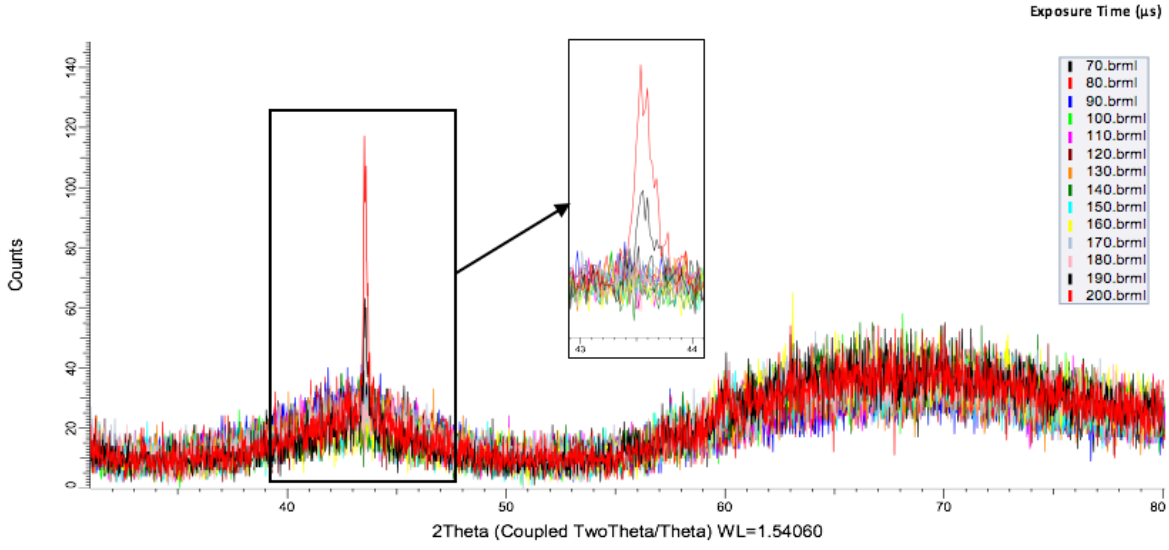

Power: **170W**

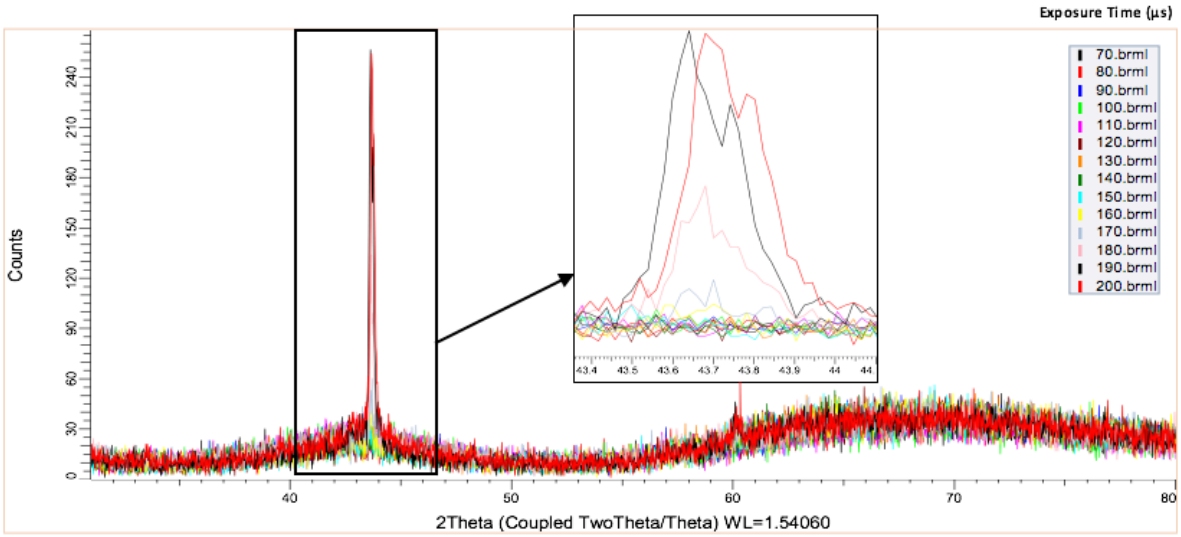

Power: **180W**

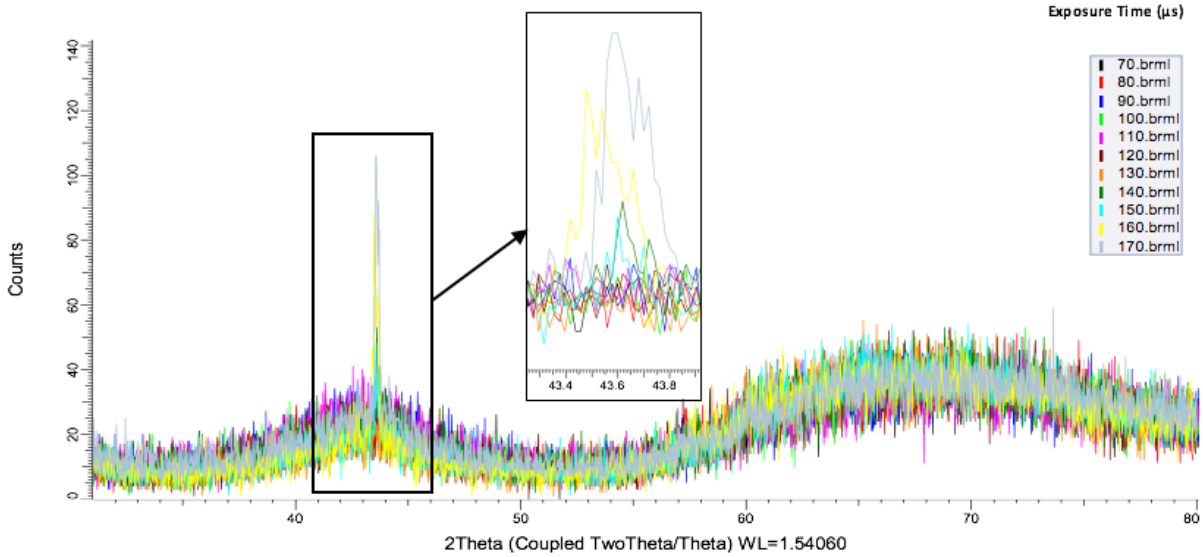

Power: **190W**

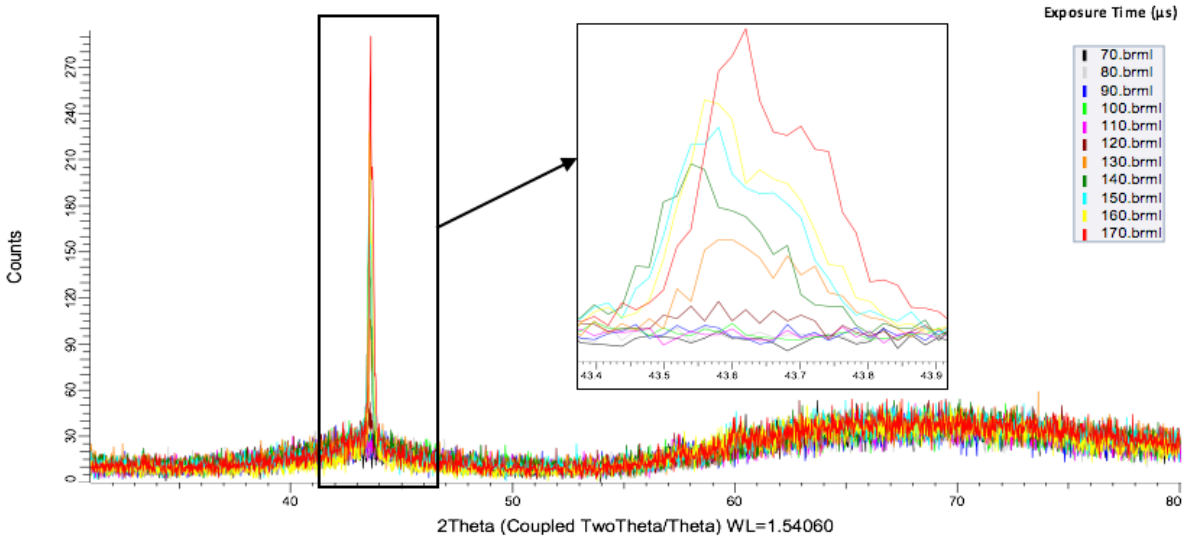

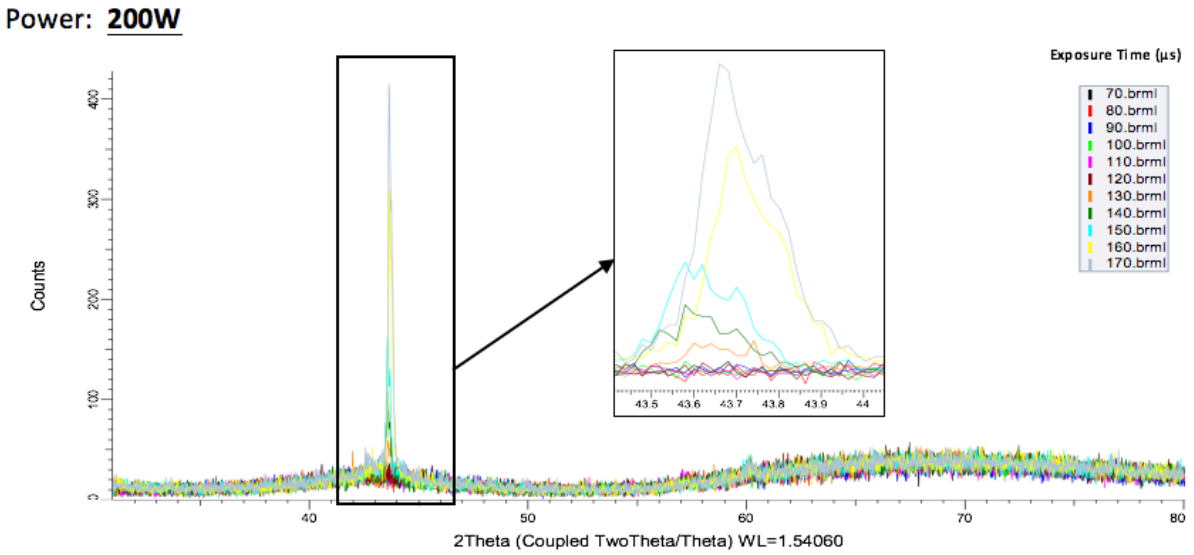

Figure 4.13- Effect of the laser power and exposure time on crystallization behaviour of SAM1651

As depicted in Fig. 4.13, when testing the cubes made from SAM1651 with X-ray diffraction, it is observed that for each laser power there is a maximum value for exposure time at which the samples would be fully amorphous. After this point, the cubes start to partially crystallize. Furthermore, this critical exposure time decreases as the laser power used increases. Also, it can be observed that the intensity of the peak representing the crystallized phase increases for a certain laser power when the exposure time used increases, which would mean the volume of the crystallized portion of the specimen has increased. In Fig. 4.14 the status of the microstructure of the specimens is shown and it depicts the onset of crystallization for each laser power and the parameter combinations that result in either fully amorphous or partially crystallized samples. Also, as it was demonstrated in section 2.6.3, numerous reports have consistently concluded that the crystallized phase appearing from the devitrification of SAM1651 is $(Cr,Fe)_{23}C_6$, for which the peaks seen at $2\theta=43°$ and $2\theta=58°$ could be assigned to. However, the peak seen at $2\theta=60°$ could not be identified. It should be noted that the focus of this study was on determining conditions at which amorphous results could be obtained and less attention was paid to the nature of the crystallization process.

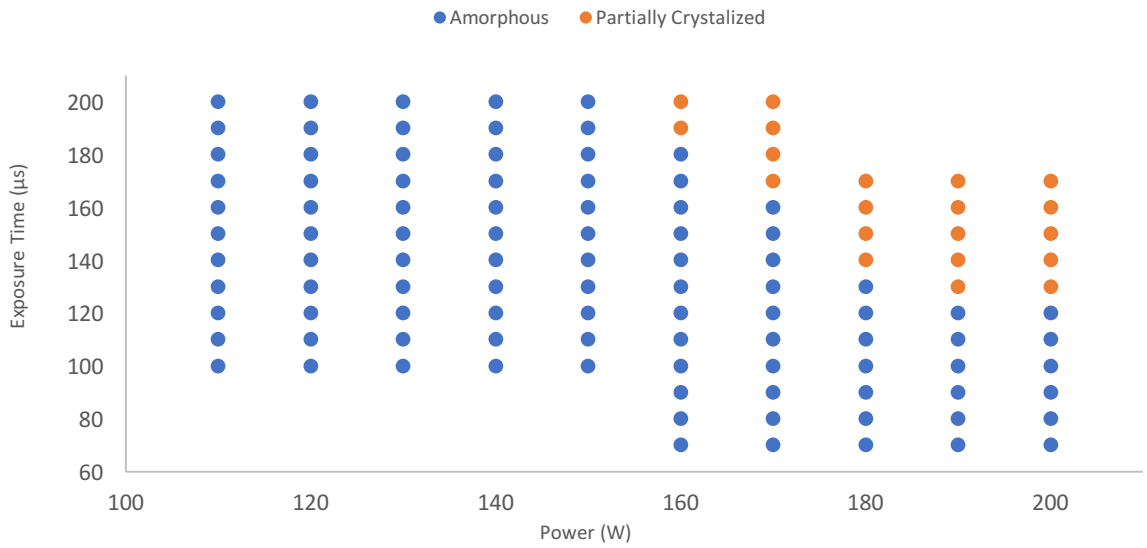

Figure 4.14- Onset of crystallization at different laser power values

4.2.4. The Effect of laser Power on Melt Pool Size

Melt pool size can also have an effect on the amorphicity of the specimens. In order to examine how the laser power and exposure time affect the individual melt pool size, finite element simulation results were used to determine the volume of the melt pool that would be the result of different power and exposure times. As shown in Fig. 4.15 when power and/or exposure time used in simulations increases, the size of the resulting melt pool increases. Processing parameters shown in Table 4.2 were kept constant for this simulation.

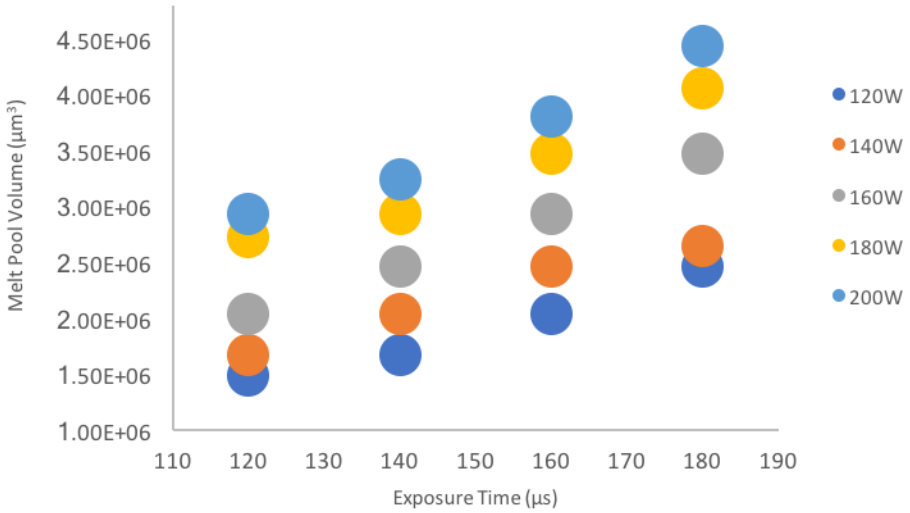

Figure 4.15- Effect of laser power and exposure time on the simulated individual melt pool size

From the data in this diagram, combined with the data presented in Fig. 4.13, we can derive the diagram shown in Fig. 4.16. It is shown that all the partially crystallized samples have a larger melt pool size of about $3.2x10^6(\mu m^3)$. The crossover seen in the graph below, is because of the fact that the parameter controlling the melt pool size is the energy density of the laser absorbed by the surface of the specimen at each melt spot which is a combination of the exposure time and laser power. This crossover can be seen in graphs pertaining to cooling rate and thermal gradient (shown in sections below) for which the same phenomenon is responsible.

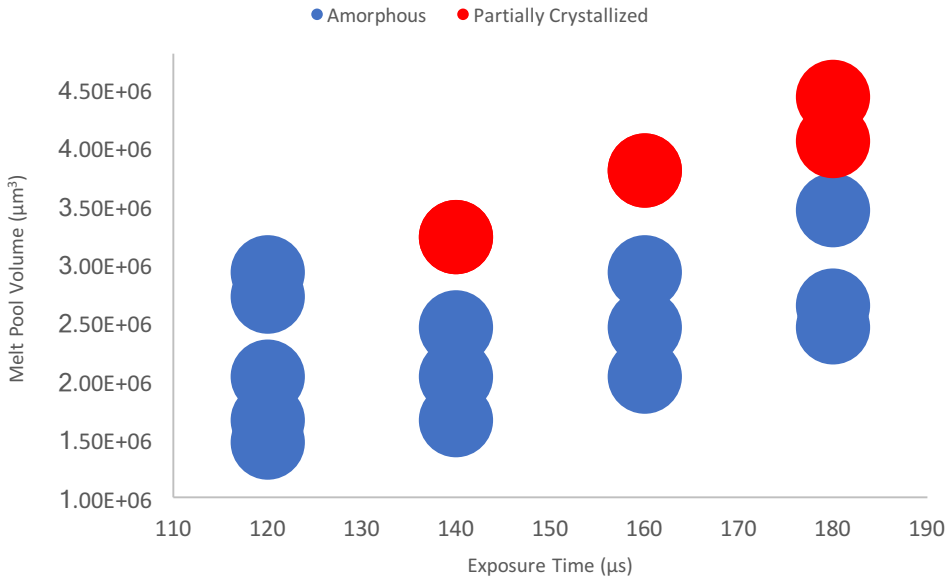

Figure 4.16- Effect of the melt pool size on amorphicity of the specimens

4.3. Effect of Thermal Gradient and Cooling Rate on the Crystallization Behaviour

4.3.1. Influence of Cooling Rate on Crystallization

The laser power and exposure time used in the SLM process have a significant effect on the thermal gradient and cooling rate experienced inside and in the vicinity of each melt pool. In order to investigate their role, other processing parameters (Table 4.2) were kept constant

and through finite element modelling, the thermal profile and thermal history of individual melt pools at specific laser powers and exposure times were obtained.

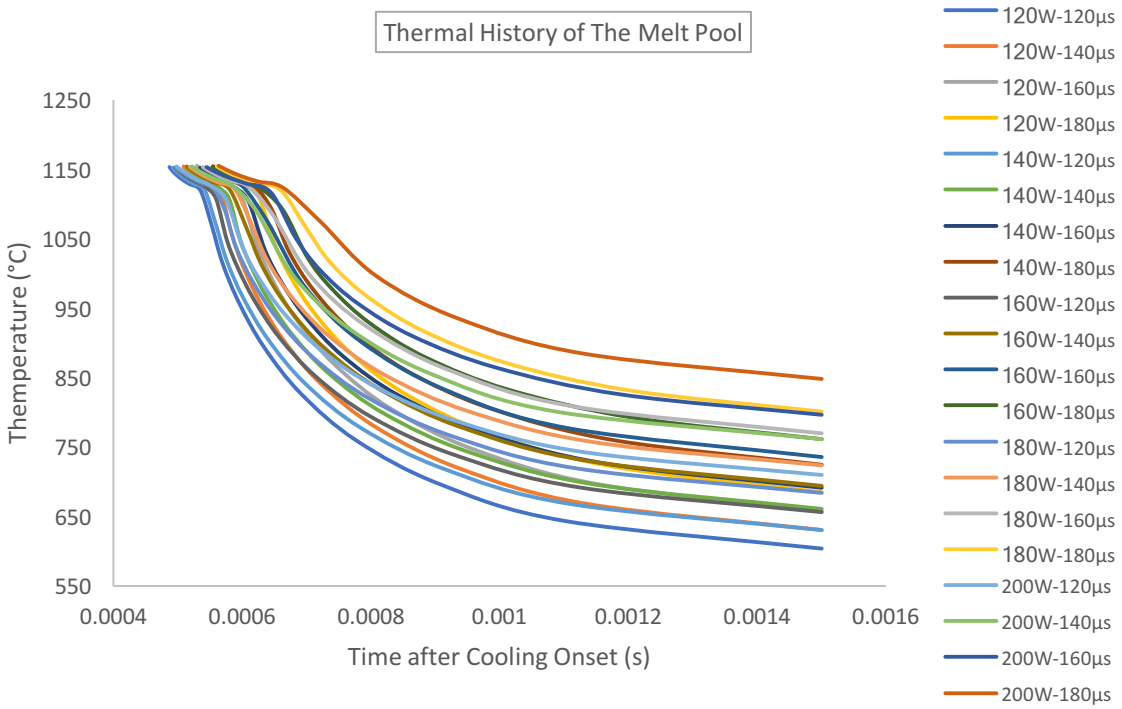

Figure 4.17- Thermal History of individual melt pools created by different laser power/exposure time combinations

The thermal history diagram depicted in Fig. 4.17, describes the temperature at the centre of a melt pool made using a specific laser power and exposure time, after the laser has turned off (moved on). From this set of data, the resulting cooling rate for each power/exposure time combination can be derived which is shown in Fig. 4.18. It can be observed that the cooling rate decreases as power and/or exposure time increases.

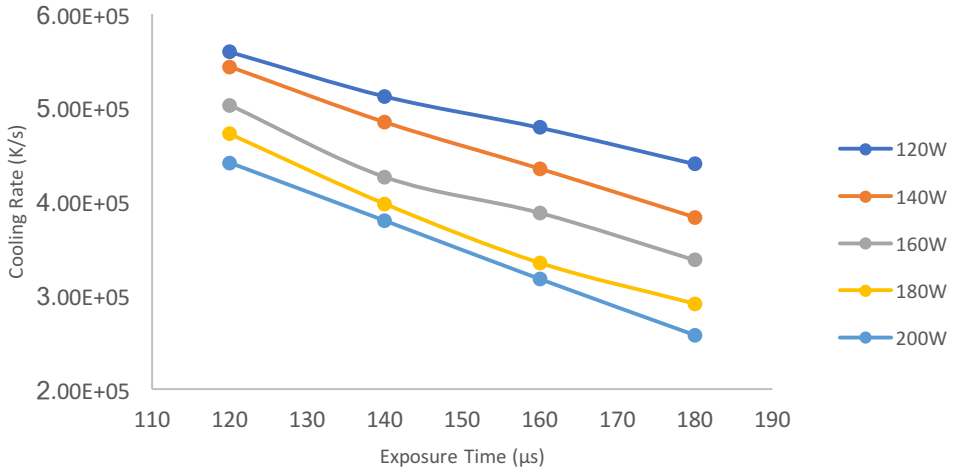

Figure 4.18- Effect of laser power and exposure time on the cooling rate of the melt pool

From the information presented in Fig. 4.18 and Fig. 4.13 (which depicts whether each set of laser power and exposure time would result in an amorphous or partially crystalline microstructure) we can assemble a diagram (shown in Fig. 4.19) that would present the correlation between the resulting cooling rate of the SLM process and the amorphicity of the specimens produced. It can be clearly observed that at lower cooling rates the possibility of the samples crystallizing is higher.

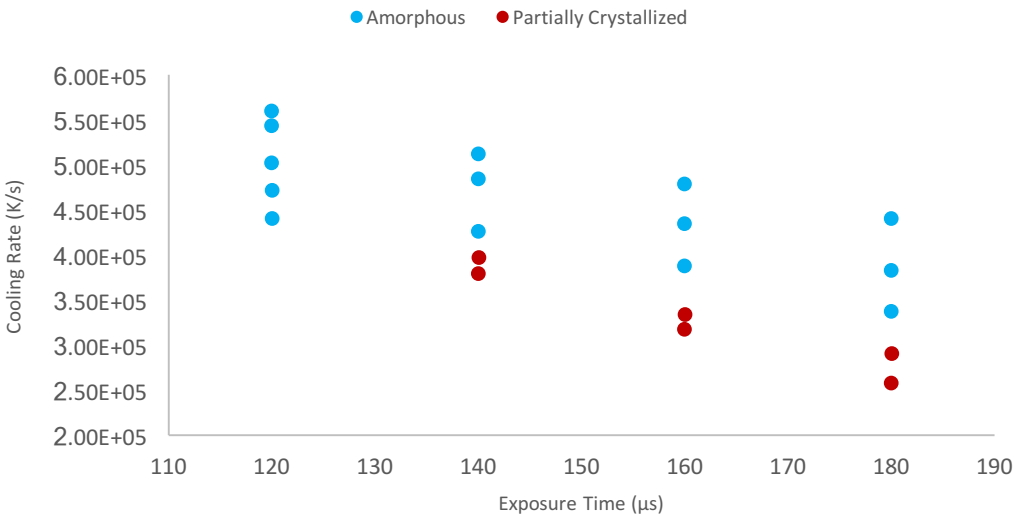

Figure 4.19- Effect of the cooling rate on amorphicity of the samples made with SLM

4.3.2. Influence of Thermal Gradient on Crystallization

Examining the thermal profile of individual melt pools, Fig. 4.20 is obtained through finite element modelling of the thermal distribution in the area around the melt pool. It describes the temperature of the material in the heat affected zone around individual melt pools that are created using specific laser powers and exposure times.

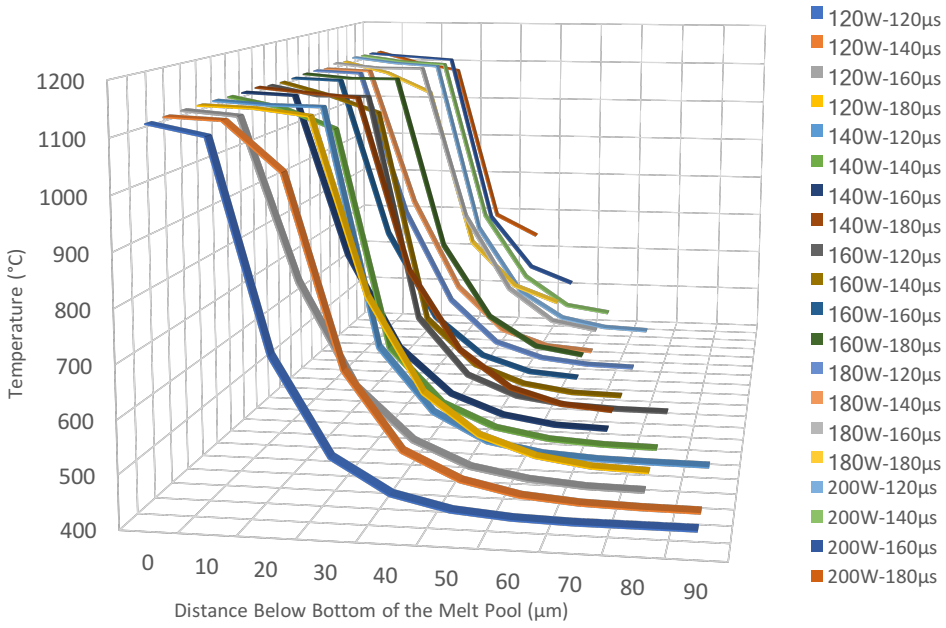

Figure 4.20 - Thermal Profile of the HAZ of melt pools created with different laser power and exposure time combinations

From the data in Fig. 4.20 the thermal gradient created in the heat affected zone can be obtained for each laser power/exposure time combination and it is shown in Fig. 4.21. When examining the patterns in this figure, three observations can be made:

a) For each laser power, as exposure time increases, a relative reduction in thermal gradient can be observed.

b) For each laser power, at smaller exposure times, thermal gradient values are almost the same and as exposure time values increase, at a specific exposure time, the thermal gradient values start to decrease dramatically in comparison.

c) The exposure time value, at which the sudden reduction in thermal gradient occurs for each laser power, shifts towards smaller values as laser power increases. The reduction does not happen at 120W, occurs at 160μs for 140W and 160W and at 140μs for 180W and 200W.

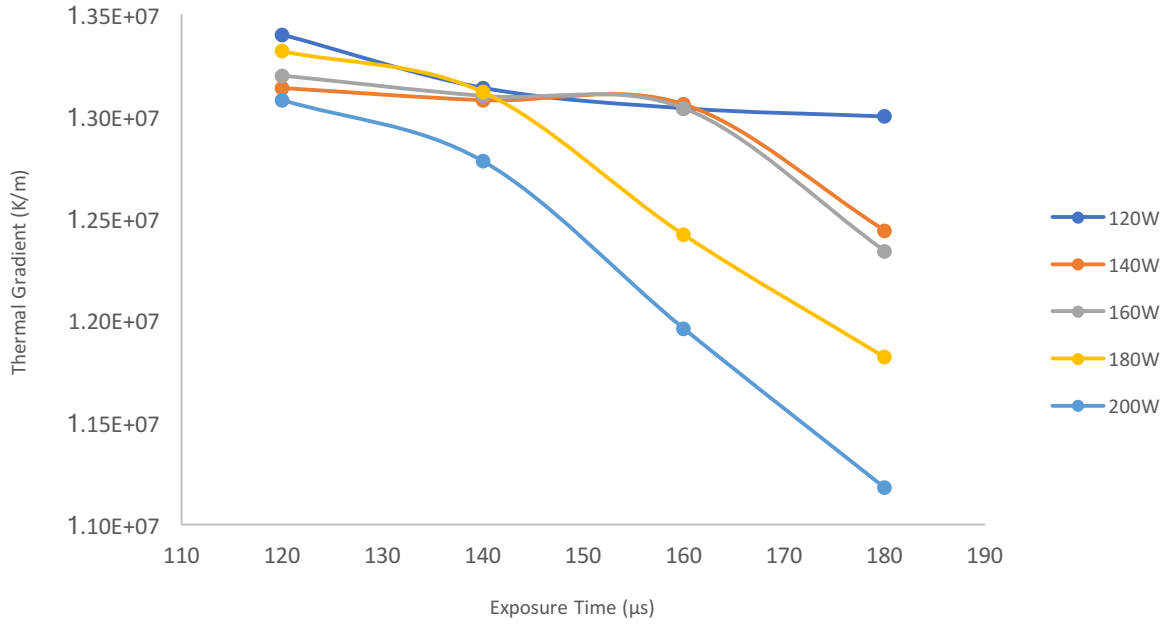

Figure 4.21- Effect of the laser power and exposure time on the thermal gradient in the HAZ area of the melt pool

In order to investigate the effect that the thermal gradient occurring during the SLM process has on the crystallization behaviour of metallic glasses, the data shown in Fig. 4.20 were utilised in conjunction with the results of the XRD tests carried out on samples built using the SLM process (Fig. 4.13). The outcome is Fig. 4.22 that demonstrates which thermal gradient would result in amorphous samples.

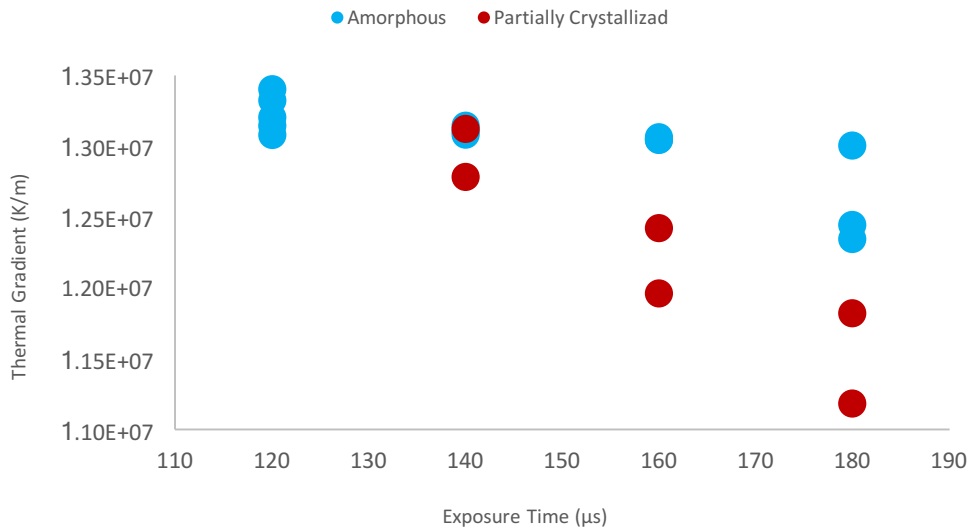

Figure 4.22- Effect of the thermal gradient on Amorphicity of the samples made with SLM

Similar to the effect that cooling rate has on the amorphicity of the samples (shown in Fig. 4.21), the diagram above presents a reverse correlation between the thermal gradient and the possibility of crystallization occurring within the samples.

4.3.3. Influence of Solidification Rate on Crystallization

Amorphicity seems to be better correlated with a combination of cooling rate and thermal gradient. Thus, Fig. 4.23 was constructed using the data in Fig. 4.19 and Fig. 4.22. As depicted, samples built with lower cooling rate and thermal gradient seem to have partially crystallized and higher values of these parameters has resulted in an amorphous microstructure.

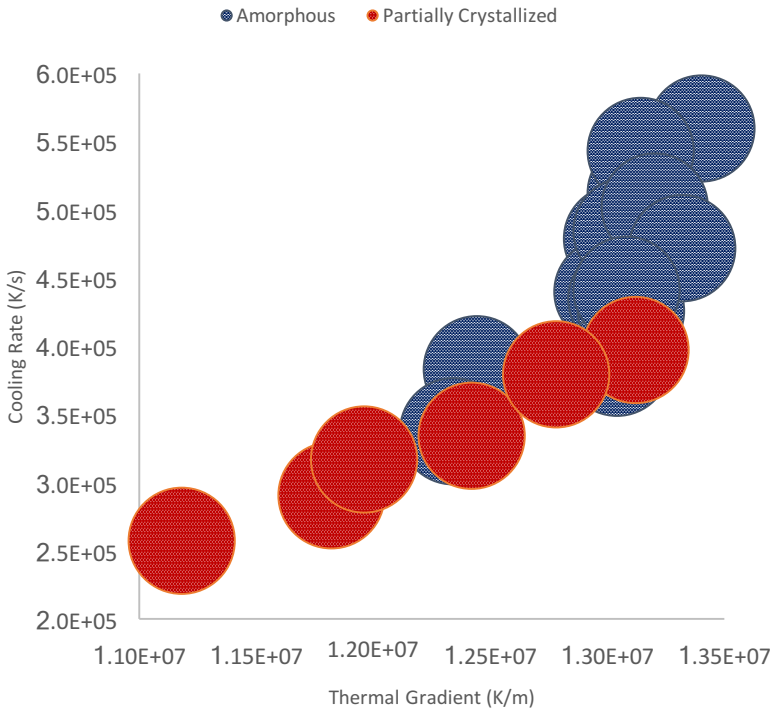

Figure 4.23- Effect of cooling rate and thermal gradient on amorphicity of the specimens

As depicted in Fig. 4.23, samples built with SLM, turn out partially crystallized when thermal gradient and cooling rate are both low and as they increase, the possibility of the microstructure being amorphous increases. Specifically, for SAM1651, when cooling rate is lower than about $1.25x10^{7}$K/s and thermal gradient is smaller than about $6.5x10^{5}$K/m for an individual melt pool (considering the other processing parameters are kept the same) samples become partially crystallized.

It can also be observed that the slope of the curve significantly changes when the microstructure of the specimens alters from amorphous at high cooling rate and thermal gradient to partially crystallized at low cooling rate and thermal gradient. The slope in this diagram represents the solidification rate ($R=\dot{T}/G$) and it depicts that the samples that experienced high solidification rate within the selective laser melting process turned out amorphous and the cubes that underwent a low solidification rate were partially crystallized.

4.4. Effect of Substrate Temperature on Thermal Gradient and Cracking

It has been reported that the main factor affecting the amount of stress accumulated inside the specimens manufactured by the selective laser melting process and hence the resulting cracking is the thermal gradient that is experienced in the heat affected zone in the vicinity of each individual melt pool. Furthermore, experiments have shown that one of the most successful ways of decreasing this thermal gradient and the subsequent cracking is by increasing the bed/substrate temperature in the SLM process.

Point Distance	Hatch Spacing	Layer Thickness
50 µm	100 µm	50 µm

Table 4.3- Processing parameters that were kept constant for this experiment

So, in order to investigate the effect of bed temperature on sample cracking, several cubes were built using various laser power/exposure time/bed temperature combinations while keeping other processing parameters (shown in Table 4.3) constant. Fig. 4.24 shows the amount of cracking (obtained through optical microscopy) within each of these samples at 298K, 423K, 573K and 723K.

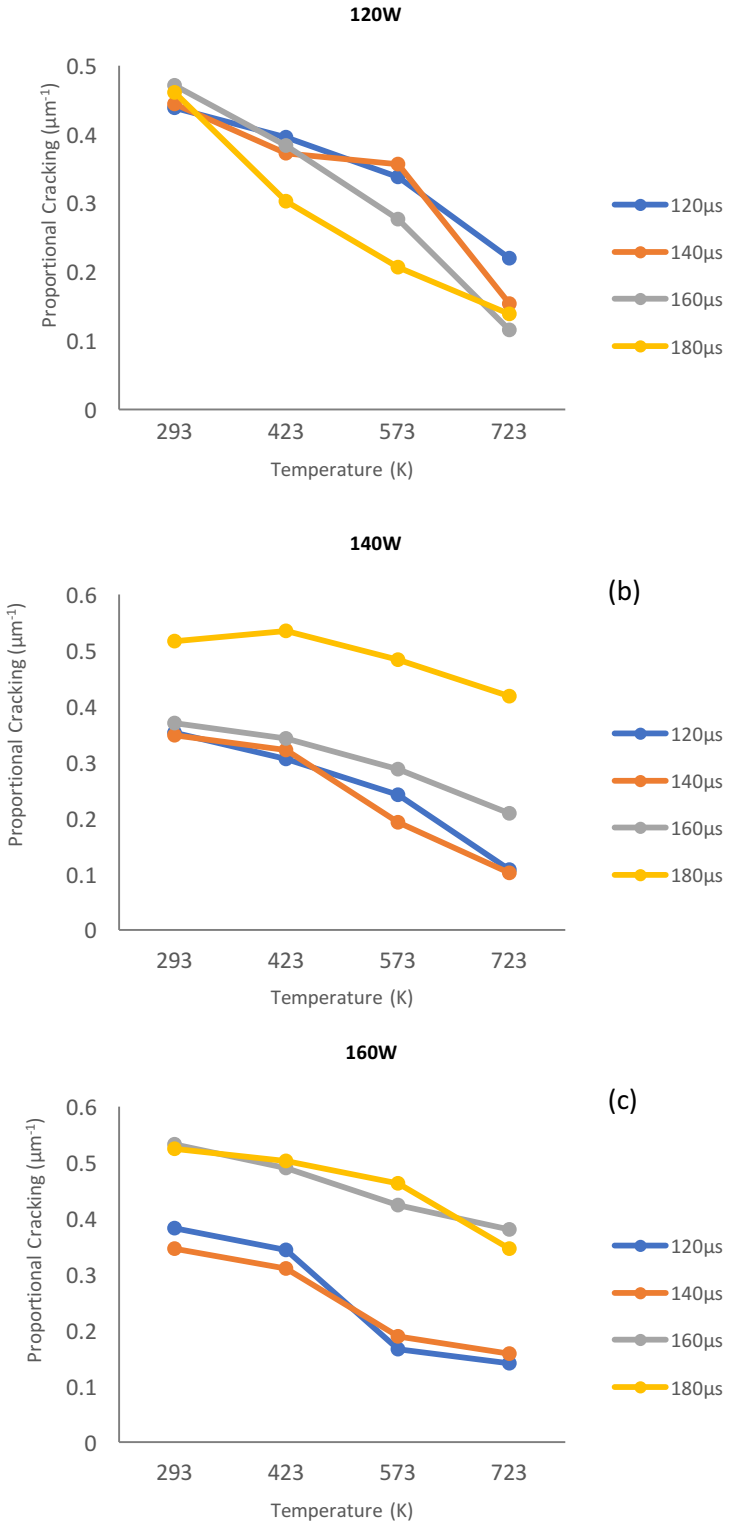

Figure 4.24- Effect of bed temperature on the amount of cracking inside samples built with laser power of 120W (a), 140W (b) and 160W (c)

It is clear from the patterns in Fig. 4.24 that as the bed temperature increases, the amount of cracking in the samples decreases. In order to test the above-mentioned hypothesis for metallic glasses, thermal profiles of heat affected zones around individual melt pools created by using different laser power/exposure time combinations of 120W-120µs, 140W-140µs and 160W-160µs were obtained through finite element modelling (presented in Fig. 4.25).

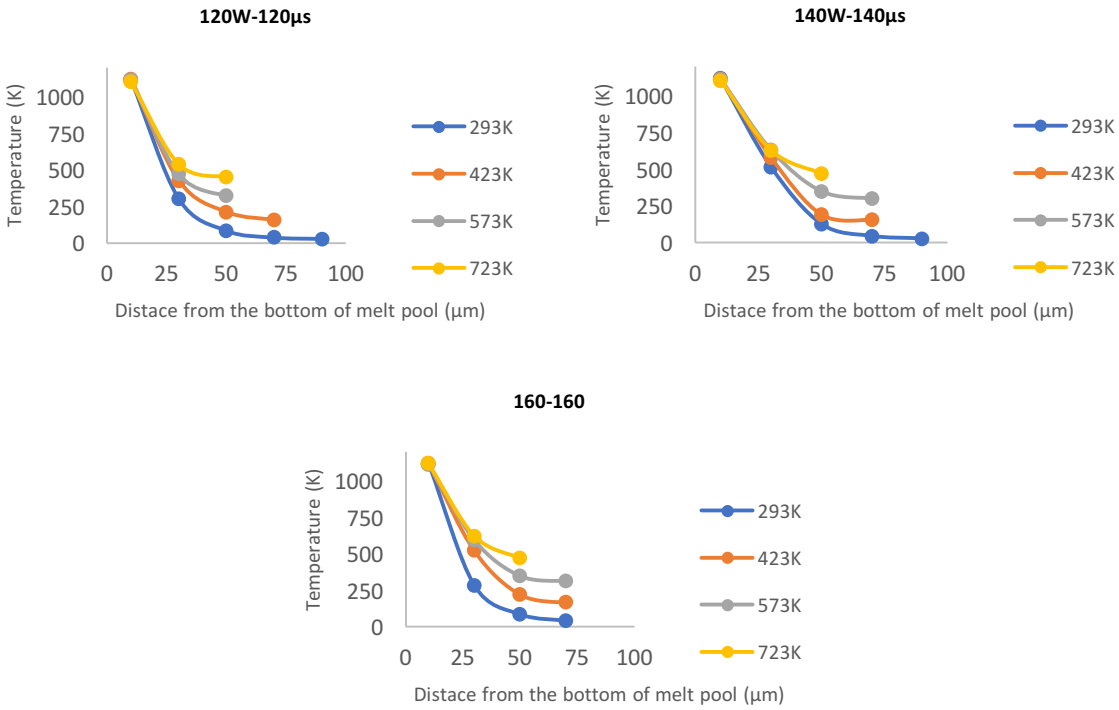

Figure 4.25- Effect of the bed temperature on the thermal profile of the HAZ area of individual melt pools created with 120W-120µs (a), 140W-140µs (b) and 160W-160µs (c)

Since the thermal gradient, that is responsible for the induced stress, occurs in the HAZ area, it is calculated by considering the temperature difference of the material right next to the liquid/solid boundary of the melt pool and the material further away in the HAZ area. From the data set in Fig. 4.25, the thermal gradient occurring inside the HAZ area of melt pools created by these parameters can be obtained and is shown in Fig. 4.26. It can be observed that for all the different parameter combinations, as the bed temperature increases, the resulting thermal gradient decreases.

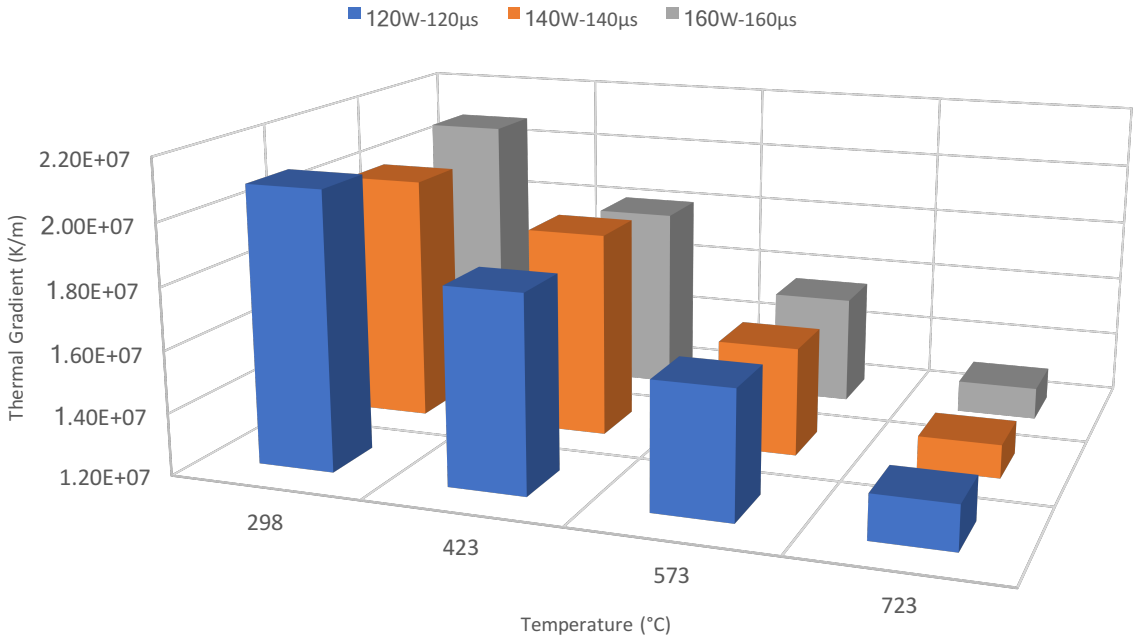

Figure 4.26- Effect of bed temperature on thermal gradient inside the HAZ area of melt pools created using different laser power/exposure time combinations

Utilizing the data set presented in Fig. 4.24 regarding the amount of cracking for each laser power/exposure time/bed temperature combination and the resulting thermal gradient from each combination (taken from the data presented in Fig. 4.26), Fig. 4.27 was constructed. This diagram clearly shows that as thermal gradient occurring in the HAZ area of the individual melt pools increases, cracking of the specimens increases as well.

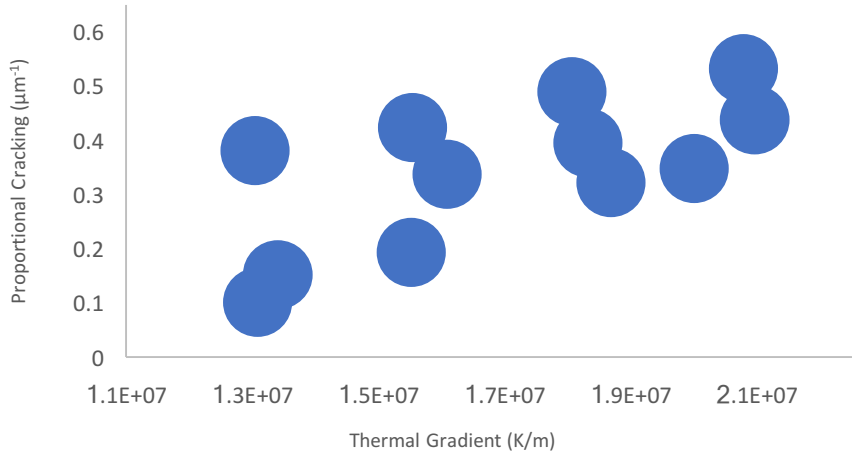

Figure 4.27- Effect of thermal gradient on the amount of cracking inside different samples

4.5. Influence of Layer Thickness

4.5.1. The Effect of Layer Thickness on Cracking

The influence of layer thickness on the behaviour of cracking inside the microstructure of the specimens made from SAM1651 with selective laser melting was investigated in terms of the proportional cracking. The samples were manufactured using different laser power, exposure time and layer thickness values and after their microstructure was analysed through optical microscopy, the results were plotted in Fig. 4.28. It can be observed that for each set of laser power and exposure time, as the layer thickness used was increased the amount of proportional cracking inside the specimens was reduced as a result.

Point Distance	Hatch Spacing	Bed Temperature
50 µm	100 µm	723 K

Table 4.4- The parameters that were kept constant during manufacturing specimens for investigating the role of layer thickness on cracking.

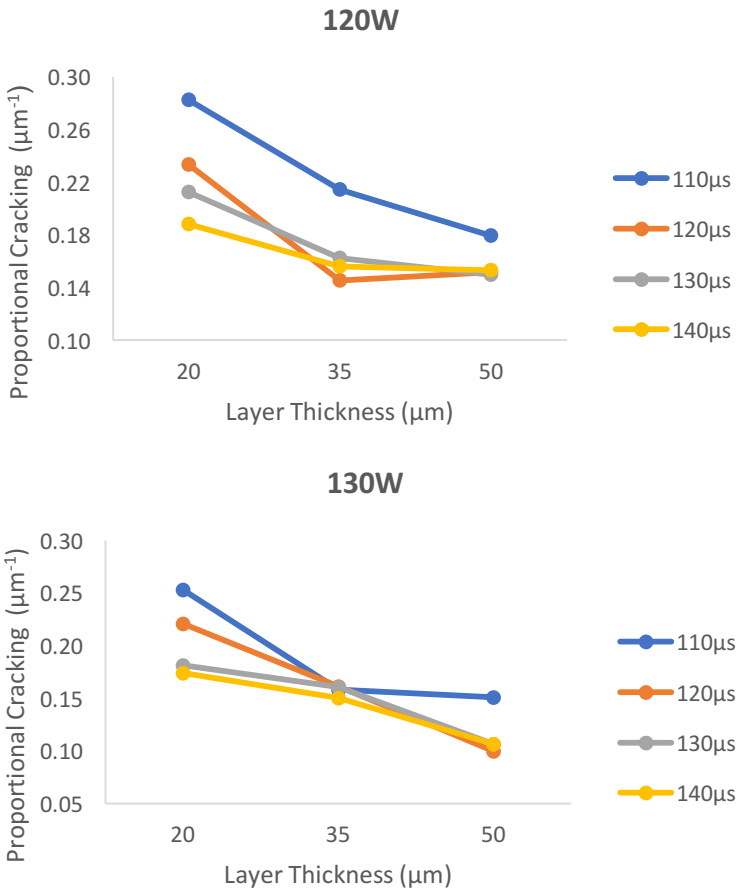

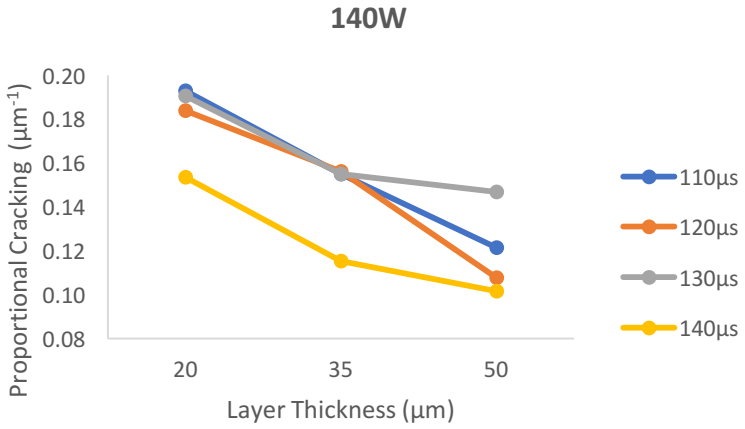

Figure 4.28- The influence of layer thickness on Cracking

4.5.2. The Effect of Layer Thickness on the Formation of Lack of Fusion Defects

The proportional lack of fusion was used to demonstrate the relationship between layer thickness and the formation of lack of fusion defects. The results from analysis of optical micrographs of the specimens manufactured using different laser power, exposure time and layer thickness values are presented in Fig. 4.29. It can be seen that for a certain laser power and exposure time, as the layer thickness value used decreases the amount of lack of fusion defects formed inside the microstructure of the samples decreased and for larger energy density input values, these defects could be almost entirely eliminated.

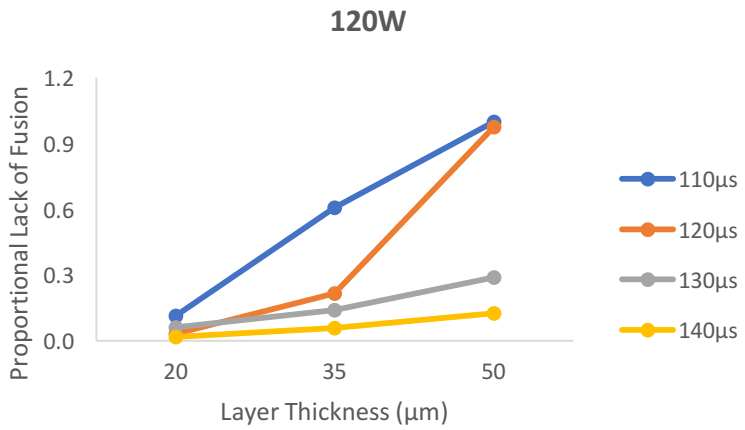

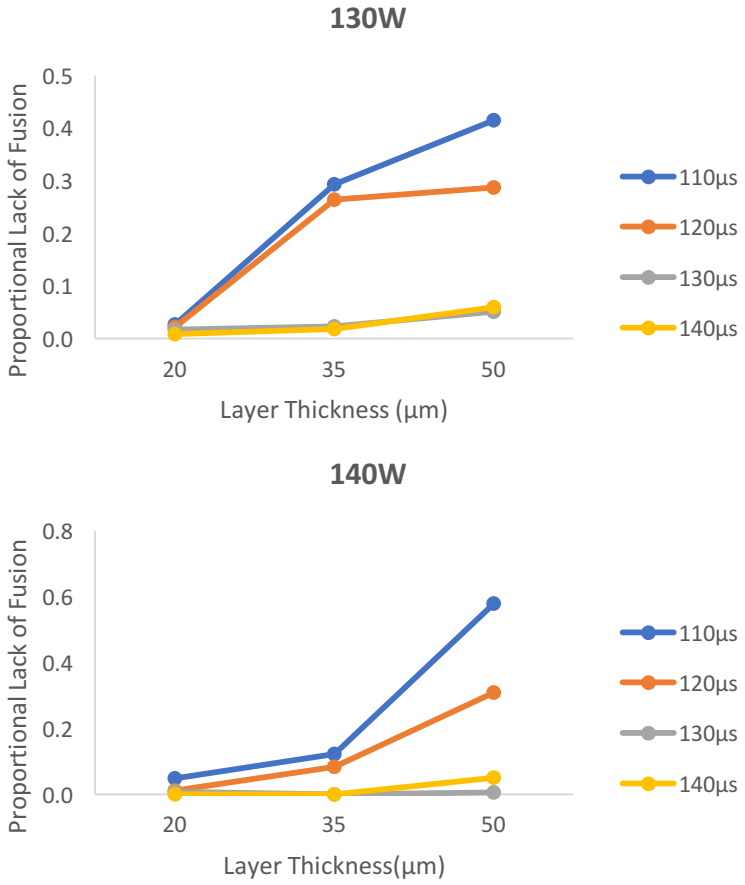

Figure 2.29- The influence of layer thickness on the formation of lack of fusion defects

4.6. Influence of Hatch Spacing

4.6.1. The Effect of Hatch Spacing on Cracking

Three different values for hatch spacing were used to build specimens utilizing several laser power and exposure times while keeping other processing parameters constant. The resulting cracks within the samples were quantified and plotted in Fig. 4.30 which shows that for each set of laser power and exposure time, as the hatch spacing increases, the amount of cracks formed inside the microstructure of the specimens decreases consequently.

Point Distance	Layer Thickness	Bed Temperature
50 µm	50 µm	723 K

Table 4.5- The parameters that were kept constant during manufacturing specimens for investigating the role of hatch spacing on cracking

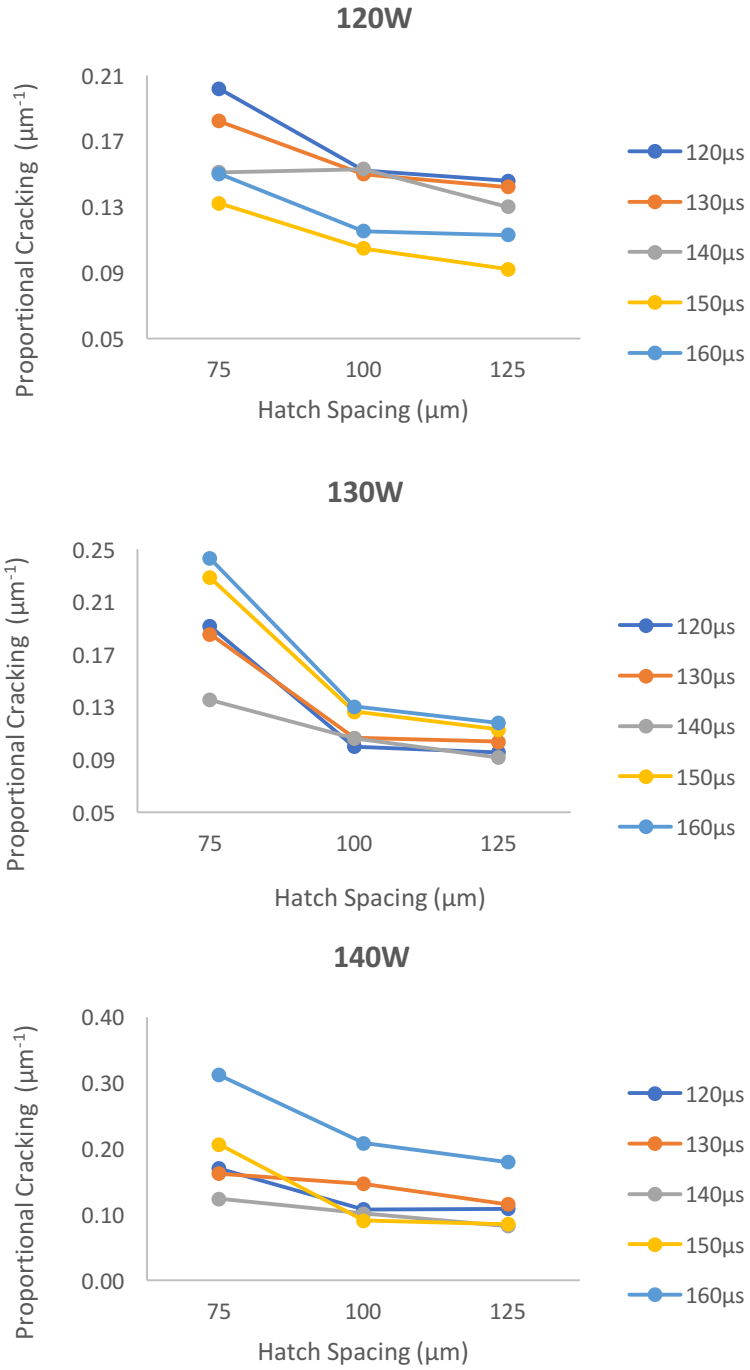

Figure 4.30- The influence of hatch spacing on cracking

4.6.2. The Effect of Hatch Spacing on the Formation of Lack of Fusion Defects

As demonstrated in Fig. 4.31 the specimens that were manufactured using similar laser power and exposure time values seem to have less lack of fusion defects in their microstructure

when the hatch spacing used to build them was smaller. This trend continues until the hatch spacing was small enough to avoid creation of any of these defects.

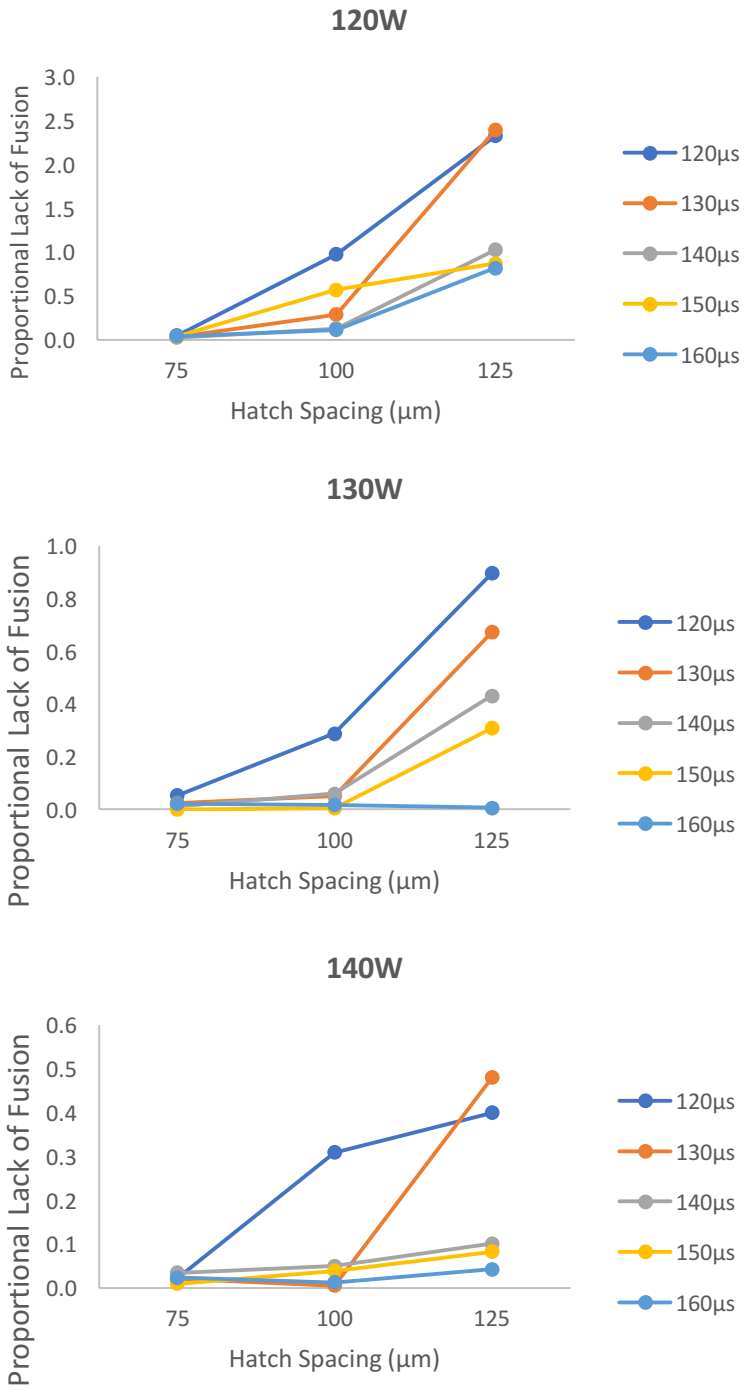

Figure 4.31- The effect of hatch spacing on the formation of lack of fusion defects

4.6.3. The Effect of Hatch Spacing on Amorphicity

Some of the specimens shown in Fig. 4.32 that were manufactured using the smallest hatch spacing of 75µm and a larger laser power and exposure time seem to have partial crystallization in their microstructure. However, the samples built with larger hatch spacing values were completely amorphous in their microstructure as shown in their XRD graphs in Fig. 4.33.

Figure 4.32- Amorphicity of the specimens built using hatch spacing of 75µm and different laser power and exposure time

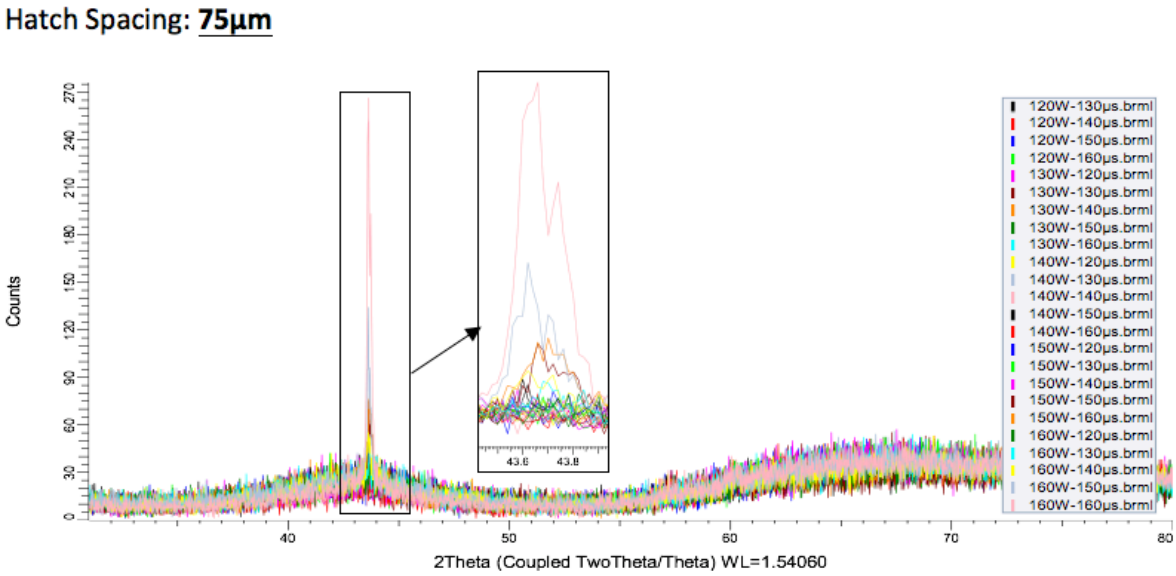

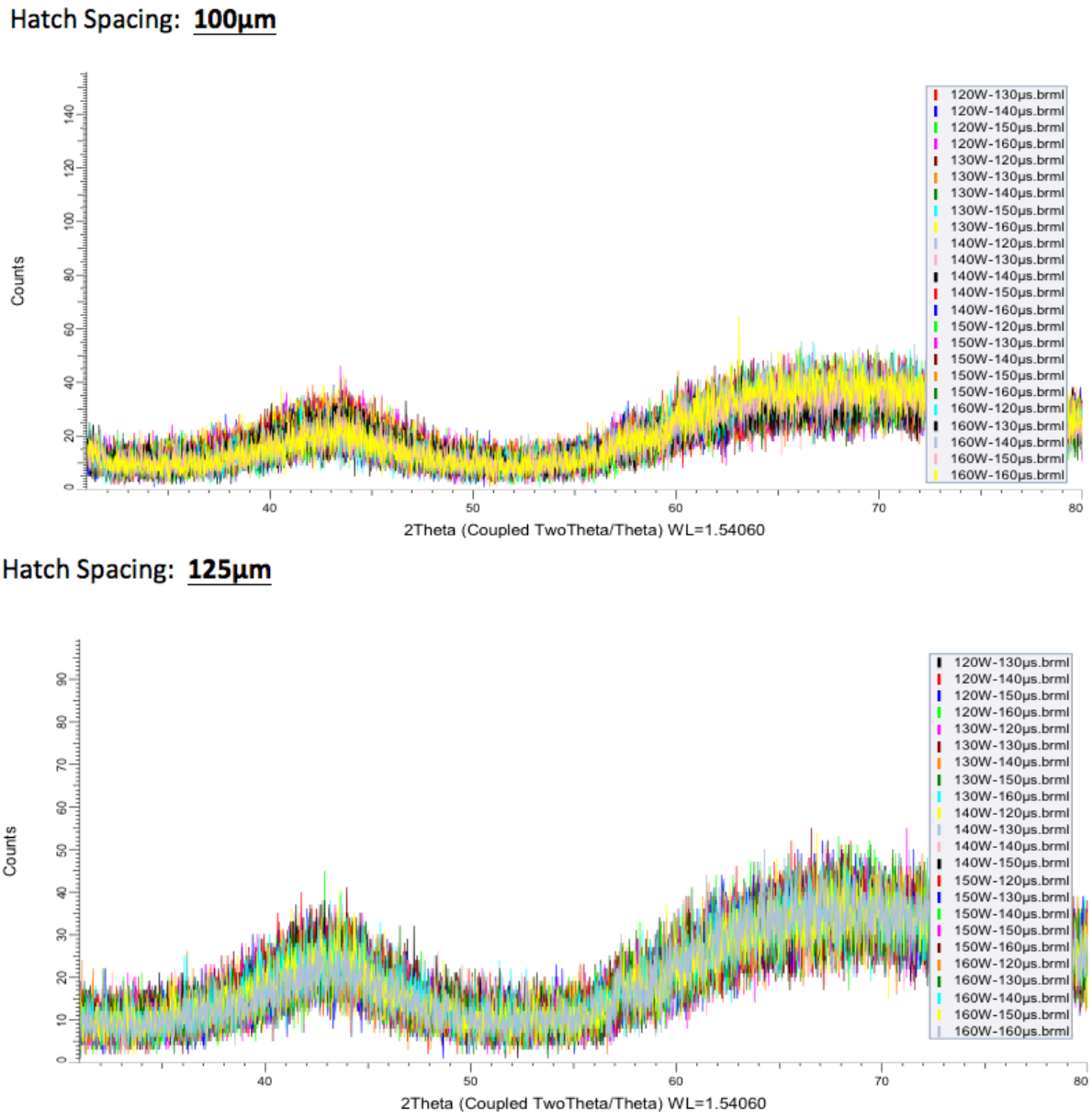

Figure 4.33- XRD patterns of the samples manufactured using different laser power, exposure time and hatch spacing values

4.7. Influence of Point Distance

4.7.1. The Effect of Point Distance on Cracking

The influence of point distance on the formation of cracks inside the specimens manufactured using different laser power, exposure time and point distance values were investigated. Fig. 4.34 shows that for each laser power and exposure time, when the point distance is the smallest, the cracking is at its highest. However as point distance used increases, cracking

decreases to a minimum and does not change significantly as it goes from 50µm to 75µm. This means that at 50µm a threshold is experienced in terms of the effect of point distance on cracking after which other factors like laser power and exposure time are controlling the amount of cracking found inside the specimens.

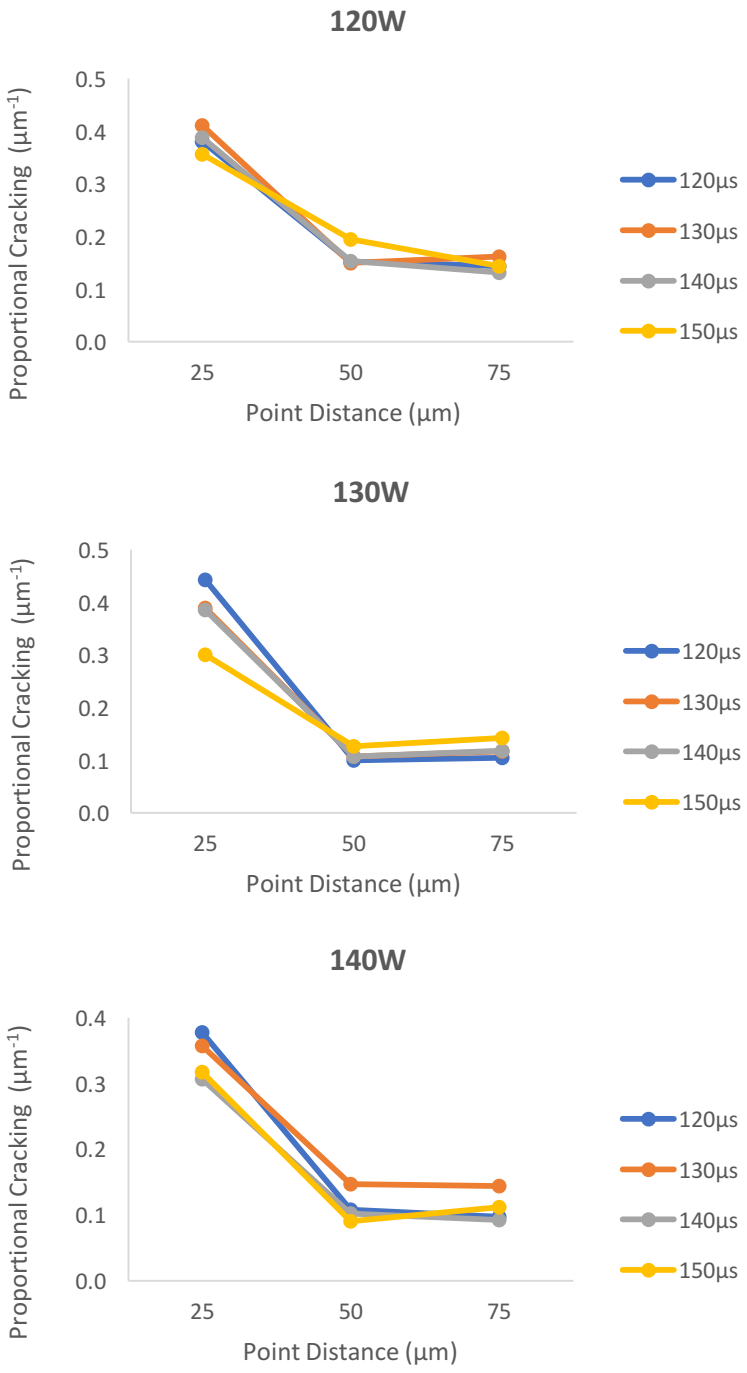

Figure 4.33- The influence of point distance on the formation of cracking

4.7.2. The Effect of Point Distance on the Formation of Lack of Fusion Defects

Similar to layer thickness and hatch spacing, point distance has an obvious influence on the lack of fusion defects. As depicted in Fig.4.34 for samples manufactured using the same laser power and exposure time, the samples made utilizing greater point distance, exhibit a larger amount of lack of fusion defects in their microstructure.

Hatch Spacing	Layer Thickness	Bed Temperature
100 µm	50 µm	723 K

Table 4.6- The parameters that were kept constant during manufacturing specimens for investigating the role of point distance on cracking.

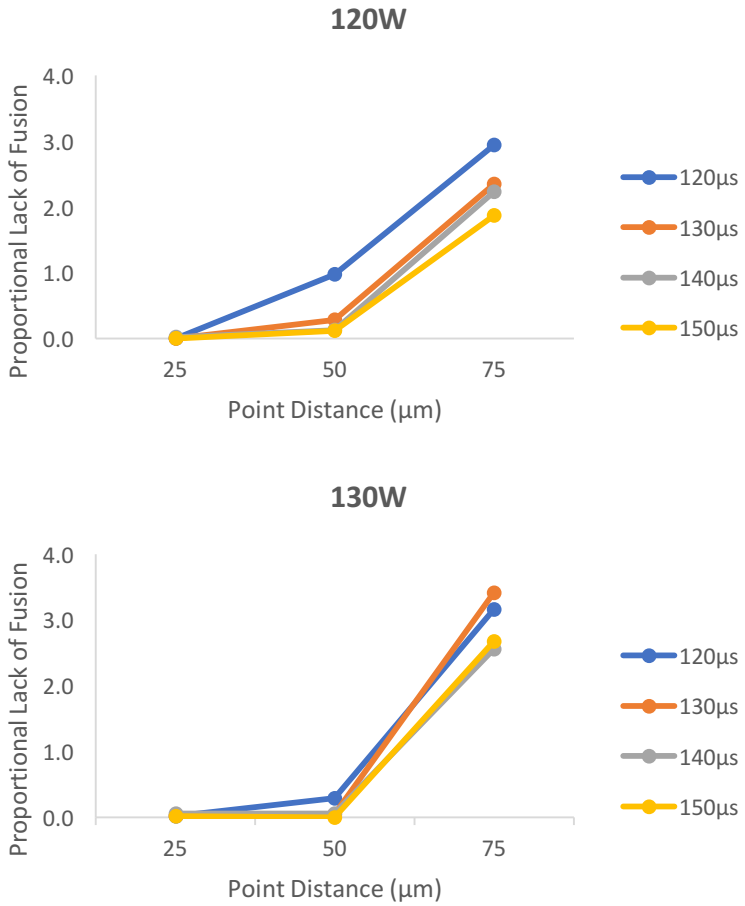

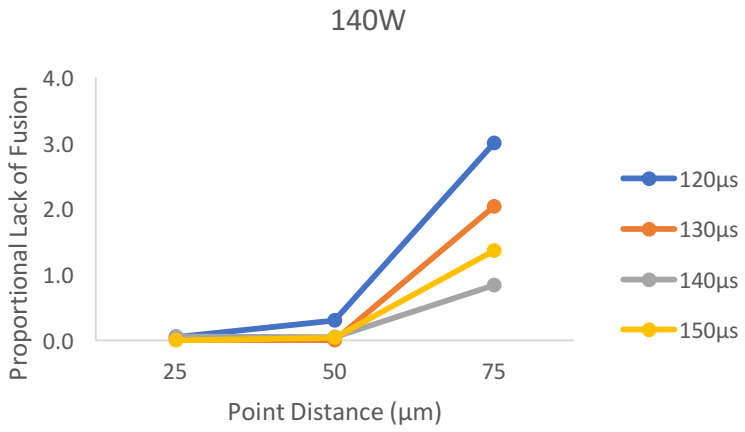

Figure 4.34- The influence of point distance on the formation of lack of fusion defects

4.7.3. The Effect of Point distance on Amorphicity

Point distance seems to have a similar but more significant effect on the amorphicity of the samples than hatch spacing. As shown in Fig. 4.35, the only samples that showed any sign of partial crystallization in their microstructure are the ones manufactured using the smallest point distance of 25µm (depicted in Fig. 4.36). Others seem to have remained fully amorphous according to their XRD patterns.

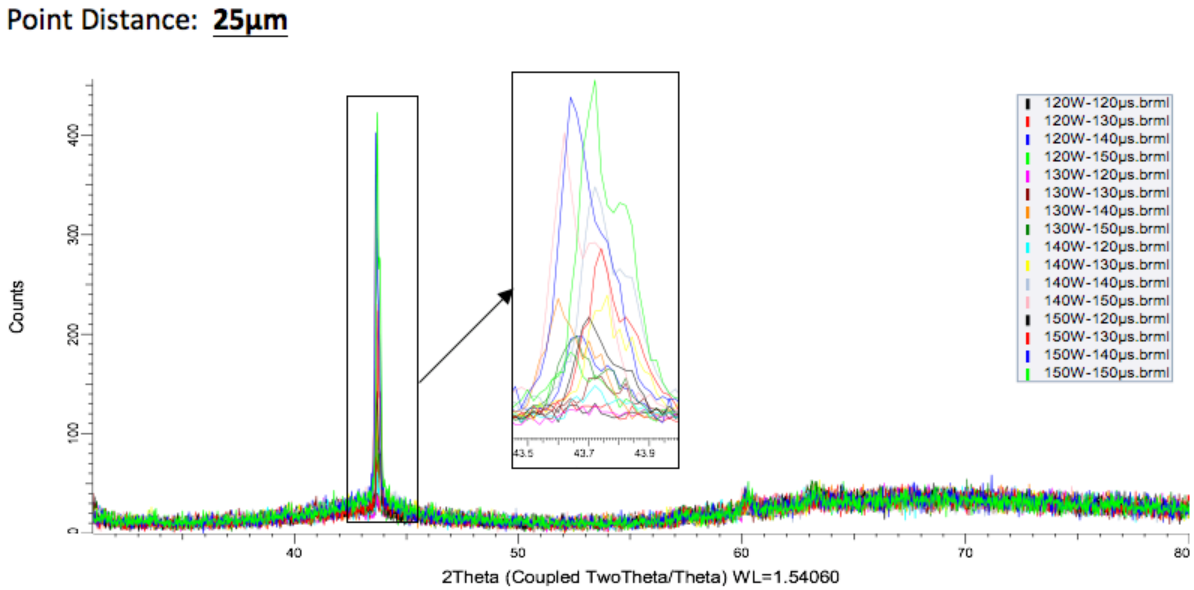

Point Distance: **50µm**

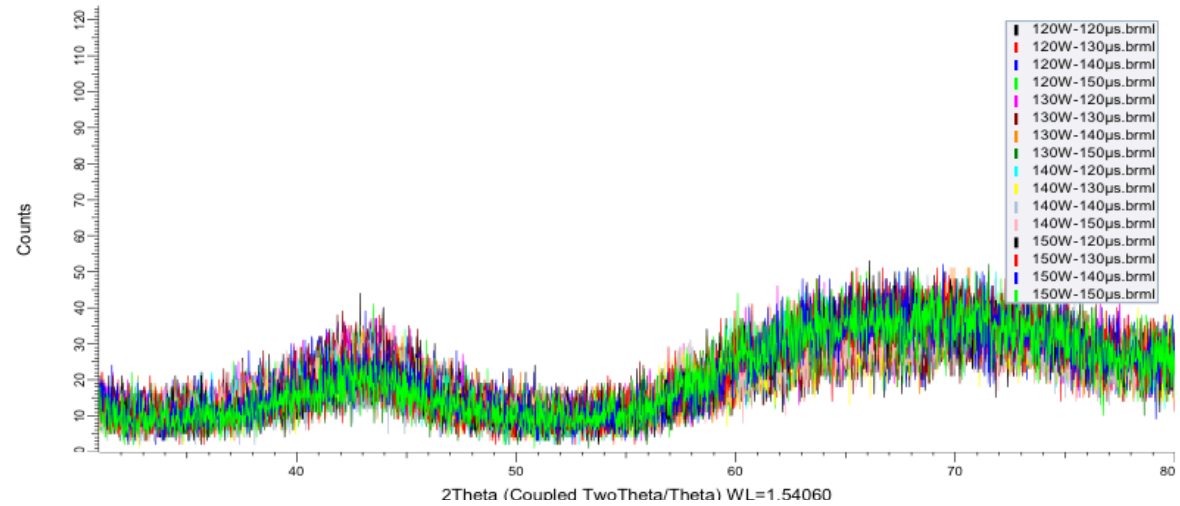

Point Distance: **75µm**

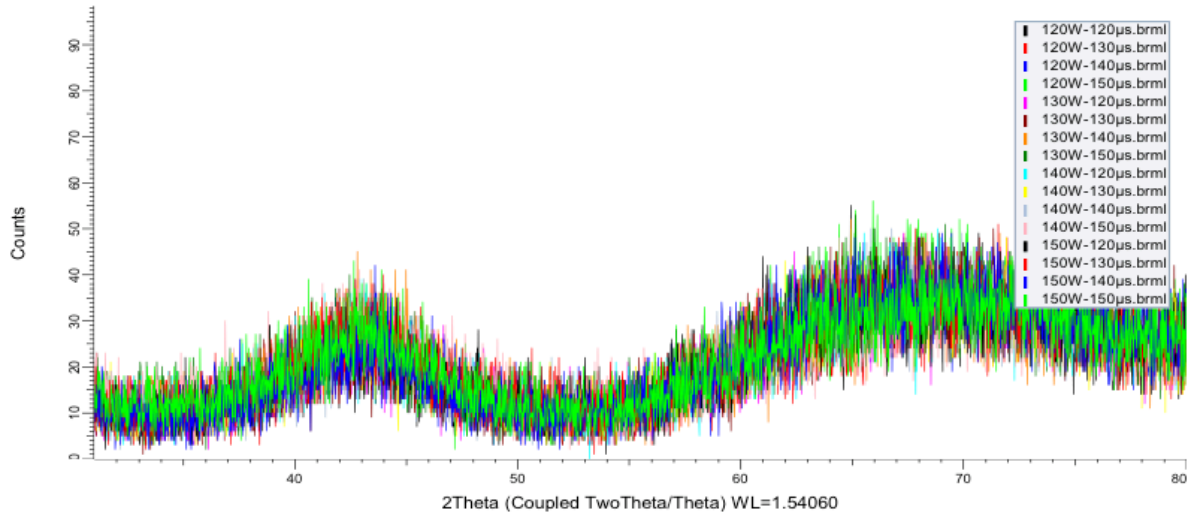

Figure 4.35- XRD patterns of the samples manufactured using different laser power, exposure time and point distance values

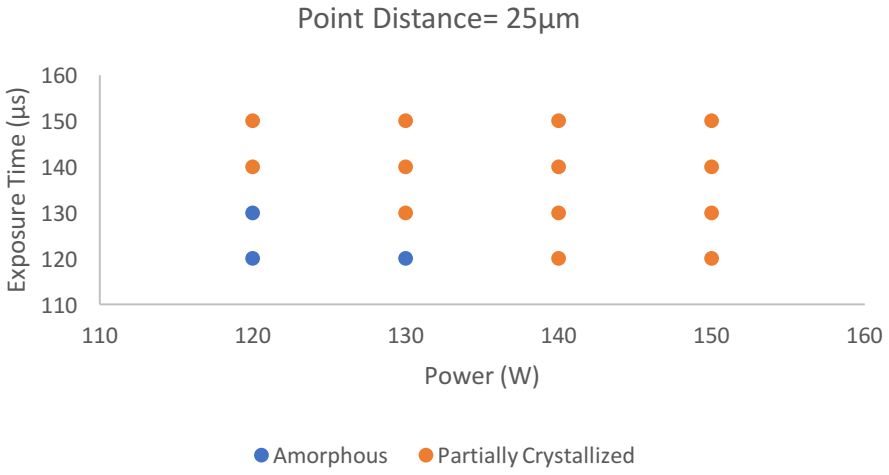

Figure 4.36- Amorphicity of the specimens built using point distance of 25µm and different laser power and exposure time

4.8. Fabrication of Complex Shapes

Using the parameters in the processing window for selective laser melting of SAM1651 powder, established in section 5.5, samples with complex shapes were manufactured to demonstrate the feasibility of their fabrication with amorphous microstructure and minimal defect formation. The exact parameters used are presented in Table 4.7. Images of these specimens are shown in Fig. 4.37.

Hatch Spacing	Layer Thickness	Point Distance	Laser Power	Exposure Time	Bed Temperature
100 µm	50 µm	50 µm	130 W	150 µs	723 K

Table 4.7 The parameters that were used during manufacturing of complex specimens

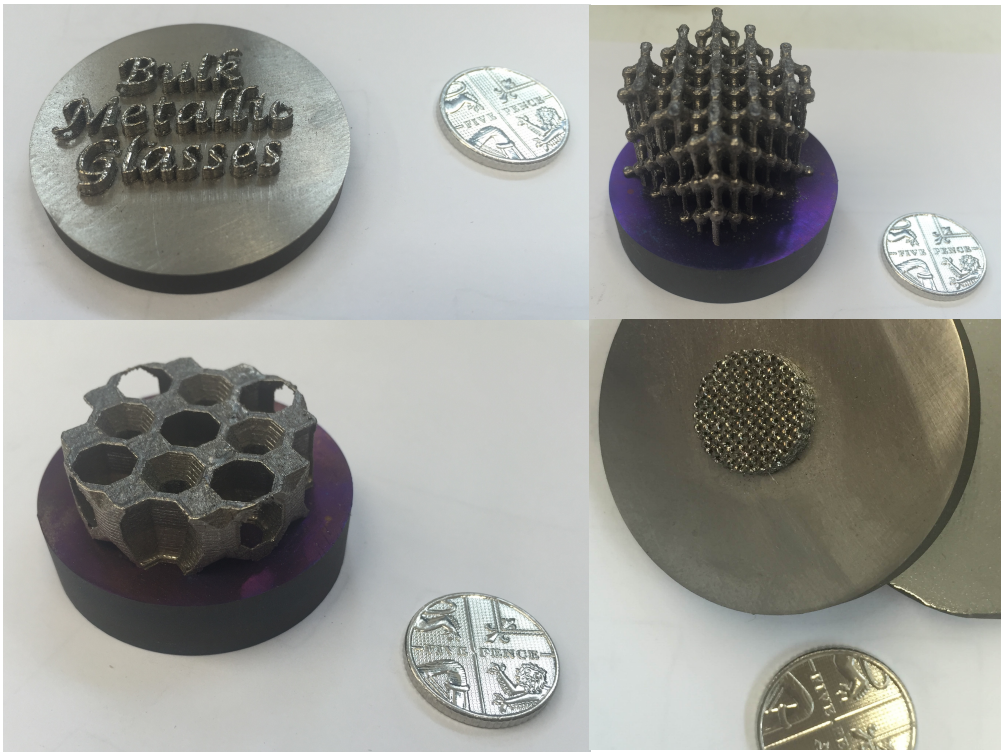

Figure 4.37- Complex shapes fabricated out of SAM1651 using the selective laser melting process.

5. Discussion

5.1. Effect of Normalized Energy Density on SLM Processing of SAM1651

As discussed before in section 2.9, E^*_0 is defined as the normalized energy density and calculated using Equation 5.1 and represents a combination of two sets of parameters. One is the processing parameters that are used in the ALM process, such as laser power, laser velocity, layer thickness, hatch spacing and substrate temperature, while the other set of parameters represents the thermal and physical characteristics of the material being processed like density, thermal capacity and melting temperature. This combination as shown by Thomas et al. (Thomas, Baxter and Todd, 2016) can be used to show the amount of heat input that is being put into the powder bed and affected lower layers.

$$E_0^* = [Aq/(2vhl)]\left[1/\rho C_p(T_m - T_0)\right] \qquad \text{Equation – 5.1}$$

While examining the same material (which means that thermal and physical characteristics of the material are of no importance comparatively), higher amounts of E^*_0 that are resulted from smaller hatch spacing, layer thickness, laser velocity or larger laser power would mean that a larger amount of heat is being put into the material that is being processed. This energy input can determine whether the resulting specimen is structurally sound or has unfavourable defects inside. These defects that can deteriorate the structural integrity of the samples include porosity, lack of fusion defects, cracks and in the case of metallic glasses, partial crystallization. So, to end up with desirable samples from the selective laser processing, the respective parameters need to be controlled and optimized.

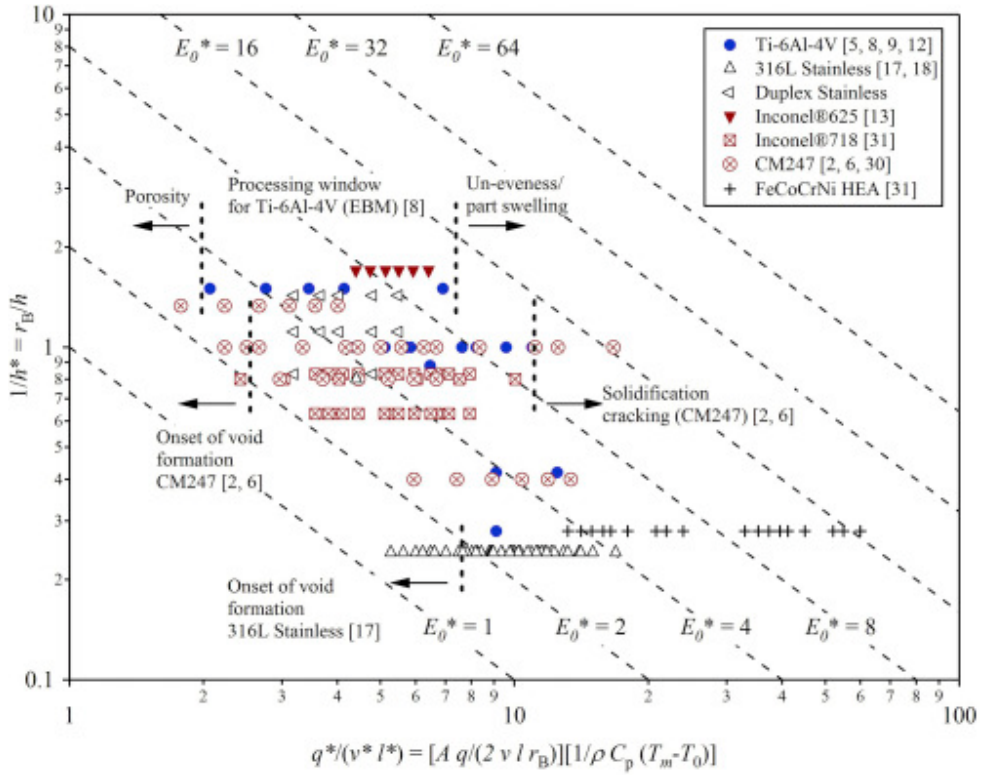

Figure 5.1- Normalized processing diagram for ALM of a range of alloy systems constructed using Equation (Thomas, Baxter and Todd, 2016)

Normalized dimensionless energy input, as shown in Thomas et al. (Thomas, Baxter and Todd, 2016) can be a good tool to do so, and it gives a way to enable researchers to predict what kind of microstructure would be the result of certain processing parameters. As an example, the diagram shown in Fig. 5.1 was constructed by Thomas el al. (Thomas, Baxter and Todd, 2016). It depicts for different materials and additive manufacturing processes the relationship between parameters and final microstructures.

In this study, however, some of the processing parameters were kept constant in order to investigate the influence of the others. The values used for hatch spacing, point distance and layer thickness during this study are shown in Table 5.1.

Point Distance	Hatch Spacing	Layer Thickness
50 µm	100 µm	50 µm

Table 5.1- Processing parameters that were kept constant for this study

Considering this, and the fact that this study was focused on one material, SAM1651, which would mean the thermal characteristics included in Equation 5.1 would be constant as well, Eq.2 can be simplified to Equation 5.2 which is as follows:

$$E_0^* = C_1[q/(v\Delta T)] \qquad \text{Equation – 5.2}$$

Where:

$$C_1 = (A/2hl)\left(1/\rho C_p\right) \qquad \text{Equation – 5.3}$$

The surface absorptivity (A) is assumed to remain constant as well. Further simplification can be done to Equation 5.2. The beam velocity included in Equation 5.1, can be calculated for the selective laser processing as:

$$v = \left[x/\left(t_{exp} + t_{move}\right)\right] \qquad \text{Equation – 5.4}$$

Where x is point distance, t_{exp} is the exposure time and t_{move} is the time the laser moves between two points of melting on the powder bed without fusing the powder. For t_{move} the default value of the SLM machine was utilized for this study, which is equal to 10µs, and is far less than the values that were used as exposure time (more than an order of magnitude) and hence can be ignored. Hence, the velocity of the SLM process was simplified to:

$$v = x/t_{exp} \qquad \text{Equation – 5.5}$$

Thus, as point distance was kept constant as well, Equation 5.2 can now be simplified as:

$$E_0^* = C_2\left(qt_{\exp}/\Delta T\right) \qquad \text{Equation – 5.6}$$

Where:

$$C_2 = C_1/x = (A/2hlx)\left(1/\rho C_p\right) \qquad \text{Equation – 5.7}$$

So, at this point, by examining the interaction between laser power, exposure time and powder bed temperature, the change in the normalized energy density input and in turn the resulting microstructural defects can be studied.

5.2. Effect of Powder Bed Temperature on Cracking of Specimens

Cracking in SAM1651 is affected by two different mechanisms. One is through porosity which is mainly affected by the laser power and exposure time used and will be discussed later. The other is the influence of powder bed temperature.

As many have reported (Shiomi *et al.*, 2004; Mercelis and Kruth, 2006; Kempen *et al.*, 2013), one of the main effective ways of controlling and reducing the stress produced within the SLM process is using a higher powder bed/substrate temperature (Ali *et al.*, 2017). This stress is responsible for the cracks inside the samples that are built from the SAM1651 using the SLM process. So, reducing the stress would help reduction of the cracking. As Kruth et al. (Kruth *et al.*, 2004) has explained the source of this stress can be attributed to the high thermal gradient that occurs in the heat affected zone around a melt pool and as this thermal gradient increases the resulting stress and therefore cracking would increase respectively.

In order to examine this hypothesis regarding the interaction between powder bed temperature and the resulting cracking, several specimens were manufactured using different laser power, exposure time and powder bed temperature values. As depicted in Fig. 4.24, in every instant as the powder bed temperature increases, the amount of cracking decreases. So, to see if, as Kruth (Mercelis and Kruth, 2006) has shown, thermal gradient in the HAZ is in fact responsible for this phenomenon, the thermal profile of the HAZ around individual melt pools created by different parameters was obtained through Finite Element Analysis and is shown in Fig. 4.25. And from this information, thermal gradients created in the HAZs were calculated and depicted in Fig. 4.26 which demonstrates that:

a) For similar powder bed temperatures, regardless of the different laser power and exposure time values utilised, the resulting thermal gradient would be very similar.

Which means powder bed temperature is the main factor controlling the thermal gradient in the HAZ of individual melt pools

b) As powder bed temperature increases, the resulting thermal gradient decreases significantly.

The next step is to combine the data in Fig. 4.24 and Fig. 4.26 which results in the diagram shown in Fig. 4.27. To have a better understanding of the interplay between laser power, exposure time, powder bed temperature and the resulting cracking, Fig. 4.27 can also be presented as Fig. 5.2:

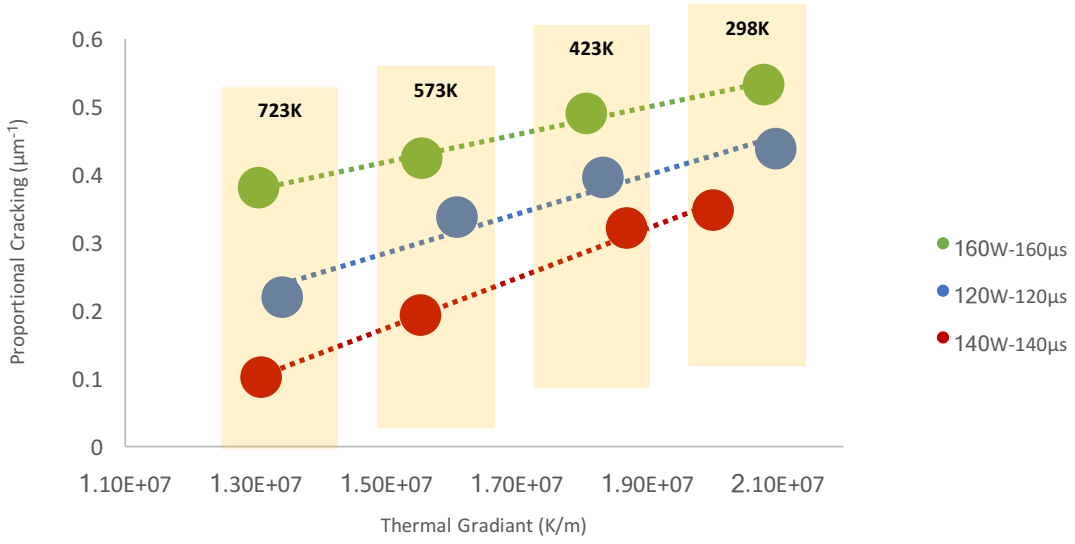

Figure 5.2- Effect of thermal gradient on the amount of cracking inside different samples

It is evident from the data in Fig. 5.2 that:

a) The main factor controlling the resulting cracking in the specimens manufactured by the SLM process is the thermal gradient. As mentioned before, the effect of laser power and exposure time on cracking is through the resulting level of porosity, when the powder bed temperature is the same, and it will be discussed later and although cracking is influenced by laser power and exposure time as well, thermal gradient seems to play a more significant role comparatively.

b) We can also see that the parameter that controls the thermal gradient in Fig. 5.2 is actually the powder bed temperature and as it increases, the consequent thermal gradient values notably decrease.

c) Combining these two facts, it can be concluded that the hypothesis put forward by Kruth et al. (Mercelis and Kruth, 2006) seems to be correct and that it applies to samples made out of the metallic glass SAM1651 through SLM processing.

Thus, going forward, the majority of the experiments were conducted using the maximum powder bed temperature obtainable by the designed in-situ raised bed temperature rig which is 723K, since the least amount of cracking is one the goals pursued when dealing with any additive manufacturing process.

As for Equation 5.6, the above conclusion means that we can go another step toward simplification of the equation, since powder bed temperature would be constant as well:

$$E_0^* = C_3\left(qt_{\exp}\right) \qquad \text{Equation – 5.8}$$

Where:

$$C_3 = C_2/\Delta T = (A/2hlx)\left(1/\rho C_p\,\Delta T\right) \qquad \text{Equation – 5.9}$$

5.3. Effect of SLM Processing Parameters on Amorphicity of Specimens

When attempting to manufacture bulk metallic glass samples, one of the main concerns is whether the process results in fully amorphous specimens or if crystallization occurs as a result of inappropriate processing parameters. Selective laser melting is not an exception in this regard. So, in this study, one of the main tests carried out on the manufactured samples was XRD testing to check the amorphicity of the samples. The results are presented in Fig. 4.13. As depicted in these diagrams there are certain sets of parameters that result in partial crystallization.

This difference in the final microstructure can be attributed to thermal history of the powder as it is being melted and solidified inside individual melt pools and the surrounding material in the heat affected zone around these melt pools. So, to investigate this, the thermal history of each individual melt pool (as a product of different sets of laser power and exposure time values) and the thermal profile of its HAZ was examined through finite element analysis and is depicted in Fig. 4.17 and Fig. 4.20. From these diagrams, the corresponding thermal gradients and cooling rates were derived as shown in Fig. 4.18 and Fig. 4.21.

In Fig. 4.18 we can see that as laser power and exposure time values used were increased the resulting cooling rate proportionally decreased. That can be attributed to the fact that as power/exposure time increases the temperature of the material around the point that the cooling rate is measured (centre of the melt pool) increases and it causes the heat flow from that point to its surroundings to slow down, hence the reduction in cooling rate.

Furthermore from Fig. 4.21, the effect of laser power and exposure time on the thermal gradient, while all other processing parameters were kept constant, is evident:

a) For each laser power, as exposure time increases, a relative reduction in thermal gradient can be observed. This is because as exposure time increases, there is more time for the temperature range around the melt pool (in the heat affected zone) to increase. And, since thermal gradient is calculated using the temperature of the area right next to the melt pool (which is always around the melting point) relative to an area that is further from the melt pool, thermal gradient values decrease as exposure time increases because the temperature of areas further from the melt pool increases as exposure time increases.

b) For each laser power, at smaller exposure times, thermal gradient values are almost the same and as exposure time values increase, at a specific exposure time, the

thermal gradient values start to decrease dramatically in comparison. This is because of the same phenomenon explained in part (a): At smaller exposure times, the temperature of the area that is further from the melt pool (which is being compared to the temperature of the area of the material right next to the melt pool to calculate the thermal gradient) is almost not affected by the temperature rise caused by the melt pool because there has not been enough time for the heat flow to affect that area, hence the similar thermal gradients in smaller exposure times. However, at a specific exposure time (for each laser power) the temperature rise caused by the melt pool starts to affect and increase the temperature of the area further from the melt pool which results in a sudden reduction in thermal gradient values.

c) The exposure time value, at which the sudden reduction in thermal gradient occurs for each laser power, shifts towards smaller values as laser power increases. The reduction does not happen at 120W, occurs at 160µs for 140W and 160W and at 140µs for 180W and 200W. The shift can be explained through the effect of laser power values on the thermal profile of the material around the melt pool. As laser power increases, the temperature of every point inside the melt pool and the heat affected zone increases as a result. The only point at which the temperature is the same for every power/exposure time combination is the solid/liquid interface which is always around the melting point. Therefore, since the temperature of the area of the material that is further away from the melt pool is increased more as laser power values increase, the sudden reduction in thermal gradient can happen at smaller exposure times since less time would be required for heat flow to affect areas of the heat affected zone further from the melt pool, hence the shift toward smaller exposure times at larger laser powers.

So, when the information presented in these two graphs were combined with the XRD test results, in order to investigate the influence of thermal gradient and cooling rate on the crystallization behaviour of SAM1651 specimens manufactured by the SLM process, Fig. 4.19 and Fig. 4.22 were constructed.

Clearly, a correlation can be seen in these two diagrams between the cooling rate and thermal gradient of the SLM process and the resulting amorphicity of the samples. It is evident that at lower values of these two parameters the tendency of the metallic glass to crystallize is higher and therefore processing parameters that yield higher cooling rate and thermal gradient values are favourable in terms of keeping the microstructure of the specimens amorphous.

The reason for this is that when the thermal gradient of the heat affected zone around an individual melt pool is smaller, it is because the temperature of the areas further from the melt pool interface iares higher and closer to the materials melting point. So, the possibility that the temperature of some areas in the HAZ are higher than the crystallization temperature of the material, increases. Also, when the cooling rate of the molten material inside the melt pool is smaller, the cooling rate of the solid material inside the HAZ would be smaller as well and when it becomes small enough to be lower than the critical cooling rate of the metallic glass, some areas of the heat affected zone, become crystallized. Furthermore, when the cooling rate of the material in the HAZ is smaller, the heat flow from the HAZ to the previously deposited layer decreases. This can cause heat accumulation during successive laser scanning, resulting in the temperature of the material increasing to higher than the crystallization temperature of the glass forming alloy and hence crystallization of the material in the HAZ occurs.

To further investigate the interplay between thermal gradient, cooling rate and crystallization behaviour, Fig. 5.3 (similar to Fig. 4.23) was created. The main observation that can be made

from this diagram is that the slope of the curve, which corresponds to solidification rate (R), where the samples are partially crystallized, is much lower in the samples that have remained fully amorphous.

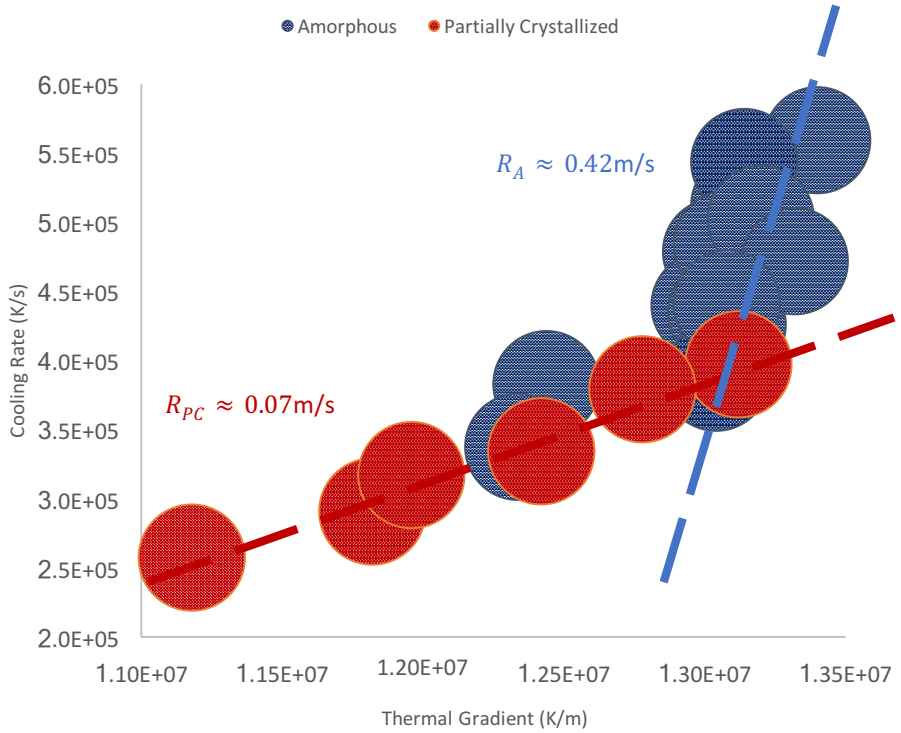

Figure 5.3- Effect of cooling rate and thermal gradient on amorphicity of the specimens

In Fig. 5.3, there are some data points that seem to have fairly similar thermal gradient and/or cooling rate that demonstrate different microstructures, some are partially crystallized while others are amorphous. This can be explained through the size of the effect of the melt pool that each laser power/exposure time creates, on amorphicity.

It is shown in Fig. 4.16 that all of the partially crystallized samples have a larger melt pool size of about $3.2 \times 10^6 (\mu m^3)$. Therefore, it can be deduced that regarding the samples that had similar cooling rate and thermal gradients, the ones that had a melt pool size of larger than this threshold would be crystallized and the ones that were smaller would be amorphous. The

effect of melt pool size on amorphicity in this situation can be attributed to the amount of crystallized portion created in the HAZ as a result of the low cooling rate and thermal gradient. The samples that seem to be amorphous from their XRD patterns and have the same thermal gradient and cooling rate of some of the partially crystalized samples have smaller melt pools and therefore smaller heat affected zones. So, the volume of the HAZ that would be affected by low thermal gradient and cooling rate and hence be crystallized, would be smaller. So, there would be a small area of the HAZ around an individual melt pool of these samples that is crystallized but this area is small enough that the XRD experiment would fail to show a relevant peak in the XRD pattern. On the other hand, samples with similar cooling rate and thermal gradient that seem to be crystallized from their XRD patterns, have larger melt pools, larger HAZs and therefore a larger area within the HAZ that is affected by the low cooling rate and thermal gradient; large enough for the XRD apparatus to pick it up during the test.

Finally, the relationship between the normalized energy density and the crystallization behaviour observed in this study can be explained accordingly. As mentioned before, E_0^* can be represented by Equation 5.8:

$$E_0^* = C_3\left(qt_{\exp}\right) \qquad \text{Equation – 5.8}$$

Where C_3 is a constant. So, if E_0^* is increased (which can be obtained by either increasing laser power or exposure time) according to Fig. 4.18 and Fig. 4.21, the resulting cooling rate and thermal gradient created within the SLM process would be smaller, with the cooling rate value showing a larger reduction. This would mean the solidification rate would decrease as well, which in turn according to Fig. 5.3 would result in a higher possibility of the specimens crystallizing. So, it can be concluded that for the purpose of keeping the microstructure fully amorphous when manufacturing samples out of metallic glasses using the selective laser melting process, it is favourable to keep the energy input at lower values.

As $E_0^* \left(\propto qt_{exp}\right) \uparrow \Longrightarrow \begin{cases} G \downarrow \\ \dot{T} \downarrow\downarrow \end{cases} \Rightarrow R = \frac{\dot{T}}{G} \downarrow \Rightarrow$ *Partial Crystallization*

5.4. Constructing a Processing Map of Selective Laser Melting SAM1651

The normalized energy density input values, calculated using Equation 5.1 can be directly used to attempt to find a processing window for the metallic glass. However, the multiplicity of the microstructural defects that can occur in the SLM manufactured specimens means that it would be much easier to rely on the simplified version of the above mentioned equation, Equation 5.8, which specifically examines the role of E^*_0 as a product of laser power and exposure time. Therefore, in this section an attempt will be made to construct a processing map for building samples of SAM1651 using the SLM process, focusing on the role of laser power and exposure time while keeping all other processing parameters constant (described in Table 4.2).

In order to produce an optimum specimen through selective laser melting of a metallic glass material, there are several aspects that need to be considered. The sample needs to be as dense as possible with the lowest amount of cracking and of course it needs to be fully amorphous. Therefore, the processing parameters should be optimized to meet all of these criteria. In trying to find a processing window that could be used to produce such specimens, each of these aspects were investigated individually. And finally, the results were compiled into a processing map.

5.4.1. Investigating the Parameters to Achieve Maximum Density

There are two different defects that influence the density of the samples built through SLM and they are produced via different mechanisms. That is why different sets of parameters

would yield the minimum amount for each of these defects and so, they need to be examined separately. One, is the pores within the samples and the other is the lack of fusion defects that are usually the result of insufficient energy input into the powder bed.

5.4.1.1. Finding the Processing Window for Minimum Porosity

From the data shown in Fig. 4.5, porosity that is present within the specimens, decreases to a minimum before increasing again when for a certain laser power, the utilized exposure time increases. This phenomenon occurs because there are two different origins for these pores. There are pores that have originated from the pores that were already present inside the powder particles before any laser melting was carried out, and then there are pores that are the result of in-situ pore formation which can occur during the SLM process, as a result of excessive energy input into the powder bed, while the laser melting is in effect. This excessive energy input can cause in-situ pore formation either by vaporising constituent elements which have lower melting points or by Argon gas entrapment in the melt pool which can happen as a result of a volatile melt pool created because of the high energy density input.

The amount of the first type decreases as the energy input increases because some of the gas that was trapped inside the powder particle is able to escape when the particle is being melted and some will remain within the final specimen as it hasn't had the chance to scape. The possibility of this type of pore disappearing during the SLM process is affected by the size and shape of the particle, the orientation and the way the surrounding particles are situated. The amount of the second type however, is either very small or does not exist at low energy input values and as the exposure time/laser power increases at some point, the in-situ pore formation process would kick in and as they increase even further the amount of this type of

pore increases as well. This is why the curves shown in Fig. 4.5 depict porosity values to decrease at lower energy density inputs and increase at higher ones.

So, since the amount of porosity within the specimens needs to be as low as possible, parameters have to be found that don't result in in-situ pore formation. As mentioned before samples that show the minimum amount of porosity inside them using optical microscopy were the ones that had the maximum amount of cracking within them (the reason for this will be discussed later). Therefore, a diagram was constructed in Fig. 4.7 that shows cracking of the specimens built with different laser power and exposure time values. From this diagram, a threshold corresponding to a maximum exposure time for each laser power can be obtained below which in-situ pore formation does not occur.

5.4.1.2. Processing Window for no Lack of Fusion Defects

As depicted in Fig. 4.10, when the exposure time values for each laser power increases the possibility of lack of fusion defects forming during the SLM process decreases. The reason for this phenomenon is that laser power and exposure time values control the size of the resulting melt pool, as shown in Fig. 4.15. As each individual melt pool gets larger, the possibility of some areas of the powder bed to remain unmelted in each layer decreases and this transition continues until the energy input value reaches a point after which no lack of fusion defects can form. So, in order to find this threshold, Fig. 4.12 was constructed which determines a minimum exposure time for each laser power above which LoF values would reach around zero.

5.4.2. Finding Parameters Yielding Minimum Cracking

As discussed before, one of the main parameters influencing the amount of cracking that occurs during the SLM process is the powder bed temperature and as a result the highest temperature achievable was used in the experiments to get the lowest cracking possible. But, laser power and exposure time also affect the amount of cracking as depicted in Fig. 4.5. In order to explain how cracking behaves as a consequence of the change in these two parameters, Fig. 5.4 should be considered which shows that at every laser power (in this case 160W as an example), as exposure time increases, the amount of cracking goes through three distinct stages.

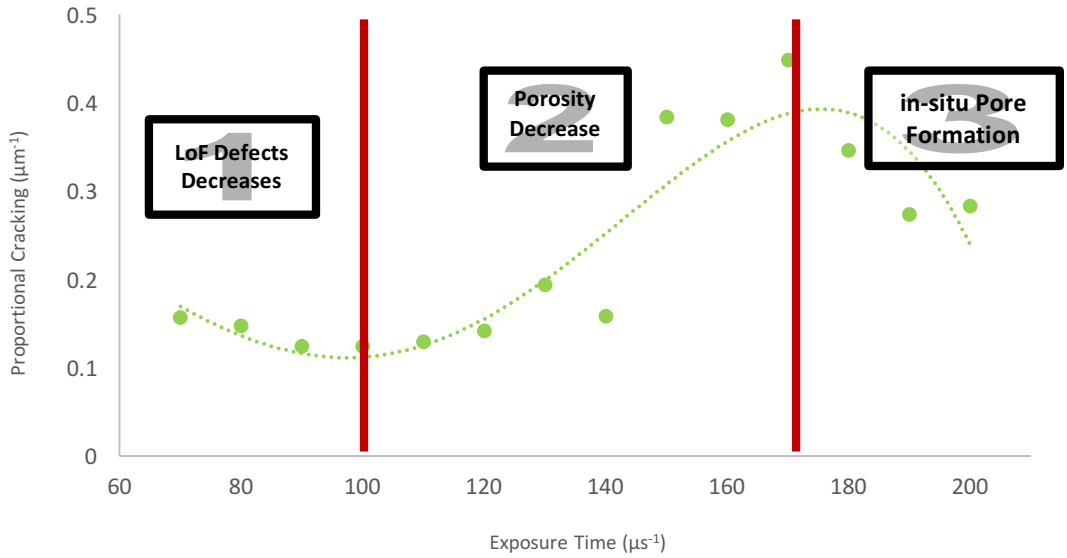

Figure 5.4- Amount of cracking at laser power of 160W vs exposure time

1) At this stage, as the exposure time increases the resulting cracking value decreases. This can be attributed to the existing lack of fusion defects at lower exposure times. The samples that are manufactured using the SLM process are under high amounts of stress due to the thermal gradients present in the process. These irregular voids cause the microstructure of the specimens to crack as a result of that. But when exposure

time and as a consequence the energy input increases, these lack of fusion defects start to decrease and this would result in the cracking of the samples decreasing to a minimum.

2) When the exposure time increases into stage 2, another mechanism starts to control the amount of cracking. At this point, there are no lack of fusion defects left in the samples and as the exposure time increases the amount of porosity (remaining from the pores inside the powder particles) which are spherical voids decreases as discussed before. These spherical pores, as explained by Kruth et al (Kempen *et al.*, 2013), act like a second phase, prohibiting cracks from growing. So, when porosity decreases (as shown Fig. 4.5) cracks would have the potential to grow longer which would result in the amount of cracking depicted in Fig. 5.4 to increase.
3) When exposure time increases to this stage, in-situ pore formation starts which means extra spherical pores start to appear in the microstructure of the specimens. These extra pores, as mentioned above prohibit crack growth and result in the amount of cracking decreasing once more.

Depending on the laser power used in the experiment these stages would move to different exposure time values. So, at the lowest values of laser power we can only observe stage one and at the higher end of laser power, only stage two and three are depicted (Fig. 4.5). This is because laser power, like exposure time has a direct relationship with energy input density and hence shows the same effect on cracking.

Since the lowest amount of cracking is favourable, the data from Fig. 4.5 was used to find the parameters that would yield cracking of less than $0.2\mu m^{-1}$ and the result is shown in Fig. 4.9. It can be observed that for every laser power, there is an exposure time value below which

gives this minimal cracking and this threshold can be utilized when constructing a processing window of this metallic glass using selective laser melting.

5.4.3. Processing Window for Sample Amorphicity

It was shown before that when processing bulk metallic glasses, the energy density input controls the crystallization behaviour of the specimens through thermal gradient and cooling rate. It was also explained that it can further control the amorphicity by changing the individual melt pool size created as result of different laser power and exposure time values. To examine this influence, Fig. 4.14 was constructed which shows that for every laser power there is an exposure time value above which specimens go through partial crystallization.

This critical exposure time, shifts to lower values as the laser power used increases. This is because of the role that laser power plays in controlling the energy input values which is similar to the effect that exposure time has. From this threshold observed in Fig.4.14, we can determine the parameters that would yield the processing window for SAM1651 samples to remain amorphous, when manufactured using the selective laser melting process.

5.5. SLM Processing Window for SAM1651

By combining the data presented in Fig. 4.7, Fig. 4.9, Fig. 4.12 and Fig. 4.14, a processing map for SAM1651 can be constructed which shows at each laser power/exposure time combination, how the samples built would turn out (Fig. 5.5). It also shows the combination of processing parameters from which the best possible result can be obtained which would satisfy the required criteria in terms of having the lowest possible amount of cracking, being as dense as possible and being fully amorphous. Outside of this optimum processing window,

one of these characteristics would be out of the range that is deemed the best possible outcome.

It can be observed that when the minimum cracking criteria has been met, amorphicity and in-situ pore formation concerns are already satisfied. So, the main two characteristics that dictate whether a cube made out of SAM1651 using the SLM process would be in the best possible processing window are the amount of cracking and lack of fusion defects. We can also see that the best parameters are located toward the middle of the processing map and as the power/exposure time combinations move toward larger values, samples start to crystallize and when they become too low, lack of fusion defects form inside the samples.

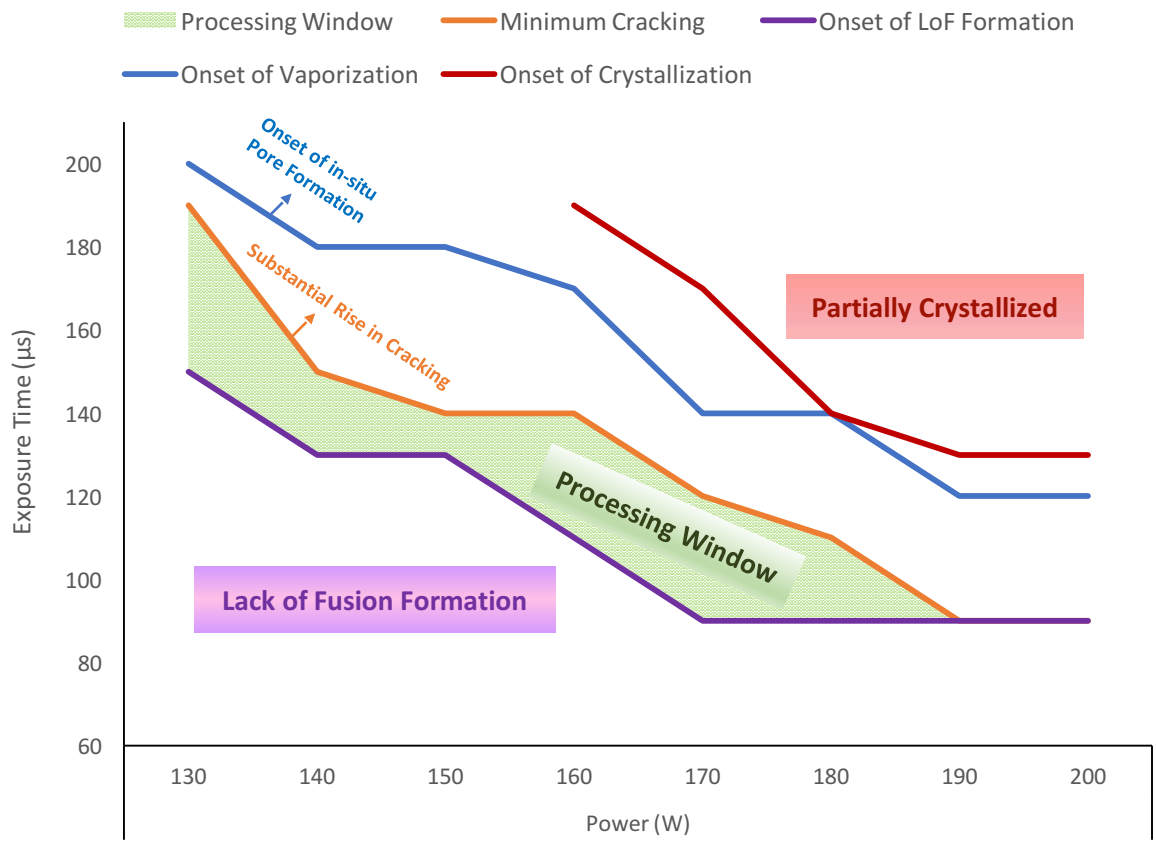

Figure 5.5- SLM Processing Window for SAM1615

Each of these boundaries provide a set of values which are the critical amounts determining if the utilized parameters would exhibit any of the unwanted defects within the resulting

microstructure of the specimens. Using these values for laser power and exposure time we can relate every threshold to the critical consequent normalized energy density input by utilizing Equation 5.8. As discussed before, the amount of E_0* put into the powder bed is directly proportional to the product of laser power and exposure time used. From this we can come up with values for E^*_0 for each of these thresholds:

$$E_0^* = C_3\left(qt_{\exp}\right) \qquad \text{Equation – 5.8}$$

Where:

$$C_3 = C_2/\Delta T = (A/2hlx)\left(1/\rho C_p\,\Delta T\right) \qquad \text{Equation – 5.9}$$

So, by putting in the values for the parameters that were kept constant in this study (shown in table 4.2), the thermal properties (Ajdelsztajn et al., 2009) and the absorptivity coefficient (A for Fe-alloys is considered to be 0.25 to 0.35 (Zheng *et al.*, 2009)) of SAM1651 into Equation 5.9 we get:

Bed Temperature	Point Distance	Hatch Spacing	Layer Thickness	Absorptivity	Density	Specific Heat Capacity	Melting Point
723 K	50 µm	100 µm	50 µm	0.3	7310 kgm^{-3}	460 $Jkg^{-1}K^{-1}$	1394 K

Table 5.2- Processing parameters that were kept constant for this experiment

$$C_3 = C_2/\Delta T = (A/2hlx)\left(1/\rho C_p\,\Delta T\right) = 265.9\ J^{-1}$$

And the average $qt_{\exp}$ for each threshold is as follows:

Onset of LoF Defects Formation	Onset of Crack Growth	Onset of in-situ Pore Formation	Onset of Crystallization
0.0170 J	0.0202 J	0.0251 J	0.0269 J

Table 5.3- Average value of qt_{exp} for each of the defect formation thresholds

From these values, the threshold values for E^*_0 can be calculated as:

Onset of LoF Defects Formation	Onset of Crack Growth	Onset of in-situ Pore Formation	Onset of Crystallization
4.52	5.37	6.67	7.15

Table 5.4- E*0 values for each of the defect formation thresholds

From this and Fig. 5.5, we can expect that when the E^*_0 used to produce SAM1651 specimens using selective laser melting, is between 4.52 and 5.37, the best possible samples would be manufactured.

To confirm this estimation, the data shown in Fig. 4.5 and Fig. 4.10 can also be used to show how energy density input, calculated from Eq. 5.1, would influence cracking and lack of fusion defect formation. So, E^*_0 was calculated for each set of laser power and exposure time values, keeping other processing factors constant (shown in table 4.2) and using the information in Fig. 4.5 and Fig. 4.10, the diagram in Fig. 5.6 was constructed. The two charts are situated in a way that the diagram can be divided into three different areas:

a) In this area, cracking is at a minimum, but significant formation of lack of fusion defects can be observed, which means the processing parameters used are not going to produce a dense specimen and therefore they are not considered to be optimized.
b) This area represents the energy density input at which both cracking and lack of fusion defects are comparatively low and hence seems to be the favourable window to manufacture specimens in.
c) And finally, in this area, although formation of lack of fusion defects is nearly non-existent, cracking within the specimens increases to its maximum potential, eliminating the set of parameters that yield these values for energy density to be used for SLM processing of this metallic glass.

The values depicted in Fig. 5.6, shows that the optimum E^*_0 for making samples with minimal crack growth and lack of fusion defects is between 4.48 and 5.34. It also shows that the

maximum cracking occurs at E^*_0 of about 6.4. These two facts confirm that the estimation made using the processing map shown in Fig. 5.5 is correct.

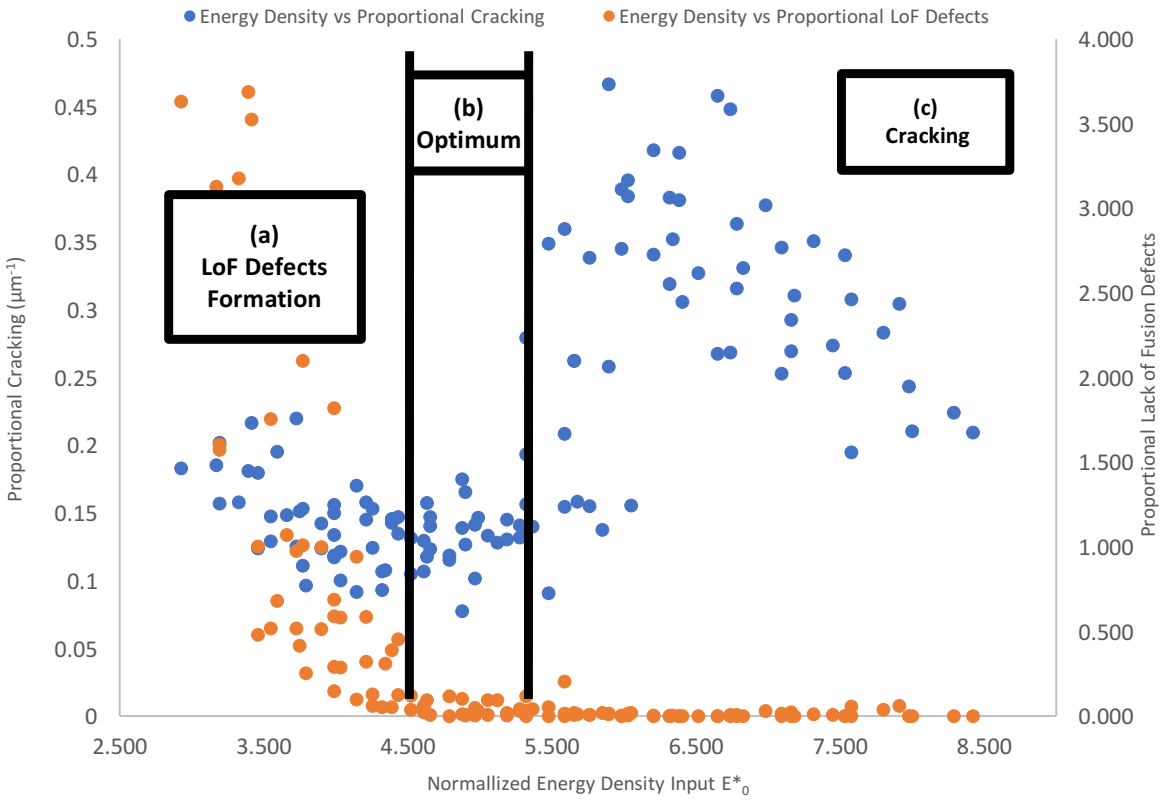

Figure 5.6- Effect of normalized energy density on the cracking and lack of fusion within the specimens

As it was mentioned in section 3.11.1, the absorptivity coefficient of solid Fe-based alloys has been reported to be between 0.25 to 0.35. So, in this study 0.3 was assumed to be the absorptivity coefficient of SAM1651. In order to examine how this assumption affects the outcome of the processing window for this alloy, Fig. 5.7 and Fig. 5.8 were constructed using absorptivity coefficient as 0.25 and 0.35 respectively. The C_3 value in the case of the absorptivity coefficient being 0.25 and 0.35 changes to 221.6 J^{-1} and 310.2 J^{-1}, respectively. This would change the E^*_0 threshold for each defect formation provided in Table 5.4 to the data shown in Table 5.5.

	Onset of LoF Defects Formation	Onset of Crack Growth	Onset of in-situ Pore Formation	Onset of Crystallization
A=0.25	3.77	4.47	5.56	5.96
A=0.35	5.27	6.26	7.78	8.34

Table 5.5- E*0 values for each of the defect formation thresholds, using 0.25 and 0.35 as the absorptivity coefficient

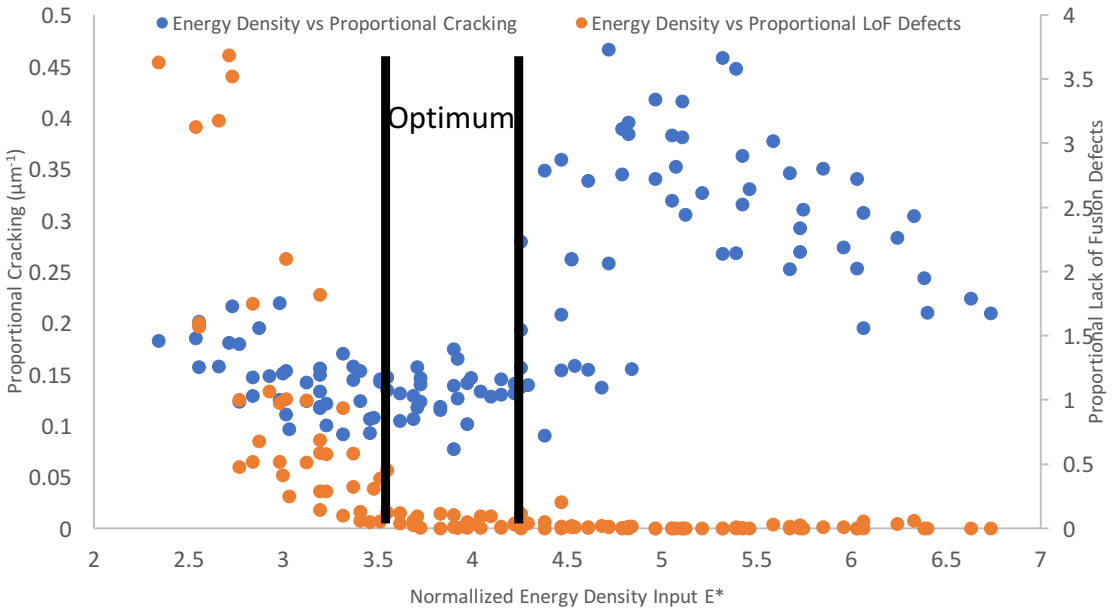

Figure 5.7- The optimum criteria of E^*_0 for processing SAM1651 when the absorptivity coefficient is assumed to be 0.25

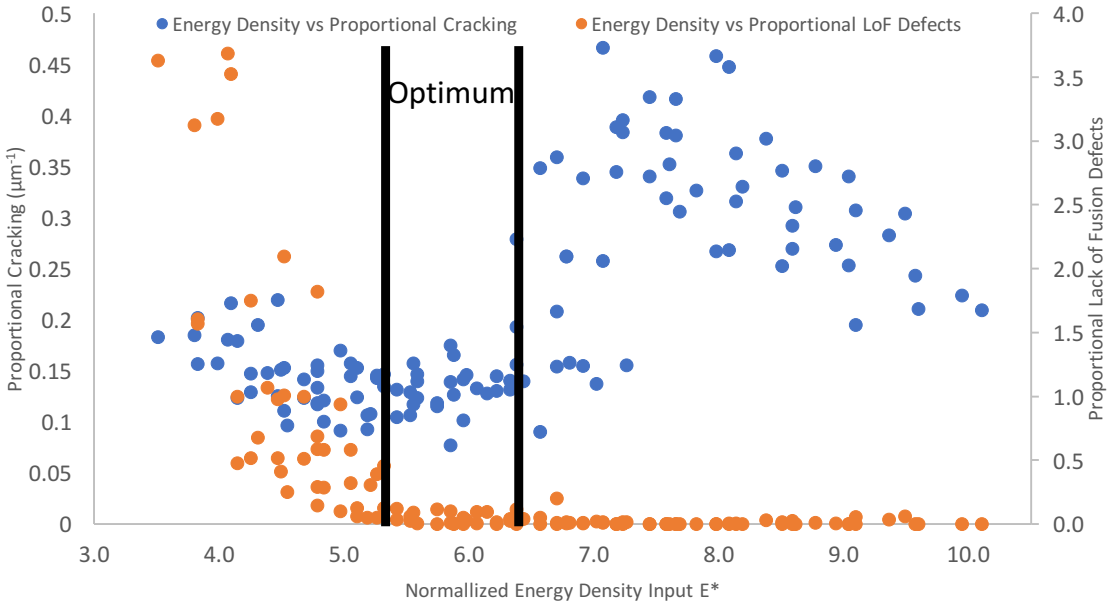

Figure 5.8- The optimum criteria of E^*_0 for processing SAM1651 when the absorptivity coefficient is assumed to be 0.35

It can be demonstrated in Fig. 5.7 that assuming the absorptivity coefficient to be smaller (0.25) shifts the processing window of E^*_0 to lower values and assuming the absorptivity

coefficient to be larger (0.35) shifts the processing window of E^*_0 to higher values. Also, the values for the onset of defect formation and the onset of crack growth shown in Table 5.5 present sufficient similarities to the optimum processing criteria depicted in Fig. 5.7 and Fig. 5.8, as they did when the absorptivity coefficient was assumed to be 0.3 in Fig. 5.6.

5.6. Influence of Layer Thickness

5.6.1. The Effect of Layer Thickness on the Formation of Lack of Fusion Defects

As mentioned before, the main reason for the formation of the lack of fusion defects is that some part of the powder layer that was supposed to be melted, did not get enough laser beam exposure and hence remained in its powder form or was partially melted. Whenever this phenomenon happens, the resulting specimen would contain some non-spherical porosity in its microstructure which is not favourable as it is detrimental to the density of the specimen and can have an adverse effect on its mechanical properties (such as fatigue).

Two of the main parameters that determine if there is this kind of defect in a specimen made by selective laser melting were discussed before. As shown before, laser power and exposure time control the size of the individual melt pool in the SLM process and that is one of the main factors in determining if the whole of the powder layer will be melted. However, there are other processing parameters that are influential in the formation of the lack of fusion defects. One of them is the thickness of the layer of powder. If the layer thickness being utilized is larger than the depth of the melt track created by a certain laser power and exposure time, then there will be some powder particles that remain unmelted throughout the specimen, because they were never exposed to enough heat input from the laser to fuse together. This is how layer thickness can influence the amount of lack of fusion defects.

In order to investigate this, for the SLM built specimens of SAM1651, three different layer thickness values were chosen and for each layer thickness an array of cubes were made using different laser power and exposure times. After measuring the amount of lack of fusion defects for each specimen through optical microscopy, it was evident that, for each set of laser power and exposure time used, as the layer thickness utilized was decreased, the amount of these defects was reduced as well.

This is in line with what was mentioned above, on how at the scope of each layer, the value of powder layer thickness can cause or prevent this kind of porosity. However, another view on the effect of layer thickness on formation of lack of fusion defects can be explained through the amount of energy input that goes inside the whole of the specimen during the SLM process. To examine if there is a correlation between this parameter and the amount of these defects, the normalized energy density for the set of parameters used to build the specimens were calculated using Equation 5.1 (keeping the parameters shown in Table 4.4 constant for all the samples) and the resulting values were plotted against the layer thickness utilized for each specimen (shown in Fig. 5.9).

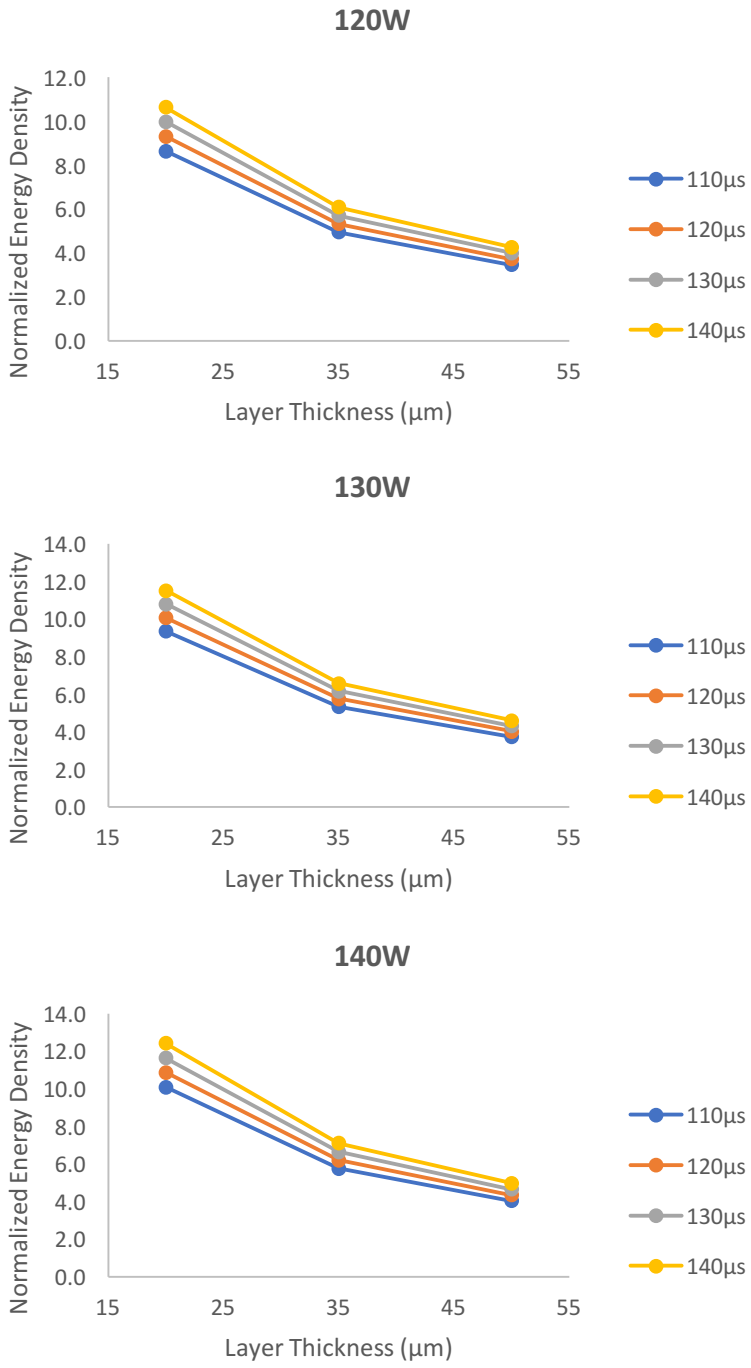

Figure 5.9- The effect of layer thickness on the normalized energy density for different laser power and exposure times

As is demonstrated in Fig. 5.9, for each set of laser power and exposure time values, when the layer thickness used in the selective laser melting process increases the amount of energy density being put into the specimen decreases. This means that the amount of heat provided for the powder to melt has decreased, which can be translated into a higher possibility for some of the powder to remain unmelted or get partial fusion leaving a higher amount of lack of fusion defects in the final microstructure of the specimen.

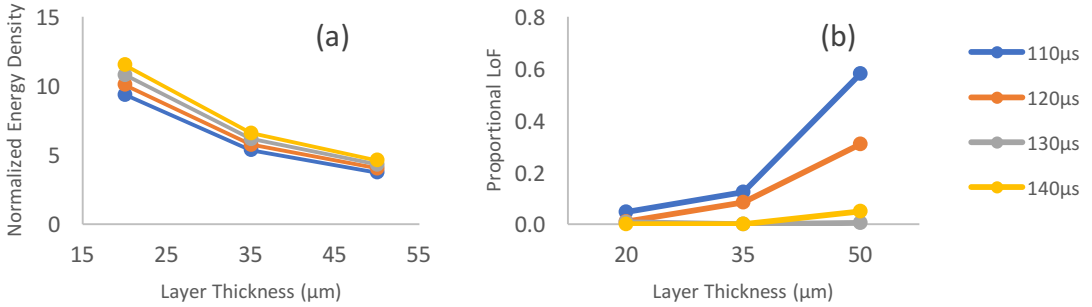

Figure 5.10- The influence of layer thickness on (a) normalized energy density and (b) formation of lack of fusion defects

So, when the lack of fusion defects plots are compared with the normalized energy graphs, this relation can be clearly noticed. For instance, in Fig. 5.10 these two diagrams are shown for 140W laser power and 110-140µs exposure time which shows that when the normalized energy density increases as a result of the layer thickness decreasing, the amount of lack of fusion defects decreases as a result. This is another reason why normalized energy density used to produce samples by the selective laser melting process can be a good indicator as to whether the resulting specimen will have lack of fusion defects inside.

It should also be mentioned that in the simulation of the selective laser melting process in this study the powder particles have been assumed to have the same the same size and shape. Although it might be possible to factor in the difference in shape and size of these particles in the modelling of the process to achieve a more accurate picture of the phenomena occurring

during the SLM process, it would require a far more complicated model. Considering the fact that the model seems to have satisfactory correlation with the experimental results, this simplification was assumed adequate. In reality, however, the different shapes and sizes of the powder particles do contribute to the formation and amount of lack of fusion defects in the specimen. The more diverse the size of the particles the higher packing density of each layer of powder, which means a smaller chance for LoF defects to occur and this is why a range of particle sizes is used in a powder batch utilized for SLM. Also, the irregular shape of particles can contribute to the formation of LoF defects, since interlocking areas can occur which could result in patches of the unmelted distributed powder to be left less dense than others.

5.6.2. Effect of Layer Thickness on the Formation of Cracks

The high heating and cooling rate involved in the selective laser melting process causes residual stresses in specimens built with this method which can in turn result in the formation of cracks if the stresses were larger than the yield strength of the material being processed, specifically if it lacked a large plasticity. Fe-based metallic glasses are often characterised as such materials, of which SAM1651 is one. So, discovering cracks inside the microstructure of the SAM1651 specimens made through the SLM process is hardly surprising.

However, it has been shown that processing parameters involved in selective laser melting can have an effect on the amount of thermal stresses caused during this process and layer thickness is one of the factors that can be influential in this regard. That is why several specimens were made using different layer thickness, laser power and exposure time values to investigate the effect that layer thickness can have on the cracking caused in the SLM process. Their microstructure was analysed through optical microscopy and several plots

were obtained demonstrating how layer thickness affects the amount of cracking in these specimens, of which Fig. 5.11 is one, which pertains to the samples built with 130W laser power and 110-140µs exposure time.

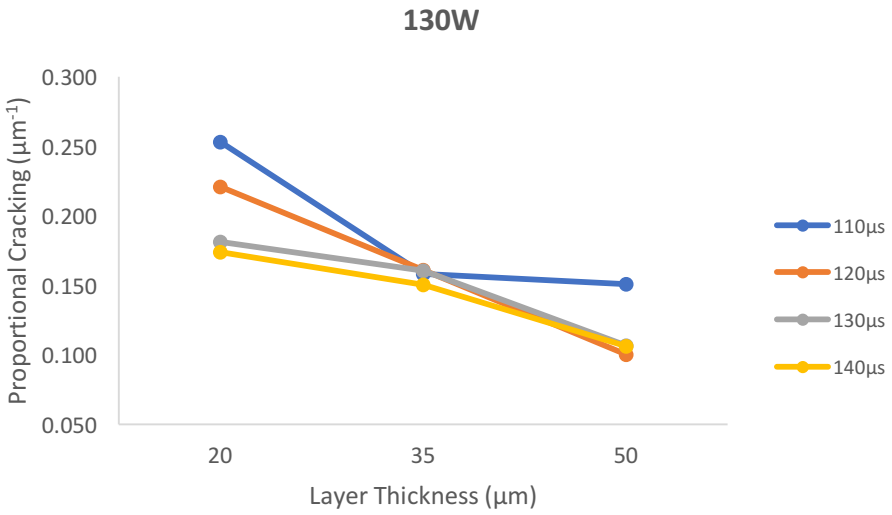

Figure 5.11- The effect of layer thickness on crack formation in samples made with 130W laser power

From this diagram, which is a good representation of the results obtained using other processing parameters, it can be clearly deduced that for a certain set of laser power and exposure time values, as the layer thickness used to build the specimen increases the amount of cracking occurring inside the samples decreases. To understand what can be the cause of this trend, examining previous research can be helpful.

In their study of the parameters influencing the amount of warping of the workpiece and the residual stresses caused as a result of the layer by layer laser densification of nickel-porcelain powder, Dai and Shaw (Dai and Shaw, 2006) found that layer thickness is inversely proportional to the amount of residual stress in the workpiece and the resulting warping. In their numerical simulation, it was revealed that the main factor controlling the deformation in the specimens was the preheating temperature of the powder bed.

However, it was also demonstrated that the z-direction stresses decreased monotonically as the layer thickness used increased. They suggested that this effect is explained through the lower thermal gradient that occurs when the powder layer thickness is larger, during the cooling period as the laser beam has moved away, which in turn is the result of the larger heat sink present when the layer thickness is larger. They also suggested that the rigidity of the solidified larger layer helps in resisting against the possible warpage that can happen during the cooling down stage.

Zaeh and Branner (Zaeh and Branner, 2010) examined several processing parameters through finite element analysis of t-shaped cantilevers made out of a tool steel (1.2709) to see how they would affect the internal residual stresses caused by the SLM process and the subsequent bending of the specimens. They found out that a smaller layer thickness can adversely affect the stresses within the cantilever and as the layer thickness increased, the resulting deformation of the specimens would be smaller, as depicted in Fig. 5.12. They speculated that the thinner layers would experience a higher temperature during the laser exposure since the same heat input were being distributed inside a smaller volume of material and this would cause a higher thermal gradient which is responsible for larger internal stresses and deformation of the t-shaped specimens after being separated through EDM from their support.

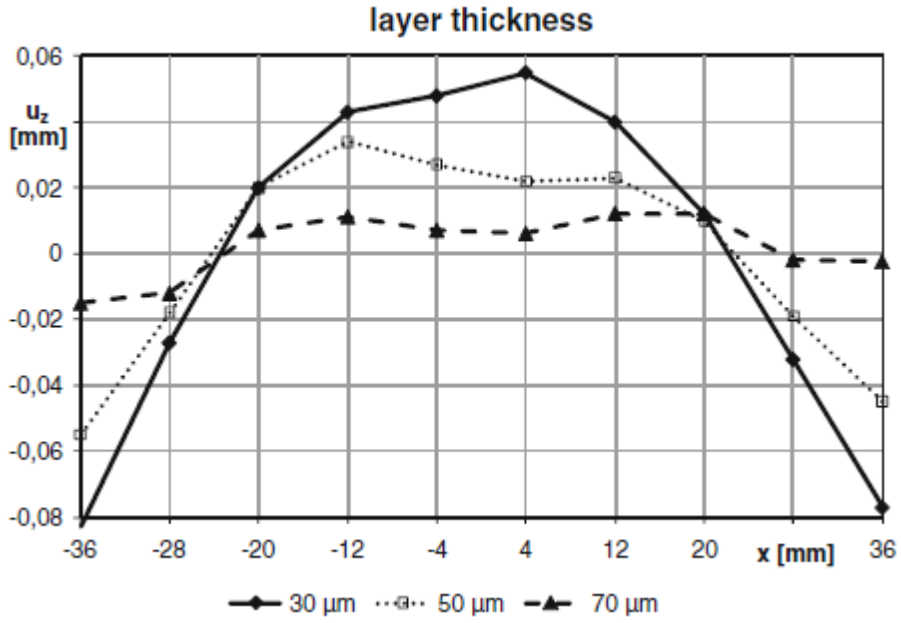

Figure 5.12- The amount of deformation within the t-shaped structure caused by different layer thickness values (Zaeh and Branner, 2010)

In another study, Kruth et al (Kruth *et al.*, 2012) used a novel method called Bridge Curvature Method for measuring the residual stresses in parts made with selective laser melting out of Ti-6Al-4V and AISI 316L stainless steel. As the Bridge-like specimens were removed from the base plate, the resulting angle of deformation would determine the amount of residual stresses within the samples. They showed that when the layer thickness used in the SLM process was reduced the angle of deformation in the resulting specimen would increase suggesting a higher residual stress in the specimen. There was no explanation as to why this phenomenon would occur.

Furthermore, Roberts (Roberts, 2012) utilized a numerical model of the temperature and stress fields present in thin specimens made out of Ti-6Al-4V with selective laser melting. He demonstrated that the halving of the layer thickness used in the SLM process can result in up to a 34% increase in the amount of residual stress in the specimens. He used the same heat sink argument which Dai and Shaw (Dai and Shaw, 2006) used to interpret their findings. However, he mistakenly stated that the thermal gradients generated are directly proportional

to the layer thickness, which is in contrast with every other research on this issue and is contradictory to the heat sink argument. Because, it would mean that when using a larger layer thickness, the resulting thermal and residual stresses would increase which is the opposite of his own findings.

Finally, a layer removal method was used by Van Belle et al (van Belle, Vansteenkiste and Boyer, 2013) to examine the influence of cooling time between successive layer deposition, manufacturing height and powder layer thickness on the thermal stresses caused during the SLM processing of a maraging steel. He presented that higher internal stresses were present in the specimens made with smaller layer thickness values, although there was no explanation of this phenomenon in his research.

Considering these findings, it can be deduced that the literature is unified on the effect that the layer thickness value has on the thermal stresses resulting from the selective laser melting process. The researchers that have provided an explanation for this phenomenon agree that smaller layer thicknesses cause larger thermal gradients which would in turn result in higher thermal and residual stresses and increase the possibility of cracking. As to why a smaller layer thickness creates larger thermal gradients, another explanation can be related to how the laser exposure interact with a smaller powder layer thickness and the solid substrate underneath. When every other processing parameter is kept constant, the amount of heat input being distributed from the laser exposure to the melt pool can be assumed to be the same for different layer thickness values. However, when the powder layer deposited is small, a portion of that heat input would be spent trying to increase the temperature of and melt the immediate solid substrate beneath the powder layer which has a larger conductivity compared to the powder. So, that energy would dissipate through the substrate without greatly increasing the temperature of the immediate solid portion of the substrate next to

the melt pool (the HAZ). Consequently, the temperature difference between the solid/liquid interface (which is always about the melting temperature of the material when the laser moves away) and the HAZ would be greater, hence a larger thermal gradient.

5.7. Influence of Hatch Spacing

5.7.1. The Effect of Hatch Spacing on the Formation of Lack of Fusion Defects

The lack of fusion defects are formed during the selective laser melting process when for some reason some portion of the powder has not been exposed enough or at all by the laser beam. The effect of insufficient laser power and exposure time was explained through how they would result in a smaller individual melt pool every time the laser beam is exposed on a spot of the powder bed. Layer thickness influence in the formation of these defects was also discussed and a larger than optimum layer thickness could mean that some portion of the powder bed remains unmelted.

Hatch spacing can have a similar effect on the possibility of formation of lack of fusion defects. Considering the way selective laser melting operates, at each layer, the laser beam travels through a single track at a time and after reaching the end of that track, it moves to the next line which is parallel to the previous one with a distance equal to the value for hatch spacing that has been provided for the machine to follow. Each of these molten and consequently solidified lines has a width which is dependent on the amount of heat being put into the powder and the thermal characteristics of the material being processed.

So, if the distance between these parallel consecutive lines is larger, then the part could be manufactured at a faster rate, improving the commercial value of the selective laser melting process. However, if it is larger than the width of each track, then there would be portions of powder that would remain unmelted which would form the lack of fusion defects in the final

specimen. This is exactly what can be seen in the results of the tests carried out to investigate the influence of hatch spacing on the formation of these defects. A series of specimens were built using different values for laser power, exposure time and hatch spacing (and keeping other processing factors shown in Table. 4.5 constant). They were analysed with optical microscopy and the results were plotted in several diagrams that demonstrate that for a certain laser power and exposure time, as the hatch spacing increases the amount of lack of fusion defects increases as well.

This phenomenon can also be explained through the use of normalized energy density. When a specimen is made using the selective laser melting process, the amount of heat going into the volume of the specimen would increase when the hatch spacing value used increases according to Equation 5.1. As a result, the possibility of some portion of powder remaining unmelted or partially melted should decrease. To investigate this, the normalized energy density for each set of processing parameters used to manufacture a specimen in the study of influence of hatch spacing on the formation of lack fusion defects were calculated using Equation 5.1 and were plotted in Fig. 5.13.

Vandenbroucke and Kruth (Vandenbroucke and Kruth, 2007) examined this relationship by manufacturing specimens out of Ti-6Al-4V and analysing their density through the Archimedes principle and SEM imaging. They found out that using smaller hatch spacing values resulted in lower densities and higher non-spherical porosities. They also calculated the energy density used in building each sample and realized that by using the higher energy densities, they could achieve larger part densities of up to 99.98%.

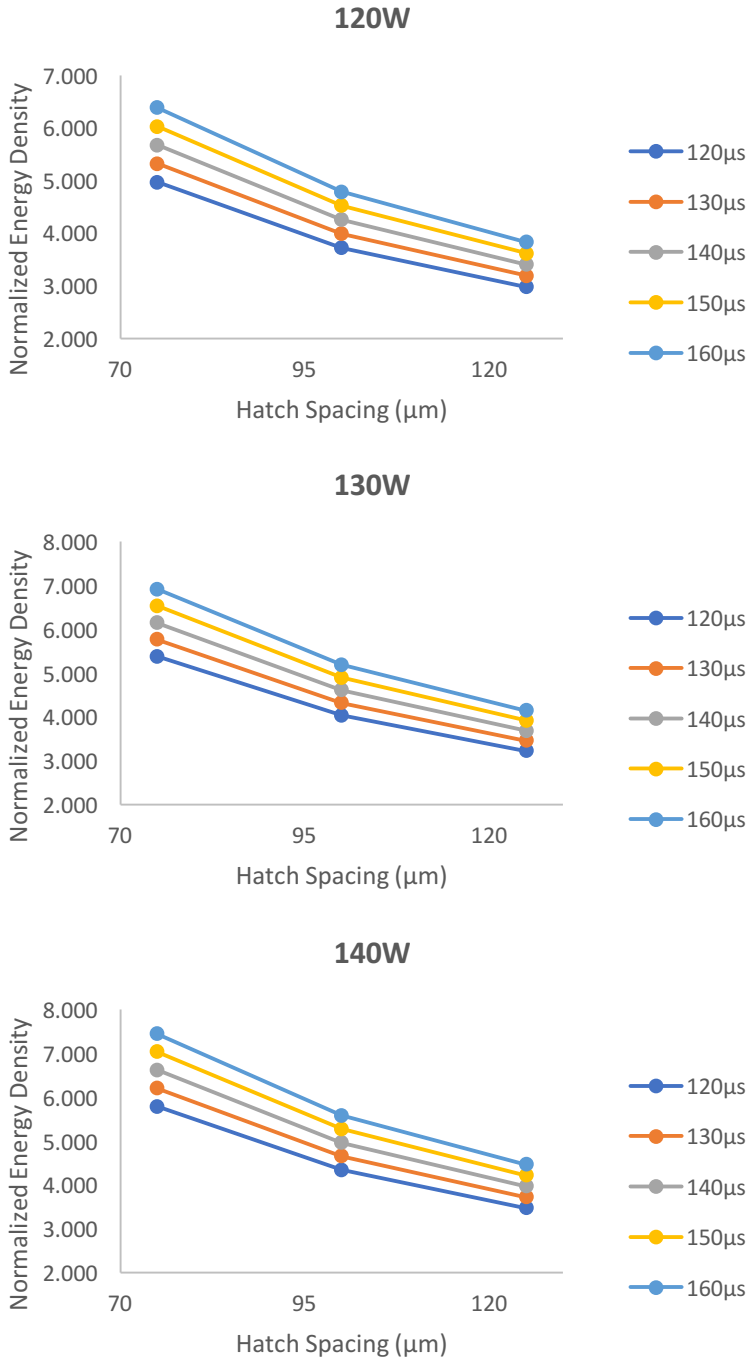

Figure 5.13- The effect of hatch spacing on the normalized energy density for different laser power and exposure times

In another study, Carter et al (Carter, Attallah and Reed, 2012) investigated this same phenomenon by making samples out of CM247LC Ni-superalloy and analysing backscattered SEM micrographs. They presented the same findings in that when hatch spacing values used

were larger, the amount of irregular shaped voids inside the microstructure of the specimens increased.

In Fig. 5.14 which depicts the relationship between the amount of lack of fusion defects and the hatch spacing used, next to how hatch spacing influences the normalized energy density for samples made using 120W laser power and 120-160µs exposure time, it can clearly be observed that when the normalized energy density used to make a specimen is increased through decreasing the hatch spacing value, the possibility of these defects forming decreases. This can further strengthen the validity of using the normalized energy density utilized to manufacture a specimen through the SLM process to predict if it would include lack of fusion defects in its microstructure.

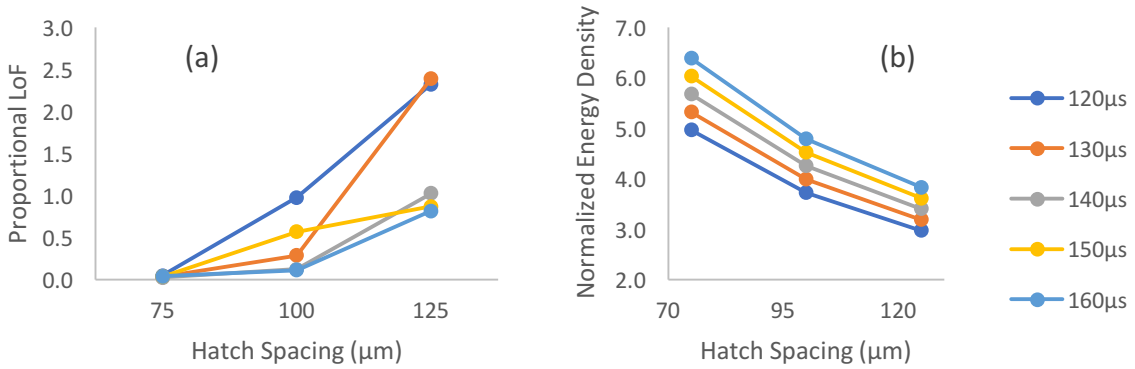

Figure 5.14- The influence of hatch spacing on (a) normalized energy density and (b) formation of lack of fusion defects

5.7.2. The Effect of Hatch Spacing on the Formation of Cracks

The cracking behaviour occurring during the selective laser melting process is directly proportional to the amount of stress the specimen is experiencing which is in turn governed by the thermal gradient and cooling rate it undergoes according to the thermal gradient mechanism theory. Different processing parameters can have an effect on these two process

properties depending on the characteristics of the material being formed and hatch spacing is not an exception in this regard.

In order to investigate the influence that hatch spacing can have on the amount of cracking that can occur in specimens made out of SAM1651 through the SLM process, several samples were manufactured using different laser power, exposure time and hatch spacing values. They were then analysed through optical microscopy and the amount of cracking in their microstructure was determined.

In Fig. 5.15, for example, the cracking of samples built with 130W laser power and 120-160µs exposure time is plotted against the hatch spacing used in each case. It can be clearly noticed that for a certain laser power and exposure time, as the hatch spacing increases, the amount of cracking present in the specimen decreases. There are previous attempts to understand the effect of hatch spacing on the stress conditions occurring in a specimen, which can be helpful in explaining this phenomenon.

In an effort to examine the effects of different processing parameters on residual stresses, Pohl et al (Pohl *et al.*, 2001) used direct metal laser sintering to build thin samples out of pure Iron and DirectSteel 50-V1 powder on top of a steel substrate that was bolted down to a base plate. After the manufacturing process was done, the steel substrate was released from its base plate and the deflection of the substrate caused by the stresses induced during the laser processing was measured.

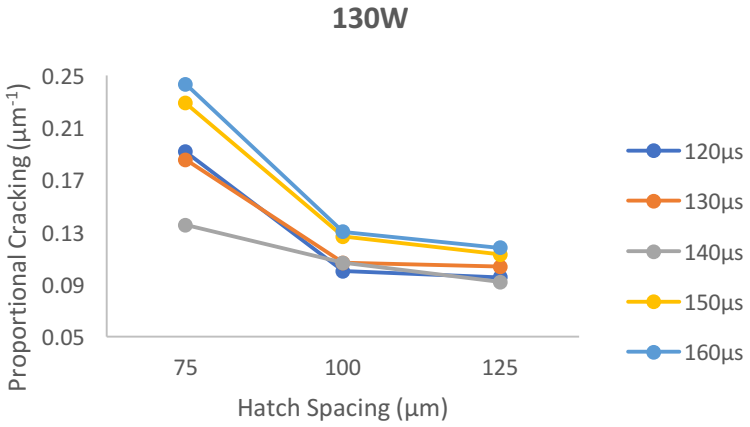

Figure 5.15- The effect of hatch spacing on crack formation in samples made with 130W laser power

As presented in Fig. 5.16, they found that while keeping every other processing parameter constant, when the hatch spacing used to build their samples was larger, the deflection occurring in the steel substrate was smaller, from which they deduced that a smaller hatch spacing would create more thermal and residual stresses in the specimen. To interpret this finding, it was suggested that utilizing a smaller hatch spacing is equal to a more localized heating of the powder bed which would create a more pronounced thermal gradient resulting in larger thermal stresses as opposed to when a more homogeneous heating regime is used. To prevent this, they concluded that whenever a slightly lower density is acceptable, using larger hatch spacing is preferable.

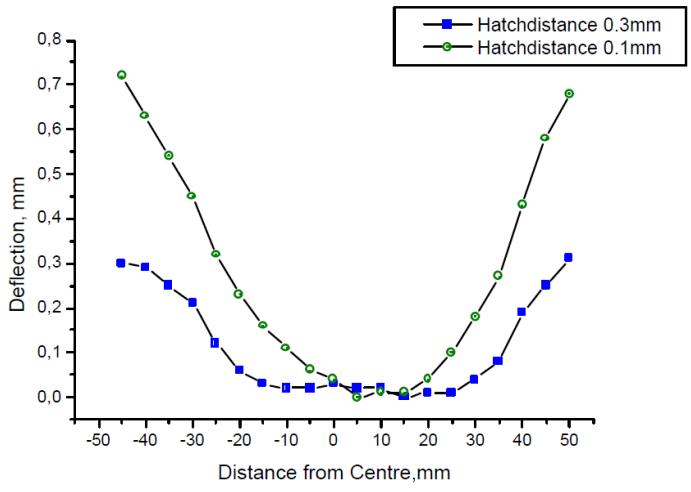

Figure 5.16- Effect of hatch spacing on deflection of the steel substrate of parts made with laser sintering (Pohl et al., 2001)

Furthermore, in the aforementioned study carried out by Carter et al (Carter, Attallah and Reed, 2012), they discovered that specimens manufactured using smaller hatch spacing values, contained more solidification cracks, as depicted in Fig. 5.17, in their backscattered SEM micrographs. They proposed that this might be occurring because a smaller hatch spacing during the selective laser melting process can cause the laser exposure to have an effect of a band of heat moving across the powder bed instead of a fast scanning point source which would help the formation of cracks inside the microstructure of the SLM made parts.

Another way of explaining this effect that hatch spacing seem to have on the stresses caused during the selective laser melting process can be through assessing how the laser exposure is interacting with the powder bed and the solidified parts of the specimen. When the hatch spacing is smaller, the amount of overlap of tracks being melted is larger. This means that when the laser beam is melting a track, a larger portion of an already solidified track, adjacent to the current one, is being melted as well in the process, which means at each point a portion of the heat input is being spent trying to heat up and melt a larger spot of the already solidified neighbouring track.

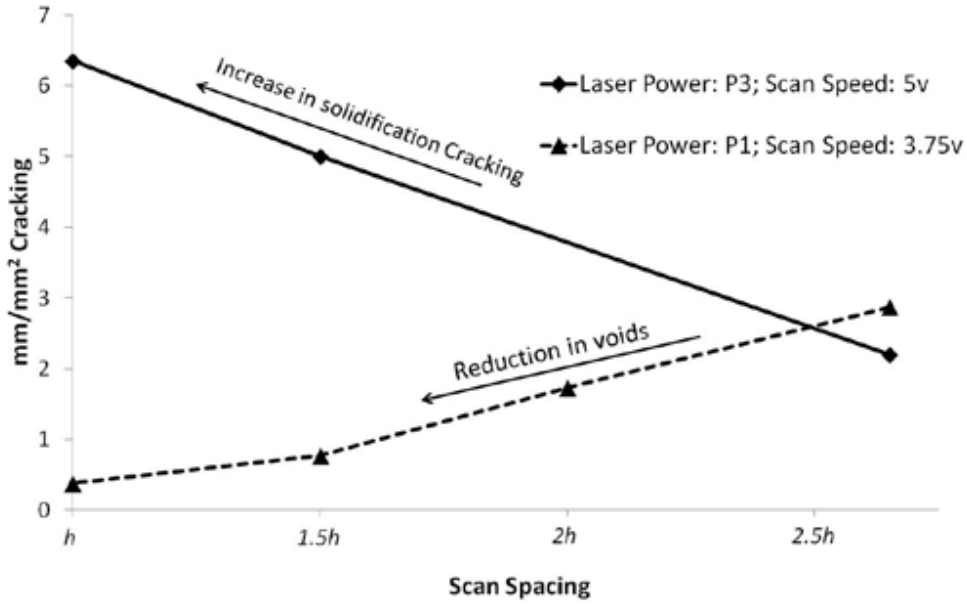

Figure 5.17- The influence of hatch spacing on cracking and void formation (Carter, Attallah and Reed, 2012)

That larger solid spot has a higher conductivity compared to its bordering powder which means that the heat would dissipate faster through the solid spot and its solid surroundings leaving the HAZ around the eventual melt pool with a lower temperature. This means that the temperature difference between the HAZ and the solid/liquid interface around the melt pool would be larger resulting in a larger thermal gradient and hence a larger thermal stress. Conversely, when the hatch spacing is large, at each exposure point, a smaller portion of the already solidified material is being heated up and melted. This results in a larger portion of the heat input being captured by the powder (which has a smaller conductivity), giving the HAZ a larger constant source of heat to raise its temperature with. This causes a smaller temperature gradient between the solid/liquid interface and the HAZ, producing smaller amounts of stress in the process.

5.7.3. The Effect of Hatch Spacing on Amorphicity of the Specimens

When the samples manufactured with different hatch spacing values were investigated through XRD testing, it was discovered that only some of the ones that were made using the smallest hatch spacing were partially crystallized and the rest were fully amorphous. If the hatch spacing used in the selective laser melting method is smaller when the laser beam is fusing a new track, it is also melting a larger portion of the previously melted and solidified track neighbouring the new one.

Since the solidified track has a larger conductivity compared to the powder portion of the material being melted to form the new track, a portion of the heat input would dissipate through it, increasing the temperature of a larger portion of the HAZ. This would result in a larger portion of the specimen experiencing a higher temperature. If this larger portion experiences a temperature higher than the crystallization temperature of the metallic glass,

that portion of the specimen would crystallize. This could be how a smaller hatch spacing could result in crystallization happening in the microstructure of the sample made with SLM.

5.8. Influence of Point Distance

5.8.1. The Effect of Point Distance on the Formation of Lack of Fusion Defects

The point distance corresponds to the spacing between the centres of two adjacent spots on which laser exposure occurs on the powder bed. If the diameter of the resulting melt pools is not large enough to cover the space between them there might be some portion of the powder that remains unmelted. The parameters that control the diameter of individual melt pools, namely laser power and exposure time, were discussed before. In this section, the effect of the point distance on the possibility of formation of lack of fusion defects will be examined.

It is conventional for the point distance used in the selective laser melting process to be chosen in a way that the resulting neighbouring melt pools overlap between 40-60% of each other's diameters to make sure that the emerging melt tracks are fully consolidated. If the point distance utilized in the SLM process is not optimized, there will be some areas of the powder bed between two consecutive melt pools that is not fused together, resulting in the formation of lack of fusion defects in the final microstructure of the specimens manufactured. Another way of looking at the influence of point distance on the formation of irregularly shaped voids is through the amount of heat that is put into the total volume of a specimen manufactured through the SLM process. For this purpose, the normalized energy density resulting from several sets of laser power, exposure time and point distance values used to manufacture different specimens were calculated using Equation 5.1. Other processing

parameters were kept constant and are presented in Table 4.6. These values were then plotted against the point distance used for each specimen (Fig. 5.18).

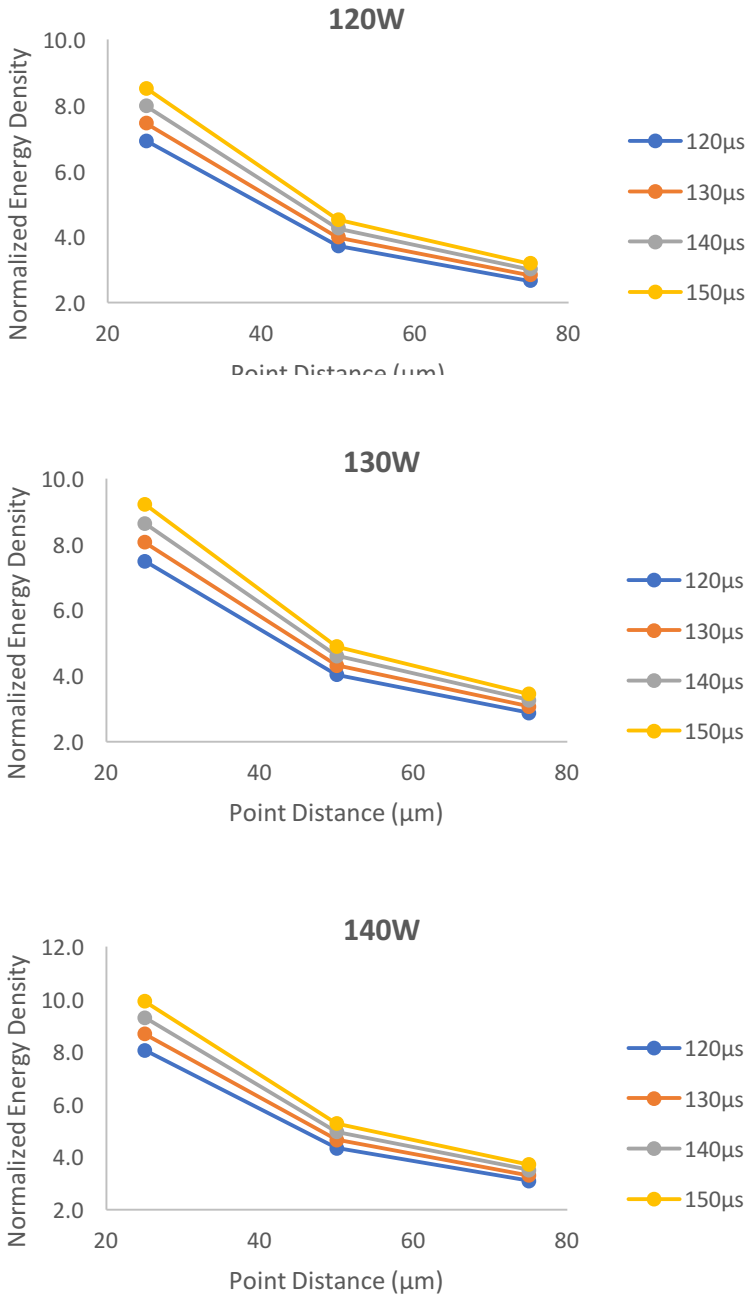

Figure 5.18- The effect of hatch spacing on the normalized energy density for different laser power and exposure times

It can be seen that when the point distance value increases, the resulting normalized energy density decreases which means a smaller amount of heat input has been irradiated into the

whole volume of the specimen. Because of this, the possibility of some portion of the powder remaining unconsolidated and forming lack of fusion defects can increase. To demonstrate this correlation, Fig.5.19 is presented as an example which shows that for specimens manufactured using 130W laser power and 120-150µs exposure time, as the point distance value utilized increases, the normalized energy density decreases and lack of fusion defects increase simultaneously. Once again, this demonstrates that the amount of normalized energy density utilized for building a specimen can be a good indication as to whether the resulting sample will have lack of fusion defects in its microstructure or not.

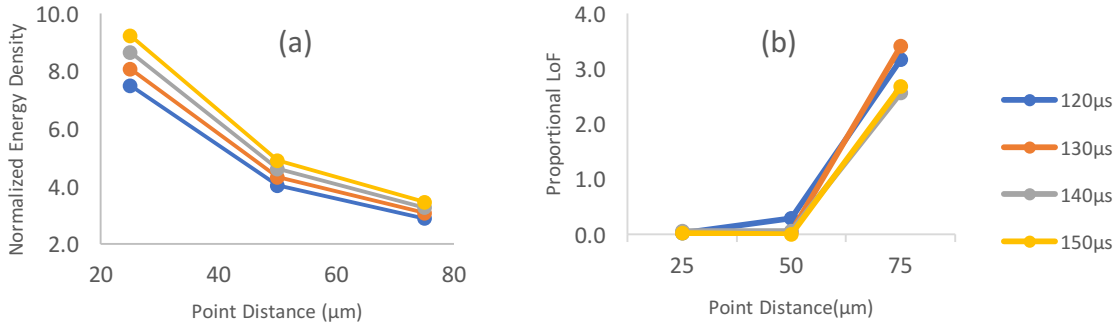

Figure 5.19- The influence of point distance on (a) normalized energy density and (b) formation of lack of fusion defects

It is worth mentioning that the reason the graphs shown in Fig. 5.9, Fig. 5.13 and Fig. 5.18 are not linear is because they are visual representations of Equation 5.1. In each graph, all other parameters constituting E_0^*, are kept constant, except for layer thickness in Fig. 5.9, hatch spacing in Fig. 5.13 and point distance in Fig. 5.18. So, the governing equations are $[E_0^* = C_4/l]$ for Fig. 5.9, $[E_0^* = C_5/h]$ for Fig. 5.13 and $[E_0^* = C_6/x]$ for Fig. 5.18, where:

$$C_4 = \left(Aqt_{exp}/2hx\right)\left(1/\rho C_p\,\Delta T\right) \qquad \text{Equation 5.10}$$

$$C_5 = \left(Aqt_{exp}/2lx\right)\left(1/\rho C_p\,\Delta T\right) \qquad \text{Equation 5.11}$$

$$C_6 = \left(Aqt_{exp}/2hl\right)\left(1/\rho C_p\,\Delta T\right) \qquad \text{Equation 5.12}$$

So, since all the governing equations are essentially different forms of the $y = \frac{1}{x}$ function, their visual representations are showing a limited part of a hyperbola, and not a linear graph.

5.8.2. The Effect of Point Distance on the Formation of Cracks

Point distance is one of the processing parameters that determines the scanning speed of the laser beam in the selective laser melting process and hence controls the amount of heat each melt track is exposed to. Therefore, it can have an effect on the thermal gradients and cooling rate occurring inside the specimen during the SLM process. If the point distance is smaller it can be assumed that a more localized heating regime is in effect during the manufacturing process that can result in larger thermal gradients and hence larger stresses inside the samples being made.

In order to investigate this influence, Fig. 5.20 was constructed as an example of cracking analysis through optical microscopy of specimens manufactured using 140W laser power, 120-150μs exposure time and different point distance values. It can be observed that when a small point distance is utilized the amount of cracking occurring inside the microstructure of the specimens increases significantly.

This phenomenon can be explained similar to what was suggested for the effect that layer thickness and hatch spacing have on the crack formation. When the point distance value used to make specimens is small, at each individual spot of the sample being made, some of the heat input created by the laser exposure would be spent trying to increase the temperature of and melt the powder present at that spot. The rest will be used for the following purpose:

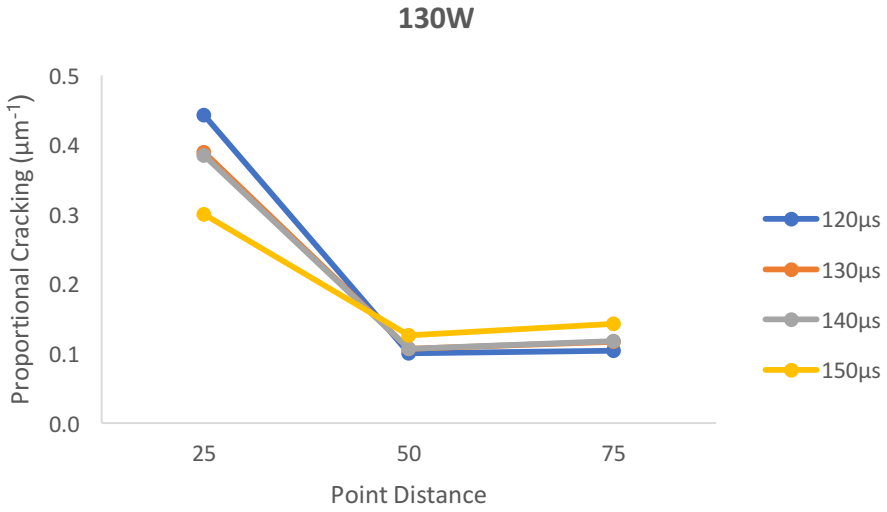

Figure 5.20- The effect of point distance on crack formation in samples made with 130W laser power

a) If the point distance is small enough so that when the laser exposure on a new spot starts, the spot that was being melted beforehand is not fully solidified, some of the heat energy would go toward increasing the temperature of the overlapping portion of the previous spot that is still liquid. Because of the higher conductivity of the liquid compared to the powder, a portion of that heat energy would dissipate into the solidified surroundings of the new melt pool before the temperature of the HAZ could increase significantly. This would result in a large thermal gradient between the solid/liquid interface of the melt pool and its HAZ and hence a large thermal stress would develop consequently.

b) If the point distance is a bit larger, the previous spot has solidified before the new spot is exposed by the laser beam. In this case some of the heat input would go toward increasing the temperature of and melting a portion of the previously solidified spot which has a smaller thermal conductivity compared to the liquid present in case (a), but still a larger conductivity compared to the powder. So, some of the heat would dissipate into the solidified portion of the specimen without increasing the

temperature of the HAZ significantly. Once again this would create a large temperature difference between the area adjacent to the liquid/solid interface and the rest of the HAZ, resulting in a large thermal gradient and hence a large thermal stress.

In either case the resulting thermal gradient is higher than when the point distance is much larger. When the point distance is much larger, laser exposure would be spent melting largely powder, which has a lower conductivity compared to either the liquid or solid form of the material. This would result in the heat being trapped for longer and hence the temperature of the HAZ would be higher resulting in a smaller temperature gradient and thermal stress.

5.8.3. The Effect of Point Distance on the Amorphicity of Specimens

The XRD patterns of the specimens built using different point distances (Fig. 4.35) show that only the ones that were manufactured with the smallest point distance show signs of partial crystallization. Since point distance is one of the constituent factors in determining the beam velocity in the selective laser melting process, one of the approaches in explaining the influence of point distance on amorphicity could be through investigating how the beam velocity interacts with the final microstructure of the specimens.

Manvatkar et al (Manvatkar, De and DebRoy, 2015) used a three dimensional transient heat transfer and fluid flow numerical simulation for a laser deposited single line multilayer 316 stainless steel structure to investigate the effect of beam velocity, among other parameters, on the resulting cooling rate occurring during the build inside the microstructure of the thin-walled samples. They found out that increasing the beam velocity corresponds to a larger cooling rate and suggested that it is due to a lower heat input per unit length.

This reduction in cooling rate during solidification, for a bulk metallic glass, could mean a higher possibility of some portions of the microstructure crystallizing if the cooling rate is reduced enough to be smaller than the critical cooling rate of the metallic glass.

Another way of looking at the effect that point distance can have on the amorphicity of specimens is through the influence it can have on the HAZ around the melt pools. When the point distance is reduced, the heat input of the laser beam would have a larger interaction with the still liquid or already solidified portion of the previous spot that was melted. Since this portion has a higher conductivity, a larger portion of the heat input will dissipate through the HAZ, increasing the temperature of a larger portion of the solidified specimen around the melt, increasing the possibility of a larger area of the HAZ experiencing a temperature higher than the crystallization temperature of the metallic glass, resulting in a higher possibility for a larger portion of the specimen to crystallize at each exposure.

5.9. Recommendations for Selective Laser Melting of SAM1651

- The powder morphology should be as close to spherical as possible. This would help flowability and reduce the risk of LoF defect formation.
- Powder particles should not have internal pores. They add to the porosity of the product significantly.
- Laser power and exposure time should be chosen from the processing window presented in Fig. 5.6.
- The higher the substrate temperature, the lower the chance of internal cracking. It should not be higher than the crystallization temperature obviously.
- Hatch spacing of 100 µm along with layer thickness and point distance of 50 µm seem to produce specimens with the lowest amount of defects.

6. Conclusions

1- It was shown that for specimens fabricated out of SAM1651 alloy through selective laser melting, temperature of the substrate plays a significant role in the amount of cracking observed in the microstructure of the samples.

2- . It was shown when the power and exposure time was increased, while keeping other processing parameters constant, the cooling rate and thermal gradient decreased as a result.

3- It was also demonstrated that when the occurring cooling rate and thermal gradient decreased the possibility and amount of crystallization in the microstructure increased consequently.

4- A few of the specimens that experienced similar cooling rate and thermal gradient values, showed different crystallization behaviour, some being fully amorphous while others were partially crystallized. This was justified through the influence of the melt pool size on the crystallization behaviour of the samples.

5- It was shown that as the exposure time increases, the number of pores inside the microstructure of the specimens decreases to a minimum before increasing again after the exposure time threshold was passed. This was explained through the notion

of existence of two types of pores. The ones that are already existing in the powder particles before the SLM process and the ones that formed during the SLM process.

6- Formation of lack of fusion defects were shown to decrease as laser power and exposure time increased and when they were high enough, lack of fusion defects were completely eliminated. This was attributed to the influence of these processing parameters on the size of the resulting melt pools.

7- It was demonstrated that, typically, for each laser power, when the exposure time increased, the resulting cracking decreased to a minimum, then increased to a maximum before decreasing again. This behaviour was explained through formation and elimination of pores and lack of fusion defects.

8- For each laser power used in the SLM process, certain exposure time values were identified to be the threshold for achieving minimal cracking, porosity, lack of fusion defects and preventing partial crystallization of the microstructure. By assembling these data points, a processing map was constructed which indicates for a set of laser power and exposure time values whether the resulting specimen would have the aforementioned defects at the minimum levels possible or higher.

9- It was discovered that to be in this processing window, the selected laser power and exposure time values had to be larger than their threshold for formation of lack of fusion defects and smaller than their threshold for minimal cracking. It was also shown

that if these values were smaller than the threshold for minimal cracking, they would also satisfy the criteria for obtaining full amorphicity and minimal formation of pores.

10- From investigating the abovementioned processing map, the normalised energy density input was shown to be an appropriate indicator for predicting the amorphicity and defect formation in the specimens. The optimised normalised energy density input was determined to be between 4.5 to 5.3 for achieving fully amorphous microstructures with minimal cracking, porosity and no lack of fusion defects.

11- The amount of lack of fusion defects were reduced as the layer thickness used in the SLM process decreased, while keeping the other parameters constant. This was associated with the depth of the melt pools created being larger or smaller than the layer thickness.

12- The amount of cracking was demonstrated to decrease as the layer thickness used in the SLM process increased. This was attributed to the larger heat sink that would be available at the side of each melt track when the layer thickness is larger, causing smaller thermal gradients.

13- Reducing hatch spacing was shown to decrease the formation of lack of fusion defects. If the hatch spacing used in the SLM process is large, complete overlapping of successive melt tracks would not happen, leaving a portion of the powder unmelted which would result in the lack of fusion defects.

14- Larger values of hatch spacing resulted in less cracking in the microstructure of the specimens.

15- Samples fabricated with smaller hatch spacing had a higher possibility of being partially crystallized.

16- Point distance has a similar effect as hatch spacing has on the formation of lack of fusion defects, meaning as it decreases, the amount of these defects decreases as a result.

17- Point distance was shown to be inversely proportional to the amount of cracking in the specimens. If the point distance is smaller it can be assumed that a more localized heating regime is in effect during the manufacturing process that can result in larger thermal gradients and hence larger stresses inside the samples being made.

18- Decreasing point distance was shown to cause crystallization in the fabricated specimens. Point distance is one of the constituent factors in determining the beam velocity in the selective laser melting process. Increasing the point distance and hence the beam velocity corresponds to a larger cooling rate which is suggested to be due to a lower heat input per unit length.

7. Future Works

7.1. One of the initial objectives of this study was to fabricate specimens from SAM1651 alloy that would be fully amorphous, dense and crack-free. This was intended to be carried out through optimisation of the processing parameters of the selective laser melting manufacturing technique. The first part of this objective was successfully achieved through fabrication of fully amorphous samples, while the other two parts were not. Therefore, the following suggestions are proposed to obtain these goals:

a) Utilising powder particles that do not have internal pores. Some of the purchased powder particles used in this study contained pre-existing internal pores that were remnants of the gas atomization stage of their production. Through optimisation of the parameters used to fabricate these powder particles, this type of porosity can be significantly reduced or even eliminated. This would considerably enhance the density of the specimens fabricated using this powder. Morphology of the powder can also be improved to become more spherical in the gas atomization stage, which would improve the flowability of the powder.

b) Reduction of the cracking in the specimens was carried out through utilising a pre-heated substrate, however it was not eliminated. Forming bulk metallic glasses in their super cooled liquid region has been shown to be very successful, because of their superplasticity in that temperature range. Hence

performing the SLM process above the glass transition temperature of the glass forming alloy might provide a good opportunity for manufacturing crack-free samples. Although crystallisation of the material should be closely monitored, as higher temperatures could cause higher levels of crystallization in the specimens.

c) Another way of combating the cracking problem could be altering the composition of the alloy. For example, it has been shown that small additions of cobalt to SAM1651 would increase the ductility and toughness of the material significantly. This addition can be done in the alloying stage, before production of the powder particle through gas atomization. Another strategy might be mixing of pure cobalt powder particles with SAM1651 powder and carrying out the SLM process using the powder mixture.

7.2. In order to obtain a better understanding of the influence of hatch spacing, layer thickness and point distance on defect formation during the SLM process, further simulation of the interaction between the laser exposure and the powder bed and the resulting thermal gradient and cooling rate can be done, using different values for these processing parameters. Also, separate modelling of the thermal stresses occurring in the specimens as a result of the interaction of these parameters can shine a better a light on the behaviour of cracking in the resulting samples.

8. References

A. Inoue, T. Masumoto, S. Arakawa, and T. I. (1978) 'Amorphous High-Carbon Alloy Steels Rapidly Quenched from Melts', *Transactions of the Japan Institute of Metals*, 19(8), pp. 303–304.

Aboulkhair, N. T. *et al.* (2014) 'Reducing porosity in AlSi10Mg parts processed by selective laser melting', *Additive Manufacturing*. Elsevier B.V., 1, pp. 77–86. doi: 10.1016/j.addma.2014.08.001.

Ajdelsztajn, L. *et al.* (2009) 'High-velocity oxygen fuel thermal spray of Fe-based amorphous alloy: A numerical and experimental study', *Metallurgical and Materials Transactions A: Physical Metallurgy and Materials Science*, 40(9), pp. 2231–2240. doi: 10.1007/s11661-009-9900-7.

Akihisa, I. *et al.* (1988) 'New Amorphous Mg-Ce-Ni Alloys with High Strength and Good Ductility : Condensed Matter', 27(12), p. L2248.

Ali, H. *et al.* (2017) 'In-situ residual stress reduction, martensitic decomposition and mechanical properties enhancement through high temperature powder bed pre-heating of Selective Laser Melted Ti6Al4V', *Materials Science and Engineering A*, 695(February), pp. 211–220. doi: 10.1016/j.msea.2017.04.033.

Alkahari, M. R. *et al.* (2012) 'Thermal Conductivity of Metal Powder and Consolidated Material Fabricated via Selective Laser Melting', *Key Engineering Materials*, 523–524, pp. 244–249. doi: 10.4028/www.scientific.net/KEM.523-524.244.

Amiya, K. and Inoue, A. (2008) 'Fe- (Cr , Mo) - (C , B) -Tm BULK METALLIC GLASSES WITH HIGH STRENGTH AND HIGH GLASS-FORMING ABILITY', *Change*, 18, pp. 0–2.
Angell, C. A. (1995) 'Formation of Glasses from Liquids and Biopolymers', *Science*, 267(5206), pp. 1924–1935. doi: 10.1126/science.267.5206.1924.

Argon, A. S. (1982) 'Mechanisms of inelastic deformation in metallic glasses', *Journal of Physics and Chemistry of Solids*, 43(10), pp. 945–961. doi: 10.1016/0022-3697(82)90111-1.
Ashby, M. F. and Greer, A. L. (2006) 'Metallic glasses as structural materials', *Scripta Materialia*, 54(3), pp. 321–326. doi: https://doi.org/10.1016/j.scriptamat.2005.09.051.

van Belle, L., Vansteenkiste, G. and Boyer, J. C. (2013) 'Investigation of Residual Stresses Induced during the Selective Laser Melting Process', *Key Engineering Materials*, 554–557, pp. 1828–1834. doi: 10.4028/www.scientific.net/KEM.554-557.1828.

Böhmer, R. *et al.* (1993) 'Nonexponential relaxations in strong and fragile glass formers', *The Journal of Chemical Physics*, 99(5), pp. 4201–4209. doi: 10.1063/1.466117.

Boom, R., Boer, F. R. De and Miedema, A. R. (1976) 'On the heat of mixing of liquid alloys', *Journal of the Less Common Metals*, 45(2), pp. 237–245. doi: https://doi.org/10.1016/0022-5088(76)90270-8.

Bremen, S., Meiners, W. and Diatlov, A. (2012) 'Selective Laser Melting. A manufacturing technology for the future?', *Laser Technik Journal*, 9, pp. 33–38. doi: 10.1002/latj.201290018.

Brif, Y., Thomas, M. and Todd, I. (2015) 'The use of high-entropy alloys in additive manufacturing', *Scripta Materialia*. Acta Materialia Inc., 99, pp. 93–96. doi: 10.1016/j.scriptamat.2014.11.037.

Busch, R. *et al.* (1995) 'Decomposition and primary crystallization in undercooled Zr 41.2Ti13.8Cu12.5Ni10.0Be 22.5 melts', *Applied Physics Letters*, 67(1995), p. 1544. doi: 10.1063/1.114487.

Carter, L. N. *et al.* (2016) 'Process optimisation of selective laser melting using energy density model for nickel based superalloys', *Materials Science and Technology*, 836(June 2017), pp. 1–5. doi: 10.1179/1743284715Y.0000000108.

Carter, L. N., Attallah, M. M. and Reed, R. C. (2012) 'Laser Powder Bed Fabrication of Nickel-Base Superalloys: Influence of Parameters; Characterisation, Quantification and Mitigation of Cracking', *Superalloys 2012*, pp. 577–586. doi: 10.1002/9781118516430.ch64.

Carter, L. N., Essa, K. and Attallah, M. M. (2015) 'Optimisation of selective laser melting for a high temperature Ni-superalloy', *Rapid Prototyping Journal*, 21(4), pp. 423–432. doi: 10.1108/RPJ-06-2013-0063.

Chen, H. . (1974) 'Thermodynamic considerations on the formation and stability of metallic glasses', *Acta Metallurgica*, 22(12), pp. 1505–1511. doi: 10.1016/0001-6160(74)90112-6.

Chen, H. S. (2000) 'Glassy metals', *Reports on Progress in Physics*, 43(4), pp. 353–432. doi: 10.1088/0034-4885/43/4/001.

Chen, N. *et al.* (2013) 'A novel Ti-based nanoglass composite with submicron-nanometer-sized hierarchical structures to modulate osteoblast behaviors', *Journal of Materials Chemistry B*, 1, p. 2568.

Cheney, J. and Vecchio, K. (2007) 'Prediction of glass-forming compositions using liquidus temperature calculations', *Materials Science and Engineering A*, 471(1–2), pp. 135–143. doi: 10.1016/j.msea.2007.02.120.

Choi, J. S. *et al.* (2007) 'Application of neutron-absorbing structural-amorphous metal (SAM) coatings for spent nuclear fuel (SNF) container to enhance criticality safety controls', *Materials Research Society Symposium Proceedings*, 985, pp. 249–254. Available at: http://www.scopus.com/inward/record.url?eid=2-s2.0-41549106817&partnerID=tZOtx3y1.

Cohen, M. H. and Grest, G. S. (1979) 'Liquid-glass transition, a free-volume approach', *Physical Review B*, 20(3), pp. 1077–1098. doi: 10.1103/PhysRevB.20.1077.

Dahotre, N. B. and Harimkar, S. P. (2008) *Laser fabrication and manufacturing of materials*, *Laser Fabrication and Machining of Materials, by N.B. Dahotre and S. Harimkar. Berlin: Springer, 2008. ISBN: 978-0-387-72343-3*.

Dai, K. and Shaw, L. (2004) 'Thermal and mechanical finite element modeling of laser forming from metal and ceramic powders', *Acta Materialia*, 52(1), pp. 69–80. doi: 10.1016/j.actamat.2003.08.028.

Dai, K. and Shaw, L. (2006) 'Parametric studies of multi-material laser densification', *Materials Science and Engineering A*, 430(1–2), pp. 221–229. doi: 10.1016/j.msea.2006.05.113.

Davies, H. A. and Lewis, B. G. (1975) 'A generalised kinetic approach to metallic glass formation', *Scripta Metallurgica*, 9(10), pp. 1107–1112.

Demetriou, M. D. *et al.* (2007) 'Expansion evolution during foaming of amorphous metals', *Materials Science and Engineering A*, 448–451, pp. 863–867. doi: 10.1016/j.msea.2006.02.299.

Demetriou, M. D. *et al.* (2011) 'A damage-tolerant glass', *Nature Materials*. Nature Publishing Group, 10, p. 123. Available at: http://dx.doi.org/10.1038/nmat2930.

Eckert, J. (1999) 'Mechanical Alloying of Bulk Metallic Glass Forming Systems', *Journal of Metastable and Nanocrystalline Materials*, 2–6, pp. 3–12. doi: 10.4028/www.scientific.net/JMNM.2-6.3.

Fan, G. J., Choo, H. and Liaw, P. K. (2007) 'A new criterion for the glass-forming ability of liquids', *Journal of Non-Crystalline Solids*, 353(1), pp. 102–107. doi: https://doi.org/10.1016/j.jnoncrysol.2006.08.049.

Farmer, J. *et al.* (2004) *High-Performance Corrosion-Resistant Materials: Iron-Based Amorphous-Metal Thermal-Spray Coatings*. Livermore, CA. doi: 10.2172/925684.

Farmer, J. *et al.* (2009) 'Iron-Based amorphous metals: High-performance corrosion-resistant material development', *Metallurgical and Materials Transactions A: Physical Metallurgy and Materials Science*, 40(6), pp. 1289–1305. doi: 10.1007/s11661-008-9779-8.

Farmer, J. C. *et al.* (1991) 'Corrosion models for performance assessment of high-level radioactive-waste containers', *Nuclear Engineering and Design*, 129(1), pp. 57–88. doi: 10.1016/0029-5493(91)90329-G.

Farmer, J. C. *et al.* (2005) 'Corrosion Characterization of Iron-Based High-Performance Amorphous-Metal Thermal-Spray Coatings', *Volume 7: Operations, Applications, and Components*, 2005, pp. 583–589. doi: 10.1115/PVP2005-71664.

Farmer, J. C. *et al.* (2006) 'Corrosion Resistance of Iron-Based Amorphous Metal Coatings', *Volume 7: Operations, Applications, and Components*, 2006, pp. 685–691. doi: 10.1115/PVP2006-ICPVT-11-93835.

Farmer, J. C. *et al.* (2007) *Corrosion Resistances of Iron-Based Amorphous Metals with Yttrium and Tungsten Additions in Hot Calcium Chloride Brine & Natural Seawater: Fe48Mo14Cr15Y2C15B6 and W-Containing Variants*, *ECS Transactions*. doi: 10.1149/1.2789251.

Fischer, P. *et al.* (2002) 'A model for the interaction of near-infrared laser pulses with metal powders in selective laser sintering', *Applied Physics a-Materials Science & Processing*, 74(4), pp. 467–474. doi: 10.1007/s003390101139.

Foroozmehr, A. *et al.* (2016) 'Finite Element Simulation of Selective Laser Melting process considering Optical Penetration Depth of laser in powder bed', *Materials and Design*. Elsevier Ltd, 89, pp. 255–263. doi: 10.1016/j.matdes.2015.10.002.

Ge, Y. *et al.* (2010) 'Temperature and strain rate dependence of deformation behavior of Zr65Al7.5Ni10Cu17.5', *Materials Chemistry and Physics*. Elsevier B.V., 124(1), pp. 25–28. doi: 10.1016/j.matchemphys.2010.06.057.

Ge, Y. N. *et al.* (2010) 'Temperature and strain rate dependence of deformation behavior of Zr65Al7.5Ni10Cu17.5', *Materials Chemistry and Physics*. Elsevier B.V., 124(1), pp. 25–28. doi: 10.1016/j.matchemphys.2010.06.057.

Gilbert, C. J., Lippmann, J. M. and Ritchie, R. O. (1998) 'Fatigue of a Zr-Ti-Cu-Ni-Be bulk amorphous metal: Stress/life and crack-growth behavior', *Scripta Materialia*, 38(4), pp. 537–542. doi: https://doi.org/10.1016/S1359-6462(97)00522-8.

Gong, H., Rafi, K., *et al.* (2014) 'Analysis of defect generation in Ti-6Al-4V parts made using powder bed fusion additive manufacturing processes', *Additive Manufacturing*. Elsevier B.V., 1, pp. 87–98. doi: 10.1016/j.addma.2014.08.002.

Gong, H., Christiansen, D., *et al.* (2014) 'Melt Pool Characterization for Selective Laser Melting of Ti-6Al-4V Pre-alloyed Powder', *Solid Freeform Fabrication Symposium*, (August), pp. 256–267.

Greer, A. L. (1993) 'Confusion by design', *Nature*, 366(6453), pp. 303–304. Available at: http://dx.doi.org/10.1038/366303a0.

Gu, D. *et al.* (2012) 'Densification behavior, microstructure evolution, and wear performance of selective laser melting processed commercially pure titanium', *Acta Materialia*, 60(9), pp. 3849–3860. doi: 10.1016/j.actamat.2012.04.006.

Gu, J. *et al.* (2013) 'Effects of annealing on the hardness and elastic modulus of a Cu36Zr48Al8Ag8 bulk metallic glass', *Materials and Design*, 47, pp. 706–710. doi: 10.1016/j.matdes.2012.12.071.

Gu, X. J., Poon, S. J. and Shiflet, G. J. (2007) 'Mechanical properties of iron-based bulk metallic glasses', *Journal of Materials Research*, 22(2), pp. 344–351. doi: 10.1557/jmr.2007.0036.

Guo, H. *et al.* (2007) 'Tensile ductility and necking of metallic glass', *Nature Materials*, 6(10), pp. 735–739. doi: 10.1038/nmat1984.

Guo, L. J. (2007) 'Nanoimprint lithography: Methods and material requirements', *Advanced Materials*, 19(4), pp. 495–513. doi: 10.1002/adma.200600882.

Guo, S. F. *et al.* (2008) 'The effect of Hf substitution for Zr on glass forming ability and magnetic property of FeCoZrMoBAlY bulk metallic glasses', *Journal of Alloys and Compounds*, 458(1–2), pp. 214–217. doi: 10.1016/j.jallcom.2007.04.015.

Guo, S. F. *et al.* (2013) 'Novel centimeter-sized Fe-based bulk metallic glass with high corrosion resistance in simulated acid rain and seawater', *Journal of Non-Crystalline Solids*, 369, pp. 29–33. doi: 10.1016/j.jnoncrysol.2013.02.026.

Guo, S. F. *et al.* (2014) 'Fe-based bulk metallic glasses: Brittle or ductile?', *Applied Physics Letters*, 105(16). doi: 10.1063/1.4899124.

Guo, S. F., Wu, Z. Y. and Liu, L. (2009) 'Preparation and magnetic properties of FeCoHfMoBY bulk metallic glasses', *Journal of Alloys and Compounds*, 468(1–2), pp. 54–57. doi: 10.1016/j.jallcom.2008.01.066.

Gusarov, A. V. and Smurov, I. (2010) 'Modeling the interaction of laser radiation with powder bed at selective laser melting', *Physics Procedia*, 5(PART 2), pp. 381–394. doi: 10.1016/j.phpro.2010.08.065.

Ha, H. M. and Payer, J. H. (2009) 'Examination of galvanic action between fe-based bulk metallic glass and crystalline alloys', *Metallurgical and Materials Transactions A: Physical Metallurgy and Materials Science*, 40(6), pp. 1334–1343. doi: 10.1007/s11661-008-9653-8.

Hara, S. *et al.* (2003) 'Hydrogen permeation through amorphous-Zr36−xHfxNi64-alloy membranes', *Journal of Membrane Science*, 211(1), pp. 149–156. doi: https://doi.org/10.1016/S0376-7388(02)00416-7.

He, Q. *et al.* (2011) 'Locating bulk metallic glasses with high fracture toughness: Chemical effects and composition optimization', *Acta Materialia*, 59(1), pp. 202–215. doi: https://doi.org/10.1016/j.actamat.2010.09.025.

Herold, U. and Koster, U. (1978) 'The influence of metal or metalloid exchange on crystallisation of amorphous Fe–B alloys', *Rapidly quenched metals III*, p. 281.

Hildal, K., Sekido, N. and Perepezko, J. H. (2006) 'Critical cooling rate for Fe48Cr15Mo14Y2C15B6 bulk metallic glass formation', *Intermetallics*, 14(8–9), pp. 898–902. doi: 10.1016/j.intermet.2006.01.036.

Hu, Y. *et al.* (2003) 'Synthesis of Fe-based bulk metallic glasses with low purity materials by multi-metalloids addition', *Materials Letters*, 57(18), pp. 2698–2701. doi: 10.1016/S0167-577X(02)01360-5.

Inoue, A. *et al.* (1991) 'Mg--Cu--Y Amorphous Alloys With High Mechanical Strengths Produced by a Metallic Mold Casting Method.pdf', *Materials transactions, JIM*, 32, pp. 609–616.

Inoue, A. *et al.* (1994) 'Preparation of bulky Zr-based amorphous alloys by a zone melting method', *Materials Transactions, JIM*, pp. 923–926. doi: 10.2320/matertrans1989.35.923.

Inoue, A. (1995) 'High Strength Bulk Amorphous Alloys with Low Critical Cooling Rates (<I>Overview</I>)', *Materials Transactions, JIM*, 36(7), pp. 866–875. doi: 10.2320/matertrans1989.36.866.

Inoue, A. (2000) 'Stabilization of metallic supercooled liquid and bulk amorphous alloys', *Acta Materialia*, 48(1), pp. 279–306. doi: 10.1016/S1359-6454(99)00300-6.

Inoue, A. *et al.* (2003) 'Cobalt-based bulk glassy alloy with ultrahigh strength and soft magnetic properties', *Nature Materials*. Nature Publishing Group, 2, p. 661. Available at: http://dx.doi.org/10.1038/nmat982.

Inoue, A. *et al.* (2003) 'Enhanced shot peening effect for steels by using Fe-based glassy alloy shots', *Materials Transactions*, 44(11), pp. 2391–2395. doi: 10.2320/matertrans.44.2391.

Inoue, A. and Gook, J. S. (1995) 'Fe-Based Ferromagnetic Glassy Alloys with Wide Supercooled Liquid Region', *Materials Transactions Jim*, pp. 1180–1183. doi: 2916147.

Inoue, A. and Shen, B. L. (2004) 'A new Fe-based bulk glassy alloy with outstanding mechanical properties', *Advanced Materials*, 16(23–24), pp. 2189–2192. doi: 10.1002/adma.200400301.

Inoue, A., Shen, B. L. and Chang, C. T. (2004) 'Super-high strength of over 4000 MPa for Fe-based bulk glassy alloys in [(Fe1-xCox)0.75B0.2Si 0.05]96Nb4 system', *Acta Materialia*, 52(14), pp. 4093–4099. doi: 10.1016/j.actamat.2004.05.022.

Inoue, A., Shinohara, Y. and Gook, J. S. (1995) 'Thermal and magnetic properties of bulk Fe-based glassy alloys prepared by copper mold casting.pdf', *Materials Transactions JIM*, pp. 1427–1433. doi: 10.2320/matertrans1989.36.1427.

Inoue, A. and Takeuchi, A. (2011) 'Recent development and application products of bulk glassy alloys', *Acta Materialia*. Acta Materialia Inc., 59(6), pp. 2243–2267. doi: 10.1016/j.actamat.2010.11.027.

Inoue, A. and Zhang, T. (1995) 'Fabrication of Bulky Zr-Based Glassy Alloys by Suction Casting into Copper Mold', *Materials Transactions, JIM*, pp. 1184–1187. doi: 10.2320/matertrans1989.36.1184.

Inoue, A., Zhang, T. and Masumoto, T. (1990) 'Zr-Al-Ni Amorphous Alloys with High Glass Transition Temperature and Significant Supercooled Liquid Region', *Materials Transactions, JIM*, pp. 177–183. doi: 10.2320/matertrans1989.31.177.

Ion, J. C., Shercliff, H. R. and Ashby, M. F. (1992) 'Diagrams for laser materials processing', *Acta Metallurgica et Materialia*, 40(7), pp. 1539–1551. doi: 10.1016/0956-7151(92)90097-X.

Izumi, H. *et al.* (1984) 'FATIGUE PROPERTIES OF AMORPHOUS Ni75Si8B17 AND Co75Si10B15 ALLOYS.', *Nippon Kinzoku Gakkai-si*, 48(4), pp. 337–371. Available at: https://www.scopus.com/inward/record.uri?eid=2-s2.0-0021121352&partnerID=40&md5=c409c98c2238f66ff358ecfda1a99c39.

Jhabvala, J. *et al.* (2010) 'On the effect of scanning strategies in the selective laser melting process', *Virtual and Physical Prototyping*, 5(2), pp. 99–109. doi: 10.1080/17452751003688368.

Johnson, W. L. (1999) 'Bulk Glass-Forming Metallic Alloys: Science and Technology', *MRS Bulletin*. Cambridge University Press, 24(10), pp. 42–56. doi: 10.1557/S0883769400053252.

Johnson, W. L. and Samwer, K. (2005) 'A universal criterion for plastic yielding of metallic glasses with a (T/Tg)2/3 temperature dependence', *Physical Review Letters*, 95(19), pp. 2–5. doi: 10.1103/PhysRevLett.95.195501.

Johnson, W. and Veazey, C. (2008) *Viscous Liquid Foam- Bulk Metallic Glass (Foam)*, *NASA Webpage*. Available at: http://www.nasa.gov/centers/marshall/news/background/facts/foam.html.

Jung, H. Y. *et al.* (2015) 'Fabrication of Fe-based bulk metallic glass by selective laser melting: A parameter study', *Materials & Design*. Elsevier Ltd, 86(August), pp. 703–708. doi: 10.1016/j.matdes.2015.07.145.

Katakam, S., Santhanakrishnan, S. and Dahotre, N. B. (2012) 'Fe-based amorphous coatings on AISI 4130 structural steel for corrosion resistance', *Jom*, 64(6), pp. 709–715. doi: 10.1007/s11837-012-0338-9.

Kawamura, Y. *et al.* (1996) 'Deformation behavior of $Zr_{65}Al_{10}Ni_{10}Cu_{15}$ glassy alloy with wide supercooled liquid region', *Applied Physics Letters*, 69(9), pp. 1208–1210. doi: 10.1063/1.117413.

Kawamura, Y. *et al.* (1998) 'Workability of the supercooled liquid in the Zr65Al10Ni10Cu15 bulk metallic glass', *Acta Materialia*, 46(1), pp. 253–263. doi: 10.1016/S1359-6454(97)00235-8.

Kawamura, Y. *et al.* (2001) 'Newtonian and non-Newtonian viscosity of supercooled liquid in metallic glasses', *Materials Science and Engineering A*, 304–306(1–2), pp. 674–678. doi: 10.1016/S0921-5093(00)01562-8.

Kempen, K. *et al.* (2013) 'Lowering thermal gradients in Selective Laser melting by pre-heating the baseplate', *Solid Freeform Fabrication Proceedings*, 24. doi: 10.1017/CBO9781107415324.004.

Khairallah, S. A. and Anderson, A. (2014) 'Mesoscopic simulation model of selective laser melting of stainless steel powder', *Journal of Materials Processing Technology*. Elsevier B.V., 214(11), pp. 2627–2636. doi: 10.1016/j.jmatprotec.2014.06.001.

Kishitake, K., Era, H. and Otsubo, F. (1996) 'Characterization of plasma sprayed Fe-10Cr-10Mo-(C,B) amorphous coatings', *Journal of Thermal Spray Technology*, 5(2), pp. 145–153. doi: 10.1007/BF02646428.

Klement, W., Willens, R. H. and Duwez, P. O. L. (1960) 'Non-crystalline Structure in Solidified Gold-Silicon Alloys', *Nature*, 187(4740), pp. 869–870. Available at: http://dx.doi.org/10.1038/187869b0.

Krakhmalev, P. and Yadroitsev, I. (2014) 'Microstructure and properties of intermetallic composite coatings fabricated by selective laser melting of Ti-SiC powder mixtures', *Intermetallics*. Elsevier Ltd, 46, pp. 147–155. doi: 10.1016/j.intermet.2013.11.012.

Kruth, J.-P. *et al.* (2012) 'Assessing and comparing influencing factors of residual stresses in selective laser melting using a novel analysis method', *Proceedings of the Institution of Mechanical Engineers, Part B: Journal of Engineering Manufacture*, 226(6), pp. 980–991. doi: 10.1177/0954405412437085.

Kruth, J. P. *et al.* (2004) 'Selective laser melting of iron-based powder', *Journal of Materials Processing Technology*, 149(1–3), pp. 616–622. doi: 10.1016/j.jmatprotec.2003.11.051.

Kumar, G., Tang, H. X. and Schroers, J. (2009) 'Nanomoulding with amorphous metals', *Nature*. Nature Publishing Group, 457(7231), pp. 868–872. doi: 10.1038/nature07718.

Lee, P. Y. *et al.* (2007) 'Fabrication of Mg-Y-Cu bulk metallic glass by mechanical alloying and hot consolidation', *Materials Science and Engineering A*, 448–451, pp. 1095–1098. doi: 10.1016/j.msea.2006.02.237.

Lewandowski, J. J. *et al.* (2008) 'Tough Fe-based bulk metallic glasses', *Applied Physics Letters*, 92(9), pp. 2006–2009. doi: 10.1063/1.2890489.

Lewandowski, J. J., Wang, W. H. and Greer, A. L. (2005) 'Intrinsic plasticity or brittleness of metallic glasses', *Philosophical Magazine Letters*, 85(2), pp. 77–87. doi: 10.1080/09500830500080474.

Li, R. *et al.* (2010) 'Densification behavior of gas and water atomized 316L stainless steel powder during selective laser melting', *Applied Surface Science*. Elsevier B.V., 256(13), pp. 4350–4356. doi: 10.1016/j.apsusc.2010.02.030.

Li, R. *et al.* (2012) 'Balling behavior of stainless steel and nickel powder during selective laser melting process', *International Journal of Advanced Manufacturing Technology*, 59(9–12), pp. 1025–1035. doi: 10.1007/s00170-011-3566-1.

Li, X. P., Kang, C. W., Huang, H., Zhang, L. C., *et al.* (2014) 'Selective laser melting of an Al86Ni6Y4.5Co2La1.5 metallic glass: Processing, microstructure evolution and mechanical properties', *Materials Science and Engineering A*, 606, pp. 370–379. doi: 10.1016/j.msea.2014.03.097.

Li, X. P., Kang, C. W., Huang, H. and Sercombe, T. B. (2014) 'The role of a low-energy-density re-scan in fabricating crack-free Al85Ni5Y6Co2Fe2 bulk metallic glass composites via selective laser melting', *Materials and Design*, 63, pp. 407–411. doi: 10.1016/j.matdes.2014.06.022.

Li, X. P. *et al.* (2015) 'Effect of substrate temperature on the interface bond between support and substrate during selective laser melting of Al-Ni-Y-Co-La metallic glass', *Materials and Design*, 65, pp. 1–6. doi: 10.1016/j.matdes.2014.08.065.

Li, X. P. *et al.* (2016) 'Selective laser melting of Zr-based bulk metallic glasses: Processing, microstructure and mechanical properties', *Materials & Design*, 112, pp. 217–226. doi: 10.1016/j.matdes.2016.09.071.

Lian, T., Day, S. D. and Farmer, J. C. (2006) 'Corrosion Resistance of Structural Amorphous Metal'. doi: 10.2172/895719.

Liu, Q. C. *et al.* (2014) 'The Effect of Manufacturing Defects on the Fatigue Behaviour of Ti-6Al-4V Specimens Fabricated Using Selective Laser Melting', *Advanced Materials Research*. Trans Tech Publications, 891–892, pp. 1519–1524. doi: 10.4028/www.scientific.net/AMR.891-892.1519.

Liu, Y. H. *et al.* (2007) 'Super Plastic Bulk Metallic Glasses at Room Temperature', *Science*, 315(5817), pp. 1385–1388. doi: 10.1126/science.1136726.

Loh, L. E. *et al.* (2014) 'Selective Laser Melting of aluminium alloy using a uniform beam profile', *Virtual and Physical Prototyping*. Taylor & Francis, 9(1), pp. 11–16. doi: 10.1080/17452759.2013.869608.

Lopez-Botello, O. *et al.* (2017) 'Two-dimensional simulation of grain structure growth within selective laser melted AA-2024', *Materials & Design*. The Authors, 113, pp. 369–376. doi: 10.1016/j.matdes.2016.10.031.

Louzguine-Luzgin, D., Louzguina-Luzgina, L. and Churyumov, A. (2012) 'Mechanical Properties and Deformation Behavior of Bulk Metallic Glasses', *Metals*, 3(1), pp. 1–22. doi: 10.3390/met3010001.

Louzguine-Luzgin, D. V *et al.* (2014) 'Optically transparent magnetic and electrically conductive Fe–Cr–Zr ultra-thin films', *physica status solidi (a)*, 211(5), pp. 999–1004. doi: 10.1002/pssa.201300560.

Lu, Z. P. *et al.* (2004) 'Structural amorphous steels', *Physical Review Letters*, 92(24), pp. 245503–1. doi: 10.1103/PhysRevLett.92.245503.

Lu, Z. P. *et al.* (2008) 'Composition effects on glass-forming ability and its indicator γ', *Intermetallics*, 16(3), pp. 410–417. doi: https://doi.org/10.1016/j.intermet.2007.12.002.

Lu, Z. P., Bei, H. and Liu, C. T. (2007) 'Recent progress in quantifying glass-forming ability of bulk metallic glasses', *Intermetallics*, 15(5–6), pp. 618–624. doi: 10.1016/j.intermet.2006.10.017.

Lu, Z. P. and Liu, C. T. (2003) 'Glass Formation Criterion for Various Glass-Forming Systems', *Physical Review Letters*, 91(11), p. 115505. doi: 10.1103/PhysRevLett.91.115505.

Lu, Z. P., Liu, C. T. and Porter, W. D. (2003) 'Role of yttrium in glass formation of Fe-based bulk metallic glasses', *Applied Physics Letters*, 83(13), pp. 2581–2583. doi: 10.1063/1.1614833.

Ma, E. (2003) 'Nanocrystalline Materials, Controlling plastic instability.', *Nature materials*, 2(1), pp. 7–8. doi: 10.1038/nmat797.

Makino, A. *et al.* (2008) 'Fe-metalloids bulk glassy alloys with high Fe content and high glass-forming ability', *Journal of Materials Research*. Cambridge University Press, 23(5), pp. 1339–1342. doi: 10.1557/JMR.2008.0180.

Manakari, V., Parande, G. and Gupta, M. (2016) *Selective Laser Melting of Magnesium and Magnesium Alloy Powders: A Review*, *Metals*. doi: 10.3390/met7010002.

Manh, H. H. (2010) *Micro and Nano-Scale Corrosion in Iron Based Bulk Metallic Glass SAM 1651 and Silver Cored MP35N LT Composite*. Available at: https://etd.ohiolink.edu/rws_etd/document/get/case1260391940/inline (Accessed: 20 February 2016).

Manvatkar, V., De, A. and DebRoy, T. (2015) 'Spatial variation of melt pool geometry, peak temperature and solidification parameters during laser assisted additive manufacturing process', *Materials Science and Technology*, 31(8), pp. 924–930. doi: 10.1179/1743284714Y.0000000701.

Martinez, R., Kumar, G. and Schroers, J. (2008) 'Hot rolling of bulk metallic glass in its supercooled liquid region', *Scripta Materialia*, 59(2), pp. 187–190. doi: 10.1016/j.scriptamat.2008.03.008.

Maskery, I. *et al.* (2016) 'Quantification and characterisation of porosity in selectively laser melted Al-Si10-Mg using X-ray computed tomography', *Materials Characterization*, 111, pp. 193–204. doi: 10.1016/j.matchar.2015.12.001.

Matsumoto, M. *et al.* (2002) 'Finite element analysis of single layer forming on metallic powder bed in rapid prototyping by selective laser processing', *International Journal of Machine Tools and Manufacture*, 42(1), pp. 61–67. doi: 10.1016/S0890-6955(01)00093-1.

Mercelis, P. and Kruth, J. (2006) 'Residual stresses in selective laser sintering and selective laser melting', *Rapid Prototyping Journal*, 12(5), pp. 254–265. doi: 10.1108/13552540610707013.

Miedema, A. R., Boom, R. and De Boer, F. R. (1975) 'On the heat of formation of solid alloys', *Journal of the Less Common Metals*, 41(2), pp. 283–298. doi: http://dx.doi.org/10.1016/0022-5088(76)90180-6.

Miller, J. (2010) *Devitrification Effects on the Structure and Corrosion of an Fe-based Bulk Metallic Glass*. Available at: http://etd.ohiolink.edu/send-pdf.cgi/Miller Jason.pdf?case1252371978.

Miller, M. and Liaw, P. (2008) *Bulk Metallic Glasses*. Springer US. doi: 10.1007/978-0-387-48921-6.

Mills, K. C. *et al.* (1998) 'Marangoni effects in welding', *Philosophical Transactions of the Royal Society A: Mathematical, Physical and Engineering Sciences*, 356(1739), pp. 911–925. doi: 10.1098/rsta.1998.0196.

Mondal, K. and Murty, B. S. (2005) 'On the parameters to assess the glass forming ability of liquids', *Journal of Non-Crystalline Solids*, 351(16–17), pp. 1366–1371. doi: 10.1016/j.jnoncrysol.2005.03.006.

Moskowitz, B. M. (1993) 'Micromagnetic Study of the Influence of Crystal Defects on Coercivity in Magnetite', *Journal of Geophysical Research*, 98(B10), pp. 18011–18026. doi: 10.1029/93JB01719.

Nishiyama, N., Amiya, K. and Inoue, A. (2007) 'Novel applications of bulk metallic glass for industrial products', *Journal of Non-Crystalline Solids*, 353(32), pp. 3615–3621. doi: https://doi.org/10.1016/j.jnoncrysol.2007.05.170.

Nishiyama, N., Amiya, K. and Inoue, A. (2007) 'Recent progress of bulk metallic glasses for strain-sensing devices', *Materials Science and Engineering: A*, 449–451, pp. 79–83. doi: https://doi.org/10.1016/j.msea.2006.02.384.

Nouri, A. S., Liu, Y. and Lewandowski, J. J. (2009) *Effects of thermal exposure and test temperature on structure evolution and hardness/viscosity of an iron-based metallic glass*, *Metallurgical and Materials Transactions A: Physical Metallurgy and Materials Science*. doi: 10.1007/s11661-008-9615-1.

Novikov, V. N., Ding, Y. and Sokolov, A. P. (2005) 'Correlation of fragility of supercooled liquids with elastic properties of glasses', *Physical Review E - Statistical, Nonlinear, and Soft Matter Physics*, 71(6), pp. 1–12. doi: 10.1103/PhysRevE.71.061501.

Nowosielski, R. and Babilas, R. (2007) 'Fabrication of bulk metallic glasses by centrifugal casting method', *Journal of Achievements in Materials and Manufacturing Engineering*, Vol. 20, n, pp. 487–490.

de Oliveira, M. F. *et al.* (2008) 'Thermodynamic and topological instability approaches for forecasting glass-forming ability in the ternary Al-Ni-Y system', *Journal of Alloys and Compounds*, 464(1–2), pp. 118–121. doi: 10.1016/j.jallcom.2007.09.094.

Pang, S. *et al.* (2002) 'Effects of Chromium on the Glass Formation and Corrosion Behavior of Bulk Glassy Fe-Cr-Mo-C-B Alloys.', *Materials Transactions*, 43(8), pp. 2137–2142. doi: 10.2320/matertrans.43.2137.

Pang, S. *et al.* (2004) 'Bulk glassy Ni(Co–)Nb–Ti–Zr alloys with high corrosion resistance and high strength', *Materials Science and Engineering: A*, 375–377, pp. 368–371. doi: https://doi.org/10.1016/j.msea.2003.10.152.

Pang, S. J. *et al.* (2002) 'Synthesis of Fe-Cr-Mo-C-B-P bulk metallic glasses with high corrosion resistance', *Acta Materialia*, 50(3), pp. 489–497. doi: 10.1016/S1359-6454(01)00366-4.

Parry, L., Ashcroft, I. A. and Wildman, R. D. (2016) 'Understanding the effect of laser scan strategy on residual stress in selective laser melting through thermo-mechanical simulation', *Additive Manufacturing*. Elsevier B.V., 12, pp. 1–15. doi: 10.1016/j.addma.2016.05.014.

Pauly, S. *et al.* (2013) 'Processing metallic glasses by selective laser melting', *Materials Today*, 16(1–2), pp. 37–41. doi: 10.1016/j.mattod.2013.01.018.

Petrzhik, M. *et al.* (2005) 'From Bulk Metallic Glasses to Amorphous Metallic Coatings', in *ISMANAM-2004*. Trans Tech Publications (Journal of Metastable and Nanocrystalline Materials), pp. 101–104. doi: 10.4028/www.scientific.net/JMNM.24-25.101.

Pohl, H. *et al.* (2001) 'Thermal stresses in direct metal laser sintering', *Proceedings of the SFF Symposium*, pp. 366–372. Available at: http://edge.rit.edu/edge/P10551/public/SFF/SFF 2001 Proceedings/2001 SFF Papers/41-Pohl.pdf.

Polivnikova, T. (2015) ‘Study and Modelling of the Melt Pool Dynamics during Selective Laser Sintering and Melting’, 6826.

Ponnambalam, V., Poon, S. J. and Shiflet, G. J. (2004) ‘Fe-based bulk metallic glasses with diameter thickness larger than one centimeter’, *Journal of Materials Research*, 19(5), pp. 1320–1323. doi: 10.1557/JMR.2004.0176.

Pozdnyakov, V. A. and Glezer, A. M. (2002) ‘Structural mechanisms of fracture in amorphous metallic alloys’, *Doklady Physics*, 47(12), pp. 852–855. doi: 10.1134/1.1536214.

Promoppatum, P. *et al.* (2017) ‘A Comprehensive Comparison of the Analytical and Numerical Prediction of the Thermal History and Solidification Microstructure of Inconel 718 Products Made by Laser Powder-Bed Fusion’, *Engineering*, 3(5), pp. 685–694. doi: 10.1016/J.ENG.2017.05.023.

Qing, W. and Bing, S. H. I. (2005) ‘Writing Process and Skills of Applications for Scientific Researching Funding Projects’, *Dianzi Keji Daxue Xuebao/Journal of the University of Electronic Science and Technology of China*, 10(20030614001), pp. 10–13. Available at: https://www.scopus.com/inward/record.uri?eid=2-s2.0-21144451679&partnerID=40&md5=bf0ceb15315c1cedb325596be6392a84.

Qiu, C., Adkins, N. J. E. and Attallah, M. M. (2013) ‘Microstructure and tensile properties of selectively laser-melted and of HIPed laser-melted Ti-6Al-4V’, *Materials Science and Engineering A*. Elsevier, 578, pp. 230–239. doi: 10.1016/j.msea.2013.04.099.

R.P. Hoogeboom (2016) ‘Thermal modelling of Selective Laser Melting: a semi-analytical approach’, *Master Thesis*, pp. 5–7.

Rao, B. S., Bhatt, J. and Murty, B. S. (2007) ‘Identification of compositions with highest glass forming ability in multicomponent systems by thermodynamic and topological approaches’, *Materials Science and Engineering A*, 448–451, pp. 211–214. doi: 10.1016/j.msea.2005.12.092.

Read, N. *et al.* (2015) ‘Selective laser melting of AlSi10Mg alloy: Process optimisation and mechanical properties development’, *Materials and Design*. Elsevier Ltd, 65, pp. 417–424. doi: 10.1016/j.matdes.2014.09.044.

Rice, J. R. and Thomson, R. (1974) ‘Ductile versus brittle behaviour of crystals’, *Philosophical Magazine*, 29(1), pp. 73–97. doi: 10.1080/14786437408213555.

Roberts, I. A. *et al.* (2009) ‘A three-dimensional finite element analysis of the temperature field during laser melting of metal powders in additive layer manufacturing’, *International Journal of Machine Tools and Manufacture*. Elsevier, 49(12–13), pp. 916–923. doi: 10.1016/j.ijmachtools.2009.07.004.

Roberts, I. A. (2012) *Investigation of Residual Stresses in the Laser Melting of Metal Powders in Additive Layer*.

Safdar, S. *et al.* (2013) 'An anisotropic enhanced thermal conductivity approach for modelling laser melt pools for Ni-base super alloys', *Applied Mathematical Modelling*. Elsevier Inc., 37(3), pp. 1187–1195. doi: 10.1016/j.apm.2012.03.028.

Schneider, S. (2001) 'Bulk metallic glasses', *Journal of Physics: Condensed Matter*, 13(34), p. 7723. Available at: http://stacks.iop.org/0953-8984/13/i=34/a=316.

Schroers, J., Nguyen, T. and Croopnick, G. A. (2007) 'A novel metallic glass composite synthesis method', *Scripta Materialia*, 56(2), pp. 177–180. doi: 10.1016/j.scriptamat.2006.08.048.

Schroers, J., Pham, Q. and Desai, A. (2007) 'Thermoplastic forming of bulk netallic glass - A technology for MEMS and microstructure fabrication', *Journal of Microelectromechanical Systems*, 16(2), pp. 240–247. doi: 10.1109/JMEMS.0007.892889.

Schroers, J., Veazey, C. and Johnson, W. L. (2003) 'Amorphous metallic foam', *Applied Physics Letters*, 82(3), pp. 370–372. doi: 10.1063/1.1537514.

Schuh, C. A., Hufnagel, T. C. and Ramamurty, U. (2007) 'Mechanical behavior of amorphous alloys', *Acta Materialia*, 55(12), pp. 4067–4109. doi: 10.1016/j.actamat.2007.01.052.

Seghairi, N. *et al.* (2012) 'Preparation and Characterization of Fe-Based Metallic Glasses with Pure and Raw Elements', *Chinese Physics Letters*, 29(11), p. 118102. doi: 10.1088/0256-307X/29/11/118102.

Seidel, M., Eckert, J. and Schultz, L. (1995) 'Formation of amorphous Zr-Al-Cu-Ni with a large supercooled liquid region by mechanical alloying', *Journal of Applied Physics*, 77(10), pp. 5446–5448. doi: 10.1063/1.359239.

Shan, X., Ha, H. and Payer, J. H. (2009) 'Comparison of crevice corrosion of fe-based amorphous metal and crystalline Ni-Cr-Mo alloy', *Metallurgical and Materials Transactions A: Physical Metallurgy and Materials Science*, 40(6), pp. 1324–1333. doi: 10.1007/s11661-008-9697-9.

Shen, J. *et al.* (2005) 'Exceptionally high glass-forming ability of an FeCoCrMoCBY alloy', *Applied Physics Letters*, 86(15), pp. 1–3. doi: 10.1063/1.1897426.

Shi, Y. *et al.* (2007) 'Temperature gradient mechanism in laser forming of thin plates', *Optics and Laser Technology*, 39(4), pp. 858–863. doi: 10.1016/j.optlastec.2005.12.006.

Shih, J. and Brugger, R. (1992) 'Gadolinium as a neutron capture therapy agent', *Med Phys*, 19(3), pp. 733–744. doi: 10.1118/1.596817.

Shiomi, M. *et al.* (1999) 'Finite element analysis of melting and solidifying processes in laser rapid prototyping of metallic powders', *International Journal of Machine Tools and Manufacture*, 39(2), pp. 237–252. doi: 10.1016/S0890-6955(98)00036-4.

Shiomi, M. *et al.* (2004) 'Residual Stress within Metallic Model Made by Selective Laser Melting Process', *CIRP Annals - Manufacturing Technology*, 53(1), pp. 195–198. doi: 10.1016/S0007-8506(07)60677-5.

Song, B. *et al.* (2012) 'Process parameter selection for selective laser melting of Ti6Al4V based on temperature distribution simulation and experimental sintering', *International Journal of Advanced Manufacturing Technology*, 61(9–12), pp. 967–974. doi: 10.1007/s00170-011-3776-6.

Spierings, A. B., Herres, N. and Levy, G. (2011) 'Influence of the particle size distribution on surface quality and mechanical properties in AM steel parts', *Rapid Prototyping Journal*, 17(3), pp. 195–202. doi: 10.1108/13552541111124770.

Sun, H. and Flores, K. M. (2010) 'Microstructural Analysis of a Laser-Processed Zr-Based Bulk Metallic Glass', *Metallurgical and Materials Transactions A*, 41(7), pp. 1752–1757. doi: 10.1007/s11661-009-0151-4.

Suryanarayana, C. and Inoue, A. (2011) *Bulk Metallic Glasses*.
Suryanarayana, C. and Inoue, A. (2013) 'Iron-based bulk metallic glasses', *International Materials Reviews*, 58(3), pp. 131–166. doi: 10.1179/1743280412Y.0000000007.

Tan, M. W. *et al.* (1996) 'The role of chromium and molybdenum in passivation of amorphous Fe-Cr-Mo-P-C alloys in de-aerated 1 M HCl', *Corrosion Science*, 38(12), pp. 2137–2151. doi: 10.1016/S0010-938X(96)00071-6.

Tanaka, T. (1982) 'Data book on fatigue strength of metallic materials', *Soc Mater Sci, Japan*, 1, p. 546.

The International Nickel Company (1982) 'Properties of Some Metals and Alloys', p. 80. Available at: https://www.nickelinstitute.org/~/media/files/technicalliterature/propertiesofsomemetalsandalloys_297_.pdf.

Thijs, L. *et al.* (2013) 'Fine-structured aluminium products with controllable texture by selective laser melting of pre-alloyed AlSi10Mg powder', *Acta Materialia*, 61(5), pp. 1809–1819. doi: 10.1016/j.actamat.2012.11.052.

Thomas, M., Baxter, G. J. and Todd, I. (2016) 'Normalised model-based processing diagrams for additive layer manufacture of engineering alloys', *Acta Materialia*. Elsevier Ltd, 108, pp. 26–35. doi: 10.1016/j.actamat.2016.02.025.

Tolochko, N. K. *et al.* (2000) 'Absorptance of powder materials suitable for laser sintering', *Rapid Prototyping Journal*, 6(3), pp. 155–161. doi: 10.1108/13552540010337029.

Trifonov, A. S. *et al.* (2015) 'Difference in charge transport properties of Ni-Nb thin films with native and artificial oxide', *Journal of Applied Physics*, 117(12), p. 125704. doi: 10.1063/1.4915935.

Turnbull, D. (1969) ‘Under what conditions can a glass be formed?’, *Contemporary Physics*. Taylor & Francis, 10(5), pp. 473–488. doi: 10.1080/00107516908204405.

Vandenbroucke, B. and Kruth, J. (2007) ‘Selective laser melting of biocompatible metals for rapid manufacturing of medical parts’, *Rapid Prototyping Journal*, 13(4), pp. 196–203. doi: 10.1108/13552540710776142.

Vilaro, T., Colin, C. and Bartout, J. D. (2011) ‘As-fabricated and heat-treated microstructures of the Ti-6Al-4V alloy processed by selective laser melting’, *Metallurgical and Materials Transactions A: Physical Metallurgy and Materials Science*, 42(10), pp. 3190–3199. doi: 10.1007/s11661-011-0731-y.

Wang, J. *et al.* (2012) ‘Rapid Degradation of Azo Dye by Fe-Based Metallic Glass Powder’, *Advanced Functional Materials*, 22(12), pp. 2567–2570. doi: 10.1002/adfm.201103015.

Wang, J.-Q. *et al.* (2012) ‘Excellent capability in degrading azo dyes by MgZn-based metallic glass powders’, *Scientific Reports*. The Author(s), 2, p. 418. Available at: http://dx.doi.org/10.1038/srep00418.

Wang, W. H. *et al.* (2004) ‘Enhancement of the soft magnetic properties of FeCoZrMoWB bulk metallic glass by microalloying’, *Journal of Physics: Condensed Matter*, 16(21), pp. 3719–3723. doi: 10.1088/0953-8984/16/21/020.

Wang, W. H. (2012) ‘The elastic properties, elastic models and elastic perspectives of metallic glasses’, *Progress in Materials Science*. Elsevier Ltd, 57(3), pp. 487–656. doi: 10.1016/j.pmatsci.2011.07.001.

Wang, Y. *et al.* (2004) ‘Dynamic adjustment of execution order in real-time databases’, in *18th International Parallel and Distributed Processing Symposium, 2004. Proceedings.*, pp. 87–93. doi: 10.1109/IPDPS.2004.1303028.

Xia, L. *et al.* (2006a) ‘Thermodynamic modeling of glass formation in metallic glasses’, *Applied Physics Letters*, 88(17), pp. 1–4. doi: 10.1063/1.2198830.

Xia, L. *et al.* (2006b) ‘Thermodynamic modeling of glass formation in metallic glasses’, *Applied Physics Letters*, 88(17), p. 171905. doi: 10.1063/1.2198830.

Yadroitsev, I. (2009) *Selective laser melting: Direct manufacturing of 3D-objects by selective laser melting of metal powders*. Saarbrücken, Germany: LAP LAMBERT Academic Publishing AG & Co. KG.

Yadroitsev, I., Bertrand, P. and Smurov, I. (2007) ‘Parametric analysis of the selective laser melting process’, *Applied Surface Science*, 253(19), pp. 8064–8069. doi: 10.1016/j.apsusc.2007.02.088.

Yamaura, S. *et al.* (2003) 'Hydrogen Permeation Characteristics of Melt-Spun Ni-Nb-Zr Amorphous Alloy Membranes', *MATERIALS TRANSACTIONS*, 44(9), pp. 1885–1890. doi: 10.2320/matertrans.44.1885.

Yang, G. *et al.* (2012) 'Laser solid forming Zr-based bulk metallic glass', *Intermetallics*. Elsevier Ltd, 22, pp. 110–115. doi: 10.1016/j.intermet.2011.10.008.

Yap, C. Y. *et al.* (2015) 'Review of selective laser melting: Materials and applications', *Applied Physics Reviews*, 2(4). doi: 10.1063/1.4935926.

Ye, X. and Shin, Y. C. (2014) 'Synthesis and characterization of Fe-based amorphous composite by laser direct deposition', *Surface and Coatings Technology*, 239, pp. 34–40. doi: 10.1016/j.surfcoat.2013.11.013.

Yu, H. *et al.* (2013) 'Ductile Biodegradable Mg-Based Metallic Glasses with Excellent Biocompatibility', *Advanced Functional Materials*, 23(38), pp. 4793–4800. doi: 10.1002/adfm.201203738.

Yuan, P. and Gu, D. (2015) 'Molten pool behaviour and its physical mechanism during selective laser melting of TiC/AlSi10Mg nanocomposites: simulation and experiments', *Journal of Physics D: Applied Physics*. IOP Publishing, 48(3), p. 35303. doi: 10.1088/0022-3727/48/3/035303.

Zaeh, M. F. and Branner, G. (2010) 'Investigations on residual stresses and deformations in selective laser melting', *Production Engineering*, 4(1), pp. 35–45. doi: 10.1007/s11740-009-0192-y.

Zberg, B., Uggowitzer, P. J. and Löffler, J. F. (2009) 'MgZnCa glasses without clinically observable hydrogen evolution for biodegradable implants', *Nature Materials*. Nature Publishing Group, 8, p. 887. Available at: http://dx.doi.org/10.1038/nmat2542.

Zehner, P. and Schulunder, E. U. (1970) 'Thermal conductivity of granular materials at moderate temperature (in German)', *Chemie-Ingenieur-Technik*, 42(14), pp. 933–941. Available at: http://www.scopus.com/inward/record.url?eid=2-s2.0-0014813535&partnerID=tZOtx3y1.

Zeng, K. *et al.* (2015) 'Comparison of 3DSIM thermal modelling of selective laser melting using new dynamic meshing method to ANSYS', *Materials Science and Technology*. Taylor & Francis, 31(8), pp. 945–956. doi: 10.1179/1743284714Y.0000000703.

Zhang, S. *et al.* (2011) 'Effects of Powder Characteristics on Selective Laser Melting of 316L Stainless Steel Powder', *Advanced Materials Research*. Trans Tech Publications, 189–193, pp. 3664–3667. doi: 10.4028/www.scientific.net/AMR.189-193.3664.

Zhang, W., Ishihara, S. and Inoue, A. (2002) 'Synthesis and Mechanical Properties of Cu-Based Cu-Zr-Ti Bulk Glassy Alloys Containing ZrC Particles.', *Materials Transactions*, 43(7), pp. 1767–1770. doi: 10.2320/matertrans.43.1767.

Zhao, X. *et al.* (2009) 'The effect of hot isostatic pressing on crack healing, microstructure, mechanical properties of Rene88DT superalloy prepared by laser solid forming', *Materials Science and Engineering A*, 504(1–2), pp. 129–134. doi: 10.1016/j.msea.2008.12.024.

Zheng, B. *et al.* (2009) 'Processing and behavior of fe-based metallic glass components via laser-engineered net shaping', *International Journal of Powder Metallurgy (Princeton, New Jersey)*, 45(4), pp. 27–39. doi: 10.1007/sll661-009-9828-y.

Zhou, X. *et al.* (2015) '3D-imaging of selective laser melting defects in a Co-Cr-Mo alloy by synchrotron radiation micro-CT', *Acta Materialia*. Acta Materialia Inc., 98, pp. 1–16. doi: 10.1016/j.actamat.2015.07.014.